An entropic approach to magnetized nonlocal transport and other kinetic phenomena in high-energy-density plasmas

Dario del Sorbo

Thesis

Submitted in fulfillment of the requirements for the degree of

Doctor of Philosophy in Physics

Université de Bordeaux, École doctorale des sciences et de l'ingénieur,
Section: Astrophysique, Plasmas, Nucléaire

An Entropic Approach to Magnetized Nonlocal Transport and Other Kinetic Phenomena in High-Energy-Density Plasmas

---

by

Dario Del Sorbo

supervised by
J.-L. Feugeas
Ph. Nicolaï
M. Olazabal-Loumé
V. Tikhonchuk

Defended on the 14th of December (2015) in Talence (France)
Board of examiners:

Ghizzo, A.	Professor, Univ. de la Lorraine (France)	**Reviewer**
Honrubia, J.	Professor, Univ. Politécnica de Madrid (Spain)	**Reviewer**
Gorini, G.	Professor, Univ. di Milano-Bicocca (Italy)	**Jury President**
Volpe, L.	Professor, Univ. de Salamanca (Spain)	**Examiner**
Feugeas, J.-L.	Research Engineer, CELIA-CEA (France)	**Examiner**
Nicolaï, Ph.	Research Engineer, CELIA-CEA (France)	**Examiner**
Olazabal-Loumé, M.	Research Engineer, CESTA-CEA (France)	**Examiner**
Tikhonchuk, V.	Professor, Univ. de Bordeaux-CELIA (France)	**Examiner**

An expert is a man who has made all the mistakes which can be made in a very narrow field.

Niels Bohr

Acknowledgments

English version

Many many people have to be acknowledge for the realization of this work. I hope to do not forget anyone...

As first, since the Ph.D. represents the end of 21 years of studies, I want to thank my family, starting from my grandparents. They had not the possibility to study so much, living their youth between two world wars. Nevertheless they understood the importance of knowledge and incited sons and grandsons to reach the highest level of competence. In particular I want to thank my grandmother Anna Maria, who passed away two years ago, after dedicating 95 years to her family.

The greatest gratitude goes to my parents which financed my studies, but also incited me to always follow my passions. Another thanks is for my brother with whom I shared the passion for mathematics but even more the difficulties of studies.

I want to thank my uncles and great-uncles for instilling me the passion for the nature, the science and the fundamental knowledge.

Without the help of my supervisors I would have never succeed to complete my thesis work. They have thought me a research method but also to go deeper in detail and to never give up to difficulties. In particular, thanks to Philippe for teaching me the importance of scientific doubt and skepticism, to Jean-Luc, for teaching me the importance of working with curiosity and passion, and to Vladimir, for being always ready to help me, and for teaching me that a result is only a starting point for a new challenge. Thank you also to Marina for giving me the opportunity to start this Ph.D. thesis work.

A remarkable thanks goes to my reviewers (Alain Ghizzo and Javier Honrubia) for accepting to read and correct my manuscript, and also to the other jury members (Giuseppe Gorini and Luca Volpe) for accepting to join the committee. It was an honor to discuss with you about my work.

My gratitude goes also to Bruno, for being always ready to help me, and to Dimitri, who, as first, gave me the possibility of being here and to show my abilities, also revealing to be a good friend.

Thank you to all the members of the CELIA lab which have proved to be always ready to help, during the working time, and to have fun together, after work. I want to thank in particular my Ph.D. mates Basil (so-called "BaBa"), Pierre, Arnaud, Mokrane, Julien, Aurore, Sébastien, Jocelan but also my "big brothers" Xavier and Guillaume for the friendship outside the work.

Thank you to the CEA for the three years financing and the opportunity to travel around the world.

I am very grateful to my girlfriend, who supported me psychologically, but also practically, by correcting text grammar and helping to overcome my defects in writing. She also tried to instill me a poetic vision of nature, without much success.

Last but not least, thank you to my friends (Manuéla, Alice, Esthera, Mattia, Federica, Claudio, Daniele, Silvia, Valeria, Vincent, Vittorio, Gemma, Marina, Luca and Roberto). During the difficulties they have always been present, ready to distract and entertain me. In particular, thank you to my flatmates (Gabriele and Giovanni, but also Nicola and Andrea), also for patience and flexibility, and thank you to Fréngo, for translating the acknowledgments in French.

Version française

Je dois remercier de nombreuses personnes pour la réalisation de ce travail. J'espère n'oublier personne...

Tout d'abord, étant donné que le doctorat représente la fin de 21 années d'études, je voudrais remercier ma famille, en commençant par mes grand-parents. Ils n'ont pas eu la possibilité d'étudier autant qu'ils l'auraient voulu, passant leur jeunesse entre deux grandes guerres. Néanmoins il ont compris l'importance de la connaissance et ont incité leurs enfants et petits enfants à atteindre le plus haut niveau de compétence. Je remercie particulièrement ma grand mère Anna Maria, décédée il y a deux ans après avoir dédié 95 ans à sa famille.

Ma plus grande gratitude va à mes parents qui ont financés mes études, mais m'ont aussi incités à toujours suivre mes passions. Je remercie également mon frère avec qui je partage la passion des mathématiques mais plus encore les difficultés lors des études.

Je veux remercier mes oncles et grand-oncles pour avoir instillé en moi la passion de la nature, des sciences et des connaissances.

Sans l'aide de mes encadrants je n'aurais jamais réussi à compléter ce travail de thèse. Ils m'ont enseigné une méthode de recherche mais aussi à être minutieux et à ne jamais baisser les bras face aux difficultés. Plus particulièrement je remercie Philippe pour m'avoir appris l'importance du scepticisme et du doute en sciences, je remercie Jean-Luc pour m'avoir appris à travailler avec curiosité et passion, et enfin je remercie Vladimir pour avoir été toujours présent pour m'aider, et pour m'avoir enseigné qu'un résultat n'est que le point de départ d'un nouveau défi. Je remercie également Marina pour m'avoir donné l'opportunité de commencer ce travail de thèse.

Des remerciements remarquables vont à mes rapporteurs (Alain Ghizzo et Javier Honrubia) pour avoir accepté de lire et corriger mon manuscrit et aussi aux autres membres de jury (Giuseppe Gorini et Luca Volpe) pour avoir accepté de se joindre au comité. C'était un honneur de discuter avec vous de mon travail.

Ma gratitude va aussi à Bruno, pour être été toujours prêt à m'aider, et à Dimitri, qui, le premier, m'a offert la possibilité d'être ici et montrer mes capacités, aussi en se révélant un bon ami.

Je remercie tous les membres du CELIA qui ont été toujours prêts à m'aider, tout au long de cette thèse, mais aussi à passer de bons moments ensemble après le travail. Je veux remercier en particulier mes camarades de doctorat Basil (appelé "Baba"), Pierre, Arnaud, Mokrane, Julien, Aurore, Sébastien, Jocelan mais aussi mes "grands frères" Xavier et Guillaume pour leur amitié après le travail.

Je remercie le CEA pour le financement de ces trois années et pour m'avoir offert l'opportunité de voyager à travers le monde.

Je suis très reconnaissant à ma copine qui m'a soutenu psychologiquement mais aussi, de façon plus matérielle, en m'aidant à surpasser mes défaut dans la rédaction et pour avoir corrigé ma grammaire. Elle a également essayé d'instiller une fibre poétique dans

ma vision de la nature, sans succès.

Enfin, merci à tous mes amis (Manuéla, Alice, Esthera, Mattia, Federica, Claudio, Daniele, Silvia, Valeria, Vincent, Vittorio, Gemma, Marina, Luca et Roberto). Durant toutes mes difficultés ils ont toujours été présents, prêts à me soutenir et à s'amuser avec moi. En particulier je remercie mes colocataires (Gabriele et Giovanni, mais aussi Nicola et Andrea) pour leur patience et leur flexibilité. Je remercie également Fréngo pour avoir traduit ces remerciements en français.

Versione italiana

Devo ringraziare moltissime persone per la realizzazione di questo lavoro. Spero di non dimenticarne nessuna...

Prima di tutto, dato che il dottorato rappresenta la fine di 21 anni di studio, voglio ringraziare la mia famiglia, cominciando dai nonni. Loro non ebbero la possibilità di studiare così tanto, vivendo la loro gioventù tra due guerre mondiali. Tuttavia compresero l'importanza della conoscenza e incitarono i loro figli e nipoti a raggiungere sempre il più alto grado di competenza. In particolare voglio ringraziare mia nonna Anna Maria, che ci ha lasciato due anni fa, dopo aver dedicato 95 anni alla sua famiglia.

La maggiore gratitudine va ai miei genitori che hanno finanziato i miei studi, ma mi hanno anche sempre spronato a seguire le mie passioni. Un altro ringraziamento va a mio fratello, con cui ho condiviso la passione per la matematica ma soprattutto le difficoltà negli studi.

Voglio ringraziare anche i miei zii e prozii per avermi instillato la passione per la natura, la scienza e la conoscenza fondamentale.

Senza l'aiuto dei miei responsabili non sarei mai riuscito a completare il mio lavoro di tesi. Loro mi hanno insegnato un metodo di ricerca ma anche ad andare sempre più a fondo e a non arrendermi mai di fronte alle difficoltà. In particolare, grazie a Philippe per avermi insegnato l'importanza del dubbio e dello scetticismo scientifico, a Jean-Luc, per avermi insegnato l'importanza di lavorare con curiosità e passione, e a Vladimir, per essere sempre stato pronto ad aiutarmi, e per avermi insegnato che ogni risultato è solo il punto di partenza per una nuova sfida. Grazie anche a Marina per avermi dato l'opportunità di questo dottorato.

Un ringraziamento particolare va ai miei controrelatori (Alain Ghizzo e Javier Honrubia) per aver accettato di leggere e correggere la mia tesi e anche agli altri membri della giuria (Giuseppe Gorini e Luca Volpe) per aver accettato di unirsi al comitato. È stato un onore discutere del mio lavoro con voi.

La mia gratitudine va anche a Bruno, per essere sempre stato pronto ad aiutarmi, e a Dimitri, che per primo mi ha dato la possibilità di essere qui a mostrare le mie abilità, rivelandosi anche un buon amico.

Grazie a tutti i membri del CELIA, che si sono dimostrati sempre pronti ad aiutarmi, durante l'orario di lavoro, e a divertirsi insieme, dopo. Voglio ringraziare in particolare i miei compagni di dottorato Basil (detto "Baba"), Pierre, Arnaud, Mokrane, Julien, Aurore, Sébastien, Jocelan ma anche i "fratelli maggiori" Xavier et Guillaume per la loro amiciza fuori dall'ufficio.

Grazie al CEA per i tre anni di finanziamento e l'opportunità di aver viaggiato intorno al mondo.

Sono molto grato alla mia ragazza che mi ha supportato psicologicamente, ma anche in pratica, correggendo la grammatica e aiutandomi a superare i miei difetti di scrittura.

Ha anche provato a instillarmi una visione poetica della natura, con scarso successo.

Infine, ringrazio i miei amici (Manuéla, Alice, Esthera, Mattia, Federica, Claudio, Daniele, Silvia, Valeria, Vincent, Vittorio, Gemma, Marina, Luca e Roberto). Durante le difficoltà sono sempre stati presenti, pronti a distrarmi o a farmi divertire. In particolare, ringrazio i miei coinquilini (Gabriele e Giovanni, ma anche Nicola e Andrea), anche per la loro pazienza e flessibilità, e ringrazio Fréngo, per tradurmi i ringraziamenti in francese.

Abstract

Hydrodynamic simulations in high-energy-density physics and inertial confinement fusion require a detailed description of energy fluxes. The leading mechanism is the electron transport, which can be a nonlocal phenomenon that needs to be described with quasi-stationary and simplified Fokker-Planck models in large scale hydrodynamic codes.

My thesis is dedicated to the development of a new nonlocal transport model based on a fast-moving-particles collision operator and on a first moment Fokker-Planck equation, simplified with an entropic closure relation. Such a closure enables a better description of the electron distribution function in the limit of high anisotropies, where small scale electrostatic instabilities could be excited.

This new model, so called M1, is successfully compared with the well known nonlocal electron transport model proposed by Schurtz, Nicolaï and Busquet, using different collision operators, and with the reduced Fokker-Planck model, based on a small-anisotropies polynomial closure relation (P1). Several typical configurations of heat transport are considered.

We show that the M1 entropic model may operate in two and three dimensions and is able to account for electron transport modifications in external magnetic fields. Moreover, our model enables to compute realistic electron distribution functions, which can be used for kinetic studies, as for the plasma stability in the transport zone. It is demonstrated that the electron energy transport may strongly modify damping of Langmuir and ion acoustic waves, while the simplified nonlocal transport models are not able to describe accurately the modifications of the distribution function and plasma wave damping.

The structure of the M1 model allows to naturally take into account self-generated magnetic fields, which play a crucial role in multidimensional simulations. Moreover, magnetic fields could also be used for the focusing of energetic particles in alternative ignition schemes. The M1 model reproduces the results of the local transport theory in plasma, developed by Braginskii, in a broad range of degrees of magnetization and predicts new results in the nonlocal regime.

This work constitutes a first validation of the entropic closure assumption in the weakly-anisotropic regime. It can be added to the existing tests, in the strongly-anisotropic regimes.

KEYWORDS: Inertial confinement fusion, High-energy-density physics, Laser-produced plasmas, Hydrodynamic simulation, Nonlocal heat transport, Plasma microscopic stability.

Contents

Chapter 1

Introduction

Matter in a thermodynamic equilibrium can be classified by its density and temperature. In this way, Fig. 1.1 shows the classification of most of the known matter. In the x-axis is plotted the mass density and, in the y-axis, the temperature. Both are given in a logarithmic scale, in order to represent different regimes which can be found in nature.

In the left-bottom of Fig. 1.1, we find unionized matter. Increasing the temperature (moving from the bottom to the top), it becomes partially ionized. Increasing more the temperature, we reach a state where the total pressure (internal and radiation) attains the value of 1 Mbar and the matter becomes radiation-dominated and strongly ionized.

Proceeding from the left-bottom to the right (increasing density), we meet two curves: strongly coupled and Fermi degenerate boundaries. Under the strongly coupled curve, collective fields and binary particle interactions define the matter structure. The Fermi

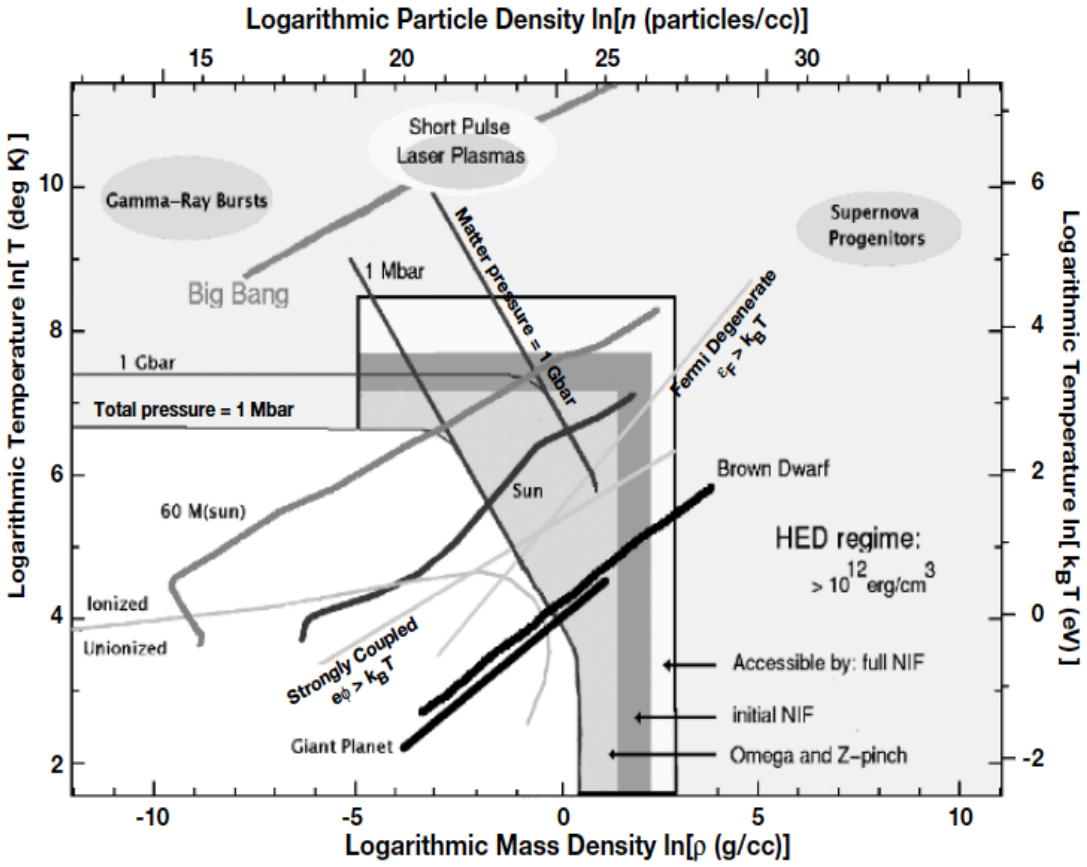

Figure 1.1: Regimes of HED physics, classified by their mass density (x-axis) and temperature (y-axis). The figure is taken from the book by R. P. Drake [1].

degeneration curve separates the classical matter (up) from the matter in which electron quantum effects are dominant (down). We see that both strongly coupled and Fermi degenerate curves span ionized (plasma) states as well as solid and liquid states. In this boundary region stands the warm and dense matter, a particular state mixing multiparticle, quantum and plasma effects. Increasing the density, we meet the 1 Mbar curve, that represents the region where the internal pressure is comparable to the energy density of an hydrogen atom. Matter under such a pressure behaves more as composed by electrons and ions than as neutral particles. Therefore, under such a pressure, matter becomes ionized. Ionized matter is classified as plasma, but classical plasma theories can be applied only to rarefied ionized gasses. The proprieties of dense matter at such a pressure are not well known. Systems subjected to a pressure higher than 1 Mbar are defined as high-energy-density (HED) plasmas [1] and are denoted by grey, in Fig. 1.1.

Many astrophysical phenomena belong to the HED states.

Stars and planets are represented in figure, from their core (top of the curve) to their external surface. Brown dwarfs as well as giant planets are composed by regimes of matter, which span from HED to strongly coupled and Fermi degenerate states. Our Sun, as well as more massive stars, span between HED and classical ionized and unionized matter.

Gamma ray bursts are the most energetic process ever observed in the universe. They are in the radiation-dominated regime of HED physics (the right side of Fig. 1.1). Even last stages of the big bang evolution span this regime.

Supernova progenitors are the astrophysical states of matter, which completely belong to the matter-dominated regime of HED physics (the left side of Fig. 1.1). They are created in collisions of two white dwarfs, which lead to a collapse of stars at the early stage of the universe evolution.

In the description of this figure we meet many natural phenomena, which are situated in the HED domain. All of them are related to astrophysics. However, on the Earth, in our laboratories, we are able to produce such conditions, thanks to Z-pinch and lasers. Future generations of lasers will be able to create short living plasmas, which correspond to the conditions present at the earlier stages of the big bang. Among the recent generation of high energy lasers, we can find the Omega laser, in the laboratory of laser energetics of the University of Rochester, and the most powerful laser constructed nowadays: the National Ignition Facility (NIF), in the Laurence Livermore National Laboratory. The regimes of matter induced by these lasers are what we are interested to describe in this manuscript.

Research in HED regimes is performed for two main reasons: in order to study astrophysics in experiments (laboratory astrophysics) and to achieve a controlled production of nuclear energy from inertial confinement fusion (ICF). We describe what this research is about, respectively, in sections 1.1 and 1.2. In section 1.3 we present the way in which the HED matter can be created in laboratory, thanks to laser-matter interactions. In section 1.4, we overview the key process in laser-matter interaction, in the regimes of interest: the electron transport. Finally in section 1.5, we present the objective of this work and the way in which it is presented in this manuscript.

1.1 Laboratory astrophysics

The HED physics concerns astrophysical objects as well as laser created plasmas. The hig-energy lasers open new possibilities for studying many astrophysical phenomena in experiments. We consider two examples.

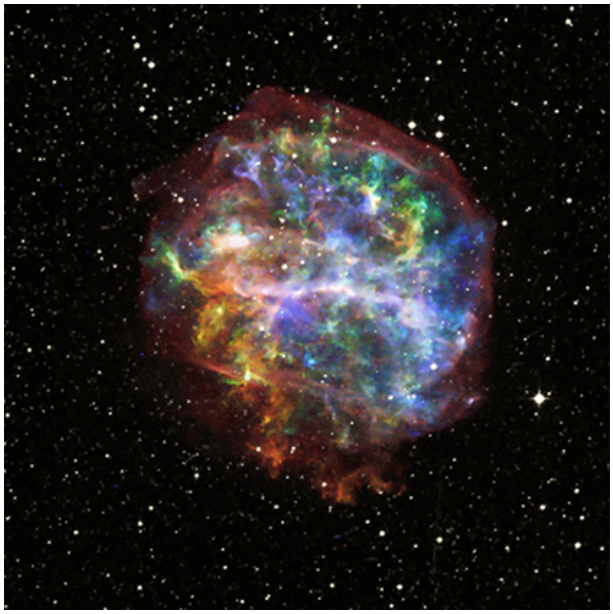

Figure 1.2: Hydrodyamic instabilities in a core-collapse supernova.

1.1.1 Dynamo in giant planets

By creating HED matter in laboratory one can perform an experimental study of realistic equations of state in extreme regimes, which have an astrophysical interest. An example is given by the study of the processes inside the core of giant planets, which are responsible for the generation of planetary magnetic fields [2, 3].

In particular, in the rocky core of Jupiter, the nature of the transition to metallic state constraints the way how the magnetic fields can be produced. The connection between equations of state and magnetic fields has been known for long time, but only in the 1980s the experimental study became possible, due to the emergence of pulsed power devices. They opened a possibility to accelerate material samples to high velocities and to create HED matter by the collision of a couple of them [1, 2].

1.1.2 Interface instabilities in core-collapse supernovae

The hydrodynamic theory describes many astrophysical processes. Hydrodynamic equations are scale invariant: what happens in a small laboratory experiment, in a short time, can be translated to the huge space and to long times. Thus HED physical experiments can reproduce astrophysical phenomena, as they happen. An example of well-scaled experiment is the study of interface instabilities in the core-collapse supernovae [1, 4].

Pre-supernova stars are composed of shells of different materials. The lighter are located on the surface while the core is composed by iron. The gravitational pressure compresses the matter and ignites the fusion reactions in each shell of the star, till to iron, which is the most stable nucleus. Once the star accumulates a Chandrasekhar mass (1.4 solar mass) of iron, the core collapses, generating a neutron star. At the same time, a blast wave emerges from the star, giving rise to the observed tremendous increase of luminosity. However, only a few percent of the hydrodynamic energy is emitted as visible light. This is due to some nonsymmetric motion related to hydrodynamic instabilities [5], shown in Fig. 1.2.

Experiments, dedicated to study the development of hydrodynamic instabilities in an appropriately scaled configuration, have been performed around the turn of the twenty-first century, with the purpose of code validation, direct observation and three dimensional analysis [4]. Using the Nova laser, the authors of [4] examined a single mode initial

perturbation of a planar target, reproducing the interface trajectory, predicted by theory.

We have seen two examples in which HED physics can be exploited in order to propose laboratory interpretation for astrophysical phenomena. However, the domain of laboratory astrophysics is very large and in expansion. In the next section we present the second main domain of research in HED physics: the ICF.

1.2 Inertial confinement fusion

HED physics experiments can be performed in order to reproduce astrophysical phenomena. However, a phenomenon as the gravitational collapse of a star cannot be reproduced as the gravitation force is too weak. The main purpose of ICF is to collapse matter by replacing the gravitational pressure with a pressure induced by high-power lasers. ICF schemes try to compress a deuterium-tritium target, till the state permitting to ignite nuclear fusion reactions and to confine thanks to the target mass. This behavior is described in detail in what follows.

1.2.1 Nuclear reactions

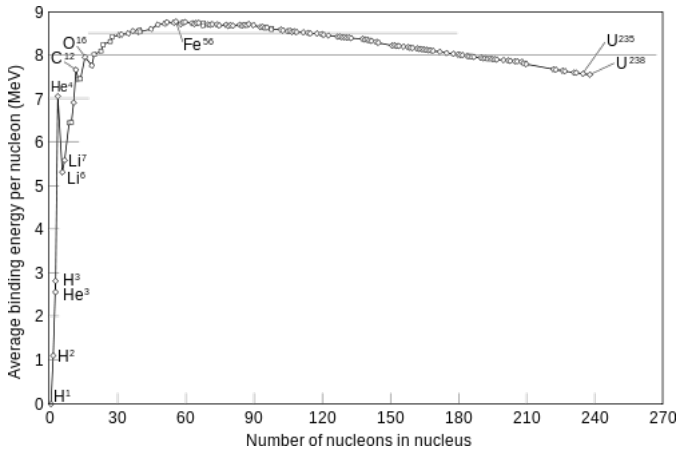

Figure 1.3: Nuclear binding energy per nucleon as a function of the nucleon number.

Figure 1.3 shows the binding energy per nucleon as a function of the nucleon number. We can make a distinction between nuclei lighter and heavier than iron. For nuclei heavier than iron, energy can be gained by splitting them. This process is called fission and it is performed since 1940s, in order to create large amounts of energy.

For nuclei lighter than iron, energy can be created by a fusion of two nuclei. In particular, one of the most energetic reactions is the fusion of hydrogen isotopes:

$$D + T \rightarrow {}^4\mathrm{He}(3.5\ \mathrm{MeV}) + \mathrm{n}(14.1\ \mathrm{MeV}), \tag{1.1}$$

where D and T are the deuterium and the tritium nuclei, ^{4}He is the nucleus of helium and n stands for neutron. Figure 1.4 summarizes the reaction schematically.

In stars, atoms are confined together by gravitation, for a long time, till the moment when a sufficiently large number of reactions occurs. The process of rapid increases of the reaction rate is called ignition and can be achieved when the time of confinement is longer than the characteristic time of nuclear interactions. The latter is defined as

$$\tau_{fus} = \frac{1}{\langle \sigma v \rangle\, n_i},$$

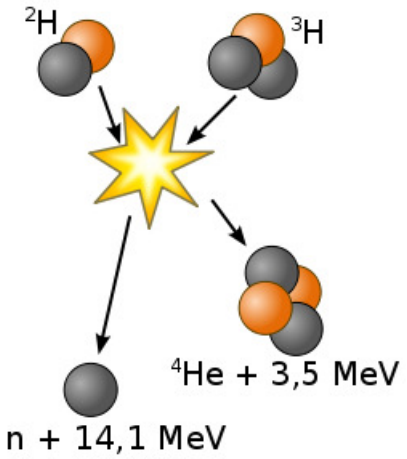

Figure 1.4: Scheme of the D-T reaction.

where n_i is the ion density, σ is the cross section for nuclear interactions and v the ion velocity. The reactivity $\langle \sigma v \rangle$ for the D-T reaction and other reactions is shown in Fig. 1.5, in function of the temperature. The ignition conditon can be expressed as

$$\tau_{fus} \langle \sigma v \rangle n_i > 1$$

and it is known as the Lawson criterion [6].

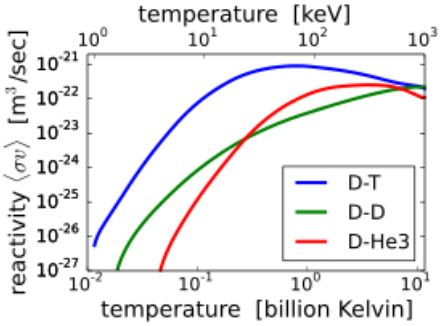

Figure 1.5: Reactivity, in function of the temperature, for nuclear reactions of hydrogen isotopes.

The gravitational confinement in stars happens in times long enough to satisfy the Lawson criterion.

In magnetic confinement fusion, the goal is to achieve plasma confinement by exploiting strong magnetic fields. These fields confine the plasma by forcing the particles to move along closed helical trajectories. The most efficient confinement is realized in a machine called Tokamak, which section is shown in Fig. 1.6. The Tokamak can achieve a particle density of about 10^{14} cm^{-3}, at a temperature attaining a few keV [7]. The time required to satisfy the Lawson criterion is $\sim$ 1 s. It is supposed that Tokamak may operate in a steady state regime.

It is also possible to confine the fuel exploiting the inertia of the target driven by laser compression. This approach is called ICF. In this type of confinement the density can be increased to $\sim 10^{25}$ cm^{-3} while the temperature to $\sim$ 10 keV [7]. For this regime, the confinement time required by the D-T reaction is $\sim$ 100 ps. Therefore, this is a pulsed process.

In the next sections we detail the different schemes of ICF.

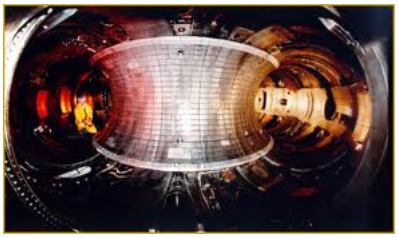

Figure 1.6: Tokamak for the magnetic confinement fusion.

1.2.2 Direct drive

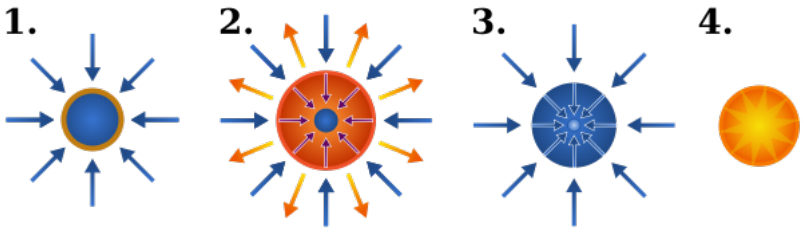

Figure 1.7: Direct drive scheme.

Historically, the first scheme proposed in order to obtain ICF, was a direct drive scheme [8]. It is resumed in Fig. 1.7: a spherical target composed by an equimolar mix of deuterium and tritium is spherically irradiated by high-power lasers (1). The target is compressed by the ablation pressure (2), till to reach a central ignition (3) which should be maintained, thanks to the inertia of the imploded mass, till a significant part of the fuel is burned (4) [7]. However, until nowadays, this has never happened, evidencing a lack of knowledge.

Open issues concerning the direct drive scheme are related to three main factors [7]. First of all, the compression uniformity is insufficient, due to the development of hydrodynamic instabilities, from small imperfections of target manufacturing or laser intensity. Secondly, theoretical predictions neglect, or strongly approximate, kinetic effects, which can play a dominant role in the regimes of interest. These are related to a nonlocal transport of energy by energetic electrons. At last, theoretical predictions hardly account for nonlinear laser-plasma interactions and parametric instabilities, such as two plasmon decay, stimulated Raman and Brillouin scattering.

The first point is beyond the scope of this manuscript, however in the next section we present different schemes whose aim is to improve the compression stability. In the next parts, we propose to improve the modeling in what concerns the second issue. A dominant role is played by the kinetic effects in the energy transport. We develop a model for their description, in such a way that it could be generalized to the hydrodynamic description of other kinetic effects. The analysis is performed in one and two dimensions, and a generalization to three dimensions can be easily achieved.

1.2.3 Stabilizing schemes

One of the main issues for ignition success is to control the stability of implosion. In the literature, many other schemes have been proposed in order to stabilize compression [9, 10, 11, 12].

In the indirect drive approach [9] the purpose is to compress the target using a black body radiation, obtained by the illumination of a closed gold cavity [13], as shown in

Fig. 1.8. In this way, the target is subjected to an irradiation governed by the Planck

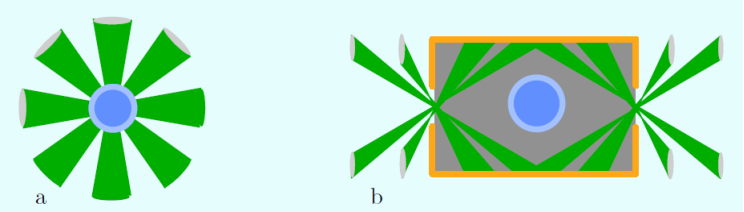

Figure 1.8: Two ignition schemes: the direct (a) and the indirect drive (b).

black body law, which is known to be uniform. The main advantage of the indirect drive is that the irradiation is more homogeneous than in a direct drive approach. It has been considered as the most promising approach to achieve the nuclear fusion. However, the NIF ignition failure has highlighted a gap between theoretical predictions and experimental results, which still needs to be filled. Even once the ignition will be achieved, this scheme is much more energy consuming, compared to the direct drive approach.

The recent advances in the development of petawatt laser pulses have opened new possibilities. The main purpose of the fast ignition scheme [10, 7] is to ignite the precompressed fuel by a separate external driver. This driver consists in a beam of relativistic electrons, accelerated by an ultra-intense laser pulse ($\sim 10^{19}$ W/cm^2). These electrons should be collimated by self-generated magnetic fields. A first approach consists in the addition of a cone, as shown in Fig. 1.9, in order to improve the collimation. The separation of the target compression from the hot spot formation opens a way to easier target designs. It still requires a high fuel compression, in order to keep ignition energy low, but it relaxes significantly the symmetry requirements: it allows non-spherical fuel configurations and a decrease in the amount of tritium in the target. However, in [14] it has been shown that the electron beam collimation cannot be easily achieved. Recent improvements propose a use of external magnetic fields in order to increase the collimation strength [15].

The shock ignition [11, 12] scheme consists in sending a second stronger shock at the end of the compression phase, shown in panel (3), in Fig. 1.7. This shock is induced by a laser pulse with a power of about $200 - 300$ TW. The spike power is compared in Fig. 1.10 with the compression pulse power. If it is synchronized, the converging shock should meet the principal shock when it is diverging. The shock transmitted to the center after collision should heat the core of the target, inducing ignition. This approach reduces significantly the energy required and could be realized with the existing lasers. However, at these regimes, laser-plasma interactions are strongly nonlinear and the effects of nonlocal energy transport should be important. This method has not been studied deeply yet but first results are encouraging [16].

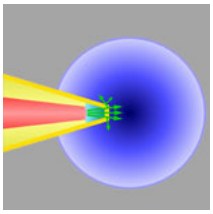

Figure 1.9: Fast ignition scheme.

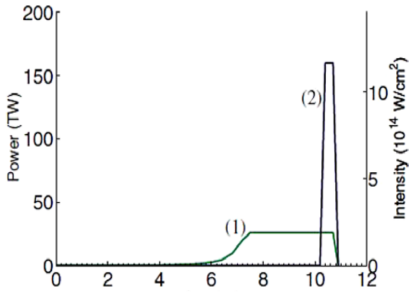

Figure 1.10: Laser pulses in shock ignition: (1) the compression pulse and (2) the shock pulse.

1.3 Laser-matter interaction at HED physics regimes

The laboratory HED physics finds a wide domain of applications. The aim of this section is to show how to create HED matter in laboratory.

There are two main ways to produce HED conditions at our regimes of interest: Z-pinch and laser compression.

The Z-pinch compression scheme consists in exploiting an axial electric current, which produces an azimuthal magnetic field cylindrically compressing the plasma [17]. Since in this manuscript we are mainly interested in a laser-produced HED matter, we do not detail this process and directly proceed to the discussion on the laser production.

The direct laser compression is driven by intense lasers, with intensities ranging between 10^{14} and 10^{15} W/cm^2. A detailed description of laser-matter interaction at these regimes can be found in [7]. We summarize the main processes in what follows.

Mainly, lasers deposit their energy at a critical density. The latter depends only on the laser wavelength. It reads

$$n_c = 1.1 \times 10^{21} \lambda_L^{-2} \text{ cm}^{-3}, \tag{1.2}$$

where λ_L must be expressed in μm. This density is typically 1-2 orders of magnitude smaller than the solid density, however, a part of the energy deposited penetrates deeper in plasma. The laser energy absorption decreases as the temperature increases.

Let us consider a solid target irradiated by an external laser source, with an energy flux q_{ex}. At first moments of interaction, the laser directly heats the solid target, as shown in panel (a) in Fig. 1.11. Since the absorption decreases with the temperature, as the solid is heated, the radiation can penetrate deeper.

After few tenths of picoseconds, the increase of temperature induces a hydrodynamic motion, called ablation flow, which generates a shock wave due to the momentum recoil. A shock wave is a discontinuity in the density profile, as shown in Fig. 1.12. It propagates supersonically and its dynamics is given by Rankine-Hugoniot equations. For perfect gases, the original density behind the shock increases by four times.

While the shock wave propagates inside the target, a rarefaction wave propagates in the opposite direction, inducing ablation. The recoil momentum maintains the shock pressure. If the target is optically thin, as in panel (b) in Fig. 1.11, the ablation is directly supported by the external laser source. On the contrary, if it is thick, the laser energy is deposited at the critical density. From there, it is transported to the ablation front with the heat flux q_{dif}, see panel (c) in Fig. 1.11. For low and intermediate ion charge materials, this heat flux is due to electron transport. For high ion charge materials, the radiative transport is equally important. Panels (b) and (c) in Fig. 1.11 correspond to quasi-stationary regime. The case (c) is of particular interest of HED physics. Along

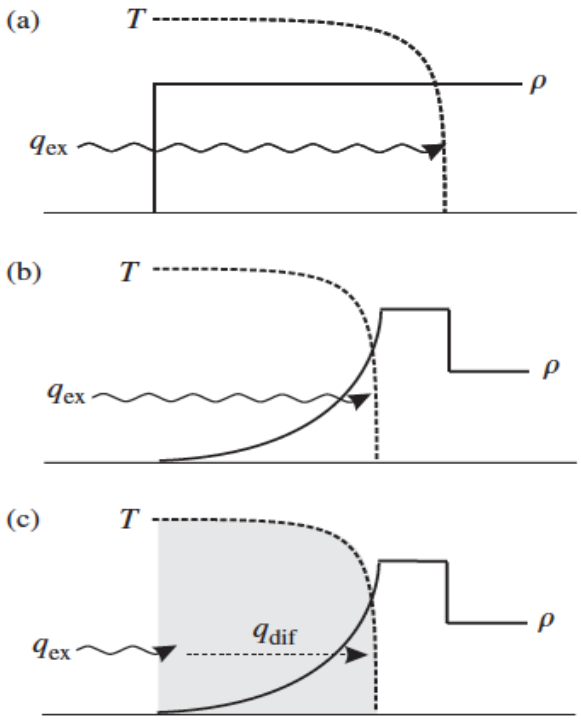

Figure 1.11: Types of heating, induced by laser-matter interaction: (a) supersonic heating, (b) ablative heating and (c) optically thick ablative heating. The figure is taken from [7].

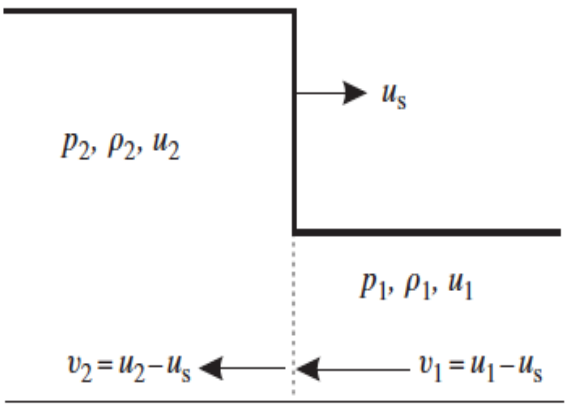

Figure 1.12: Scheme of a shock wave.

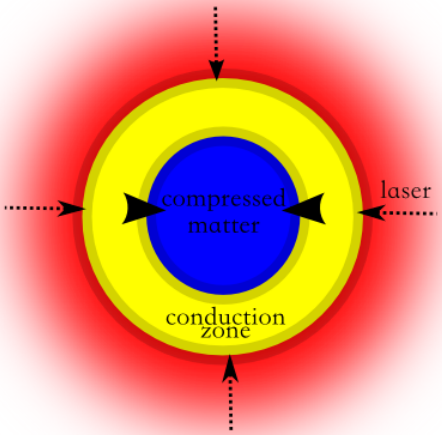

Figure 1.13: Spherical compression of a target.

the manuscript, we consider low and intermediate ion charge materials and focus on the electron transport.

In summary, in the quasi-stationary interaction regime, in plasmas made of low or intermediate ion charge materials, the laser penetrates the corona of the target and deposits its energy at a critical density. From the critical zone, the energy is transported by the electron heat conduction through the conduction zone, shown in Fig. 1.11 (c) in grey. The energy deposited in a dense plasma induces the ablation. Its recoil compresses the target. The shocked region, behind the ablation front, is in a state of a warm and dense matter. Proceeding inside the matter we reach the shock front and, after, the unperturbed solid.

The stationary regime ends when the shock reaches the rear side of the target. Then if the laser continues to irradiate, an acceleration phase begins. In a spherically or cylindrically shaped target, as shown in Fig 1.13, the acceleration phase leads to a target compression, creating HED plasmas.

For the plasmas of interest of this manuscript, a key role is played by the electron transport. This process is introduced in the next section.

1.4 Entropy and electron transport

Particles in a plasma (electrons and ions) follow laws of classical mechanics [18]. They collide and drift under the action of electromagnetic fields. Their macroscopic (averaged) quantities, are characterized by the temperature, density and pressure.

A spatial inhomogeneity of these parameters gives rise for the transport phenomena.

Boltzmann and Maxwell have developed a statistical approach [19], a kinetic theory, describing the many-particle systems out-of-equilibrium. The major property of the kinetic process in a closed system is the loss of information or, in other words, an increase of disorder, which macroscopically corresponds to the increase of entropy (H-theorem). The thermodynamic equilibrium corresponds to a state where the entropy is maximized.

The temporal direction towards more probable states, described by the H-theorem, breaks the temporal symmetry, leading to the macroscopic world of quantity transport, as we see it.

In this manuscript, we focus on the electron transport, which is the motion electrons, induced by the spatial inhomogeneity of the plasma density and temperature. In the

hydrodynamic theory, where the characteristic inhomogeneity scale length is much longer than the electron mean free parth (MFP), it is described by a diffusion equation. This corresponds to regimes close to the local thermodynamic equilibrium, which are not always corresponding to the HED conditions. Below, we summarize cases where the assumption of a local diffusion is not respected.

In the fast ignition scheme, the energy is transported into the plasma by a relativistic electron beam, which is very anisotropic. This process cannot be described with hydrodynamic theories. Touati et al. [20] used a kinetic model based on one main direction of transport and on a local angular entropy maximization assumption, in order to account for a high degree of anisotropy of the electron distribution function (EDF).

Nonlinear laser-matter interactions become important for intensities above $\sim 10^{15}$ W/cm^2. They can generate very energetic and anisotropic electron beams [7]. The transport of these anisotropic electrons plays a key role in the laser-driven implosions, particularly in the shock ignition scheme [16].

HED physics considers regimes where temperature gradients are very sharp compared to the electron MFP. Then the hot electrons can penetrate and deposit their energy deeply in cold regions, leaving no time for thermalization. This kind of transport is called nonlocal since electrons move on hydrodynamic scales.

One of the most affected quantity by nonlocal effects is the heat flux, which is driven by suprathermal electrons. It can be significantly modified, compared to the classical diffusion limit, thus affecting overall plasma simulations and its stability on a microscopic level.

The nonlocal models proposed in [21, 22, 23] are based on phenomenological assumptions and are limited to the description of heat fluxes in the condition of small deviation from the diffusion approximation. In particular, the monodimensional model by Liciani Mora and Virmont [21] (LMV) describes the nonlocal heat flux as a linear combination of local fluxes, with a phenomenological weight coefficient, dependent on the MFP. This model has not been generalized to multidimensional configurations and strong temperature gradients. The model by Schutz Nicolaï and Busquet [22] (SNB) generalizes the heat flux expression to three dimensions and accounts for the dependence of the electron MFP on its energy. It was reinterpreted as a kinetic approach for suprathermal electrons, with a strongly simplified phenomenological collision model. The electric field is induced by the return current of cold electrons. Its effect on suprathermal electrons is accounted as an empirical reduction of the MFP. The model is limited to the case of small anisotropies. Its generalization in order to account for magnetic fields effects [24] is mathematically complicated. In the model developed by Colombant, Manheimer and Goncharov [23], the split in thermal and suprathermal contributions is directly performed on the heat flux propagators, which weight are given from phenomenological kinetic arguments. This model has not been generalized to three dimensions neither to magnetized plasmas and is more time consuming than the SNB model [25].

Our purpose is to generalize the entropic approach of the M1 model, used for relativistic electron beams [20, 26], to nonlocal transport of suprathermal electrons, in order to improve the electron transport description in the case of strong temperature gradients and external magnetic fields.

1.5 Thesis objectives and structure

The objectives of this thesis work are the followings.

- **To derive an electron transport model, which accounts for strong deviations from equilibrium, in angles and energies.** Such a property is charac-

teristic of a kinetic description, which, however, is time expensive. Our purpose is to reduce this description to two steps. As first, we simplify the collision model, assuming that the electron transport is mainly due to suprathermal electrons, which collides with thermal electrons and ions. Then, we decrease the number of dimensions through an angular interpolation of the reduced equation, closed by an angular entropy maximization principle. This closure defines our M1 model as an exponential angular function, which allows to preserve the description of strong angular anisotropies.

- **Consider the effect of electron transport on a microscopic plasma stability.** The kinetic description performed by our model correctly accounts for all energy contributions and it provides a better description of the EDF, compared to models based on the linear anisotropy assumption. It enables studies of small scale kinetic effects, such as the development of microscopic instabilities, induced by the electron transport, within the hydrodynamic framework. Examples of electron plasma and ion-acoustic wave instabilities, driven by the heat flux, are presented and compared with the linear description in angles.

- **Adapt the electron transport model for external and self-generated magnetic fields.** Local and nonlocal models which describe magnetized electron heat transport are mathematically very complicated since they are functions of tensor transport coefficients. Our model approaches this problem in a different way, since the reduced kinetic equation naturally accounts for magnetic fields, being mathematically simple and based on strong assumptions. The adaptation to magnetized regimes is obtained defining the magnetized nonlocal electric field, thanks to some phenomenological assumptions.

The manuscript is organized in three parts. In part I, the state of the art of plasma physics and nonlocal transport theories is summarized. Part II deals with the theoretical development of our nonlocal model, so called M1. In part III, the M1 model is applied to the description of the nonlocal regime of HED plasmas.

More in detail, in chapter 2, the main theories for the description of plasma physics (kinetic theory, classical electrodynamics and hydrodynamics) are discussed. In chapter 3 the state of the art of nonlocal transport theories is discussed, presenting a historical perspective of the models developed and highlighting that ones which play a key role in the manuscript, in order to develop the new model or to test it. In chapter 4 an analysis of reduced collision operator is performed, in order to chose the most suitable. In chapter 5 the M1 model is developed, while its numerical implementation is discussed in chapter 6. Stationary applications of the M1 model to unmagnetized plasmas are studied in chapter 7 and to magnetized plasmas in chapter 8. Finally, conclusions are drawn in chapter 12.

Part I

State of the Art

Chapter 2

Plasma physics

The HED physics includes a wide range of states of ionized matter. These phenomena are described by classical plasma theories. So it is essential to display what are these theories and what are the states of matter that they describe.

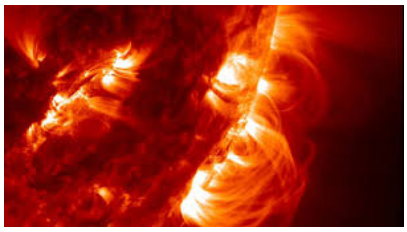

Solid, liquid and gas are the three states of matter, well known from the remote past. However, the modern physics has brought to overcome the limits of this reduced categorization of matter next to the discovery of new states, such as Bose-Einstein condensates, liquid crystals, superfluids, supersolids, supermagnets, warm and dense matter and many others. Among these new states, one of the most important is definitely the state of plasma. Plasmas are classified as the fourth state of fundamental matter. They are ionized matter, strongly influenced by electromagnetic fields. Most of the visible matter of the universe is in this state (almost 99%). Stars and nebulae are the most common plasmas, visible from the space. Plasmas were present also in the very early stages of the cosmological history of the universe, such as the gluon-quark plasma and the quantum-electrodynamic plasma. On Earth, plasmas can be seen as fire, thunders and aurora borealis. Moreover, they can be created in laboratory.

In particular, in this chapter we limit our discussion to non-relativistic plasmas. They can be considered as gasses in which coexist several populations of charged particles with different masses and charges: the ions and the electrons. Plasmas are globally neutral.

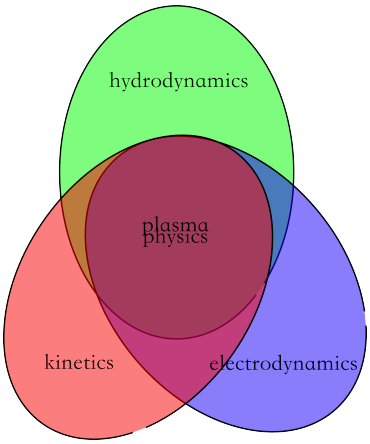

From a theoretical point of view, the physics of plasmas is given by a combination of three of the fundamental existing physical theories: the out-of-equilibrium statistical mechanics (kinetic theory), the hydrodynamics and the electrodynamics. In particular, the kinetic theory describes how plasmas approach the local thermal equilibrium, from a chaotic state; the hydrodynamics describes the averaged behavior of plasmas near local thermal equilibrium; the electrodynamics describes as well the propagation of small electromagnetic perturbations, as of the global plasma neutrality as the strong fields, as the damping and the growth of plasma waves.

In this chapter, the three descriptions of plasma are presented from a theoretical and phenomenological point of view. Section 2.1, treats the kinetic description of plasmas, section 2.2 the electrodynamics of plasmas, in their classical (non-quantum) limit and

section 2.3 the hydrodynamic theory and simulation codes.

2.1 Kinetics of plasmas

Plasma is a classical many-body system of particles, which move following the rules of classical mechanics, colliding and drifting under microscopic and macroscopic electromagnetic fields. Of course, this system is deterministic. However, it is unreasonable to suppose to be able to solve such a complex system exactly. In the nineteenth century, Boltzmann proposed to solve complex systems in a stochastic way, coupling for the first time physics and statistics and overcoming the determinism. The kinetics of plasmas is studied with this statistic theory, which in the manuscript is referred as the kinetic theory [19].

The kinetic theory is the most fundamental and microscopic way to describe a plasma. In the manuscript, we exploit this description in order to predict nonlocal effects, in the condition where the fluid description breaks down.

In this section we summarize the kinetic theory, emphasizing the approximations which are exploited later.

2.1.1 Binary collisions

Let us define the distribution function of N particles $f^{(N)}(t, \vec{x}_1, \vec{v}_1, ..., \vec{x}_N, \vec{v}_N)$ as the density of particles in $6N$-dimensional phase space of the whole gas, normalized to unity. The Liouville's theorem asserts that the volume in the phase space of an isolated system is invariant with respect to canonical transformations [27]. In classical mechanics, this reads

$$\frac{d}{dt}f^{(N)} = \frac{\partial}{\partial t}f^{(N)} + \sum_{j=1}^{N}\left[\vec{\nabla}\left(f^{(N)}\cdot\vec{v}_j\right) + \vec{\nabla}_v\left(f^{(N)}\cdot\vec{a}_j\right)\right] = 0, \tag{2.1}$$

with $\vec{x}_j$ and $\vec{a}_j$ the velocity and the acceleration of a generic particle j.

In practice, it is difficult to solve a $6N$ dimensional system for a plasma with a very large number of particles. Let us define a reduced n-particles distribution function ($n < N$) as

$$f^{(n)}(t, \vec{x}, \vec{v}) = \int_{\mathbb{R}^{6N}} d^3x_n d^3v_n ... d^3x_N d^3v_N f^{(N)}(t, \vec{x}_1, \vec{v}_1, ..., \vec{x}_n, \vec{v}_n, ..., \vec{x}_N, \vec{v}_N).$$

Its time evolution is given by integrating Eq. (2.1) on $d^3x_n d^3v_n ... d^3x_N d^3v_N$. For the one particle distribution function, we have

$$\frac{d}{dt}f^{(1)} = \frac{\partial}{\partial t}f^{(1)} + \vec{\nabla}\left(f^{(1)}\vec{v}_1\right) + \vec{\nabla}_v\left(f^{(1)}\vec{a}_1\right) = -N\int_{\mathbb{R}^6} d^3x_2 d^3v_2 \vec{a}_{1,2}\frac{\partial}{\partial v_1}f^{(2)}, \tag{2.2}$$

where $\vec{a}_{1,2}$ is the acceleration of particle 1, induced by particle 2, while $\vec{a}_1$ is the acceleration induced by external fields to particle 1. Equation (2.2) needs to be closed. Iterating the process, we set a hierarchy in which each equation depends on the higher order distribution function, till the closure at the N-particles distribution function. It is desirable to close the system before. For this reason we apply the hypothesis of weak correlations or binary collisions, assuming $f^{(3)} = 0$. This leads to

$$\begin{aligned}\frac{d}{dt}f^{(2)} = &\frac{\partial}{\partial t}f^{(2)} + \vec{\nabla}_1\left(f^{(2)}\vec{v}_1\right) + \vec{\nabla}_{v_1}\left(f^{(2)}\vec{a}_1\right) + \vec{\nabla}_{v_1}\left(f^{(2)}\vec{a}_{1,2}\right)\\ &+ \vec{\nabla}_2\left(f^{(2)}\vec{v}_2\right) + \vec{\nabla}_{v_2}\left(f^{(2)}\vec{a}_2\right) + \vec{\nabla}_{v_2}\left(f^{(2)}\vec{a}_{2,1}\right)\\ &= 0.\end{aligned} \tag{2.3}$$

Since we only consider binary collisions, particles are uncorrelated before and after each collision. In these cases the two particles distribution function can be written as

$$f^{(2)}(t,\vec{x}_1,\vec{v}_1,\vec{x}_2,\vec{v}_2) = f^{(1)}(\vec{x}_1,\vec{v}_1)f^{(1)}(\vec{x}_2,\vec{v}_2) + g_{12}(\vec{x}_1,\vec{v}_1,\vec{x}_2,\vec{v}_2). \tag{2.4}$$

Collision effects depend only on the irreducible part of the pair distribution function g_{12}. If we apply the hypothesis of spatial homogeneity, Eq. (2.4) loses its time dependence.

The phase space volume and the relative velocity of particles do not change in an elastic collision. Injecting Eqs. (2.3) and (2.4) in Eq. (2.2) and solving the equation for g_{12} in the limit of weak (binary) correlation, we find the Boltzmann equation

$$\frac{\partial}{\partial t}f + \vec{v}\cdot\vec{\nabla}f + \vec{a}\cdot\vec{\nabla}_v f = \left(\frac{\partial f}{\partial t}\right)_{\text{coll}}, \tag{2.5}$$

where we defined $f = Nf^{(1)}$ as the total distribution function of a weakly collisional gas, in the 6-dimensional phase space. In cylindrical coordinates (r,θ,z), the Boltzmann collision integral for a population of particles 1, colliding with a population of particles 2, reads

$$\left(\frac{\partial f}{\partial t}\right)_{\text{coll}} = \int_{\mathbb{R}^3} d^3v_2 \int_{\mathbb{R}^2} d^2\sigma_{1,2}||\vec{v}_{\text{rel}}||^2[f(\vec{v}_1')f(\vec{v}_2') - f(\vec{v}_1)f(\vec{v}_2)]\,, \tag{2.6}$$

where $\vec{v}_{\text{rel}} = \vec{v}_2 - \vec{v}_1$ is the relative velocity. The prime superscript denotes the velocities prior the collision, and $\sigma_{1,2}$ is the cross-section. To consider collisions between different species of particles, we need to add several corresponding collision operators of the form (2.6).

The Boltzmann equation cannot be applied to strongly coupled plasmas, where many particle correlations are important. However it is able to describe chaotic states of a classical (binary collisions, without quantum effects) plasma.

2.1.2 Diffusion approximation

In fully-ionized plasmas, collision effects are predominantly due to the accumulation of many small angular deviations (diffusion approximation) [18]. In this case the equation of transport can be derived from simple assumptions.

Let $w(\vec{v},\Delta\vec{v})d^3\Delta v$ be the probability that a particle with a velocity $\vec{v}$ at a time t acquires a velocity $\vec{v}+\Delta\vec{v}$ in a time $t+\Delta t$. The distribution function at a time t can be expressed as

$$f(t,\vec{v}) = \int_{\mathbb{R}^3} d^3\Delta v f(t-\Delta t,\vec{v}-\Delta\vec{v})w(\vec{v},\Delta\vec{v}) \tag{2.7}$$

Small angle deflections mean small velocity increments. We expand the term fw of equation (2.7) in powers of $\Delta\vec{v}$, retaining only terms up to the second order. This allows us to write the equation as the temporal derivative of the distribution function, due to collisions:

$$\left(\frac{\partial f}{\partial t}\right)_{\text{coll}} = -\vec{\nabla}_v\left(\frac{d\langle\Delta\vec{v}\rangle}{dt}f\right) + \frac{1}{2}\vec{\nabla}_v\otimes\vec{\nabla}_v : \left(\frac{d\langle\Delta\vec{v}\otimes\Delta\vec{v}\rangle}{dt}f\right), \tag{2.8}$$

where

$$\begin{cases} \frac{d\langle\Delta\vec{v}\rangle}{dt} = \frac{1}{\Delta t}\int_{\mathbb{R}^3} d^3\Delta v\Delta\vec{v} \\ \frac{d\langle\Delta\vec{v}\otimes\Delta\vec{v}\rangle}{dt} = \frac{1}{\Delta t}\int_{\mathbb{R}^3} d^3\Delta v\Delta\vec{v}\otimes\Delta\vec{v} \end{cases}.$$

Symbols $\otimes$ and : respectively denote the tensor product and the tensor scalar product.

Equation (2.5), with the collision term in the form of Eq. (2.8), is the Fokker-Planck (FP) equation [18]. Thanks to the diffusion approximation, it is no more an integral-differential equation, but only a differential one.

The Boltzmann equation (2.6), can be reduced to the limit where it assumes the same form of Eq. (2.8). In order to study heat transport, in this manuscript, we consider the electron collisions, with electrons and ions. Hence, the acceleration in Eq. (2.5) is induced by the Lorentz force:

$$\vec{a} = -\frac{e}{m_e}\left(\vec{E} + \frac{\vec{v}_e}{c} \times \vec{B}\right).$$

From now on, the subscript e indicates electrons, i ions and j ranges between both particles. We develop Eq. (2.6) as before:

$$f_e(\vec{v}_e')f_j(\vec{v}_j') - f_e(\vec{v}_e)f_j(\vec{v}_j) \approx \left(\Delta\vec{p}\cdot\vec{\nabla}_{\Delta\vec{p}} + \frac{1}{2}\Delta\vec{p}\otimes\Delta\vec{p} : \vec{\nabla}_{\Delta\vec{p}}\otimes\vec{\nabla}_{\Delta\vec{p}}\right) f_e(\vec{v}_e)f_j(\vec{v}_j).$$

The collisions between particles are supposed to be Coulombian, so we can use the Rutherford cross section [18]

$$d^2\sigma_{e,j} = (2q_e q_j \mu_{ej})^2 \frac{d^2\Omega}{\Delta\vec{p}^4},$$

where $\mu_{ej} = m_e m_j/(m_e + m_j)$ is the reduced mass, $\vec{\Omega}$ the solid angle of velocity directions and $\Delta\vec{p}$ the momentum increment. We now integrate the simplified collision operator. Because of particle shielding, the maximum length at which two particles can interact is the Debye length

$$\lambda_{De} = \sqrt{\frac{T_e}{4\pi n_e e^2}}.$$

This imposes a minimum on the angular integration, which finally leads to the Landau collision term

$$\left(\frac{\partial f_e}{\partial t}\right)_{\text{coll}} = \sum_{j=e,i}\frac{\partial}{\partial\vec{p}_e}\int_{\mathbf{R}^3} d^3v_j\bar{\bar{U}}\left(\frac{\partial f_e}{\partial\vec{p}_e}f_j - \frac{\partial f_j}{\partial\vec{p}_j}f_e\right), \tag{2.9}$$

with

$$\bar{\bar{U}} = \frac{U_0}{2}\frac{\vec{v}_{\text{rel}}^2\bar{\bar{I}} - \vec{v}_{\text{rel}}\otimes\Delta\vec{v}}{\vec{v}_{\text{rel}}^2},$$

with the scattering potential

$$U_0 = \frac{4\pi e^2 q_j^2 \Lambda_{ej}}{||\vec{v}_{\text{rel}}||}$$

and with the Coulomb logarithm Λ_{ej}, which accounts for the angular integration and the charge shielding.

The FP equation is limited to the description of weakly correlated classical plasmas. However, it is often used for the kinetic description of HED plasmas.

2.1.3 Local thermodynamic equilibrium

In the limit of frequent collisions, whatever are initial conditions, plasmas tend toward the same state: the local thermal equilibrium. This behavior is forced by the maximization of entropy principle, which is intrinsic in the Boltzmann equation.

H-Theorem

The kinetic entropy of an electron gas is defined as [19]

$$H[f_e] = -\int_{\mathbb{R}^6} d^3x d^3v \left(f_e \log f_e - f_e\right). \tag{2.10}$$

The H-theorem states that the entropy of a closed system can only increase in time, that is

$$\frac{d}{dt}H \geq 0.$$

Solving the time derivative of the entropy, we have

$$\frac{d}{dt}H = -\int_{\mathbb{R}^6} d^3x d^3v \log(f_e)\frac{\partial}{\partial t}f_e.$$

The time derivative of the EDF is given by the Boltzmann equation in (2.5), which leads to

$$\frac{d}{dt}H = -\int_{\mathbb{R}^6} d^3x d^3v \log f_e \left(\frac{\partial f_e}{\partial t}\right)_{\text{coll}}. \tag{2.11}$$

This means that only collisions change the entropy. It can be demonstrated that the Boltzmann collision operator (2.6) and the FP operator (2.8) verify the theorem [19].

Relaxation to equilibrium

Let us consider a gas composed of species at the same local temperature. The function which sets to zero the Landau collision operator is the Maxwellian distribution function. For electrons, it reads

$$f_e^m = \frac{n_e}{(2\pi)^{3/2}v_{th}^3}e^{-v^2/(2v_{th}^2)},$$

where $v_{th} = \sqrt{T_e/m_e}$. This means that the Maxwellian EDF maximizes the entropy, since

$$\frac{d}{dt}H[f_e^m] = 0.$$

Such a state is defined as the local thermal equilibrium and this is the limit to which tends EDFs, after many collisions. Thus, collisions will always lead to a local thermal equilibrium.

As the Boltzmann and the FP collision operators are complicated, Bhatnagar, Gross and Krook (BGK) have proposed a simplified one [28]. It is a phenomenological operator, which captures the main physics of collisions, at a qualitative level. It imposes the relaxation to equilibrium, verifying the H-theorem and the conservation of the number of particles, their momentum and total energy. In general, collisions impose equilibrium after a characteristic collision time τ, which is independent on the particle velocity and which choice depends on the assumptions done. The collision operator reads

$$\left(\frac{\partial f_e}{\partial t}\right)_{\text{coll}} = -\frac{f_e - f_e^m}{\tau}.$$

We stress that in this model the energy diffusion is neglected. However, as we will see, a modified version of the BGK collision operator is frequently used in many nonlocal models, in order to describe the local thermalization.

2.2 Electromagnetic waves in a plasma

Plasmas are dielectric media: they are characterized by the response to external fields, leading to electromagnetic waves. Such a phenomenon is studied by coupling the laws of the plasma kinetics with the laws of classical electrodynamics. We summarize such laws in this section.

2.2.1 Maxwell's equations

The four Maxwell's equations describe the dynamics of electromagnetic fields.

Equation

$$\vec{\nabla} \cdot \vec{B} = 0 \tag{2.12}$$

asserts the absence of magnetic monopoles. The Faraday's law

$$\vec{\nabla} \times \vec{E} = -\frac{1}{c}\frac{\partial}{\partial t}\vec{B} \tag{2.13}$$

describes the electromagnetic induction. In such a phenomenon, closed circuitations of electric fields become sources of magnetic fields. The Poisson's equation

$$\vec{\nabla} \cdot \vec{E} = 4\pi\rho_E \tag{2.14}$$

sets the laws of the electrostatics. A density of charges ρ_E acts as source of the electric field. The Ampere's law

$$\vec{\nabla} \times \vec{B} = -\frac{1}{c}\frac{\partial}{\partial t}\vec{E} + \frac{4\pi}{c}\vec{j} \tag{2.15}$$

shows that an electric current $\vec{j}$ acts as a source of magnetic and electric fields.

The system composed by Eq. (2.12), (2.13), (2.14) and (2.15) forms the Maxwell's equations. This system implies the continuity equation

$$\frac{\partial}{\partial t}\rho_E + \vec{\nabla} \cdot \vec{j} = 0,$$

which correspond to the charge conservation.

Dealing with materials, it is convenient to introduce the displacement field $\vec{D}$, by including the internal charge and current of the material in Maxwell's equations: $\rho_E = \rho_E^{int} + \rho_E^{ext}$ and $\vec{j} = \vec{j}^{int} + \vec{j}^{ext}$. Then

$$\vec{\nabla} \cdot \vec{D} = \vec{\nabla} \cdot \vec{E} - 4\pi\rho_E^{int} \tag{2.16}$$

and

$$\frac{\partial}{\partial t}\vec{D} = \frac{\partial}{\partial t}\vec{E} - 4\pi\vec{j}^{int}, \tag{2.17}$$

where the internal charge and the current density in a fully-ionized plasma read:

$$\rho_E^{int} = Zen_i - en_e,$$
$$\vec{j}^{int} = Zen_i\vec{u}_e - en_e\vec{u}_i,$$

with $\vec{u}_e$ and $\vec{u}_i$ as the electron and ion macroscopic velocities. The current conservation now reads reads

$$\frac{\partial}{\partial t}\rho_E^{int} + \vec{\nabla} \cdot \vec{j}^{int} = 0.$$

In the linear electrodynamics, there is a linear relation that accounts for the material response to external fields. According to Eqs. 2.16 and 2.17, it reads

$$\vec{D} = \bar{\bar{\epsilon}} \cdot \vec{E}.$$

This is a convolution integral, in space and time. The second-order tensor $\bar{\bar{\epsilon}}$ is the dielectric permittivity. In unmagnetized plasmas, $\bar{\bar{\epsilon}}$ is a symmetric tensor of the second order. It can be found by solving the Eqs. 2.16 and 2.17.

2.2.2 Dielectric permittivity

In this section, the analysis is performed in the Fourier space. In this space, variables are of the form $e^{-i\omega t+i\vec{k}\cdot\vec{x}}$. Hence the derivative on time becomes $\partial/\partial t \to -i\omega$ and the derivative on space $\vec{\nabla} \to i\vec{k}$.

An analytical definition for the dielectric permittivity of a plasma follows from the kinetic theory. In general, $\bar{\bar{\epsilon}}$ is a symmetric second-order tensor, depending only from the wavevector $\vec{k}$. Thus it can be split in longitudinal and transverse parts

$$\bar{\bar{\epsilon}} = \epsilon^l \frac{\vec{k}\otimes\vec{k}}{k^2} + \epsilon^{tr}\left(\bar{\bar{I}} - \frac{\vec{k}\otimes\vec{k}}{k^2}\right).$$

The polarization $\vec{P}$, for a fully-ionized plasma is defined by the following equation [29]

$$\vec{j} = \frac{\partial}{\partial t}\vec{P}.$$

In the Fourier's space, the Ohm's law reads

$$\vec{j} = \bar{\bar{\sigma}} \cdot \vec{E}$$

which leads to

$$\vec{P} = \frac{i\bar{\bar{\sigma}}}{\omega} \cdot \vec{E}.$$

The displacement field can be defined as a function of the polarization, as $\vec{D} = \vec{E} + \vec{P}$. This leads to

$$\bar{\bar{\epsilon}} = \bar{\bar{I}} + \frac{4\pi i\bar{\bar{\sigma}}}{\omega},$$

which is split in the longitudinal and transverse parts

$$\begin{cases} \epsilon^l = 1 + \frac{4\pi i\sigma^l}{\omega} \\ \epsilon^{tr} = 1 + \frac{4\pi i\sigma^{tr}}{\omega} \end{cases}. \tag{2.18}$$

We present a simplified kinetic approach, in order to evaluate of the electric conductivity σ. We assume the distribution function as a sum of a stationary term f_{stat} and a periodic perturbation δf: $f = f_{stat} + \delta f$. In the framework of a BGK equation, we find:

$$-i\omega\delta f + i\vec{k}\cdot\vec{v}\delta f - \frac{e}{m_e}\left(\vec{E} + \frac{\vec{v}}{c}\times\vec{B}\right)\cdot\vec{\nabla}_v f_{stat} = -\nu_{\text{eff}}\delta f, \tag{2.19}$$

where

$$\nu_{\text{eff}} = \frac{4\sqrt{2\pi}}{3}\frac{Z^2e^4n_i\Lambda_{ei}}{m_e^2v_{th}^3}$$

is an effective collision frequency for electron-ion collisions in a plasma and Z is the ion charge. Since f_{stat} is stationary, it depends only on the module of velocity. The term $\vec{\nabla}_v f_{stat}$ is parallel to the velocity $\vec{v}$ and its scalar product with the magnetic force is zero. Equation (2.19) gives a definition for the current $\vec{j}$, which is proportional to the applied electric field. It reads

$$\vec{j} = -e\int_{\mathbf{R^3}} d^3v\delta f\vec{v} = \left(-i\int_{\mathbf{R^3}} d^3v \frac{\frac{e^2}{m_e}\vec{v}\otimes\vec{\nabla}_v f_{stat}}{\omega - \vec{k}\cdot\vec{v} + i\nu_{\text{eff}}}\right)\cdot\vec{E} = \bar{\bar{\sigma}}\cdot\vec{E}.$$

Then an analytic expression for the electrical conductivity allows to define the dielectric permittivity according to (2.18):

$$\bar{\bar{\epsilon}} = \bar{\bar{I}} + \sum_j \delta\bar{\bar{\epsilon}}_j.$$

where sums are over the plasma species and

$$\delta\bar{\bar{\epsilon}}_j = \frac{4\pi e^2}{m_e\omega}\int_{\mathbf{R^3}} d^3v \frac{\vec{v}\otimes\vec{\nabla}_v f_j}{\omega - \vec{k}\cdot\vec{v} + i\nu_{\text{eff}}}. \tag{2.20}$$

We project it in the longitudinal direction ($\vec{k}\otimes\vec{k}/k^2$) and we find

$$\delta\epsilon_j^l = \frac{4\pi e^2}{m_e\omega k^2}\int_{\mathbf{R^3}} d^3v \frac{\vec{k}\cdot\vec{v}}{\omega - \vec{k}\cdot\vec{v} + i\nu_{\text{eff}}}\vec{k}\cdot\vec{\nabla}_v f_j.$$

Exploiting the relation $\vec{k}\cdot\vec{v}/(\omega - \vec{k}\cdot\vec{v} + i\nu_{\text{eff}}) = -1 + (\omega + i\nu_{\text{eff}})/(\omega - \vec{k}\cdot\vec{v} + i\nu_{\text{eff}})$, the longitudinal conductivity reads

$$\delta\epsilon_j^l = \frac{4\pi e^2}{m_e k^2}\left(1 + i\frac{\nu_{\text{eff}}}{\omega}\right)\int_{\mathbf{R^3}} d^3v \frac{\vec{k}\cdot\vec{\nabla}_v f_j}{\omega - \vec{k}\cdot\vec{v} + i\nu_{\text{eff}}}. \tag{2.21}$$

The transverse conductivity appears multiplying Eq. (2.20) by $\bar{\bar{I}} - \vec{k}\otimes\vec{k}/k^2$. After an integration by parts, it reads

$$\delta\epsilon_j^{tr} = \frac{4\pi e^2}{m_e\omega}\int_{\mathbf{R^3}} d^3v \frac{f_j}{\omega - \vec{k}\cdot\vec{v} + i\nu_{\text{eff}}}. \tag{2.22}$$

We have presented an analytical form for the dielectric permittivity, based on the kinetic approach. It can be calculated for any given EDF. In the next section we show that the knowledge of the permittivity allows to calculate the electromagnetic wave dispersion.

2.2.3 Electromagnetic wave dispersion

The aim of this section is to derive an analytical equation for the electromagnetic wave dispersion in a plasma. The analysis is performed in the Fourier space, as in the previous section.

For fully-ionized plasmas, magnetic dipoles only come from nuclei and are very small ($\bar{\bar{\mu}} \approx \bar{\bar{I}}$). So magnetic plasma responses can be neglected.

Here, we consider the electrostatic waves. Such waves are longitudinal [18], the wavevector is parallel to the direction of the electric field $\vec{E}$, thus the dielectric permittivity is a scalar.

The Poisson's equation is the only equation required in order to describe electrostatic waves. In the Fourier space, in the absence of external sources and assuming the plasma quasineutral ($\rho_E \approx 0$), it reads

$$i\vec{k}\cdot\vec{D} = 0.$$

Thus, an electric field can exist in a plasma, without external sources, if and only if

$$\epsilon^l(\omega, \vec{k}) = 0. \tag{2.23}$$

This equation is called dispersion equation of a longitudinal plasma wave.

Now, we consider the transverse part of the dielectric permittivity. The transverse term ϵ^{tr} enters in the Ampere's law (2.15). The Fourier transformation, in the absence of external sources, reads

$$i\vec{k} \times \vec{B} = -\frac{i\omega\epsilon}{c}\vec{E}.$$

Considering it with the Fourier transformation of the Faraday's law (2.13)

$$i\vec{k} \times \vec{E} = \frac{i\omega}{c}\vec{B}$$

we obtain the wave equation for an electric field

$$\bar{\bar{\epsilon}} \cdot \vec{E} - N^2\vec{E} + \frac{c^2}{\omega^2}\left(\vec{k} \cdot \vec{E}\right)\vec{k} = 0, \tag{2.24}$$

where $N = ck/\omega$ is the refraction index. From Eq. (2.24), a dispersion relation can be derived. Projecting Eq. (2.24) in the transverse direction $\times\vec{k}$, we find the transverse dispersion relation

$$\epsilon(\omega, \vec{k}) = N^2. \tag{2.25}$$

The solution of the dispersion equations (2.23) and (2.25) allows to determine the frequency ω of each wave as a function of the wavenumber $\vec{k}$. These relations describe the spatial and time evolution of the wave (specified by the wave number). In the next section we analyze in detail longitudinal waves, which play an important role in plasma physics.

2.2.4 Longitudinal waves in a plasma

Collective effects in a plasma are due to the interaction of plasma particles with electromagnetic fields. Thus, in plasma, electromagnetic waves transport a signal from one point to another. These waves are periodic sinusoidal perturbations in space and time of plasma quantities. Their properties are described by the dielectric permittivity tensor, through the diffusion equation. Here we consider the longitudinal waves.

Langmuir waves

The Langmuir waves are high-frequency electron oscillations corresponding to the electric field perturbations on a microscopic scale. For the high-frequency assumption, the phase velocity ω/k of waves is much higher than the thermal velocity $\omega/k \gg v_{th}$ and the collision frequency is small $\nu_{\text{eff}} \ll \omega$.

A dispersion equation for the longitudinal waves corresponds to zeros of the longitudinal dielectric permittivity $\epsilon^l(\omega, k) = 0$, as predicted by the dispersion equation (2.23). Because of their inertia, ions do not play a role in Langmuir waves. From Eq. (2.21), through an integration by parts, the dielectric permittivity reduces to [19, 18]

$$\begin{aligned}\epsilon^l(\omega, k) &= 1 + \frac{4\pi e^2}{m_e k^2}\left(1 + i\frac{\nu_{\text{eff}}}{\omega}\right)\int_{\mathbf{R^3}} d^3v \frac{\vec{k} \cdot \vec{\nabla}_v f_e}{\omega - \vec{k} \cdot \vec{v} + i\nu_{\text{eff}}} \\ &= 1 + \frac{4\pi e^2}{m_e k^2}\left(1 + i\frac{\nu_{\text{eff}}}{\omega}\right)\int_{\mathbf{R^3}} d^3v \frac{f_e}{(\omega - \vec{k} \cdot \vec{v} + i\nu_{\text{eff}})^2}.\end{aligned} \tag{2.26}$$

The Taylor's development of Eq. (2.26), for $\omega/k \gg v_{th}$, $\nu_{\text{eff}}/\omega \ll 1$ and for a Maxwellian distribution (hydrodynamic hypothesis) leads to

$$\epsilon^l(\omega, k) \approx 1 - \frac{\omega_{pe}^2}{\omega^2}\left(1 + 3\frac{k^2 v_{th}^2}{\omega^2} - i\frac{\nu_{\text{eff}}}{\omega}\right), \tag{2.27}$$

with the electron plasma frequency defined as $\omega_{pe} = \sqrt{4\pi e^2 n_e/m_e}$.

In the cold collisionless plasma limit ($v_{th} \approx 0$ and $\nu_{\text{eff}} \approx 0$) the solution to the dispersion equation is $\omega = \pm\omega_{pe}$. Injecting this solution in Eq. (2.27) we have

$$1 - \frac{\omega_{pe}^2}{\omega^2}\left(1 + 3\frac{k^2 v_{th}^2}{\omega_{pe}^2} - i\frac{\nu_{\text{eff}}}{\omega_{pe}}\right) = 0 \Rightarrow \omega \approx \pm\left[\omega_{pe}\left(1 + \frac{3}{2}k^2\lambda_{De}^2\right) - i\frac{\nu_{\text{eff}}}{2}\right],$$

where $\lambda_{De} = v_{th}/\omega_{pe}$ is the Debye length, which defines the distance at which the plasma screens electric fields.

Two solutions are represented in Fig. 2.1. They weakly displace from the plasma frequency for high values of $k\lambda_{De}$. Positive solutions correspond to waves propagating forward and negative solutions to waves propagating backward.

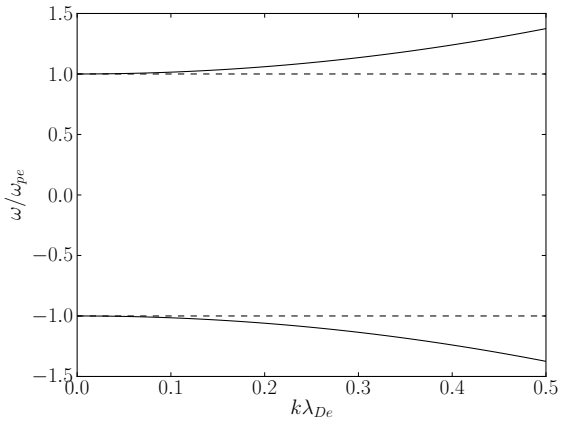

Figure 2.1: Two solutions of the Langmuir wave dispersion equation.

As we show in the third part of the manuscript, Langmuir waves may be affected by the nonlocal transport.

Ion-acoustic waves

The ion-acoustic waves are also longitudinal waves, but of a low-frequency ($\omega \ll \omega_{pe}$), corresponding to correlated quasineutral electron and ion oscillations. The phase velocity is in the range $v_{th} \gg \omega/k \gg v_{thi}$.

The dielectric permittivity reads [19, 18]

$$\epsilon^l(\omega, k) = 1 + \delta\epsilon_e^l + \delta\epsilon_i^l = 1 + \frac{4\pi e^2}{m_e\omega k^2}\int_{\mathbf{R^3}} d^3v \frac{\vec{k}\cdot\vec{v}}{\omega - \vec{k}\cdot\vec{v}}\vec{k}\cdot\vec{\nabla}_v f_e + \frac{\omega_{pi}^2}{\omega^2}\left(1 + 3\frac{k^2 v_{thi}^2}{\omega^2}\right),$$

where we have assumed Maxwellian and collisionless ions, with the thermal velocity $v_{thi} = \sqrt{T_i/m_i}$ and the ion plasma frequency $\omega_{pi} = \sqrt{4\pi Z^2 e^2 n_i/m_i}$. For a Maxwellian EDF, the dispersion equation is

$$1 + \frac{1}{k^2\lambda_{De}^2} + \frac{\omega_{pi}^2}{\omega^2}\left(1 + 3\frac{k^2 v_{thi}^2}{\omega^2}\right) = 0.$$

Neglecting v_{thi} we recover the approximate solution $\omega \approx \pm kc_s/\sqrt{1 + k^2\lambda_{De}^2}$, with $c_s = \sqrt{ZT_e/m_i}$ as the sound speed. Injecting this solution in the dispersion equation we have

$$\omega \approx \pm\sqrt{\frac{k^2 c_s^2}{1 + k^2\lambda_{De}^2} + 3k^2 v_{thi}^2}.$$

Reminding that $\lambda_{De} = c_s/\omega_{pi} = v_{th}/\omega_{pe}$, the solution of the dispersion equation can be rewritten as

$$\frac{\omega}{\omega_{pi}} \approx \pm\sqrt{\frac{k^2\lambda_{De}^2}{1+k^2\lambda_{De}^2} + 3k^2\lambda_{De}^2\frac{T_i}{ZT_e}}.$$

We plot it in Fig. 2.2, for $ZT_e/T_i = 10$.

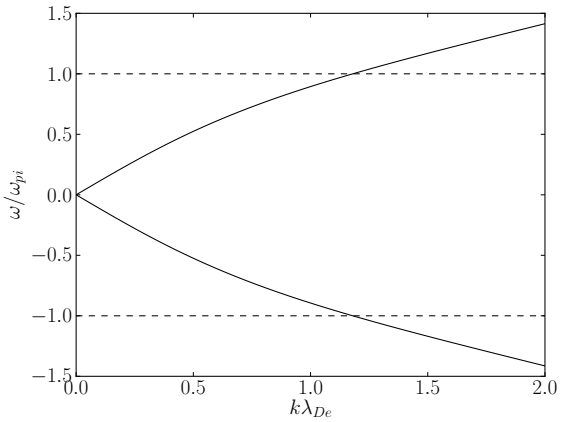

Figure 2.2: Two solutions of the ion-acoustic wave dispersion equation, for $ZT_e/T_i = 10$.

Ion-acoustic waves are coupled to low energy electrons, which can be influenced by electric fields. These electric fields are strongly modified by the nonlocal transport. Thus, indirectly, also ion-acoustic waves are influenced by the nonlocal transport.

2.2.5 Landau damping, and linear theory of instabilities

Integrals (2.21) and (2.22) present a pole for $\omega - \vec{k}\cdot\vec{v} + i\nu_{\text{eff}} = 0$. The way to solve such integrals is to apply the residue theorem, by deviating the integral path around the pole, in the complex plane $\mathbb{C}$, over a small radius semi-circle. According to the casuality principle, the perturbation should disappear in the past. Since the wave temporal evolution is exponential $\propto e^{-i\omega t}$, the complex deviation of the path has necessarily to pass below the pole, in order to assure that ω is defined in the upper part of the complex plane ($\Im(\omega) \geq 0$). Such a path is shown in Fig. 2.3, for 1D plasmas. Applying the residue

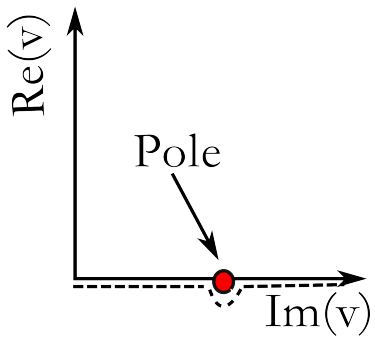

Figure 2.3: Monodimensional scheme of the integral path, around the pole, for the computation of the dielectric permittivity.

theorem along the complex path, the pole reduces to

$$\frac{1}{\omega - \vec{k}\cdot\vec{v} + i\nu_{\text{eff}}} = \frac{P}{\omega - \vec{k}\cdot\vec{v} + i\nu_{\text{eff}}} - i\pi\delta(\omega - \vec{k}\cdot\vec{v} + i\nu_{\text{eff}}),$$

where P stands for the principal value.

The complex path highlights a complex nature of the dielectric permittivity. The imaginary part is responsible for the wave damping. Indeed Eqs. (2.23) and (2.25) set the dispersion relations, respectively for longitudinal and transverse waves. Making the distinction between the real and the imaginary part, we have

$$\begin{cases} \Re\{\epsilon^l[\Re(\omega)+i\Im(\omega)]\}+i\Im\{\epsilon^l[\Re(\omega)+i\Im(\omega)]\}=0 \\ \Re\{\epsilon^{tr}[\Re(\omega)+i\Im(\omega)]\}+i\Im\{\epsilon^{tr}[\Re(\omega)+i\Im(\omega)]\}=N^2 \end{cases} .$$

We assume that imaginary components of both dielectric permittivity and frequency are small compared to the real components. Under this assumption we make the linear Taylor development of the dielectric permittivity. The first order correction leads to

$$\begin{cases} \gamma = \frac{\Im\{\epsilon^l[\Re(\omega)\}}{\frac{\partial}{\partial\omega}\Re\{\epsilon^l[\Re(\omega)]\}} \\ \gamma = \frac{\Im\{\epsilon^{tr}[\Re(\omega)\}}{\frac{\partial}{\partial\omega}\Re\{\epsilon^{tr}[\Re(\omega)]\}+N^2} \end{cases} , \tag{2.28}$$

Where we have defined $\gamma = -\Im(\omega)$. For simplicity, along the manuscript we refer to ω as its real part. Using this formalism the time evolution of plasma waves reads $\propto e^{-i\omega t-\gamma t}$. Thus, if $\gamma > 0$, the wave is damped in time. This phenomenon of collisionless damping is called Landau damping [18] and γ is called damping factor. On the contrary, if $\gamma < 0$, plasma wave amplitude increases exponentially in time. This waves can be excited in stream instabilities. Despite the linear theory is not valid for large amplitudes, it is useful to define conditions where they develop and turbulent states may be created.

As an example we consider a collisionless plasma with the wavevector $\vec{k}$ parallel to the z axis.

$$\begin{cases} \delta\epsilon_j^l = \frac{4\pi e^2}{m_e k}\int_0^\infty dv_z \frac{\frac{\partial}{\partial v_z}F_z}{\omega-kv_z} \\ \delta\epsilon_j^{tr} = \frac{4\pi e^2}{m_e \omega}\int_0^\infty dv_z \frac{F_z}{\omega-kv_z} \end{cases} ,$$

where we have assumed that the one direction EDF reads

$$F_z = \int_{\mathbf{R}^2} dv_x dv_y f_j.$$

The imaginary part of the electrical permittivity is

$$\begin{cases} \Im(\delta\epsilon_j^l) = \frac{4\pi e^2}{m_e k^2}\frac{\partial}{\partial v_z}F_z|_{v_z=\omega/k} \\ \Im(\delta\epsilon_j^{tr}) = \frac{4\pi e^2}{m_e k\omega}F_z|_{v_z=\omega/k} \end{cases} ,$$

We conclude that longitudinal wave instabilities are induced by sign variations of the one-direction EDF velocity derivative. The transverse wave instabilities come from the sign of the denominator in Eq. (2.28).

In the third part of the manuscript we study damping and stability of the longitudinal plasma waves, in the nonlocal electron transport regime.

2.3 Hydrodynamics of plasmas and HED codes

Another description of plasmas is based on hydrodynamics. Such a description takes into account the time and spatial evolution of macroscopic variables, which figure out as averaged quantities of the kinetic theory. This approach is justified near the local thermodynamic equilibrium.

Most of codes used to describe ICF plasmas and many laboratory astrophysical codes are based on this description, since it is fast and deals with macroscopic quantities. In this section the hydrodynamics is described as it is implemented in the CHIC code (Code d'Hydrodynamique et d'Implosion du CeLIA) [30], one of the main 2D ICF codes, used to describe the academic experiments in ICF and HED physics in France.

2.3.1 Hydrodynamic equations: the monofluid two temperatures model

The hydrodynamic theory is based on three equations which can be obtained from the average in the velocity space of the FP equations, assuming near-Maxwellian particle distribution functions. In this manuscript we deal with a monofluid description, with two temperatures, as it is done in the CHIC code.

Continuity equation

The continuity equation describes the conservation of mass for each species in a fluid and can be derived integrating Eq. (2.5) in d^3v. For electrons, it reads

$$\frac{\partial}{\partial t}\rho_e + \vec{\nabla}\cdot\rho_e\vec{u}_e = 0,$$

where $\vec{u}_e$ is the macroscopic electron velocity and $\rho_e = m_e n_e$ is the mass density. This equation corresponds to a constant total number of particles. Similar equation can be obtained for ions, assuming the plasma to be quasineutral ($n_e = Zn_i$):

$$\frac{\partial}{\partial t}\rho_i + \vec{\nabla}\cdot\rho_i\vec{u}_i = 0.$$

Adding the two continuity equations we have the monofluid continuity equation

$$\frac{\partial}{\partial t}\rho + \vec{\nabla}\cdot\rho\vec{u} = 0, \tag{2.29}$$

where $u = (\rho_e u_e + \rho_i u_i)/(\rho_e + \rho_i)$ and where we have supposed $\rho = \rho_e + \rho_i \approx \rho_i$, with an error up to $m_e/m_i \approx 2\cdot 10^{-3}$.

Momentum equation

The momentum transport equation is obtained by multiplying Eq. (2.5) by $\vec{p}_e$ and integrating in d^3v:

$$\frac{\partial}{\partial t}\rho_e\vec{u}_e + \vec{\nabla}\cdot\bar{\bar{P}}_e = -en_e\left(\vec{E} + \frac{\vec{u}_e}{c}\times\vec{B}\right) + R_{ei}, \tag{2.30}$$

where $\bar{\bar{P}}_e = \rho_e\vec{u}_e\otimes\vec{u}_e$ is the electron pressure tensor and R_{ei} a friction term due to electron-ion collisions. The total momentum conservation implies $R_{ei} = -R_{ie}$. The plasma is supposed to be isotropic, thus $\bar{\bar{P}}_e = P_e\bar{\bar{I}}$. Similarly, we deduce the same equation for ions:

$$\frac{\partial}{\partial t}\rho_i\vec{u}_i + \vec{\nabla}\cdot\bar{\bar{P}}_i = Zen_i\left(\vec{E} + \frac{\vec{u}_i}{c}\times\vec{B}\right) - R_{ei}.$$

Adding the two equations we have the Euler equation:

$$\frac{\partial}{\partial t}\rho\vec{u} + \vec{\nabla}\cdot\bar{\bar{P}} = \frac{1}{c}\vec{j}\times\vec{B}. \tag{2.31}$$

Here $P = P_e + P_i$ is the total pressure and $\vec{j} = \vec{j}_i + \vec{j}_e = en_e(\vec{u}_i/Z - \vec{u}_e)$ is the electric current.

Energy equations

The third equation describes the energy transport. For electrons, it can be obtained by multiplying Eq. (2.5) by the microscopic kinetic energy $\epsilon = \frac{1}{2}m_e v_e^2$. By using Eq. (2.30), it can be presented as

$$\frac{\partial}{\partial t}\left(\frac{1}{2}\rho_e u_e^2 + \frac{3}{2}n_e T_e\right) + \vec{\nabla}\cdot\left(\frac{1}{2}\rho_e u_e^2 \vec{u}_e + \frac{5}{2}n_e T_e \vec{u}_e + \vec{q}_e\right) = \vec{j}_e \cdot \vec{E} + W_{ei}, \tag{2.32}$$

with

$$\vec{q}_e = <\epsilon \vec{v} n_e> = \int_{\mathbf{R}^3} d^3v \epsilon \vec{v} f_e, \tag{2.33}$$

as the heat flux and

$$W_{ei} = \int_{\mathbf{R}^3} d^3v \frac{1}{2} m_e v^2 C_{ei},$$

as the energy exchange. We neglect the energy dissipation due to the friction force. Thus

$$W_{ei} = -2\frac{m_e}{m_i}\nu_{ei}(v_{th}) n_e (T_e - T_i)$$

is the rate of energy exchange between the electron and ion species, with $\nu_{ei}(v_{th}) = 4\pi Z e^2 n_e \Lambda_{ei}/(m_e v_{th}^2)$ being the electron-ion average collision frequency. In the same way, assuming that collisions between ions are weak, Eq. (2.32) for ions reads

$$\frac{\partial}{\partial t}\left(\frac{1}{2}\rho_i u_i^2 + \frac{3}{2}n_i T_i\right) + \vec{\nabla}\cdot\left(\frac{1}{2}\rho_i u_i^2 \vec{u}_i + \frac{5}{2}n_i T_i \vec{u}_i + \vec{q}_i\right) = \vec{j}_i \cdot \vec{E} + W_{ie}. \tag{2.34}$$

Equations (2.29), (2.31), (2.32) and (2.34) constitute the monofluid bitemperature hydrodynamic model. The system is closed by Eq. (2.33). In the derivation we have assumed $\bar{\bar{P}} = P\bar{\bar{I}}$ and a perfect gas equation of state, which reads $P_j = n_j T_j$, with j ranging between e and i.

2.3.2 The CHIC code

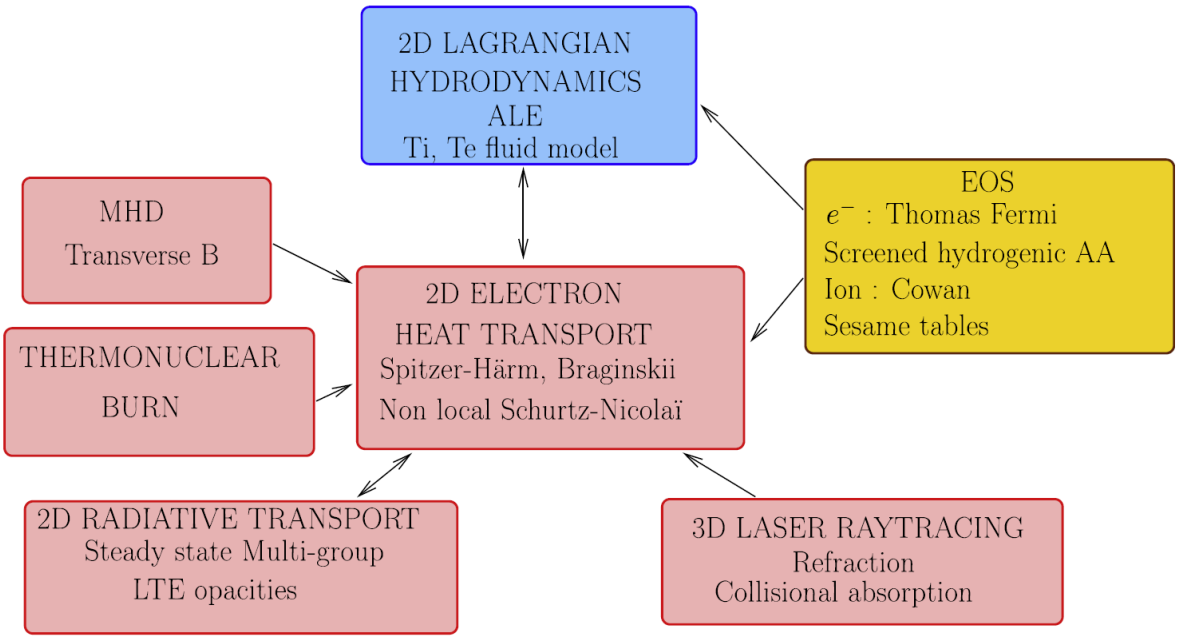

Figure 2.4: Structure of the CHIC code.

The CHIC code [30] is a hydrodynamic code, created for modeling laser-plasma interactions at HED regimes. Its structure is resumed in Fig. 2.4.

At each temporal step, a bidimensional monofluid two temperatures hydrodynamic model is solved, using a Lagrangian approach. This numerical tool can operate in planar or axisymmetric geometry. It is based on the following system of hydrodynamic equations:

$$\begin{cases} \frac{\partial}{\partial t}\rho + \vec{\nabla}\cdot\rho\vec{u} = 0 \\ \frac{\partial}{\partial t}\rho\vec{u} + \vec{\nabla}(P_e + P_i) = 0 \\ \frac{\partial}{\partial t}\left(\frac{3}{2}P_e\right) + \vec{\nabla}\cdot\vec{q}_e = -2\frac{m_e}{m_i}\nu_{ei}(v_{th})n_e(T_e - T_i) + W_{fus} + W_r + W_l \\ \frac{\partial}{\partial t}\left(\frac{3}{2}P_i\right) - \vec{\nabla}\cdot k_i\vec{\nabla}T_i = 2\frac{m_i}{m_e}\nu_{ie}(v_{th})n_i(T_e - T_i) \end{cases}, \tag{2.35}$$

which corresponds to a monofluid, characterized by two temperatures (electrons and ions).

The hydrodynamic system can be closed with a perfect gas or realistic equation of state (such as QEOS model [31] or SESAME tables [32]). It can include thermonuclear reactions W_{fus}, and a detailed radiation transport W_r, based on tabulated opacity data. This transport is computed assuming the radiation field quasistationary and weakly anisotropic (multigroup diffusion). The code uses a 3D ray tracing technique for describing the inverse Bremsstrahlung laser absorption W_l.

Thermonuclear reactions, radiation transport and laser absorption are modeled as sources of the electron energy equation.

The CHIC code is used for the interpretation of ICF and astrophysical experiments. The modeling of the two-dimensional heat flux $\vec{q}_e$ plays a key role in this description. In the CHIC code, it accounts for the effects of magnetization and is extended to regimes of nonlocal transport, by using a practical model [22, 24], based on a phenomenological treatment of electric and magnetic fields. The latter is limited to weak anisotropies and, in case of magnetization, present a complex mathematical structure. Our purpose is to improve this description, developing a new model for the electron heat flux $\vec{q}_e$, based on kinetic assumptions, an entropic argument and on a correct treatment of fields. This allows to account for strong anisotropies in energy and angles, to extend the analysis to a kinetic scale and leads to a mathematically simpler structure for the magnetized transport.

In particular, every temporal steps of a CHIC simulation, our M1 model is able to solve a simplified and stationary FP equation, for each energy group. From this equation it deduces the EDF, which energy integration leads to the heat flux. This flux can be injected in the system 2.35, as $\vec{q}_e$.

In section 6.2.2, we present the numerical scheme in which the M1 model has been implemented. This scheme limits the M1 domain of validity to the case where electrons are decelerated, which is typical of nonlocal transport. Nevertheless, this condition is not always respected, especially when plasmas are irradiated by lasers and are involved in a hydrodynamic movement. For this reason we have succeed to couple the M1 model to the CHIC code only for the resolution of the heat equation (last equation of (2.35)).

Before to detail the M1 model, some discussions on the state of the art of heat transport theories are presented.

Chapter 3

Heat transport theories

There are two theories describing macroscopic quantities in a plasma: the kinetic theory and the hydrodynamics. The hydrodynamic description is less accurate than the kinetic theory, however it is more suitable in order to perform large scale HED simulations, since it is much less time consuming.

The hydrodynamic equations have to be closed by defining the electron heat flux. Most of the hydrodynamic codes compute it under the assumption of being close to the local thermodynamic equilibrium. In that case, expressions for the heat flux was obtained by Spitzer and Härm (SH) [33]. Nevertheless, in the SH theory, the electrons which transport the heat are suprathermal: they are characterized by a velocity ~ 3.7 times the local thermal velocity. Since the electron mean free path (MFP) depends on the fourth power of velocity, these suprathermal electrons have a free path ~ 187 times longer than the thermal MFP. Thus, they can transport heat along large distances. If temperature profiles are sharp enough, the hot electrons can perturb the cold region, distancing it from the local thermodynamic equilibrium. In the same way, the cold EDF is deviated from the Maxwellian EDF. In these configurations, the local transport theory becomes insufficient.

Many theories have been proposed in order to describe nonlocal transport in hydrodynamic simulations. Most of them are time consuming and limited to one-dimensional geometry. The only exception is the one proposed by Schurtz, Nicolaï and Busquet [22, 34, 35] (SNB), based on the multi-group transport scheme. In the SNB model, nonlocal effects are computed by finding at each temporal step the energy distribution of fast electrons, from a stationary and simplified Fokker-Planck (FP) equation, assuming a weak anisotropy and a small deviation from equilibrium of the suprathermal part of the electron distribution function (EDF). In this model, the electric and magnetic field effects on suprathermal electrons are taken into account through phenomenological corrections [24]. These corrections can be very complex and numerically unstable.

Moreover, magnetic fields modify the heat transport. Their effects have been described by Braginskii [36], in the hydrodynamic regime, close to the local thermodynamic equilibrium. Nicolaï, Feugeas and Schurtz tired to extend their model to magnetized plasmas [24] but it is subject to many approximations, which limit its validity and affect the stability of calculations.

In this chapter we describe the classical framework of reduced models in section 3.1 and the local theory of heat transport in section 3.2. Then we discuss the main nonlocal models for unmagnetized plasmas in section 3.3 and finally the magnetized theory in section 3.4.

3.1 Reduced models

The heat flux is defined as the energy transported from a hot region to a cold one over a time unit and through surface unit. The nature of heat transport is intrinsically kinetic. Thus, we need to solve the FP equation in order to properly account for such a phenomenon. In this section we present a method of solving the FP equation, by using different assumptions on the velocity directions, in order to correctly calculate the heat exchange.

3.1.1 Velocity direction moment hierarchy

The FP equation is defined in the six dimensional phase-space ($\vec{x}$,$\vec{v}$). It is incompatible with the hydrodynamic equations defined in three dimensional space. The number of dimensions in the kinetic equation can be decreased by performing a hierarchy of moment integrations, in the same way as in section 2.3.1. This integration is performed over the velocity direction vector $\vec{\Omega}$. This allows to reduce the system: from six $(\vec{x}, v, \vec{\Omega})$ to four $(\vec{x}, v)$ dimensions. We proceed as follows.

We define the EDF moments as

$$\bar{\bar{f}}_l(\vec{x}, v, t) = \int_{S_2} d^2\Omega f_e(\vec{x}, \vec{v}, t) \underbrace{\otimes\vec{\Omega}}_{l-\text{times}} ,$$

where $\bar{\bar{f}}_l$ is a l-order tensor representing the l-th moment of the EDF. In particular, the first three moments read

$$\begin{cases} f_0 = \int_{S_2} d^2\Omega f_e \\ \vec{f_1} = \int_{S_2} d^2\Omega f_e \vec{\Omega} \\ \bar{\bar{f}}_2 = \int_{S_2} d^2\Omega f_e \vec{\Omega} \otimes \vec{\Omega} \end{cases} . \tag{3.1}$$

As previously, we define the zero-moment of the Boltzmann equation (2.5), by integrating the latter in $\int_{S^2} d^2\Omega$:

$$\int_{S^2} d^2\Omega \left[\frac{\partial f}{\partial t} + v\vec{\Omega}\cdot\vec{\nabla} f - \frac{e}{m_e}\left(\vec{E} + \frac{v}{c}\vec{\Omega}\times\vec{B}\right)\cdot\left(\vec{\Omega}\frac{1}{v^2}\frac{\partial}{\partial v}v^2 + \frac{1}{v}\frac{\partial}{\partial\vec{\Omega}}\right) f = \left(\frac{\partial f}{\partial t}\right)_{\text{coll}}\right]$$
$$\Rightarrow \frac{\partial f_0}{\partial t} + v\vec{\nabla}\cdot\vec{f_1} - \frac{e\vec{E}}{m_e v^2}\cdot\frac{\partial}{\partial v}\left(v^2\vec{f_1}\right) = \left(\frac{\partial f_0}{\partial t}\right)_{\text{coll}} ,$$

where S^2 is the unit sphere and

$$\frac{\partial}{\partial\vec{\Omega}} = \hat{e}_\theta \frac{1}{\sin\theta}\frac{\partial}{\partial\theta}\sin\theta + \hat{e}_\phi \frac{1}{\sin\theta}\frac{\partial}{\partial\phi}$$

is the angular derivative in spherical coordinates, The zero moment equation gives f_0 as a function of $\vec{f_1}$, which is given by the first moment equation. The latter is obtained by integrating Eq. (2.5) over $\int_{S^2} d^2\Omega\vec{\Omega}$:

$$\int_{S^2} d^2\Omega\vec{\Omega}\otimes\left[\frac{\partial f}{\partial t} + v\vec{\Omega}\cdot\vec{\nabla} f - \frac{e}{m_e}\left(\vec{E} + \frac{v}{c}\vec{\Omega}\times\vec{B}\right)\cdot\vec{\nabla}_v f = \left(\frac{\partial f}{\partial t}\right)_{\text{coll}}\right] \Rightarrow$$
$$\frac{\partial\vec{f_1}}{\partial t} + v\vec{\nabla}\cdot\bar{\bar{f}}_2 - \frac{e}{m_e}\int_{S^2} d^2\Omega\left(\vec{E} + \frac{v}{c}\vec{\Omega}\times\vec{B}\right)\cdot\left[\vec{\nabla}_v\left(f\otimes\vec{\Omega}\right) - f\vec{\nabla}_v\left(\otimes\vec{\Omega}\right)\right] = \left(\frac{\partial\vec{f_1}}{\partial t}\right)_{\text{coll}}$$
$$\Rightarrow$$
$$\frac{\partial\vec{f_1}}{\partial t} + v\vec{\nabla}\cdot\bar{\bar{f}}_2 - \frac{e}{m_e v^2}\frac{\partial}{\partial v}\left(v^2\bar{\bar{f}}_2\cdot\vec{E}\right) + \frac{e}{m_e v}\left(f_0\bar{\bar{I}} - \bar{\bar{f}}_2\right)\cdot\vec{E} + \frac{e}{m_e c}\vec{f_1}\times\vec{B} = \left(\frac{\partial\vec{f_1}}{\partial t}\right)_{\text{coll}} .$$

This equation depends on the second moment $\bar{\bar{f}}_2$. The following equation for the moment $\bar{\bar{f}}_2$ depends on a higher moment $\bar{\bar{f}}_3$. The system needs to be closed making some assumption on the last moment.

Matte and Virmont [37] described the nonlocal heat transport, by solving a FP equation, based on the Landau operator and performing angular moment integrations. They showed that it is sufficient to stop the moment hierarchy at the first moment equation, in order to describe the heat transport.

In summary, the angular moment hierarchy, limited to the first moment equation reads

$$\begin{cases} \frac{\partial f_0}{\partial t} + v\vec{\nabla}\cdot\vec{f}_1 - \frac{e\vec{E}}{m_e v^2}\cdot\frac{\partial}{\partial v}\left(v^2\vec{f}_1\right) = \left(\frac{\partial f_0}{\partial t}\right)_{\text{coll}} \\ \frac{\partial \vec{f}_1}{\partial t} + v\vec{\nabla}\cdot\bar{\bar{f}}_2 - \frac{e}{m_e v^2}\frac{\partial}{\partial v}\left(v^2\bar{\bar{f}}_2\cdot\vec{E}\right) + \frac{e}{m_e v}\left(f_0\bar{\bar{I}} - \bar{\bar{f}}_2\right)\cdot\vec{E} + \frac{e}{m_e c}\vec{f}_1\times\vec{B} = \left(\frac{\partial \vec{f}_1}{\partial t}\right)_{\text{coll}} \end{cases} . \tag{3.2}$$

Stopping the system to the first moment we limit the description to only one direction of anisotropy. However, except the case of many beam superpositions, this description is sufficient. The system (3.2) still needs to be closed and a relation for $\bar{\bar{f}}_2$ needs to be given. In what follows we will present a way to close the system. A second closure relation will be derived in the next part of the manuscript.

Another important point is the description of the collision operator in the hand right side of Eq. (3.2). The complete form is too complex to be used in a fast and practical model. As we show below, various approximations can be done.

3.1.2 Velocity-dependent BGK collision operator

The main effect of collisions is to induce the thermalization, which corresponds to the reduction of the EDF to a Maxwellian function. The simplest collision operator has been derived by Bhatnagar, Gross and Krook (BGK) [28]. It describes the thermalization process, in a characteristic time τ_e. In its original formulation, given in [28], it can be expressed as $-(f_e - f_e^m)/\tau_e$, where the collision time $\tau_e = 3\sqrt{m_e T_e^3}/(4\sqrt{2\pi} n_e Z e^4 \Lambda_{ei})$ does not depend on velocity but only on the hydrodynamic variables. However, this formulation does not lead to the description of a nonlocal transport, which is induced by the different velocity contributions. A first improvement is to use a modified version of the BGK collision operator accounting for different velocity contributions: $-\nu_{ee}(v)(f_e - f_e^m)$, with $\nu_{ee}(v) = 4\pi n_e e^4 \Lambda_{ee}/(m_e^2 v^3)$.

In the Lorentz gas approximation ($Z \gg 1$), the first two moments of the BGK collision operator read

$$\begin{cases} \left(\frac{\partial f_0}{\partial t}\right)_{\text{coll}} = -\nu_{ee}(f_0 - f_0^m) \\ \left(\frac{\partial \vec{f}_1}{\partial t}\right)_{\text{coll}} = -\nu_{ei}\vec{f}_1 \end{cases} ,$$

where $\nu_{ei} = \nu_{ei}\Lambda_{ee}/(Z\Lambda_{ei})$ and $\nu_{ei} = 4\pi Z n_e e^4 \Lambda_{ei}/(m_e^2 v^3)$ are the electron-electron and the electron-ion collision frequencies. Modified expressions for the collision frequency can be used, in order to take into account low-Z effects:

$$\begin{cases} \left(\frac{\partial f_0}{\partial t}\right)_{\text{coll}} = -\nu_{ee}(f_0 - f_0^m) \\ \left(\frac{\partial \vec{f}_1}{\partial t}\right)_{\text{coll}} = -\nu_{ei}^*\vec{f}_1 \end{cases} ,$$

with ν_{ei}^* given by tabulated or analytical expressions [38, 39]. It reads

$$\nu_{ei}^* = \frac{Z + 4.2}{Z + 0.24}\nu_{ei}. \tag{3.3}$$

This BGK collision operator accounts for the velocity dependence but does not conserve the energy moments (number of particles, momentum and energy).

For simplicity, in this manuscript we refer to the velocity-dependent BGK collision operator simply as BGK.

3.1.3 Small anisotropies

The classical approach for closing the system (3.2) is to develop the EDF as a spherical harmonic series, stopped at the first order.

As a special case of Fourier series, the spherical harmonics are a way to represent a function as the sum of simple sine waves. In particular, they are suitable to represent functions on the surface of a sphere, in terms of spherical coordinates. On the unit sphere S^2, the development reads

$$f_e(\vec{x}, v, \vec{\Omega}) = \sum_{l=0}^{\infty} \sum_{m=-l}^{l} f_l^m(\vec{x}, v) Y_l^m(\vec{\Omega}), \tag{3.4}$$

where

$$f_l^m = \int_{S^2} d^2 f_e \Omega (Y_l^m)^*(\vec{\Omega}),$$

$$Y_l^m(\vec{\Omega}) = (-1)^m \sqrt{\frac{2l+1}{4\pi} \frac{(l-m)!}{(l+m)!}} e^{im\phi} P_l^m(\cos\theta)$$

and

$$P_l^m(x) = (-1)^m (1-x^2)^{m/2} \frac{d^m}{dx^m} \left\{ \frac{1}{2^l l!} \frac{d^l}{dx^l} \left[\left(x^2-1\right)^l \right] \right\}$$

is the associated Legendre polynomial, for positive m. The sumbol $*$ means complex conjugate. For negative m,

$$P_l^{-m}(x) = (-1)^m \frac{(l-m)!}{(l+m)!} P_l^m(x).$$

It is more convenient to work in the real space. Then the first four coefficients of spherical harmonics read

$$\begin{aligned} Y_{l=0} &= \frac{1}{4\pi}, \\ Y_{l=0}^{m=-1} &= \frac{3}{8\pi} \Omega_x, \\ Y_{l=0}^{m=0} &= \frac{3}{4\pi} \Omega_z, \\ Y_{l=0}^{m=1} &= \frac{3}{8\pi} \Omega_y, \end{aligned}$$

where

$$\vec{\Omega} = \begin{pmatrix} \Omega_x \\ \Omega_y \\ \Omega_z \end{pmatrix} = \begin{pmatrix} \cos\phi \sin\theta \\ \sin\phi \sin\theta \\ \cos\theta \end{pmatrix}.$$

In the same way, the first four f_l^m read

$$\begin{aligned} f_{l=0} &= \frac{1}{4\pi} f_0, \\ f_{l=0}^{m=-1} &= \frac{3}{8\pi} f_{1x}, \\ f_{l=0}^{m=0} &= \frac{3}{4\pi} f_{1z}, \\ f_{l=0}^{m=1} &= \frac{3}{8\pi} f_{1y}, \end{aligned}$$

where

$$\vec{f_1} = \begin{pmatrix} f_{1x} \\ f_{1y} \\ f_{1z} \end{pmatrix}.$$

According to Eq. (3.4), the EDF can be written as [40]

$$f_e(\vec{x}, v, \vec{\Omega}, t) = \frac{1}{4\pi} f_0(\vec{x}, v, t) + \frac{3}{4\pi} \vec{\Omega} \cdot \vec{f_1}(\vec{x}, v, t), \tag{3.5}$$

In what follows we refer to Eq. (3.5) as the P1 approximation. In this approximation, the EDF is composed by an isotropic and a linearly anisotropic terms, respect to the velocity direction vector $\vec{\Omega}$.

The P1 approximation imposes another physical constraint to the first-moment stopped hierarchy: it is limited to nearly isotropic systems ($||\vec{f_1}||/f_0 < 1$). If $||\vec{f_1}||/f_0 > 1$, the EDF becomes negative for some directions. Since the EDF is a probability density, it must necessarily be positive. The nearly isotropic limit can be reasonably assumed only for low velocity electrons and, small gradients.

According to Eq. (3.1), the P1 approximation leads to the closure of $\bar{\bar{f}}_2$

$$\bar{\bar{f}}_2 = \frac{f_0}{3}.$$

For the plasmas of interest of this work, the heat transport phenomena develop on a fast time scale, compared to the characteristic time of the hydrodynamic evolution. Thus, frequently transport models are assumed to be stationary. We always use this assumption in our work. Correspondingly, a simplified and closed moment hierarchy reads

$$\begin{cases} v\vec{\nabla} \cdot \vec{f_1} - \frac{e\vec{E}}{m_e v^2} \cdot \frac{\partial}{\partial v}(v^2 \vec{f_1}) = -\nu_{ee}(f_0 - f_0^m) \\ \frac{v}{3}\vec{\nabla} f_0 - \frac{e\vec{E}}{3m_e}\frac{\partial}{\partial v} f_0 + \frac{e}{m_e c}\vec{f_1} \times \vec{B} = -\nu_{ei}^* \vec{f_1} \end{cases}. \tag{3.6}$$

In the system (3.6), the collision operators are phenomenological. However, they are convenient and used in many heat transport models. Some of them are presented in next sections.

3.2 Heat fluxes in the local thermal equilibrium

The heat transport is calculated under the assumption of a small departure from the local thermodynamic equilibrium. So Eq. (3.5) reads

$$f_e(\vec{x}, v, \vec{\Omega}, t) = \frac{1}{4\pi} f_0^m(\vec{x}, v, t) + \frac{3}{4\pi} \vec{\Omega} \cdot \vec{f_1}(\vec{x}, v, t),$$

where $f_0^m = 4\pi f_e^m = 4\pi n_e/(2\pi v_{th}^2)^{3/2} e^{-\frac{mv^2}{2T_e}}$ is the Maxwellian zero moment. Only the second equation in (3.6) has to be solved and reads

$$\frac{v}{3}\vec{\nabla} f_0^m - \frac{e\vec{E}}{3m_e} \cdot \frac{\partial}{\partial v} f_0^m + \frac{e}{m_e c}\vec{f_1^m} \times \vec{B} = -\nu_{ei}^* \vec{f_1^m}. \tag{3.7}$$

In such conditions the plasma is collisional and the MFP is small compared to the gradient lengths.

3.2.1 Spitzer-Härm theory

The classical model of heat transport was proposed by Spitzer and Härm [33]. This model is implemented in all hydrodynamic codes. We present it in this section.

In the stationary limit of unmagnetized plasmas, the Ampere's equation leads to a zero electric current

$$\vec{j_e} = -e \int_{\mathbf{R}^3} d^3v \vec{v} f_e = -e \int_0^\infty dv v^3 \vec{f_1} = 0.$$

By making explicit $\vec{f_1}$ in the second equation of the system (3.6), in the unmagnetized regime, the zero current condition reads

$$\vec{j_e} = \frac{e}{3} \int_0^\infty dv \frac{v^4}{\nu_{ei}^*} \vec{\nabla} f_0 - \frac{e^2 \vec{E}}{3 m_e} \int_0^\infty dv \frac{v^3}{\nu_{ei}^*} \frac{\partial}{\partial v} f_0 = 0, \tag{3.8}$$

which leads to an analytic form for the electric field:

$$\vec{E} = -\frac{m_e}{6e} \frac{\int_0^\infty \vec{\nabla} f_0 v^7 dv}{\int_0^\infty f_0 v^5 dv}. \tag{3.9}$$

This relation is only valid under the Lorentz gas approximation, when the electron-electron collisions can be neglected in Eq. (3.7). For $f_0 = 4\pi f_e^m$ we have

$$\vec{E}_{SH} = -\frac{T_e}{e} \left(\frac{\vec{\nabla} n_e}{n_e} + \xi \frac{\vec{\nabla} T_e}{T_e} \right). \tag{3.10}$$

The coefficient ξ equals 2.5 is in the Lorentz gas limit. Electron-electron collisions modify the electric field and that effect can be taken into account in the same way as the electron-ion collision frequency in Eq. (3.7), using the following expression:

$$\xi(Z) = 1 + \frac{3}{2} \frac{Z + 0.477}{Z + 2.15}, \tag{3.11}$$

which is a function of Z, ranging from 1.7 ($Z = 1$) to 2.5 ($Z = \infty$) and accounting for electron-electron collisions in the equation for $\vec{f_1}$ [33].

Knowing the electric field, one can find the first moment of the EDF, which reads

$$\vec{f_1^m} = -\frac{\lambda_{ei}^*}{3} \left(\frac{m_e v^2}{2T_e} - 4 \right) f_0^m \frac{\vec{\nabla} T_e}{T_e}, \tag{3.12}$$

where $\lambda_{ei}^* = v/\nu_{ei}^*$.

From Eq. (2.33), using Eq. (3.12), the local SH flux reads

$$\begin{aligned} \vec{q}_{SH} &= \frac{1}{2} m_e \int_{\mathbf{R}^3} d^3v v^2 \vec{v} f_e \\ &= \frac{1}{2} m_e \int_{\mathbf{R}} dv v^5 \vec{f_1} \\ &= -k_{SH}(T_e) \vec{\nabla} T_e, \end{aligned}$$

with the thermal conductivity

$$k_{SH}(T_e) = 0.4 \frac{Z}{Z + 0.2 \log(Z) + 3.44} \frac{20 (2/\pi)^{3/2} T_e^{5/2}}{m_e^{1/2} e^4 Z \Lambda_{ei}}. \tag{3.13}$$

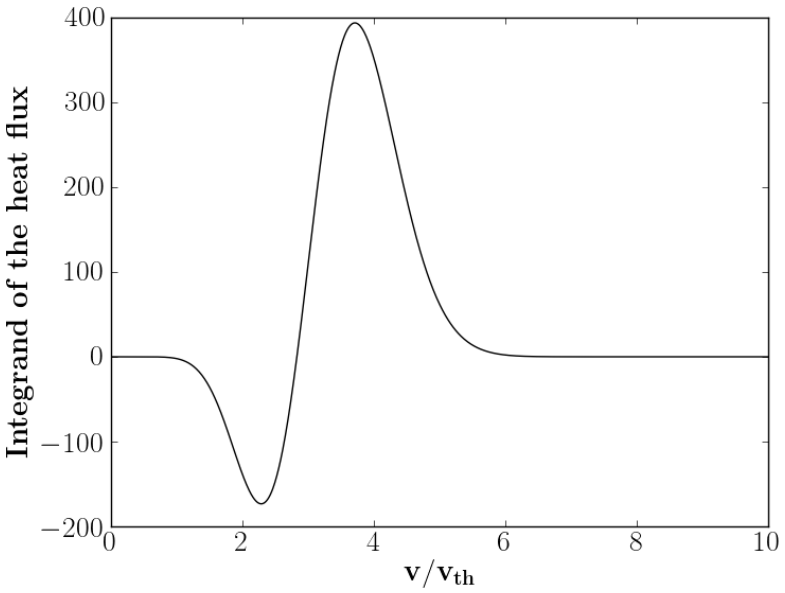

Figure 3.1: Integrand function of the local heat flux, as a function of the velocity, normalized to the thermal velocity.

This expression is valid for plasmas with an arbitrary ion charge.

We have seen that, in the local limit, the heat flux depends only on hydrodynamic variables. In particular, it is proportional to the temperature gradient, and the thermal conductivity depends strongly on the temperature ($\propto T_e^{5/2}$). In its original derivation [33], the computation of k_{SH} for $Z = 1$ has been done numerically. However, it is also possible to derive it from the complete Landau collision operator, by accounting for the electron-electron collisions.

3.2.2 Limits of the local theory and the flux limitation model

The integrand function of the heat flux in Eq. (2.33), with the local flux of Eq. (3.12), is

$$\propto \tilde{v}^9(\tilde{v}^2/2 - 4)e^{\tilde{v}^2/2}, \tag{3.14}$$

where $\tilde{v} = v/v_{th}$ is the velocity normalized to the local thermal velocity $v_{th} = \sqrt{T_e/m_e}$. This function is plotted in Fig. 3.1. We see that heat is mostly transported by suprathermal electrons, with velocities 3.7 times the thermal velocity [22]. This means that heat is transported by electrons with the collisional path 187 times the thermal MFP, since the electron collision length depends on the fourth power of velocity. Thus, if temperature gradients are sharp, electrons can deeply penetrate in plasma and can deposit their energy far from where they are originated.

The limit of the SH theory is given by the condition

$$||\vec{f}_e^{(1)}(v = 3.7v_{th})|| \leq f_e^{(0)}(v = 3.7v_{th})$$

which corresponds to the condition [21]

$$\lambda_{ei}/L_T < 2 \cdot 10^{-3}, \tag{3.15}$$

where $L_T = T_e/||\vec{\nabla}T_e||$ is the temperature gradient length. This relation assures a positive EDF. When the MFP overpasses the limit of 2×10^{-3} times the temperature gradient length, the local theory is no more valid and nonlocal corrections are needed.

In order to describe the heat flux outside the limit imposed by the condition (3.15), most of hydrodynamic codes limit the flux to a certain fraction of the free streaming (FS) flux. The latter is a limit value for heat fluxes. It describes a flux carried by thermal electrons toward a void. It reads

$$q_{FS} = n_e m_e v_{th}^3.$$

In its simplest form, the flux limitation (FL) theory reads

$$q_{lim} = min(q_{SH}, \phi q_{FS}),$$

where ϕ is the flux limiter. Often in ICF simulations it is fixed to be $3 - 7\%$. Also a harmonic limitations can be implemented:

$$\frac{1}{q_{lim}} = \frac{1}{q_{SH}} + \frac{1}{\phi q_{FS}}.$$

The flux limitation model is a phenomenological one: the value of ϕ is chosen in order to reproduce experimental results. Moreover, it is not able to reproduce all the features of nonlocal fluxes.

3.3 Nonlocal models

When $\lambda_{ei}/L_T > 2 \cdot 10^{-3}$, the energetic electrons, which transport heat, can penetrate in the plasma and deposit their energy nonlocally. In other words, the electron transport may modify the original Maxwellian distribution. Such a behavior has a kinetic origin. However it is unreasonable to think to solve a FP code on hydrodynamic temporal and spatial scales. Thus, many intermediate models have been proposed. We analyze them here, presenting their advantages and deficiencies.

3.3.1 Monodimensional convolution models

First of all, Matte and Virmont [37] have described nonlocal transport by solving a FP equation, based on the Landau operator, and on different orders of the spherical harmonic development of the EDF. The have shown that the linear development (3.5) is sufficient for modeling the heat transport. Even if accurate, this theory is too much time consuming to be coupled with a hydrodynamic code, even in one dimension.

Subsequently more simplifications have been proposed. They are based on the convolution of temperature gradient over the electron MFP. In this section we overview the main ones.

LMV model

One of the first nonlocal models has been proposed by Luciani, Mora and Virmont (LMV) [21]. They evaluated the local heat flux in plasma, by using a propagator, which depends on an effective hydrodynamic MFP. The propagator accounts for electron-electron and electron-ion collisions and depends on hydrodynamic variables. The effective MFP reads

$$\lambda_e = \sqrt{\lambda_{ee}\lambda_{ei}} = \frac{T_e^2}{4\pi n_e \sqrt{Z+1} e^4}.$$

Mathematically, the LMV heat flux is structured as a convolution of a local SH heat flux

$$q_{LMV} = \int \frac{dx'}{\lambda_e(x')} w(x, x') q_{SH}(x'), \tag{3.16}$$

where

$$q_{SH} = -k_{SH}\frac{\partial}{\partial x}T_e$$

is the monodimensional local SH flux, with the conductivity given by Eq. (3.13). The kernel w is

$$w(x,x') = \frac{1}{2a}e^{-\frac{|\int_{x'}^{x} dx'' n_e(x'')|}{a\lambda_e(x')n_e(x')}}. \tag{3.17}$$

The constant a is adjusted to ≈ 32, by comparison with FP simulations.

In the local limit $\lambda_e \longrightarrow 0$, the kernel $w/\lambda_e(x')$ behaves as a Dirac δ-function and the heat flux relaxes to q_{SH}. In the nonlocal limit, with a constant density, it can be approximated to 1 in the point of the temperature gradient maximum. Integrating Eq. (3.16), around this maximum, we find that the maximum heat flux is the 12% of the FS flux.

The heat flux (3.16) is simple enough to be implemented in a fluid code. However, this model is in practice limited to monodimensional simulations, and it is also too much time consuming.

Improvements of the convolution theory

Bendib, Luciani and Matte [41] proposed a correction in order to account for electric field effects. This correction is given by a comparison with kinetic equations. It consists in the replacement of the original kernel w (3.17) in Eq. (3.16), with a new kernel w', which is defined as

$$w'(x,x') = w(x,x')e^{\frac{eE(x')-eE(x)}{T_e(x')}},$$

where E is the local electric field, given by Eq. (3.10).

Albritton et al. (AWBS) [42] based their kernel on a simplified FP equation [43]. They proposed a collision operator for fast electrons, which is analyzed in detail in the second part of the manuscript. Based on kinetic assumptions, the AWBS operator improves the LMV model. However, it is based on the convolution of a kernel and so limited to monodimensional analysis and it has a complicated form. The AWBS model leads to more realistic results [44]. It has been improved in order to take into account electric field effects [45], following the scheme in the previous section.

Epperlein and Short developed a new kernel based on a fitted Fourier space solution of the flux limitation, obtained with a FP code [44]. This fit has been obtained while studying the flux limitation of a periodic sinusoidal perturbation of the temperature, for different wavelengths, which are related with the degree of nonlocality. The inverse Fourier transformation of the FP solution leads to a kernel for the description of the heat transport.

The models resumed in this section are more or less accurate. However they are all based on a convolution of the temperature. This time consuming form is not suitable for a multidimensional analysis and applies only to small amplitude temperature perturbations.

3.3.2 Multidimensional generalization

The multidimensional generalization of the LMV model has been performed by Schurtz Nicolaï and Busquet (SH) [22]. It is based on arguments similar to the LMV model, but it was reinterpreted with a kinetic formalism.

Convolution formalism

The nonlocal theory accounts for the contributions of all spatial points $\vec{x}' = s\vec{\Omega}_x$ around the reference point $\vec{x}$.

The natural way to generalize Eq. (3.16), is to write it as

$$\vec{q}_{SNB} = \int \frac{d^3x'}{\lambda_e(\vec{x}')} \bar{\bar{w}}(\vec{x}, \vec{x}') \cdot \vec{q}_{SH}(\vec{x}'). \tag{3.18}$$

The integral is represented in spherical coordinates $d^3x' = d^2\Omega_x s^2 ds$ and the second order tensorial kernel is assumed to be isotropic $\bar{\bar{w}} = w_0 \vec{\Omega}_x \otimes \vec{\Omega}_x$.

This integral expression can be considered as a solution of a linear transport equation of the form of Eq. (3.18)

$$\vec{\Omega}_x \cdot \vec{\nabla} q_{SNB} = \frac{1}{\lambda_{SNB}} \left(\frac{3}{4\pi} \vec{\Omega}_x \cdot \vec{q}_{SH} - q_{SNB} \right), \tag{3.19}$$

where q_{SNB} is the modulus of $\vec{q}_{SNB}$ and λ_{SNB} an effective MFP. In order to be a solution of Eq. (3.19), the kernel of Eq. (3.18) should have the following form

$$w_0 = \frac{3}{4\pi} e^{-\int_{\vec{x}}^{\vec{x}'} \frac{d^3\vec{x}''}{\lambda_{SNB}(\vec{x}'')}}.$$

However the kernel describing the heat transport cannot be symmetric: if a temperature gradient exists between $\vec{x}$ and $\vec{x}'$, the weight w_0 of the first point should be different from the weight of the latter. In the LMV model it happens, since the kernel involves a spatially dependent MFP $\lambda_e(x')$. Unfortunately, a nonsymmetric kernel would lead to a non-self-adjoint transport equation, which has no physical sense. The only way to recover the symmetry breaking, is to separately transport the contribution of each velocity, using velocity dependent kernels. So Eq. (3.19) has to be solved separately for each velocity. This proposal has an evident physical sense as the electron collision length in plasmas depends on its energy.

The energy domain is divided in N_g energy groups, characterized by an upper bound E_g. As shown in Eq. (3.14), the contribution of each energy group g to the SH flux is proportional to

$$\int_{E_{g-1}/T_e}^{E_g/T_e} d\beta \beta^4 (\beta - 4) e^{-\beta},$$

where the term $\beta - 4$ is due to the return current of cold electrons, which do not play a key role in the nonlocal transport. For low energies, it is partially compensated by the Joule heating. For this reason, this factor is dropped off. The new term $\beta^4 e^{-\beta}$ has an analytical primitive. Moreover, in the whole energy domain, $\beta^4(\beta-4)e^{-\beta}$ and $\beta^4 e^{-\beta}$ have the same integral, 24. Now the energy dependent transport equation reads

$$\vec{\Omega}_x \cdot \vec{\nabla} q_g = \frac{1}{\lambda_g} \left(\frac{3}{4\pi} \vec{\Omega}_x \cdot \vec{U}_g - q_g \right), \tag{3.20}$$

where

$$\vec{U}_g = \frac{1}{24} \int_{E_{g-1}/T_e}^{E_g/T_e} d\beta \beta^4 e^{-\beta} \vec{q}_{SH},$$

and

$$\lambda_g = 2 \left(\frac{E_{g-1/2}}{T_e} \right)^2 \lambda_e$$

is an effective MFP. The SNB flux now reads

$$\vec{q}_{SNB} = \sum_g \int_{s^2} d^2\Omega_x \vec{\Omega}_x q_g.$$

In the context of multidimensional hydrodynamic simulation codes, a diffusion approximation of Eq. (3.20), is easy to handle and it has the desirable properties of damping. The zero order angular momentum reads

$$H_g = \int_{S^2} d^2\Omega_x q_g.$$

The P1 expansion reads

$$q_g = \frac{1}{4\pi} H_g + \frac{3}{4\pi} \vec{\Omega}_x \cdot \vec{q}_g,$$

where $\vec{q}_g$ is also interpreted as the first moment. From the zero and the first angular moments of Eq. (3.20), we find

$$\begin{cases} H_g = -\lambda_g \vec{\nabla} \cdot \vec{q}_g \\ \frac{\lambda_g}{3} \vec{\nabla} H_g = \vec{U}_g - \vec{q}_g \end{cases}$$

which leads to the equation

$$\begin{cases} \left(\frac{1}{\lambda_g} - \vec{\nabla} \frac{\lambda_g}{3} \cdot \vec{\nabla} \right) H_g = -\vec{\nabla} \cdot \vec{U}_g \\ \vec{q}_{SNB} = \vec{q}_{SH} - \sum_g \frac{\lambda_g}{3} \vec{\nabla} H_g \end{cases}.$$

The model is further improved by the addition of electric field corrections. A definition for the electric field is given in Eq. (3.10), by the SH theory. The electric field accelerates low energy electrons and slows down fast electrons, which are responsible for the nonlocal transport. Though they are energetic, high velocity electrons weakly modify the electric field, since they are few in number. This justifies the use of the local electric field from the SH theory. Its effect on nonlocal electrons is treated in a semiqualitative way: an electron with energy ϵ cannot travel longer distance than ϵ/eE, under a constant electric field of magnitude E. Thus the MFP is harmonically reduced by this factor to

$$\frac{1}{\lambda_g^E} = \frac{1}{\lambda_g} + \frac{|e\vec{E}_{SH}|}{\epsilon_g}. \tag{3.21}$$

The model finally reads

$$\begin{cases} \left(\frac{1}{\lambda_g} - \vec{\nabla} \frac{\lambda_g^E}{3} \cdot \vec{\nabla} \right) H_g = -\vec{\nabla} \cdot \vec{U}_g \\ \vec{q}_{SNB} = \vec{q}_{SH} - \sum_g \frac{\lambda_g^E}{3} \vec{\nabla} H_g \end{cases}.$$

Kinetic reinterpretation

Historically, the SNB model has been proposed in the formalism presented above. However it can be reinterpreted, starting from kinetic assumptions, as it is shown here.

The SNB model is based on the system (3.6), with the Z-fitted BGK collisional operator, which neglects the energy diffusion. The main assumption of this model is the splitting of the EDF in a local part, which leads to the SH flux, and a nonlocal part of suprathermal electrons, which leads to nonlocal effects:

$$\begin{cases} f_0 = f_0^m + \Delta f_0 \\ \vec{f}_1 = \vec{f}_1^m + \Delta \vec{f}_1 \end{cases}.$$

As described in section 3.2, the local terms (denoted with the subscript m) are given by well-known analytic relations: the isotropic term is a Maxwellian function and the

anisotropic term is given by Eq. (3.12). Solving Eq. (3.6), neglecting electric field effects as well as second order terms in Δf_e, we find the diffusion equation for the suprathermal electrons. It reads

$$\begin{cases} \left(\frac{1}{\lambda_{ee}} - \vec{\nabla}\frac{\lambda_{ei}^E}{3}\vec{\nabla}\right)\Delta f_0 = -\vec{\nabla}\cdot\vec{g}_1^m \\ \Delta\vec{f}_1 = -\frac{\lambda_{ei}^*}{3}\vec{\nabla}\Delta f_0 \end{cases},$$

where the source term

$$\vec{g}_1^m = -\frac{\lambda_{ei}^*}{3} f_0^m \frac{\vec{\nabla}T_e}{T_e}$$

is a simplified form of Eq. (3.12), neglecting the return current, and

$$\lambda_{ej} = v/2\nu_{ej} \tag{3.22}$$

is the effective collisional electron free path (see formula 23 of [22]), with $j = e, i$. The electric field effect on the electron transport is empirically taken into account for each energy group through a harmonic reduction of the electron-ion MFP to a physical stopping length

$$\frac{1}{\lambda_{ei}^E} = \frac{1}{\lambda_{ei}} + \frac{|e\vec{E}_{SH}|}{\epsilon}.$$

The nonlocal correction of the heat flux is given by $\Delta\vec{f}_1$:

$$\vec{q}_{SNB} = 2\pi m_e \int_0^\infty (\vec{f}_1^m + \Delta\vec{f}_1)v^5 dv = \vec{q}_{SH} + \Delta\vec{q}.$$

Finally the model can be resumed as

$$\begin{cases} \left(\frac{1}{\lambda_{ee}} - \vec{\nabla}\frac{\lambda_{ei}^E}{3}\vec{\nabla}\right)\Delta f_0 = -\vec{\nabla}\cdot\vec{g}_1^m \\ \vec{q}_{SNB} = \vec{q}_{SH} - 2\pi m_e \int_0^\infty \frac{\lambda_{ei}^*}{3}\vec{\nabla}\Delta f_0 v^5 dv \end{cases}.$$

If the velocity space is discretized in groups g, the model can be reinterpreted as

$$\begin{cases} H_g = -2\pi m_e \Delta f_0(v_g) v_g^5 dv_g \\ \vec{U}_g = \vec{g}_1^m(v_g) \end{cases}$$

The equivalence between this kinetic formalism and the convolution formalism is thus demonstrated.

In the third part of this manuscript we show that the main effects of nonlocal transport are flux limitation and preheating. Although the SNB model is computationally efficient and operates in three spatial directions, it cannot describe fast electrons at the kinetic scale.

In contrast to the other models, the SNB model overcomes the monodimensional limit. However, as it has been described in this section, it is not able to account for magnetic fields and assumes a weak anisotropy of the EDF. We discuss these issues in the next section.

3.3.3 Hybrid split-convolution model

In the 2008, a new nonlocal model has been developed by Colombant, Manheimer and Goncharov (CMG) [23]. This model is based on an approach similar to SNB, which consists in splitting the heat flux in two terms. The first one is given by local electrons,

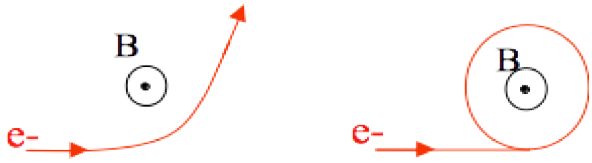

Figure 3.2: Effect of magnetic fields on electrons: their trajectory are turned and, if magnetic fields are strong enough, they can be forced to turn around.

characterized by a short MFP, and the second one is due to the nonlocal correction. In this way, the heat flux is written as

$$\begin{aligned} q_{CMG}(x) &= -\int_0^{\epsilon_{cr}} d\epsilon k(x,\epsilon)\frac{\partial}{\partial x}T_e(x) - \int dx' \int_{\epsilon_{cr}}^{\infty} d\epsilon k(x,x',\epsilon)\frac{\partial}{\partial x}T_e(x) \\ &= -W_1(x,\epsilon_{cr})k_{SH}(x)\frac{\partial}{\partial x}T_e(x) - W_2(x,\epsilon_{cr})\int dx' \int_{\epsilon_{cr}}^{\infty} d\epsilon \Pi(x,x',\epsilon), \end{aligned}$$

where k_{SH} is given by Eq. (3.13). The first term on the right side represents the local contribution, equal to the local heat flux, weighted with a factor W_1. The second term represents the contribution of nonlocal electrons.

The derivation of the CMG model is similar to the kinetic derivation of the SNB model. The linearized FP equation in (3.6) is solved for f_1. The so-obtained solution can be analytically integrated under certain hypotheses: the electron-electron and electron-ion collision frequencies have the same velocity dependence (high velocity limit), and a single Coulomb logarithm describes both collision processes. Electric fields, as in SNB, are assumed to be local and stationary. The solution for f_1 reads

$$f_1(x) = -\frac{\varsigma(Z)}{2}\int_{-\infty}^{\infty} dx' f_{1L}\hat{k}(x',v)e^{-|\int_{x'}^{x} dx''\hat{k}(x'',v)|}.$$

The expressions for ς and $\hat{k}$ are given in the original paper [23], and f_{1L} is defined as a local perturbation to the Maxwellian equilibrium distribution (in the SNB approach it is Δf_0). By computing the fifth velocity moment of f_1, one obtains the final expression for both the convolution operator and the associated weighting functions. The convolution kernel can be derived both in the limit of zero-current [23], and in the limit of pressure balance [46].

A crucial issue is the choice of the critical energy that discriminates the local and nonlocal contributions. It is proposed to use $\epsilon_{cr} \approx 5T_e$.

The main problem of this nonlocal model is its multidimensional generalization, which has not been developed yet. Another limit is accounting for magnetic fields. Moreover, Marocchino et al. [25] demonstrated that the CMG model is computationally slower than the SNB model, by a factor $2-3$.

3.4 Magnetized heat fluxes

When an intense laser pulse interacts with a plasma, it induces noncollinear temperature and density gradients, which, are responsible for the creation of strong magnetic fields [47] (of the order of mega-Gauss).

The magnetic fields modify the movement of electrons, as shown in Fig. 3.2. They force electrons to rotate, inducing the energy transport perpendicular to the temperature gradients, even in the local case. Moreover, if magnetic fields are strong enough, they can force electrons to turn around, reducing their effective MFP.

We present here the state of the art of models, which describes the effects of magnetic fields on the electron heat flux.

3.4.1 Local regime

The theory of electron transport in magnetized plasmas has been derived by Braginskii in 1950s [36]. He found expressions for the electron heat flux vector in an external magnetic field by performing an expansion of the FP equation in Laguerre polynomials stopped at the third order. We follow his notation in this paragraph.

The mean time between two collisions of an electron in a plasma, close to the local thermodynamic equilibrium is

$$\tau_e = \nu_e^{-1} = \frac{3}{4}\frac{\sqrt{m_e T_e^3}}{\sqrt{2\pi} n_i Z^2 e^4 \Lambda_{ei}}.$$

The averaged electron MFP is $\lambda_e = v_{th}\tau_e$. If the plasma is magnetized, electrons rotate in the external magnetic field $\vec{B}_0$. The frequency of this rotation (electron girofrequency) is

$$\omega_B = \frac{eB_0}{m_e c}.$$

Comparing these two quantities, we estimate the magnetic field influence on the electron energy transport. The Hall parameter $\omega_B\tau_e$ is the measure of this influence.

Under the assumption of a stationary process, the electric current follows from the Ampere's law (2.15):

$$\vec{j} = \frac{c}{4\pi}\vec{\nabla} \times \vec{B}, \tag{3.23}$$

where $\vec{B}$ is the induced (self-consistent) magnetic field. Assuming a perfect gas equation of state, the electron pressure reads $p_e = n_e T_e$.

The electric field, for a magnetized plasma reads [36, 38, 24]

$$\vec{E} = -\frac{\vec{\nabla} p_e}{e n_e} + \frac{\vec{j} \times \vec{B}}{c e n_e} + \bar{\bar{\alpha}} \cdot \frac{\vec{j}}{e^2 n_e^2} - \bar{\bar{\beta}} \cdot \frac{\vec{\nabla} T_e}{e}. \tag{3.24}$$

In Eq. (3.24), $\bar{\bar{\alpha}}$ and $\bar{\bar{\beta}}$ are second-order tensors, which respectively account for the electrical resistivity and the thermoelectric conductivity. Applied to a generic vector $\vec{V}$, the components of the electrical resistivity tensor can be expressed as

$$\bar{\bar{\alpha}} \cdot \vec{V} = \alpha_\parallel \hat{b} \cdot (\hat{b} \cdot \vec{V}) - \alpha_\perp \hat{b} \times (\hat{b} \times \vec{V}) - \alpha_\wedge \hat{b} \times \vec{V},$$

where the versor $\hat{b}$ denotes the direction of the magnetic field $\vec{B}_0 = B_0\hat{b}$. In an analogous way, the thermoelectric conductivity tensor can be expressed as

$$\bar{\bar{\beta}} \cdot \vec{V} = \beta_\parallel \hat{b} \cdot (\hat{b} \cdot \vec{V}) - \beta_\perp \hat{b} \times (\hat{b} \times \vec{V}) + \beta_\wedge \hat{b} \times \vec{V}.$$

The symbols $\parallel$, $\perp$ mean parallel and perpendicular to the magnetic field, while $\wedge$ means crossed between the magnetic field and the generic vector.

The Braginskii's heat flux reads

$$\vec{q}_B = -\bar{\bar{k}} \cdot \vec{\nabla} T_e - \bar{\bar{\beta}} \cdot \vec{j}\frac{T_e}{e}. \tag{3.25}$$

The thermoelectric tensor accounts for the friction force. The second-order tensor $\bar{\bar{k}}$ is the thermal conductivity and accounts for the thermal force. Its components read

$$\bar{\bar{k}} \cdot \vec{V} = k_\parallel \hat{b} \cdot (\hat{b} \cdot \vec{V}) - k_\perp \hat{b} \times (\hat{b} \times \vec{V}) + k_\wedge \hat{b} \times \vec{V}.$$

As we will see in chapter 8, for the regimes analyzed in this study, the dominant term in Eq. (3.25) is the thermal conductivity term. Assuming the second term negligible, we can limit magnetic effects to the local flux limitation and rotation.

Let us consider a two-dimensional flow and a magnetic field perpendicular to the plane. Consequently, the plasma is homogeneous along the magnetic field and we are not interested on the parallel tensor component. The electrical resistivity, the thermoelectric and the thermal conductivity are defined by

$$\begin{aligned}
\alpha_\perp &= \frac{m_e n_e}{\tau_e}\frac{1-\alpha_0'-(\omega_B\tau_e)^2\alpha_1'}{\Delta},\\
\alpha_\wedge &= \frac{m_e n_e}{\tau_e}\frac{\alpha_0''+(\omega_B\tau_e)^2\alpha_1''}{\Delta}\omega_B\tau_e,\\
\beta_\perp &= \frac{\beta_0'+(\omega_B\tau_e)^2\beta_1'}{\Delta},\\
\beta_\wedge &= \frac{\beta_0''+(\omega_B\tau_e)^2\beta_1''}{\Delta}\omega_B\tau_e,\\
k_\perp &= \frac{p_e\tau_e}{m_e}\frac{\gamma_0'+(\omega_B\tau_e)^2\gamma_1'}{\Delta},\\
k_\wedge &= \frac{p_e\tau_e}{m_e}\frac{\gamma_0''+(\omega_B\tau_e)^2\gamma_1''}{\Delta}\omega_B\tau_e,
\end{aligned}$$

where $\Delta = \delta_0 + \delta_1(\omega_B\tau_e)^2 + (\omega_B\tau_e)^4$ and the values of the Braginskii's coefficients are given as interpolations of the values computed by Braginskii [36], in function of the ion charge Z. For the electrical resistivity they are

$$\begin{aligned}
\alpha_0' &= \left[\left(\frac{0.3008}{Z}+0.976\right)\frac{1}{Z}+0.4924\right]\frac{1}{Z}+0.0678,\\
\alpha_1' &= \frac{1.786}{Z}+4.630,\\
\alpha_0'' &= \left(\frac{0.3714}{Z}+0.3142\right)\frac{1}{Z}+0.094,\\
\alpha_1'' &= 1.704,
\end{aligned}$$

for the thermoelectric conductivity

$$\begin{aligned}
\beta_0' &= \left[\left(\frac{0.3768}{Z}+1.2998\right)\frac{1}{Z}+0.8583\right]\frac{1}{Z}+0.146,\\
\beta_1' &= \frac{1.303}{Z}+3.798,\\
\beta_0'' &= \left(\frac{0.7215}{Z}+1.4545\right)\frac{1}{Z}+0.877,\\
\beta_1'' &= 1.50
\end{aligned}$$

and for the thermal conductivity

$$\begin{aligned}
\gamma_0' &= \left[\left(\frac{0.909}{Z}+4.405\right)\frac{1}{Z}+5.406\right]\frac{1}{Z}+1.20,\\
\gamma_1' &= \frac{1.414}{Z}+3.250,\\
\gamma_0'' &= \left(\frac{2.31}{Z}+9.31\right)\frac{1}{Z}+10.23,\\
\gamma_1'' &= 2.50.
\end{aligned}$$

The Δ coefficients are

$$\delta_0 = \left[\left(\frac{1.3008}{Z} + 1.5956\right)\frac{1}{Z} + 0.7778\right]\frac{1}{Z} + 0.0961,$$
$$\delta_1 = \left(\frac{1.35}{Z} + 5.958\right)\frac{1}{Z} + 7.482.$$

In this section we have presented the magnetic field transport equations from the magnetohydrodynamics, according to the original theory by Braginskii [36]. The magnetic field changes the direction and the modulus of energy fluxes and it is essential for the description of a magnetized heat transport. A more precise calculation of Braginskii's coefficients has been performed in [38] by Epperlein and Haines, numerically solving the local FP equation, using a finite difference representation of the equation. They improved the coefficient precision up to 15%.

3.4.2 Approach for a nonlocal generalization

Braginskii's theory is limited to local regimes. Magnetic fields add a degree of complexity to plasmas, making difficult the elaboration of a nonlocal theory of magnetized transport. Nicolaï, Feugeas and Schurtz proposed an approach for this analysis in [24], based on the original SNB model. We resume here the main ideas.

The solution of the first moment of system (3.6), acconting for magnetic fields, is

$$\vec{f_1} = \frac{\lambda^*_{ei}}{1 + \left(\frac{\omega_B \lambda^*_{ei}}{v}\right)^2}\left(-\vec{\nabla} f_0 - \frac{\omega_B \lambda^*_{ei}}{v}\hat{b} \times \vec{\nabla} f_0 + \frac{e\vec{E}}{m_e v}\frac{\partial}{\partial v} f_0 + \frac{\omega_B \lambda^*_{ei}}{v}\hat{b} \times \frac{e\vec{E}}{m_e v}\frac{\partial}{\partial v} f_0\right). \tag{3.26}$$

Assuming $f_0 = f_0^m$, the anisotropic part $\vec{f}_1^m$ can be expressed as a function of the temperature and current gradients [24]. It reads

$$\vec{f}_1^m = -C_\perp \frac{\vec{j}}{3 v_{th} e n_e} - C_\wedge \hat{b} \times \frac{\vec{j}}{3 v_{th} e n_e} - D_\perp \frac{v_{th}}{3\nu_e}\frac{\vec{\nabla} T_e}{T_e} - D_\wedge \hat{b} \times \frac{v_{th}}{3\nu_e}\frac{\vec{\nabla} T_e}{T_e}, \tag{3.27}$$

with $\nu_e = \sqrt{2}\pi n_e Z e^4 \lambda_{ei} / \sqrt{m_e T_e^3}$,

$$C_\perp = \frac{u^4\phi_7 + u^7\phi_{10}(\omega_B\tau_e)^2}{\phi_7^2 + (\phi_{10}\omega_B\tau_e)^2} f_0^B,$$
$$C_\wedge = \frac{u^7\phi_7 + u^4\phi_{10}(\omega_B\tau_e)^2}{\phi_7^2 + (\phi_{10}\omega_B\tau_e)^2}\omega_B\tau_e f_0^B,$$
$$D_\perp = \left[u^6 - \frac{u^4[\phi_7\phi_9 + \phi_{10}\phi_{12}(\omega_B\tau_e)^2] - u^7[\phi_7\phi_{12} + \phi_{10}\phi_9(\omega_B\tau_e)^2]}{\phi_7^2 + (\phi_{10}\omega_B\tau_e)^2}\right] f_0^B,$$
$$D_\wedge = \left[u^9 - \frac{u^4[\phi_7\phi_{12} + \phi_{10}\phi_9(\omega_B\tau_e)^2] + u^7[\phi_7\phi_9 + \phi_{10}\phi_{12}(\omega_B\tau_e)^2]}{\phi_7^2 + (\phi_{10}\omega_B\tau_e)^2}\right]\omega_B\tau_e f_0^B,$$

$u = v/v_{th}$ and

$$f_0^B = \frac{f_0^m}{1 + u^6(\omega_B\tau_e)^2}.$$

The coefficients ϕ_n are velocity integrals, which read

$$\phi_n = \frac{4}{3\sqrt{\pi}}\int_0^\infty du \frac{u^n e^{-u^2}}{1 + (\omega_B\tau_e u^3)^2}.$$

From the integration of Eq. (3.27) over the energy, Braginskii's electric field and heat flux can be deduced. This expression is used as a source for finding nonlocal fluxes. As it is done in section 3.3.2, the EDF moments are split in local (Maxwellian) and nonlocal contributions. Equation (3.6) is solved for the nonlocal contribution, after some reductions. Due to the low energy nature of electrons, which modify electric and magnetic fields, magnetic fields are assumed to be local and the electric field effect on nonlocal electrons is neglected. Since magnetic fields reduce the nonlocality of the system, we can again apply the assumption of a linear deviation from the local transport. Then, Eq. (3.6) reduces to

$$\begin{cases} -\frac{\Delta f_0}{\lambda_{ee}} + \frac{\vec{\nabla}}{3} \cdot \left[\frac{\lambda^*_{ei}}{1+(u^3\omega_B\tau_e)^2} (\vec{\nabla} + u^3\omega_B\tau_e\hat{b}\times)\Delta f_0 \right] = \vec{\nabla} \cdot g_1^m \\ \Delta\vec{f}_1 = \frac{\lambda^*_{ei}}{1+(u^3\omega_B\tau_e)^2} (\vec{\nabla} + u^3\omega_B\tau_e\hat{b}\times)\Delta f_0 \end{cases} . \tag{3.28}$$

The solution of system (3.28) leads to the following expression for the total heat flux

$$\vec{q}_{SNB-B} = \vec{q}_B + 2\pi m_e \int_0^\infty \Delta\vec{f}_1 v^5 dv.$$

In this case corrections are added to the Braginskii's local flux.

The simplified FP system (3.28) emphasizes the magnetized effects on the nonlocal transport. The reduction of the effective MFP from λ^*_{ei} to $\frac{\lambda^*_{ei}}{1+(u^3\omega_B\tau_e)^2}$ leads to a reduction of nonlocal effects. The cross $\hat{b}$ term induces a flux rotation, also for the nonlocal corrections.

The generalization to magnetized plasmas of the SNB model is complex, due to a large number of integral coefficients, which characterize this theory. Moreover, this theory implies many approximations, which limit its domain of validity. For all these reasons, the theory has never achieved a big success in the laser-plasma community. That is the reason which motivates us to look for a different approach to the magnetized electron transport.

Part II

A New Reduced Approach

Chapter 4

Reduced collision models

In order to be able to make realistic predictions, the HED physical simulations require to account for kinetic effects, such as relativistic electron transport, hot electron generation, nonlocal transport and stream instability development. Even if this manuscript is only devoted to nonlocal transport regimes, for the reasons explained above, it is suitable to model kinetic effects in a way which could be easily generalized or extended to the regimes where these phenomena take place. Thus, it is suitable to use a collision operator able to describe strongly anisotropic as well as isotropic regimes.

In section 2.1 we have presented a statistical description of the electron motion in a plasma. After the definition of an EDF, we have derived its temporal evolution from classical mechanics, under the assumption of binary and small angle collisions. This equation, so called FP equation, is resumed here:

$$\frac{\partial}{\partial t}f_e+\vec{v}\cdot\vec{\nabla}f_e+\vec{a}\cdot\vec{\nabla}_v f_e=\sum_{j=e,i}\frac{\partial}{\partial\vec{p}_e}\int_{\mathbf{R}^3}d^3v_j\frac{4\pi e^2q_j^2\Lambda_{ej}}{2||\vec{v}_{\text{rel}}||}\frac{\vec{v}_{\text{rel}}^2\bar{\bar{I}}-\vec{v}_{\text{rel}}\otimes\vec{v}_{\text{rel}}}{\vec{v}_{\text{rel}}^2}\left(\frac{\partial f_e}{\partial\vec{p}_e}f_j-\frac{\partial f_j}{\partial\vec{p}_j}f_e\right).$$

The right hand side term is the Landau collision operator, derived in section 2.1.2. This operator is rather complex and difficult to be solved numerically.

The aim of this work is to derive a simple transport model, which can be used at every temporal step of a hydrodynamic simulation, in order to account for kinetic corrections. The Landau collision operator is not suitable, even for a fully-kinetic simulation. It is not reasonable to use it coupled with hydrodynamic codes. Classical transport models, described in chapter 3, are based on empirical collision operators, such as the BGK operator [28]. However, the BGK collision operator is not able to describe the energy diffusion. The goal of this chapter is to improve previous models, accounting for more accurate description of collisions.

In this chapter, reduced collision operators are derived, computed and analyzed. Under the assumption of inertial ions and fast electrons, in section 4.1, a reduced collision operator is derived. In section 4.2, a further simplification is performed, in order to derive the most suitable operator to deal with the physics of nonlocal energy transport. In section 4.3, an analysis of the entropy of the reduced collision operators is performed. Conclusions on the choice of the most suitable collision operator are drawn in section 4.4.

4.1 Reduced collision operators

The Landau collision operator can be split in two terms, accounting respectively for electron collisions with ions and with electrons:

$$\left(\frac{\partial f_e}{\partial t}\right)_{\text{coll}}=C_{ei}+C_{ee},$$

where

$$C_{ei} = \frac{\partial}{\partial \vec{p}_e} \int_{\mathbf{R}^3} d^3 v_i \frac{4\pi Z^2 e^4 \Lambda_{ei}}{2||\vec{v}_{\rm rel}||} \frac{\vec{v}_{\rm rel}^2 \bar{\bar{I}} - \vec{v}_{\rm rel} \otimes \vec{v}_{\rm rel}}{\vec{v}_{\rm rel}^2} \left(\frac{\partial f_e}{\partial \vec{p}_e} f_i - \frac{\partial f_i}{\partial \vec{p}_i} f_e \right) \tag{4.1}$$

accounts for electron-ion collisions and

$$C_{ee} = \frac{\partial}{\partial \vec{p}_e} \int_{\mathbf{R}^3} d^3 v_e \frac{4\pi e^4 \Lambda_{ee}}{2||\vec{v}_{\rm rel}||} \frac{\vec{v}_{\rm rel}^2 \bar{\bar{I}} - \vec{v}_{\rm rel} \otimes \vec{v}_{\rm rel}}{\vec{v}_{\rm rel}^2} \left(\frac{\partial f_e}{\partial \vec{p}_e} f_e - \frac{\partial f_e}{\partial \vec{p}_e} f_e \right)$$

for electron-electron collisions. We stress that $\vec{v}_{\rm rel}$ is the relative velocity between the two colliding particles.

In this section we perform reductions of these operators in order to find the most suitable form, compatible with the physical processes we aim to describe.

4.1.1 Inertial ions

As specified in the first part of the manuscript, we consider fully-ionized plasmas composed of one species of ions and one of electrons. While ions and electrons are accelerated by the same force, the fraction between their velocities is $v_e/v_i = Am_i/m_e \approx 1.8 \times 10^3 A$. Thus, describing electron collisions, it is reasonable to assume the ions to be immobile $v_i \approx 0$, making an error of 0.0005%.

Assuming $v_i = 0$ means to assume $\vec{v}_{\rm rel} \approx \vec{v}_e$. For this reason the second term of the right hand of Eq. (4.1) reduces to zero. Moreover, the distribution function of fixed ions is a Dirac's delta function: $f_i(\vec{v}) = n_i \delta(\vec{v}_i)$. Then, Eq. (4.1) becomes

$$C_{ei} = \frac{\partial}{\partial \vec{v}_e} \frac{\nu_{ei}}{2} \left(\vec{v}_e^2 \bar{\bar{I}} - \vec{v}_e \otimes \vec{v}_e \right) \frac{\partial f_e}{\partial \vec{v}_e}$$

In spherical coordinates it becomes [48, 49]

$$C_{ei} = \frac{\nu_{ei}}{2} \frac{\partial^2}{\partial \vec{\Omega}^2} f_e, \tag{4.2}$$

where

$$\frac{\partial^2}{\partial \vec{\Omega}^2} = \frac{1}{\sin\theta} \frac{\partial}{\partial \theta} \left(\sin\theta \frac{\partial}{\partial \theta} \right) + \frac{1}{\sin^2\theta} \frac{\partial^2}{\partial \phi^2}$$

is the Laplace-Beltrami operator.

Equation (4.2) limits the role of electron-ion collisions to the angular diffusion. Such an interaction can be seen as an elastic ball (electron) bunching against a heavy sphere (ion): the first does not lose energy but its trajectory can be deviated.

4.1.2 Suprathermal electron collisions

In section 3.2.2 and in Fig. 3.1 we have shown that the electrons which transport the heat are suprathermal. We simplify the collision operator, exploiting this property.

We split electrons in a thermal (th) and suprathermal (s) population. Since the suprathermal population transports the heat, these electrons are considered as projectiles. In the same way, the thermal electron population is treated as a background. By definition, thermal electrons are described bt a Maxwellian distribution function (f_e^m). Assuming that supratermal electrons come from a hot region at temperature T_h and deposit their energy to the thermal population in a cold region at temperature $T_c \leq T_h$, the ratio between thermal and suprathermal electron velocities is $v_{th}/v_s \sim 0.27\sqrt{T_c/T_h}$. We assume that this ratio is small $\ll 1$.

We proceed splitting the Landau collision operator (2.9) in the radial and the angular velocity directions:

$$C_{ee} = C_{ee}^{r} + C_{ee}^{\Omega}.$$

They respectively read

$$C_{ee}^{r} = \frac{1}{p_s^2}\frac{\partial}{\partial p_s} p_s^2 \frac{\vec{v}_s}{v_s} \int d^3 v_{th} f_e^m \left(\cdot \bar{\bar{U}} \cdot \frac{\partial f_s}{\partial \vec{p}_s} + \otimes \frac{\partial}{\partial \vec{p}_{th}} : \bar{\bar{U}} f_s \right) \tag{4.3}$$

and

$$C_{ee}^{\Omega} = \frac{1}{p_s}\frac{\partial}{\partial \vec{\Omega}} \int d^3 v_{th} f_e^m \left(\cdot \bar{\bar{U}} \cdot \frac{\partial f_s}{\partial \vec{p}_s} + \otimes \frac{\partial}{\partial \vec{p}_{th}} : \bar{\bar{U}} f_s \right), \tag{4.4}$$

where

$$\frac{\partial}{\partial \vec{\Omega}} = \frac{1}{\sin\theta}\left(\frac{\partial}{\partial \theta} \sin\theta \hat{e}_\theta + \frac{\partial}{\partial \phi} \hat{e}_\phi \right).$$

Angular contribution

The angular contribution to the electron-electron Landau collision operator is given by Eq. (4.4). It is composed of two terms. The second term depends on

$$\frac{\partial \bar{\bar{U}}}{\partial \vec{p}_{th}} = 4\pi e^4 \Lambda_{ee} \frac{\vec{v}_{\rm rel}}{m_e ||\vec{v}_{\rm rel}||^3} \approx 4\pi e^4 \Lambda_{ee} \frac{\vec{v}_{\rm rel}}{m_e v_s^3}, \tag{4.5}$$

where the approximated value is due to the assumption $v_{th}/v_s \ll 1 \Rightarrow ||\vec{v}_{\rm rel}|| \approx v_s$. This term reduces to a boundary term, since

$$\frac{\partial}{\partial \vec{\Omega}} \cdot \vec{v}_{\rm rel} = \frac{\partial}{\partial \vec{\Omega}} \cdot \vec{v}_s.$$

The first term reads

$$\begin{aligned} \int d^3 v_{th} f_e^m \frac{\partial}{\partial \vec{\Omega}} \cdot \bar{\bar{U}} \frac{\partial}{\partial \vec{p}_s} &= \frac{4\pi e^4 \Lambda_{ee}}{2} \int d^3 v_{th} \frac{f_e^m}{||\vec{v}_{\rm rel}||^3} \left(||\vec{v}_{\rm rel}||^2 \frac{\partial}{\partial \vec{\Omega}} \cdot \frac{\partial}{\partial \vec{p}_s} + \frac{\partial}{\partial \vec{\Omega}} \otimes \vec{v}_{\rm rel} \right. \\ &\quad \left. : \vec{v}_{th} \otimes \frac{\partial}{\partial \vec{p}_s} \right) \\ &= \frac{4\pi e^4 \Lambda_{ee}}{2} \int d^3 v_{th} \frac{f_e^m}{||\vec{v}_{\rm rel}||^3} \left(||\vec{v}_{\rm rel}||^2 \frac{\partial}{\partial \vec{\Omega}} \cdot \frac{\partial}{\partial \vec{p}_s} + \frac{\partial}{\partial \vec{\Omega}} v_{th}^2 \cdot \frac{\partial}{\partial \vec{p}_s} \right) \\ &\approx \frac{4\pi e^4 \Lambda_{ee}}{2} \frac{n_e}{m_e v_s^2} \frac{\partial^2}{\partial \Omega^2}. \end{aligned}$$

As above, the approximated value is due to the assumption $||\vec{v}_{\rm rel}|| \approx v_s$.

Finally the angular contribution reads

$$C_{ee}^{\Omega} = \frac{\nu_{ee}}{2} \frac{\partial^2}{\partial \Omega^2} f_s.$$

Similarly to electron-ion collisions, the angular contribution describes elastic collisions of suprathermal electrons with slow thermal electrons, with a frequency equal to ν_{ee}.

Energy diffusion

The electron-electron Landau collision operator, describing the energy diffusion, is given by Eq. (4.3). It is also composed of two terms. With Eq. (4.5), and for the Maxwellian distribution of thermal electrons, the second term reduces to an odd function of each thermal velocity component, integrated over an even domain $(-\infty, +\infty)$. Thus, it is zero. The remaining term can be written as

$$C_{ee}^r = \frac{1}{p_s^2}\frac{\partial}{\partial p_s} p_s^2 \int d^3 v_{th} f_e^m \left(\frac{\vec{v}_s}{v_s} \cdot \bar{\bar{U}} \cdot \frac{\vec{v}_s}{v_s} \frac{\partial f_s}{\partial p_s} + \frac{\vec{v}_s}{v_s} \cdot \bar{\bar{U}} \cdot \frac{\partial f_s}{\partial \vec{\Omega}} + \frac{\vec{v}_s}{v_s} \otimes \frac{\partial}{\partial \vec{p}_{th}} : \bar{\bar{U}} f_s \right),$$

where the gradient is projected on the radial and the angular directions. Since even powers of the velocity lead to a zero integral, for reasons of symmetry, the first term of this equation is proportional to

$$\begin{aligned}
\int d^3 v_{th} f_e^m \frac{\vec{v}_s}{v_s} \cdot \bar{\bar{U}} \cdot \frac{\vec{v}_s}{v_s} &= 2\pi e^4 \Lambda_{ee} \int d^3 v_{th} f_e^m \frac{v_s^2 v_{th}^2 + 2 v_s^2 v_s \cdot v_{th} - (\vec{v}_s \cdot \vec{v}_{th})^2}{v_s^2 ||\vec{v}_{\mathrm{rel}}||^3} \\
&\approx 2\pi e^4 \Lambda_{ee} \int d^3 v_{th} f_e^m \frac{v_s^2 v_{th}^2 - (\vec{v}_s \cdot \vec{v}_{th})^2}{v_s^5} \\
&= 4\pi e^4 \Lambda_{ee} \frac{v_{th}^2 n_e}{v_s^3}.
\end{aligned}$$

The second term is zero because it is a product of two perpendicular vectors. It can be seen while projecting $\bar{\bar{U}}$ on $\vec{v_s}$ on the left and on its perpendicular direction, on the right. The third term is proportional to

$$\int d^3 v_{th} f_e^m f_s \frac{\vec{v}_s}{v_s} \otimes \frac{\partial}{\partial \vec{p}_{th}} : \bar{\bar{U}} = 4\pi e^4 \Lambda_{ee} \int d^3 v_{th} f_e^m f_s \frac{\vec{v}_s}{v_s} \cdot \frac{\vec{v}_s}{m_\beta ||\vec{v}_{\mathrm{rel}}||^3} \approx \frac{4\pi e^4 \Lambda_{ee} n_e}{m_e v_s^2} f_s.$$

This value is obtained exploiting the symmetry of the integral on v_{th}.

The energy contribution can be now evaluated as:

$$C_{ee}^r = \nu_{ee} v_s \frac{\partial}{\partial v_s} \left(\frac{v_{th}^2}{v_s} \frac{\partial}{\partial v_s} + 1 \right) f_s.$$

This operator is composed of a diffusion and a friction term, which depend on the second and first order velocity derivative, respectively.

4.2 AWBS collision operator

In the previous section we have derived a simplified collision operator for suprathermal electrons, colliding with background thermal electrons and ions. Starting from that derivation, we present here a higher degree of simplification, emphasizing the analytical derivation and the good properties of the resulting collisional operator.

4.2.1 Analytical derivation

Since the collisions which we are interested in involves only suprathermal electrons, we interpret f_s as the whole EDF f_e. Then, the total collision operator reads

$$\left(\frac{\partial f_e}{\partial t} \right)_{\mathrm{coll}} = \nu_{ee} v \frac{\partial}{\partial v} \left(\frac{v_{th}^2}{v} \frac{\partial}{\partial v} + 1 \right) f_e + \frac{\nu_{ee} + \nu_{ei}}{2} \frac{\partial^2}{\partial \vec{\Omega}^2} f_e. \tag{4.6}$$

It can be easily proved that a Maxwellian distribution function satifies the following relation:

$$\left(\frac{v_{th}^2}{v}\frac{\partial}{\partial v}+1\right)f_e^m=0.$$

Then, the thermalization term in Eq. (4.6) can be represented as:

$$\left(\frac{\partial f_e}{\partial t}\right)_{\text{coll}}=\nu_{ee}v\frac{\partial}{\partial v}\left(\frac{v_{th}^2}{v}\frac{\partial}{\partial v}+1\right)(f_e-f_e^m)+\frac{\nu_{ee}+\nu_{ei}}{2}\frac{\partial^2}{\partial\vec{\Omega}^2}f_e. \tag{4.7}$$

The effect of electron-electron collisions is now written explicitly. They assure a relaxation to the equilibrium (thermailization), the energy losses and the angular diffusion. The collisions with ions contribute to the angular diffusion:

$$\left(\frac{\partial f_e}{\partial t}\right)_{\text{coll}}=\underbrace{\nu_{ee}v\frac{\partial}{\partial v}\left(\frac{v_{th}^2}{v}\frac{\partial}{\partial v}+1\right)\overbrace{(f_e-f_e^m)}^{\text{thermalization}}}_{\text{energy diffusion and friction}}+\underbrace{\frac{\nu_{ee}+\nu_{ei}}{2}\frac{\partial^2}{\partial\vec{\Omega}^2}f_e}_{\text{angular diffusion}}.$$

The collision operator (4.7) remains complex and computationally expensive. We make another simplification, assuming that the differences between the EDF and the Maxwellian distribution are relatively small. So, the second-order derivative is small compared to the first-order derivative. By neglecting the second order derivative, we obtain the new collision operator

$$\left(\frac{\partial f_e}{\partial t}\right)_{\text{coll}}=\nu_{ee}v\frac{\partial}{\partial v}(f_e-f_e^m)+\frac{\nu_{ee}+\nu_{ei}}{2}\frac{\partial^2}{\partial\vec{\Omega}^2}f_e. \tag{4.8}$$

This approach has been proposed by Albritton et al. [42], and we call it AWBS operator.

The AWBS operator describes the angular diffusion as well as the thermalization but it does not account for the energy diffusion. It presents useful properties for the electron transport, which are analyzed below.

4.2.2 Proprieties of the AWBS operator

The AWBS collision operator presents many suitable properties for the description of nonlocal transport. First of all it is simple but in the same time it is able to describe three physical processes. Let us compare the properties of the AWBS collision operator with the fast particles collision operator (4.6) and with the operator used in the SNB model, which is composed of inertial ions and relaxing electrons (BGK term):

$$\left(\frac{\partial f_e}{\partial t}\right)_{\text{coll}}=\underbrace{\nu_{ee}\overbrace{(f_e-f_e^m)}^{\text{thermalization}}}_{\text{relaxation}}+\underbrace{\frac{\nu_{ei}}{2}\frac{\partial^2}{\partial\vec{\Omega}^2}f_e}_{\text{ion angular diffusion}}. \tag{4.9}$$

First, it can be demonstrated that the AWBS collision operator conserves the number of particles. The local particle density reads

$$n_e=\int_{\mathbb{R}^3}d^3v f_e.$$

From the FP equation, the time variation of the particle density reads

$$\frac{dn_e}{dt}+\vec{\nabla}\cdot(n_e\vec{u}_e)=\int_{\mathbb{R}^3}d^3v\left(\frac{\partial f_e}{\partial t}\right)_{\text{coll}}. \tag{4.10}$$

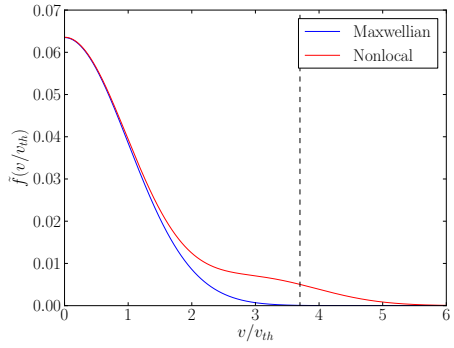

(a) EDFs analized: unperturbed (Maxwellian) distributions and a nonlocal distribution.

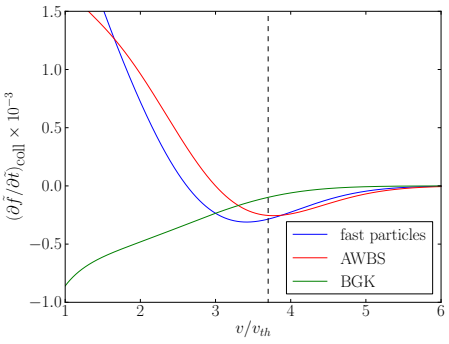

(b) Comparision of collision terms.

Figure 4.1: Comparison of the collision terms given by Eqs. (4.6) (fast particles), (4.8) (AWBS) and (4.9) (BGK), for a typical nonlocal EDF. The analysis is done in function of the velocity, normalized on the thermal velocity. Vertical dashed lines denote the point of maximum contribution of the local heat flux.

For both collision operators (4.6) and (4.8), the right hand side of Eq. (4.10) is zero. On the contrary, the BGK collision operator described in section 3.1.2, does not conserve the number of particles.

These results can be extended to the conservation of the electric charge. Not conserving the number of particles and the charge can lead to errors in calculations of plasma density and electric fields. However, in contrast to the fast particles collision operator (4.7), both AWBS (4.8) and BGK (4.9) do not conserve the momentum and the energy of electrons.

Let us consider the effect of different treatments of the energy relation, for the three collision operators (fast particles, AWBS and BGK), on the evolution of a typical nonlocal EDF. We present the collision operators (4.6), (4.8) and (4.9) in a normalized form:

$$\left(\frac{\partial\tilde{f}}{\partial\tilde{t}}\right)_{\rm coll} = \frac{v_{th}^3}{n_0\nu_{th}}\left(\frac{\partial f_e}{\partial t}\right)_{\rm coll} = \tilde{v}^{-2}\frac{\partial}{\partial\tilde{v}}\left(\tilde{v}^{-1}\frac{\partial}{\partial\tilde{v}}+1\right)(\tilde{f}-\tilde{f}^m),$$

$$\left(\frac{\partial\tilde{f}}{\partial\tilde{t}}\right)_{\rm coll} = \frac{v_{th}^3}{n_0\nu_{th}}\left(\frac{\partial f_e}{\partial t}\right)_{\rm coll} = \tilde{v}^{-2}\frac{\partial}{\partial\tilde{v}}(\tilde{f}-\tilde{f}^m)$$

and

$$\left(\frac{\partial\tilde{f}}{\partial\tilde{t}}\right)_{\rm coll} = \frac{v_{th}^3}{n_0\nu_{th}}\left(\frac{\partial f_e}{\partial t}\right)_{\rm coll} = -\tilde{v}^{-3}(\tilde{f}-\tilde{f}^m),$$

where

$$\tilde{f}^m = \frac{v_{th}^3}{n_0}f_e^m = \frac{1}{(2\pi)^{3/2}}e^{-\tilde{v}^2/2}$$

is the Maxwellian EDF. We consider here an isotropic EDF since the angular diffusion terms are the same for all three collision operators. We analyze the typical nonlocal case of a local (Maxwellian) EDF, perturbed by a suprathermal ($\sim 3v_{th}$) EDF:

$$\tilde{f} = \tilde{f}^m + \frac{10^{-1}}{(2\pi)^{3/2}}e^{-(\tilde{v}-3)^2/2}.$$

This nonlocal EDF is compared with the unperturbed (Maxwellian) EDF in Fig. 4.1a. The corresponding collision terms are shown in Fig. 4.1b. The AWBS term agrees with the fast electron term for velocities higher then $2v_{th}$ and differences are reduced as the velocity increases. Since the heat transport contribution is maximum at $3.7v_{th}$, the description is

sufficient. On the contrary, the BGK operator underestimates the modulus of the stopping power for $3.7v_{th}$, and in general gives different results for lower velocities.

These examples show that the AWBS collision operator is more accurate, than the BGK operator. This conclusion can be qualitatively generalized for other cases of a Maxwellian function perturbed by suprathermal electrons. Note that, for velocities $\lesssim v_{th}$, operators (4.6) and (4.8) are no more able to perform realistic predictions. However, these regimes are out of the domain of interest for the nonlocal transport.

The first two moments of the AWBS collision operator read

$$\begin{cases} \left(\frac{\partial f_0}{\partial t}\right)_{\text{coll}} = \nu_{ee} v \frac{\partial}{\partial v}(f_0 - f_0^m) \\ \left(\frac{\partial \vec{f_1}}{\partial t}\right)_{\text{coll}} = \nu_{ee} v \frac{\partial}{\partial v}\vec{f_1} + \frac{\nu_{ee}+\nu_{ei}}{2}\frac{\partial^2}{\partial \vec{\Omega}^2}\vec{f_1} \end{cases} .$$

In the Lorentz gas limit $\nu_{ei} \gg \nu_{ee}$, the first moment collision operator equals to the one used in SNB.

4.3 *H*-theorem with reduced collision operators

In section 2.1.3, we have shown that the kinetic entropy of a closed system

$$H[f_e] = -\int_{\mathbb{R}^6} d^3x d^3v \left(f_e \log f_e - f_e\right)$$

does not decrease with time (H-theorem). This condition can be written as

$$\frac{d}{dt}H = -\int_{\mathbb{R}^6} d^3x d^3v \log f_e \left(\frac{\partial f_e}{\partial t}\right)_{\text{coll}} \geq 0,$$

that is, only collisions may change the entropy.

In this section, we consider a compatibility of the reduced collision operators with the H-theorem.

4.3.1 Electron-ion collisions

The electron-ion collision operator is given by Eq. (4.2). This collision operator verify the H-theorem

$$\begin{aligned} \frac{d}{dt}H &= -\int_{\mathbb{R}^6} d^3x d^3v \log f_e \frac{\nu_{ei}}{2}\frac{\partial^2}{\partial \vec{\Omega}^2} f_e \\ &= \int_{\mathbb{R}^3} d^3x \int_0^\infty dv \frac{\nu_{ei} v^2}{2}\left[\int_0^{2\pi} d\phi \int_0^\pi d\theta \frac{\sin\theta}{f_e}\left(\frac{\partial f_e}{\partial \theta}\right)^2 + \int_0^\pi \frac{d\theta}{\sin\theta}\int_0^{2\pi} d\phi \frac{1}{f_e}\left(\frac{\partial f_e}{\partial \phi}\right)^2\right] \\ &\geq 0, \end{aligned} \tag{4.11}$$

because $\sin\theta \geq 0$ and $f_e \geq 0$. By performing the integration by parts, we find the border terms $[\log f_e \sin\theta \frac{\partial f_e}{\partial \theta}]_{\theta=0}^{\theta=\pi}$ and $[\log f_e \frac{\partial f_e}{\partial \phi}]_{\phi=0}^{\phi=2\pi}$ are zero.

Thus the electron-ion collision operator respects the entropy principle.

4.3.2 Fast colliding electrons

For the collision operator Eq. (4.6), the entropy equation reads

$$\frac{d}{dt}H = -\int_{\mathbb{R}^6} d^3x d^3v \log f_e \left[\nu_{ee} v \frac{\partial}{\partial v}\left(\frac{v_{th}^2}{v}\frac{\partial}{\partial v} + 1\right) f_e + \frac{\nu_{ee}+\nu_{ei}}{2}\frac{\partial^2}{\partial \vec{\Omega}^2} f_e\right].$$

The last term on the right hand side is equal to Eq. (4.11), with a factor $Z+1$. Thus, it verifies the entropy principle. After an integration by parts, the first term becomes

$$\begin{aligned}
&-\int_{\mathbb{R}^6} d^3x d^3v \log f_e \nu_{ee} v \frac{\partial}{\partial v}\left(\frac{v_{th}^2}{v}\frac{\partial}{\partial v}+1\right) f_e \\
&= \nu_{ee} v^3 \int_{\mathbb{R}^3} d^3x \int_{S^2} d^2\Omega \left\{ \left[\log f_e \left(\frac{v_{th}^2}{v}\frac{\partial f_e}{\partial v} + f_e \right) \right]_{v=0}^{v=\infty} + \int_0^\infty dv \frac{1}{f_e}\frac{\partial f_e}{\partial v}\left(\frac{v_{th}^2}{v}\frac{\partial}{\partial v}+1\right) f_e \right\} \\
&= \nu_{ee} v^3 \int_{\mathbb{R}^3} d^3x \int_{S^2} d^2\Omega \int_0^\infty dv \frac{v_{th}^2}{v f_e}\left(\frac{\partial f_e}{\partial v}\right)^2 \\
&\geq 0.
\end{aligned}$$

Thus, the collision operator of fast electrons respects the entropy principle.

4.3.3 AWBS collision operator

The entropy time evolution for the AWBS collision operator (4.8), reads

$$\frac{d}{dt}H = -\int_{\mathbb{R}^6} d^3x d^3v \log f_e \left[\nu_{ee} v \frac{\partial}{\partial v}\left(f_e - f_e^m\right) + \frac{\nu_{ee}+\nu_{ei}}{2}\frac{\partial^2}{\partial \vec{\Omega}^2} f_e \right]. \tag{4.12}$$

The second term on the right hand side respects the entropy principle. The first term, after an integration by parts, reads

$$\begin{aligned}
-\int_{\mathbb{R}^6} d^3x d^3v \log f_e \nu_{ee} v \frac{\partial}{\partial v}\left(f_e - f_e^m\right) = -\nu_{ee} v^3 \int_{\mathbb{R}^3} d^3x \int_{S^2} d^2\Omega \Bigg\{ \left[\nu_{ee} v^3 \log f_e \left(f_e - f_e^m\right) \right]_{v=0}^{v=\infty} \\
- \int_0^\infty dv \nu_{ee} v^3 \frac{f_e - f_e^m}{f_e} \Bigg\} \\
= \nu_{ee} v^3 \int_{\mathbb{R}^3} d^3x \int_{S^2} d^2\Omega \int_0^\infty dv \frac{f_e - f_e^m}{f_e}\frac{\partial}{\partial v} f_e,
\end{aligned}$$

which is not always positively defined.

The reason why the H-theorem is not always respected is due to omission of the diffusion term, passing from Eq. (4.6) to Eq. (4.8). During this passage we lose a physical process: the energy conservation. Otherwise, we could multiply Eq. (4.12) by a constant of motion

$$\propto \int_{\mathbb{R}^6} d^3x d^3v \log f_e^m \left(\frac{\partial f_e}{\partial t}\right)_{\text{coll}} = 0, \tag{4.13}$$

which would bring to the demonstration of the H-theorem. Nevertheless, the condition $f_e \geq f_e^m \wedge \frac{\partial}{\partial v} f_e \geq 0$ is verified in the case of nonlocal transport: when a hot EDF is deposited in a cold region.

4.3.4 BGK collision operator

The BGK collision operator, with a velocity-dependent frequency, as it is presented in section 3.1.2, is given by Eq. (4.9). The entropy equation with this operator reads

$$\begin{aligned}
\frac{d}{dt}H &= -\int_{\mathbb{R}^6} d^3x d^3v \log f_e \left[-\nu_{ee}\left(f_e - f_e^m\right) \right] \\
&= \int_{\mathbb{R}^3} d^3x \int_{S^2} d^2\Omega \int_0^\infty \nu_{ee} v^2 \log f_e \left(f_e - f_e^m\right).
\end{aligned}$$

It is evident that the H-theorem is not respected. Moreover, this collision operator does not conserve the energy and the number of particles. Otherwise, we could multiply Eq. (4.12) by the constant of motion (4.13), which would bring to the thesis.

Thus, the AWBS operator presents certain advantages, compared to the BGK collision operator, but the energy conservation and the entropy growth are not respected.

4.4 Perspectives of reduced operators

The existent nonlocal transport models are based on the BGK collision operator [28], as described in section 3.1.2. In this chapter we have presented an improved AWBS reduced collision operator, which presents some advantages. First of all, it accounts for more physical processes than the BGK operator. In particular, it describes the electron energy dissipation, which is of a major importance for the description of the nonlocal transport. Moreover, the AWBS operator is able to describe the transport of energetic electrons, strongly deviated from a Maxwellian distribution and highly anisotropic beams. Nowadays, a challenge for the plasma physics and in particular for ICF, is to account for such kinetic phenomena at a hydrodynamic time scale.

The FP equation, with the AWBS operator presented in this chapter is the framework for the reduced model developed in this manuscript.

Chapter 5

First moment models

In chapter 4 we have presented a simplified FP equation, by performing a reduction of the Landau collision operator. Accounting the collisions of suprathermal electrons with ions and thermal electrons and neglecting second order velocity-derivative of the EDF we have introduced the AWBS collision operator [42]. The AWBS-FP equation reads

$$\frac{\partial}{\partial t}f_e + \vec{v}\cdot\vec{\nabla}f_e + \vec{a}\cdot\vec{\nabla}_v f_e = \nu_{ee}v_e\frac{\partial}{\partial v}(f_e - f_e^m) + \frac{\nu_{ee}+\nu_{ei}}{2}\frac{\partial^2}{\partial\vec{\Omega}^2}f_e.$$

In order to propose a fast kinetic model for hydrodynamic codes, we proceed further in the simplification of the AWBS operator, since it is defined in the six-dimensional phase space ($\vec{x}$,$\vec{v}$) and remains too much time consuming.

The SNB model, described in section 3.3.2, has been reinterpreted as a reduced and strongly simplified FP equation. However, as shown in 3.4.2, the splitting of the EDF in a local and nonlocal parts makes it difficult to generalize this model to magnetized plasmas. Moreover, a generalization to strong anisotropic processes is also impossible, due to the P1 closure (described in section 3.1.3).

For these reasons, we choose to develop a new model, based on a more fundamental assumption: the entropy maximization. In this model magnetic fields could be easily treatable, as they do not affect the structure of the collisional operator.

In section 5.1, the first moment hierarchy of the AWBS-FP equation is derived, without fixing the closure relation. In section 5.2, the P1 closure relation is presented: the AWBS-P1 first moment model is an improvement of the SNB model. A second improvement is presented in section 5.3. It is based on the entropic closure relation, which allows to extend the domain of validity of the model to high anisotropies. It opens an opportunity to describe both kinetic corrections in energy and in angle with the same model. Advantages and disadvantages of the models are discussed.

5.1 AWBS-FP first moment model

The FP equation can be resolved by developing it in a series of moments in the velocity direction $\vec{\Omega}$. The main issues related to this approach are the following.

When do we stop the hierarchy? Is a first angular moment development sufficient for describing nonlocal transport or do we need a second or higher angular moment development? How do we close the system, keeping the main physical properties? How do we account for nonlocal electric fields? And for magnetic fields? Is the model sufficiently fast to be coupled with a multidimensional hydrodynamic code?

In this section, we try to answer to all these questions.

5.1.1 AWBS-FP hierarchy arrest

We want to reduce the number of dimensions, in order to simplify the AWBS-FP equation. This is done through the construction of the angular moment hierarchy, described in section 3.1.1. It has been shown in [37] that in order to describe the nonlocal transport it is sufficient to stop the hierarchy at the first moment. Such an hierarchy is shown in Eq. (3.2) and has been derived from an integration over the velocity direction vector $\vec{\Omega}$ of the FP equation.

The characteristic time evolution of kinetic systems is given by the effective collision time $\sim \sqrt{\tau_{ee}\tau_{ei}}$. Since this time is very short compared to the characteristic hydrodynamic time $\sim L_\nabla/c_s$ (with c_s as the sound speed and L_∇ as the gradient lenght), electrons have the time to adjust themselves to the equilibrium. Thus, the first two moment hierarchy of the AWBS-FP equation simplifies to:

$$\begin{cases} v\vec{\nabla}\cdot\vec{f}_1 - \frac{e\vec{E}}{m_e v^2}\cdot\frac{\partial}{\partial v}\left(v^2\vec{f}_1\right) = \nu_{ee} v \frac{\partial}{\partial v}\left(f_0 - f_0^m\right) \\ v\vec{\nabla}\cdot\bar{\bar{f}}_2 - \frac{e}{m_e v^2}\frac{\partial}{\partial v}\left(v^2\bar{\bar{f}}_2\cdot\vec{E}\right) + \frac{e}{m_e v}\left(f_0\bar{\bar{I}} - \bar{\bar{f}}_2\right)\cdot\vec{E} + \frac{e}{m_e c}\vec{f}_1\times\vec{B} = \nu_{ee} v\frac{\partial}{\partial v}\vec{f}_1 - \nu_{tot}\vec{f}_1 \end{cases} \tag{5.1}$$

where total collision frequency is $\nu_{tot} = \nu_{ee} + \nu_{ei}$. Three quantities in this system are determined in what follows: $\bar{\bar{f}}_2$, $\vec{E}$ and $\vec{B}$.

5.1.2 Equations for the electric and magnetic fields

The time evolution of the electric field is given by the Ampere's law. Under the assumption of stationary solutions, it is given by Eq. (3.23). Two cases can be considered: unmagnetized and magnetized plasmas.

Unmagnetized plasmas

In case of unmagnetized plasmas, without external sources, Eq. (3.23) reduces to

$$\vec{j} = 0,$$

that is, the electric field is adjusted in a way to respect the zero-current condition.

In the unmagnetized local limit, Eq. 3.24 reduces to

$$\vec{E} = -\frac{\vec{\nabla}p}{en_e} - \beta_\perp(\omega_B\tau_e = 0)\frac{\vec{\nabla}T_e}{e}. \tag{5.2}$$

In Fig. 3.1, we have shown the integrand of the local heat flux, as a function of the velocity. That there are two electron fluxes, propagating in opposite directions. A suprathermal flux, which transports the heat and a slower return current, induced by the zero-current electric field. Since the return current electrons are slower, this flux is less susceptible to nonlocal effects. This has been shown in [24]. Thus, for weakly nonlocal conditions, the electric fields could be determined from the local equation (5.2).

When electrons are strongly nonlocal, the model needs to account for nonlocal corrections to the electric field [50]. In section 3.2.1, we have derived a kinetic relation given by Eq. (3.9), for electric fields, accounting for nonlocal effects. It has been derived under the assumption of a Lorentz gas. We can extend its validity to low-Z plasmas, multiplying by the factor $\xi/2.5$, as it is done for the local field in Eq. (3.10):

$$\vec{E}_{NL} = -\frac{\xi}{2.5}\frac{m_e}{6e}\frac{\int_0^\infty \vec{\nabla}f_0 v^7 dv}{\int_0^\infty f_0 v^5 dv}. \tag{5.3}$$

This nonlocal expression is valid in the limit $\vec{\nabla}T_e/T_e \gg \vec{\nabla}n_e/n_e$, which is frequently respected in practice. In the extreme case of $Z = 1$ and $\vec{\nabla}T_e/T_e \ll \vec{\nabla}n_e/n_e$, the error is $\sim 30\%$, which is smaller than in the models assuming local electric fields.

Magnetized plasmas

In magnetized plasmas, the zero-current condition is replaced by the stationary Ampere's law (3.23):

$$\vec{j} = \frac{c}{4\pi}\vec{\nabla} \times \vec{B}.$$

Unfortunately, it is not anymore possible to invert the kinetic equation to express the electric field, explicitly.

As it has been proposed in the previous section, a solution could be to calculate electric fields in a local approximation. Magnetic field localizes the transport, as shown in section 3.4.2. This fact justifies the local approximation.

Electric fields in the local approximation are given by Eq. (3.24). We apply this equation introducing the kinetic-hydrodynamic quantities: the electron density and the electron pressure

$$n_K = \int_{\mathbb{R}} dv f_0,$$
$$p_K = \frac{2}{3}\int_{\mathbb{R}} dv \epsilon f_0.$$

According to the perfect gas equation of state, the kinetic electron temperature reads $T_K = p_K/n_K$. By using these definitions in Eq. (3.24), the expression for the local-kinetic electric field reads

$$\vec{E}_{Lk} = -\frac{\vec{\nabla}p_K}{en_K} + \frac{\vec{J}\times\vec{B}}{cen_K} + \bar{\bar{\alpha}}_K \cdot \frac{\vec{J}}{e^2 n_K^2} - \bar{\bar{\beta}}_K \cdot \frac{\vec{\nabla}T_K}{e}. \tag{5.4}$$

The kinetic electrical resistivity and thermoelectric conductivity, detailed in section 3.4.1, are defined as functions of the transport coefficients: $\bar{\bar{\alpha}}_K = \bar{\bar{\alpha}}(n_K, T_K)$, $\bar{\bar{\beta}}_K = \bar{\bar{\beta}}(n_K, T_K)$.

The model proposed in this section is able to treat also density gradients. However, it is phenomenological. In the limit of a zero magnetic field $\omega_B\tau_e \approx 0$ it applies also to unmagnetized plasmas. It reduces to Eq. (5.2). However, this model presents some differences with the respect to the rigorous kinetic model. In particular, the local-kinetic electric field result closer to the local formulation, than the nonlocal electric field (5.3). Such small differences in the electric field increase with the nonlocality. They do not affect significantly the heat transport, as long as it remains weakly nonlocal ($\lambda_0/L_T \leq 0.3$). Magnetic fields are defined by external sources, computed with the local approximation, by magnetohydodynamic codes.

5.1.3 Open issues

In this section we have reduced the AWBS-FP equation to the system (5.1). The latter is stopped at the first moment and is characterized by three free functions: the second moment $\bar{\bar{f}}_2$, the electric and magnetic fields. The equations for electric and magnetic fields are summarized in section 5.1.2. The closure relations are discussed in next section. Two distinct models are presented, differing by the description of kinetic-scale effects and the validity domain.

5.2 Polynomial closure for the AWBS-FP moment hierarchy

A polynomial closure for the system (5.1) is presented here. It was derived in section 3.1.3, from a spherical harmonics development, stopped at the first order. It reads

$$f_e = \frac{f_0}{4\pi} + \frac{3}{4\pi}\vec{\Omega}\cdot\vec{f_1}.$$

The limits of this approach are the following:

- it depends linearly on velocity directions $\vec{\Omega}$, thus it cannot deal with more than one direction of anisotropy;
- its domain of validity is limited to small anisotropies $|\vec{f_1}| \ll f_0$, since in the opposite case the EDF becomes negative, which does not make physical sense.

Starting from the P1 approximation, in this section we develop two new transport models, which are used along the manuscript for a comparison with the entropic model.

5.2.1 P1 model

As shown in section 3.1.3, the P1 approximation leads to the closure relation $\bar{\bar{f}}_2 = f_0\bar{\bar{I}}/3$. This closure, with the definition of electromagnetic fields, given in section 3.1, sets a new model for Eq. (5.1):

$$\begin{cases} v\vec{\nabla}\cdot\vec{f_1} - \frac{e\vec{E}}{m_e v^2}\cdot\frac{\partial}{\partial v}\left(v^2\vec{f_1}\right) = \nu_{ee} v\frac{\partial}{\partial v}\left(f_0 - f_0^m\right) \\ \frac{v}{3}\vec{\nabla}f_0 - \frac{e\vec{E}}{3m_e}\frac{\partial}{\partial v}f_0 + \frac{e}{m_e c}\vec{f_1}\times\vec{B} = \nu_{ee} v\frac{\partial}{\partial v}\vec{f_1} - \left(\nu_{ee}+\nu_{ei}\right)\vec{f_1} \end{cases}. \tag{5.5}$$

In the manuscript this system of equations is called P1 model.

The P1 model is much more simple than the system (5.1) and explicitly accounts for electric and magnetic fields. This is different from nonlocal models, as shown in section 3.4.2.

Despite its good properties, the P1 closure has a limited domain of validity, as we have shown in section 3.1.3. Concerning the nonlocal regime, the nonlocal transport is limited to relatively small temperature gradients. Moreover, the P1 approximation cannot be generalized to strongly anisotropic EDFs, such as transport induced by parametric instabilities as well as relativistic electron transport.

The P1 model is analogous to system (3.6), for the AWBS collision operator. The latter has been used for development of the SNB model. In order to understand the limitations of the AWBS operator, it is interesting to extend the SNB model by using the system (5.5).

5.2.2 Improvement of the SNB model

The SNB model has been described in section 3.3.2. The kinetic interpretation of this model agrees with the FP results, if the effective electron MFP is reduced by a factor of 2 compared to the kinetic theory. An improved model, using a more precise collision operator, allows to recover a correct expression for the MFP.

We start from the system (5.5). Similarly to section 3.3.2, we use the Lorentz gas approximation $Z \gg 1$. The low-Z limit is obtained by using a numerical fit.

In the Lorentz gas approximation, the electron-electron collisions, in the equation for $\vec{f_1}$, are accounted for by modifying the electron-ion collision frequency. So the system (5.5) reduces to

$$\begin{cases} v\vec{\nabla}\cdot\vec{f_1} - \frac{e\vec{E}}{m_e v^2}\cdot\frac{\partial}{\partial v}\left(v^2\vec{f_1}\right) = \nu_{ee} v\frac{\partial}{\partial v}\left(f_0 - f_0^m\right) \\ \frac{v}{3}\vec{\nabla}\cdot f_0 - \frac{e\vec{E}}{3m_e}\cdot\frac{\partial}{\partial v}f_0 + \frac{e}{m_e c}\vec{f_1}\times\vec{B} = -\nu_{ei}^*\vec{f_1} \end{cases}, \tag{5.6}$$

where ν_{ei}^* is defined in Eq. (3.3) in order to account for the electron-electron collisions. Thus, the difference of the AWBS operator from the SNB model concerns the equation for f_0. The new effect added to the SNB model is the energy dissipation.

Following section 3.3.2, we split the EDF to the thermal and suprathermal parts, similarly to the SNB model:

$$\begin{cases} f_0 = f_0^m + \Delta f_0 \\ \vec{f_1} = \vec{f_1^m} + \Delta\vec{f_1} \end{cases}.$$

Neglecting the electric field, we reduce the model to the following diffusion equation for suprathermal electrons:

$$\begin{cases} \left(\frac{v}{\lambda_{ee}}\frac{\partial}{\partial v} + \vec{\nabla}\frac{\lambda_{ei}^E}{3}\vec{\nabla}\right)\Delta f_0 = \vec{\nabla}\vec{g_1^m}. \\ \Delta\vec{f_1} = -\frac{\lambda_{ei}^*}{3}\vec{\nabla}\Delta f_0 \end{cases}, \tag{5.7}$$

with $\vec{g_1^m}$ defined as the simplified Maxwellian flux

$$\vec{g_1^m} = -\frac{\lambda_{ei}^*}{3} f_0^m \frac{\vec{\nabla}T_e}{T_e},$$

as in section 3.3.2. The local electric field effects on suprathermal electrons are taken into account through the reduction of the collision MFP to the maximum value $\frac{\epsilon}{|e\vec{E}_{SH}|}$, dependent on the local electric field:

$$\frac{1}{\lambda_{ei}^E} = \frac{1}{\lambda_{ei}} + \frac{|e\vec{E}_{SH}|}{\epsilon},$$

where the electric field is given by Eq. (3.10).

Finally the heat flux reads

$$\vec{q}_{AWBS-SNB} = 2\pi m_e \int_0^\infty (\vec{f_1^m} + \Delta\vec{f_1}) v^5 dv = \vec{q}_{SH} + \Delta\vec{q}.$$

An important difference between the SNB model described in section 3.3.2 and the improved model concerns the electron MFP. The authors of [22] have been forced to use an effective MFP, given by Eq. (3.22), in order to reproduce the results of test cases. In contrast, in the improved SNB model, the MFP has the standard definition: $\lambda_{ej} = m_e^2 v^4/(4\pi n_e Z_j e^4 \Lambda_{ej})$, where $Z_j = 1$, for $j = e$, and it is the ionization number, for $j = i$.

In this manuscript we refer to the original SNB model as BGK-SNB, since it is based on the BGK operator. We refer to AWBS-SNB as the improved SNB model, based on the AWBS collision operator, described in this section.

5.2.3 Conclusions on P1 models

In this section we have developed two new first moment models, both based on the AWBS collision operator and on the P1 approximation.

The P1 model has shown to be a good candidate for the description of magnetized nonlocal transport, since in its formulation magnetic fields are explicit. However, its domain of validity is strongly limited by the P1 approximation. As we show in the next part, it is limited to weakly kinetic effects and weakly anisotropic processes.

In this section we have applied the AWBS collision operator to the SNB nonlocal transport model. Contrary to BGK-SNB, the AWBS-SNB model allows to use the MFP standard definition without multiplicative factors. Results of the improvement are presented in the next part. The improved model has the same limitations of the original SNB model, related to the difficulties in accounting for magnetic fields.

A new closure model allows to overcome the previous limitations. It is presented in the next section.

5.3 Entropic closure

A closed and isolated system evolves to equilibrium, moving to more probables states, due to the collisions between particles. The second law of thermodynamics asserts that the entropy increases, reaching the state of equilibrium. This law finds its statistical interpretation in the H-theorem, described in section 2.1.3. In this chapter we are developing a new first moment model, based on an entropic closure. This model is called M1, for its first moment closure.

5.3.1 Angular entropy maximization principle

All closed statistical systems respect the H-theorem. We apply this theorem, in order to find a closure relation for the system (3.2) [51].

In difference from the macroscopic entropy quantity, integrated over the phase-space, we define the angular mesoscopic entropy, integrated only over the velocity directions:

$$H_v[f_e] = -\int_{S_2} d^2\Omega \left(f_e \log f_e - f_e\right). \tag{5.8}$$

The integration of this entropy over the space and the velocity modulus, leads to the macroscopic entropy definition (2.10).

The angular entropy maximization principle asserts that for each point of the space and for each value of the velocity magnitude, the angular entropy (5.8) is maximized:

$$\frac{d}{dt} H_v \geq 0.$$

The physical meaning of the angular entropy maximization is that information is lost over angular scattering. This also means that the angular scattering is a local process, leading to the isotropization of the EDF. This assumption is reasonable asserting that the energy and the angular scattering are uncorrelated. Following the calculation presented in section 4.3, it is easy to demonstrate that the ion collision term respects the angular entropy principle, since it concerns only the angular scattering.

Moreover, imposing the angular entropy principle, the macroscopic system is forced to respect the H-theorem:

$$\frac{d}{dt} H_v \geq 0 \Rightarrow \frac{d}{dt} H = \int_{\mathbf{R}^3} d^3x \int_0^\infty dv \frac{d}{dt} H_v \geq 0.$$

5.3.2 First moment angular entropic closure

We apply the angular entropic principle for closing the system (5.1) [52, 20].

We are looking for the underlying EDF, which respects the angular entropy maximization principle, depending on the first two angular moments, defined in (3.1). This maximization problem, with two constraints, corresponds to the following Lagrangian operator

$$L[f_e] = H_v[f_e] - \alpha_0 \left(f_0 - \int_{S_2} d^2\Omega f_e \right) - \vec{\alpha}_1 \cdot \left(\vec{f}_1 - \int_{S_2} d^2\Omega \vec{\Omega} f_e \right),$$

where α_0 and $\vec{\alpha}_1$ are two Lagrangian multipliers. The EDF which maximizes the Lagrangian functional follows from the equation

$$\frac{d}{df_e} L[f_e] = 0.$$

Its solution reads

$$f_e = N e^{\alpha_0 + \vec{\alpha_1} \cdot \vec{\Omega}}, \tag{5.9}$$

where N is a normalization constant. The advantage of using this closure relation is that the underlying EDF is an exponential function. Thus, it is positively defined.

The first two moments of Eq. (5.9) read

$$\begin{cases} f_0 = 4\pi N \frac{\sinh|\vec{\alpha}_1|}{|\vec{\alpha}_1|} e^{\alpha_0} \\ \vec{f}_1 = 4\pi N \frac{\sinh|\vec{\alpha}_1|}{|\vec{\alpha}_1|} e^{\alpha_0} \left(\coth|\vec{\alpha}_1| - \frac{1}{|\vec{\alpha}_1|} \right) \frac{\vec{\alpha}_1}{|\vec{\alpha}_1|} \end{cases}.$$

or

$$\begin{cases} f_0 = 4\pi N \frac{\sinh|\vec{\alpha}_1|}{|\vec{\alpha}_1|} e^{\alpha_0} \\ \vec{\Omega}_v = \frac{\vec{f}_1}{f_0} = \left(\coth|\vec{\alpha}_1| - \frac{1}{|\vec{\alpha}_1|} \right) \frac{\vec{\alpha}_1}{|\vec{\alpha}_1|} \end{cases}, \tag{5.10}$$

where $\vec{\Omega}_v$ is the anisotropy vector, such that $0 \leq ||\vec{\Omega}_v|| \leq 1$. The inversion of the second equation in (5.10) provides the expression of the coefficient $\vec{\alpha}_1$ and hence a relation of the underlying EDF to the first two angular moments. This inversion was numerically performed and tabulated in [52]. This expression can be interpolated analytically with a precision better than 5% as

$$\vec{\alpha}_1 \approx \frac{3\vec{\Omega}_v}{1 - \frac{\vec{\Omega}_v^2}{2}\left(1 + \vec{\Omega}_v^2\right)}.$$

Then the underlying EDF takes the following form

$$f_e = f_0 \frac{|\vec{\alpha}_1|}{4\pi \sinh|\vec{\alpha}_1|} e^{\vec{\alpha_1} \cdot \vec{\Omega}}. \tag{5.11}$$

Using the moment definitions, we can write

$$\bar{\bar{f}}_2 = \bar{\bar{\chi}}(f_0, \vec{f}_1) f_0, \tag{5.12}$$

with

$$\bar{\bar{\chi}}(f_0, \vec{f}_1) = \frac{1}{3}\bar{\bar{I}} + \frac{\vec{\Omega}_v^2}{2}\left(1 + \vec{\Omega}_v^2\right)\left(\frac{\vec{f}_1 \otimes \vec{f}_1}{\vec{f}_1^2} - \frac{1}{3}\bar{\bar{I}} \right).$$

This new closure relation is nonlinear, it accounts for an anisotropy of the second order moment of the EDF.

5.3.3 M1 model

The angular moment hierarchy (3.2), stopped at the first moment equation and closed with Eq. (5.12), is called M1 model. It provides access to strongly anisotropic EDFs [52, 20, 26]. The M1 model used in this manuscript is based on the AWBS collision operator:

$$\begin{cases} v\vec{\nabla}\cdot\vec{f_1} - \frac{e\vec{E}}{m_e v^2}\cdot\frac{\partial}{\partial v}\left(v^2\vec{f_1}\right) = \nu_{ee} v\frac{\partial}{\partial v}\left(f_0 - f_0^m\right) \\ v\vec{\nabla}\cdot\bar{\bar{f}}_2 - \frac{e}{m_e v^2}\frac{\partial}{\partial v}\left(v^2\bar{\bar{f}}_2\cdot\vec{E}\right) + \frac{e}{m_e v}\left(f_0\bar{\bar{I}} - \bar{\bar{f}}_2\right)\cdot\vec{E} + \frac{e}{m_e c}\vec{f_1}\times\vec{B} = \nu_{ee} v\frac{\partial}{\partial v}\vec{f_1} - \nu_{tot}\vec{f_1} \\ \bar{\bar{f}}_2 = \bar{\bar{\chi}}(f_0,\vec{f_1})f_0 \\ \bar{\bar{\chi}}(f_0,\vec{f_1}) = \frac{1}{3}\bar{\bar{I}} + \frac{\vec{\Omega}_v^2}{2}\left(1+\vec{\Omega}_v^2\right)\left(\frac{\vec{f_1}\otimes\vec{f_1}}{\vec{f_1}^2} - \frac{1}{3}\bar{\bar{I}}\right) \end{cases}.$$

The relations for electromagnetic fields are defined in section 5.1.2. This system takes into account major physical processes characterizing the nonlocal transport in a simple and computationally efficient manner.

The advantage of the M1 model is in its capacity to strongly describe anisotropic distributions. However, its implementation depends on the considered physical processes. Specifically, in this manuscript, a simplified form of the collisional operator is chosen, which is sufficient for the description of the heat transfer and hot electron thermalization. This form is different from the previous scheme [20] dedicated to the transport of relativistic electrons, which does not conserve the number of electrons and does not account for their thermalization. In the nonlocal transport context, these issues are of primary importance.

The important feature of the M1 model is the exponential form of the EDF, which assures the flux limitation, one of the main effects of nonlocal transport, together with preheating. Mathematically, this follows from the Cauchy-Schwarz inequality:

$$\|\vec{f_1}\| \leq \int_{S_2} d^2\Omega \|\vec{f_e}\|\|\vec{\Omega}\| = f_0.$$

This feature is always respected, even in the case of strongly anisotropic EDFs.

The limiting approximation of this model, as well as of P1, is the description of electromagnetic fields. The equation for electric fields is too complex and time consuming for a numerical solution. The simplification used to find an analytic expression impose reductions of the domain of the model validity. This restriction can be improved in future developments.

In the next part, we compare the M1 model with two other new models described in this section and with the existing models, for the description of nonlocal transport.

Chapter 6

Numerical schemes

Models which describe the transport can be classified by their mathematical structure. Mainly, plasma physics deals with two categories: the diffusive and the advective models. Diffusive equations are partial differential equations of the second order in space and the first order in time, while advective equations are of the same order in space and time, in our case, the first order.

In chapter 5, we developed three new nonlocal transport models. These models describe the electron transport in one, two or three spatial dimensions. Two of them describe plasmas at a kinetic scale and in external magnetic fields. The aim of this chapter, is to present numerical schemes allowing to find solutions of the differential equations, which characterize these models.

The three developed models are AWBS-SNB, P1 and M1. The AWBS-SNB model is based on the diffusion equation

$$\left(\frac{v}{\lambda_{ee}}\frac{\partial}{\partial v}+\vec{\nabla}\frac{\lambda_{ei}^{E}}{3}\vec{\nabla}\right)\Delta f_0=\vec{\nabla}\vec{g}_1^{m},$$

for the nonlocal part of the EDF. On the contrary, the P1 and the M1 models are based on the electron transport equations, forming an advective system

$$\begin{cases} v\vec{\nabla}\cdot\vec{f}_1-\frac{e\vec{E}}{m_e v^2}\cdot\frac{\partial}{\partial v}\left(v^2\vec{f}_1\right)=\nu_{ee}v\frac{\partial}{\partial v}\left(f_0-f_0^m\right) \\ v\vec{\nabla}\cdot\bar{\bar{f}}_2-\dfrac{e}{m_e v^2}\dfrac{\partial}{\partial v}\left(v^2\bar{\bar{f}}_2\cdot\vec{E}\right)+\dfrac{e}{m_e v}\left(f_0\bar{\bar{I}}-\bar{\bar{f}}_2\right)\cdot\vec{E}+\dfrac{e}{m_e c}\vec{f}_1\times\vec{B}=\nu_{ee}v\dfrac{\partial}{\partial v}\vec{f}_1-\nu_{tot}\vec{f}_1 \end{cases}$$

with different closure relations.

In this chapter we present the numerical schemes for solving these two mathematical structures. We analyze advantages and drawbacks of each of two forms. In particular, in section 6.1 we present a numerical solution for the AWBS-SNB model, in one and two dimensions. In section 6.2, we describe a numerical solution for the moment models P1 and M1. Finally, in section 6.3, a comparison between diffusive and advective solutions is given, for a simplified equation.

6.1 AWBS-SNB model

For simplicity we first present the monodimensional numerical scheme. Then it is generalized to two and three dimensions.

Since the AWBS-SNB model is based on a diffusion equation, the general theory can be found in [53].

6.1.1 Monodimensional scheme

At each hydrodynamic step the SNB model is used, providing the heat flux. The latter is computed as follows. Assuming one spatial dimension, we define i and g as discrete indexes for the continuous variables x and v. The first equation of the system (5.7) is a diffusion equation. The diffusion coefficient is $D_i^g = \frac{\lambda_{ei}^E(x_i,v_g)}{3}$. Its value at mesh nodes can be computed by a harmonic average:

$$\frac{1}{D_{i+1/2}^g} = \frac{1}{D_i^g} + \frac{1}{D_{i+1}^g},$$

which ensures a continuity of the discrete flux between two cells. We define $A_i^g = -1/\lambda_{ee}(x_i, v_g)$ Then the discretized AWBS-SNB diffusion equation reads

$$\sum_i T_{ji}^g \Delta_i^g = S_j^g - \frac{A_j^g}{v_{g+1} - v_g} \Delta_j^{g+1}, \tag{6.1}$$

where

$$\bar{\Delta}^g = \begin{pmatrix} \vdots \\ \Delta f_0(x_{i-1}, v_g) \\ \Delta f_0(x_i, v_g) \\ \Delta f_0(x_{i+1}, v_g) \\ \vdots \end{pmatrix},$$

$$\bar{S}^g = \begin{pmatrix} \vdots \\ \frac{\partial}{\partial x} g_1(x_{i-1}, v_g) \\ \frac{\partial}{\partial x} g_1(x_i, v_g) \\ \frac{\partial}{\partial x} g_1(x_{i+1}, v_g) \\ \vdots \end{pmatrix},$$

and

$$\bar{\bar{T}}^g = \begin{pmatrix} \ddots & \ddots & \ddots & \ddots & \ddots & \ddots & \ddots & & \\ \cdots & 0 & a_{i-1}^g & b_{i-1}^g & c_{i-1}^g & 0 & 0 & 0 & \cdots \\ \cdots & 0 & 0 & a_i^g & b_i^g & c_i^g & 0 & 0 & \cdots \\ \cdots & 0 & 0 & 0 & a_{i+1}^g & b_{i+1}^g & c_{i+1}^g & 0 & \cdots \\ & & \ddots & \ddots & \ddots & \ddots & \ddots & \ddots & \ddots \end{pmatrix},$$

is a tridiagonal matrix. The components are

$$\begin{cases} a_i^g = \frac{D_{i-1/2}^g}{(x_i - x_{i-1})(x_{i+1/2} - x_{i-1/2})} \\ b_i^g = \frac{A_i^g}{v_{g+1} - v_g} - \frac{D_{i+1/2}^g}{(x_{i+1} - x_i)(x_{i+1/2} - x_{i-1/2})} - \frac{D_{i-1/2}^g}{(x_i - x_{i-1})(x_{i+1/2} - x_{i-1/2})} \\ c_i^g = \frac{D_{i+1/2}^g}{(x_{i+1} - x_i)(x_{i+1/2} - x_{i-1/2})} \end{cases}.$$

The numerical diffusion equation (6.1) is solved implicitly, by inverting $\bar{\bar{T}}^g$, for each g, using the Jacoby method. At the space boundaries, Δf is imposed to be zero and the system is solved from the highest velocity, to the lower one, assuming Δf equal to zero for the highest velocity. In this way we find $\Delta f_0(x_i, v_g)$ and deduce the numerical flux, as

$$q_{AWBS-SNB\,i} = q_{SH\,i} - \sum_{g=0}^{G} 2\pi m_e D_i^g \frac{\Delta f_0(x_{i+1/2} v_g) - \Delta f_0(x_{i-1/2} v_g)}{x_{i+1/2} - x_{i-1/2}} v_g^5 (v_{g+1/2} - v_{g+1/2}),$$

where G is the index of the highest value of the velocity.

6.1.2 Bidimensional scheme

This scheme can be generalized to two spatial dimensions.The system reads

$$\bar{\bar{M}}^g \bar{U}^g = \bar{S}^g_{2D}.$$

We define i and j, respectively as the indexes for discrete variables x and y. The matrix $\bar{\bar{M}}^g$ is a block matrix, which diagonal block corresponds to $\bar{\bar{T}}^g$, in the monodimensional scheme. The latter is reinterpreted as the matrix block for a fixed j :

$$\bar{\bar{M}}^g = \begin{pmatrix} \ddots & \ddots & \ddots & \ddots & \ddots & \ddots & \ddots & & \\ \cdots & 0 & \bar{\bar{L}}^g_{i,j-1} & \bar{\bar{T}}^g_{i,j-1} & \bar{\bar{R}}^g_{i,j-1} & 0 & 0 & 0 & \cdots \\ \cdots & 0 & 0 & \bar{\bar{L}}^g_{i,j} & \bar{\bar{T}}^g_{i,j} & \bar{\bar{R}}^g_{i,j} & 0 & 0 & \cdots \\ \cdots & 0 & 0 & 0 & \bar{\bar{L}}^g_{i,j+1} & \bar{\bar{T}}^g_{i,j+1} & \bar{\bar{R}}^g_{i,j+1} & 0 & \cdots \\ & & \ddots & \ddots & \ddots & \ddots & \ddots & \ddots & \ddots \end{pmatrix}.$$

The new off-diagonal blocks are the following diagonal matrices:

$$\bar{\bar{L}}^g_i = \begin{pmatrix} \ddots & \ddots & \ddots & \ddots & \ddots & & \\ \cdots & 0 & l^g_{i,j-1} & 0 & 0 & 0 & \cdots \\ \cdots & 0 & 0 & l^g_{i,j} & 0 & 0 & \cdots \\ \cdots & 0 & 0 & 0 & l^g_{i,j+1} & 0 & \cdots \\ & & \ddots & \ddots & \ddots & \ddots & \ddots \end{pmatrix}$$

and

$$\bar{\bar{R}}^g_i = \begin{pmatrix} \ddots & \ddots & \ddots & \ddots & \ddots & & \\ \cdots & 0 & r^g_{i,j-1} & 0 & 0 & 0 & \cdots \\ \cdots & 0 & 0 & r^g_{i,j} & 0 & 0 & \cdots \\ \cdots & 0 & 0 & 0 & r^g_{i,j+1} & 0 & \cdots \\ & & \ddots & \ddots & \ddots & \ddots & \ddots \end{pmatrix},$$

with

$$\begin{cases} l^g_{i,j} = \frac{D^g_{i,j-1/2}}{(y_j - y_{j-1})(y_{j+1/2} - x_{j-1/2})} \\ r^g_{i,j} = \frac{D^g_{i,j+1/2}}{(y_{j+1} - y_j)(y_{j+1/2} - x_{j-1/2})} \end{cases}.$$

The two-dimensional unknown array reads

$$\bar{U}^g = \begin{pmatrix} \vdots \\ \bar{\Delta}^g_{j-1} \\ \bar{\Delta}^g_j \\ \bar{\Delta}^g_{j+1} \\ \vdots \end{pmatrix}$$

and the source

$$\bar{S}^g_{2D} = \begin{pmatrix} \vdots \\ \bar{S}^g_{j-1} - \frac{\bar{A}^g_{j-1}}{v_{g+1} - v_g} \Delta^{g+1}_j \\ \bar{S}^g_j - \frac{\bar{A}^g_j}{v_{g+1} - v_g} \Delta^{g+1}_j \\ \bar{S}^g_{j+1} - \frac{\bar{A}^g_{j+1}}{v_{g+1} - v_g} \Delta^{g+1}_j \\ \vdots \end{pmatrix}.$$

The unknown $\bar{U}^g$ is calculated explicitly through the inversion of the Jacobi's matrix $\bar{\bar{M}}^g$.

Three-dimensional generalization can be obtained by constructing a block-matrix equation, with the blocks being the matrices for the two-dimensional resolution. We limit our work to one and two-dimensional simulations.

6.2 P1 and M1 numerical scheme

The aim of this section is to show how the P1 (subsection 5.2.1) and the M1 model (subsection 5.3.3) have been numerically encoded and what are the limits of these numerical schemes.

The numerical scheme is the same for both models only differing by a source term, which represents the closure relation.

Since the mathematical derivation of the scheme is complicated and this manuscript concerns the physical aspects, we present a simplified derivation, which captures the essential points. Its generalization can be found in [54].

6.2.1 Moment equations in the energy space

The EDF is defined in the phase space $(\vec{x},\vec{v})$ or in the reduced phase space $(\vec{x},v)$. However, calculations in the velocity space can be numerically difficult, since the EDF is not zero at the boundary $v=0$. On the contrary, in the energy space, the EDF is zero at both extremes of the domain $(0,+\infty)$, which simplifies the calculations.

We define the energy EDF $\psi(\vec{x},\epsilon,\vec{\Omega})$, such that it presents the same number of particles in the infinitesimal square $d^3xd\epsilon d^2\Omega$, as $f_e(\vec{x},v,\vec{\Omega})$, in the infinitesimal square $d^3xdvv^2d^2\Omega$:

$$dN = d^3xdvv^2d^2\Omega f_e(\vec{x},v,\vec{\Omega}) = d^3xd\epsilon d^2\Omega\psi(\vec{x},\epsilon,\vec{\Omega}).$$

This leads to

$$f_e(\vec{x},v,\vec{\Omega}) = \frac{m_e}{v}\psi(\vec{x},\epsilon,\vec{\Omega}).$$

In the same way the moments read

$$\begin{cases} f_0(\vec{x},v,\vec{\Omega}) = \frac{m_e}{v}\psi_0(\vec{x},\epsilon,\vec{\Omega}) \\ \vec{f_1}(\vec{x},v,\vec{\Omega}) = \frac{m_e}{v}\vec{\psi_1}(\vec{x},\epsilon,\vec{\Omega}) \\ \bar{\bar{f}}_2(\vec{x},v,\vec{\Omega}) = \frac{m_e}{v}\bar{\bar{\psi}}_2(\vec{x},\epsilon,\vec{\Omega}) \end{cases}.$$

In order to simplify the moment hierarchy, we redefine the moments as

$$\begin{cases} \Psi_0 = m_e v^2\psi_0 = v^3 f_0 \\ \vec{\Psi}_1 = m_e v^2\vec{\psi_1} = v^3\vec{f_1} \\ \bar{\bar{\Psi}}_2 = m_e v^2\bar{\bar{\psi}}_2 = v^3\bar{\bar{f}}_2 \end{cases}.$$

With these relations, the system (5.1) reads

$$\begin{cases} \vec{\nabla}\cdot\vec{\Psi}_1 = \frac{\partial}{\partial\epsilon}\left(S_{tot}\Psi_0\right) - \frac{\partial}{\partial\epsilon}\left(S_\epsilon\Psi_0^m\right) - \frac{S_\epsilon}{2\epsilon}\left(\Psi_0-\Psi_0^m\right) + \frac{e}{2\epsilon}\vec{E}\cdot\vec{\Psi}_1 \\ \vec{\nabla}\cdot\bar{\bar{\Psi}}_2 = \frac{\partial}{\partial\epsilon}\left(S_{tot}\vec{\Psi}_1\right) + \frac{\partial}{\partial\epsilon}\left[e\left(\bar{\bar{\Psi}}_2 - \frac{\vec{\Psi}_1\otimes\vec{\Psi}_1}{\Psi_0}\right)\cdot\vec{E}\right] - \left(\frac{S_\epsilon}{2\epsilon}+\nu_{tot}\right)\vec{\Psi}_1 - \frac{e\left(\Psi_0\vec{E}+v\vec{\Psi}_1\times\vec{B}\right)}{2\epsilon} \\ \bar{\bar{\Psi}}_2 = \bar{\bar{\Upsilon}}\Psi_0 \end{cases} \tag{6.2}$$

with

$$S_\epsilon = m_e v\nu_{ee}$$

being the stopping power and

$$S_{tot} = e\vec{E}\cdot\frac{\vec{\Psi}_1}{\Psi_0} + S_\epsilon.$$

being an effective stopping power. The thermalization is given by the Maxwellian EDF $\Psi_0^m = v^3 f_0^m$. The closure equation reads

$$\bar{\bar{\Upsilon}} = \begin{cases} \frac{1}{3} & \text{for P1} \\ \chi(\Psi_0,\vec{\Psi}_1) & \text{for M1} \end{cases}.$$

The first two moment equations of (6.2) can be written with a single matrix equation:

$$\vec{\nabla}\cdot\bar{\bar{F}} = \frac{\partial}{\partial\epsilon}\left[\left(S_{tot}\bar{\bar{I}} + \bar{\bar{M}}\right)\cdot\bar{\Phi}\right] + \bar{\bar{A}}\cdot\bar{\Phi} + \bar{\Gamma}, \tag{6.3}$$

where $\bar{\bar{I}}$ is the 3×3 identity matrix. In two spatial dimensions, the components of the compact moment hierarchy read

$$\bar{\Phi} = \begin{pmatrix} \Psi_0 \\ \Psi_{1x} \\ \Psi_{1y} \end{pmatrix},$$

$$\bar{\bar{F}} = \begin{pmatrix} \vec{\Psi}_1 \\ \vec{\Psi}_{2x} \\ \vec{\Psi}_{2y} \end{pmatrix},$$

$$\bar{\bar{M}} = \begin{pmatrix} 0 & & 0 & 0 \\ \frac{e\left(\Psi_{2xx}-\frac{\Psi_{1x}\Psi_{1x}}{\Psi_0}\right)E_x}{\Psi_0} + \frac{e\left(\Psi_{2xy}-\frac{\Psi_{1x}\Psi_{1y}}{\Psi_0}\right)E_y}{\Psi_0} & & 0 & 0 \\ \frac{e\left(\Psi_{2yx}-\frac{\Psi_{1y}\Psi_{1x}}{\Psi_0}\right)E_x}{\Psi_0} + \frac{e\left(\Psi_{2yy}-\frac{\Psi_{1y}\Psi_{1y}}{\Psi_0}\right)E_y}{\Psi_0} & & 0 & 0 \end{pmatrix},$$

$$\bar{\bar{A}} = \begin{pmatrix} -\frac{S_\epsilon}{2\epsilon} & \frac{e}{2\epsilon}E_x & \frac{e}{2\epsilon}E_y \\ \frac{e}{2\epsilon}E_x & -\frac{S_\epsilon}{2\epsilon}-\nu_{tot} & -\frac{ev}{2\epsilon}B_z \\ \frac{e}{2\epsilon}E_y & \frac{ev}{2\epsilon}B_z & -\frac{S_\epsilon}{2\epsilon}-\nu_{tot} \end{pmatrix}$$

and

$$\bar{\Gamma} = \begin{pmatrix} -\frac{\partial}{\partial\epsilon}\left(S_\epsilon\Psi_0^m\right) + \frac{S_\epsilon}{2\epsilon}\Psi_0^m \\ 0 \\ 0 \end{pmatrix}.$$

In Eq. (6.3), it is supposed that the magnetic field is perpendicular to the plane of simulation.

In the energy space, the moment hierarchy well behaves on the energy boundaries and so it is more suitable for a numerical solution.

6.2.2 Numerical solution of the transport equation

Solution of a transport equation is mathematically complicated. We start here from a simplified form and then generalize it to Eq. (6.3).

Simple transport equation

Let us define $f(x,t)$, as a distribution function depending only on time and space. Neglecting also the collision integral, the transport equation reads

$$\frac{\partial}{\partial t}f + v\frac{\partial}{\partial x}f = 0, \tag{6.4}$$

where v is a constant. It can also be written as

$$\frac{d}{dt}f[x(t=0)+vt] = 0.$$

Since there are no collisions, f is conserved in the phase space. Thus

$$\text{if } \; f(x,t=0)\geq 0 \Rightarrow f(x,t)\geq 0 \;\forall t. \tag{6.5}$$

This is also in agreement with the probabilistic nature of EDF.

The general theory of transport equations can be found in [55].

We develop $f(x, t = 0)$ to the second order in the Taylor series in space

$$f(x + dx, t) = f(x, t) + dx\frac{\partial}{\partial x}f(x, t) + \frac{dx^2}{2}\frac{\partial^2}{\partial x^2}f(x, t) + o\left(dx^3\right)$$

and to the first order in time

$$f(x, t + dt) = f(x, t) + dt\frac{\partial}{\partial t}f(x, t) + o\left(dx^2\right).$$

We define n and i as the discrete indexes, respectively running over t and x, such that $f(x, t)$ corresponds to $f^{n,i}$. Assuming a linear discretization, the transport equation reads

$$\frac{f^{n+1,i} - f^{n,i}}{\Delta t} + v\frac{f^{n,i+1} - f^{n,i-1}}{2\Delta x} = 0,$$

where Δ denotes a positive increment. The solution is

$$f^{n+1,i} = f^{n,i} - v\frac{f^{n,i+1} - f^{n,i-1}}{2\Delta x}\Delta t. \tag{6.6}$$

However, this scheme is unstable. It can be proven with a counter example. Let us assume $f^{0,i}$, as follows:

$$f^{0,i} = \begin{cases} 1 & \text{if } i > 1 \\ 0 & \text{if } i \leq 1 \end{cases}.$$

In this case Eq. (6.6) becomes

$$f^{1,1} = -\frac{v}{2}\frac{dt}{dx}.$$

Since $dt \geq 0$ and $dx \geq 0$, the result disagrees with (6.5). Thus the solution is unstable.

One may solve Eq. (6.4), by decentralizing the space derivative

$$\frac{f^{n+1,i} - f^{n,i}}{\Delta t} + v\frac{f^{n,i} - f^{n,i-1}}{\Delta x} = 0. \tag{6.7}$$

Then the solution is

$$f^{n+1,i} = \left(1 - v\frac{\Delta t}{\Delta x}\right) f^{n,i} + v\frac{\Delta t}{\Delta x}f^{n,i-1}.$$

It is positively defined if and only if

$$\begin{cases} v \geq 0 \\ 1 - v\frac{\Delta t}{\Delta x} \geq 0 \end{cases}.$$

The second condition gives us a constraint on the discretization of time:

$$\Delta t \leq \frac{\Delta x}{v},$$

which is known as the Courant, Friedrichs and Lewy (CFL) condition [53].

We may remove the condition $v \geq 0$, by rewriting Eq. (6.7) as

$$\frac{f^{n+1,i} - f^{n,i}}{\Delta t} + v_+\frac{f^{n,i} - f^{n,i-1}}{\Delta x} - v_-\frac{f^{n,i+1} - f^{n,i}}{\Delta x} = 0, \tag{6.8}$$

where

$$\begin{cases} v_+ = \max(v, 0) \\ v_- = \min(v, 0) \end{cases}.$$

The latter expression can be written as

$$\begin{cases} v = v_+ + v_- \\ |v| = v_+ - v_- \end{cases},$$

leading to

$$\begin{cases} v_+ = \frac{1}{2}\left(v + |v|\right) \\ v_- = \frac{1}{2}\left(v - |v|\right) \end{cases}.$$

The solution of Eq. (6.8) reads

$$f^{n+1,i} = \left(1 - |v|\frac{\Delta t}{\Delta x}\right) f^{n,i} + v_+ \frac{\Delta t}{\Delta x} f^{n,i-1} - v_- \frac{\Delta t}{\Delta x} f^{n,i+1},$$

from which the CFL condition reads

$$\Delta t \leq \frac{\Delta x}{|v|}.$$

The solution can be rewritten as a function of v and $|v|$:

$$\frac{f^{n+1,i} - f^{n,i}}{\Delta t} + \frac{F_{HLL}^{n,i+1/2} - F_{HLL}^{n,i-1/2}}{\Delta x} = 0, \tag{6.9}$$

where

$$F_{HLL}^{n,i+1/2} = v_+ f^{n,i} + v_- f^{n,i+1} = \frac{v}{2}\left(f^{n,i} + f^{n,i+1}\right) + \frac{|v|}{2}\left(f^{n,i} - f^{n,i+1}\right).$$

In two dimensions, the same scheme can be used. We show in what follows, that the scheme, so called HLL, can be generalized to the M1 and P1 systems. In the next section we use a generalized form of Eq. (6.9).

Resolution of the moment hierarchy

Equation (6.3) is stationary but the energy variable can be interpreted as time in Eq. (6.9), since the electron energy may only decrease but not increase. The energy losses described by the AWBS collision operator impose to solve this equation from the highest energy to the lowest, in accordance with the transition of particles from more energetic states to the lower ones. This is similar to the principle of causality, for time.

As a first step, we discretize the phase-space, similarly as in Eq. (6.9). We define i as an index running over the x direction, j over the y direction and g over the kinetic energy ϵ. Therefore, all functions of the continuous variables (x, y, ϵ) are expressed as functions of the discrete variables (i, j, g). For example, for a generic function X, the variables are expressed as follows:

$$X_0^{i,j,g} = X_0(x^i, y^j, \epsilon^g).$$

The discretized Eq. (6.3) reads

$$\begin{aligned} &\frac{\bar{F}_{HLL}^{i+1/2,j,g+1} - \bar{F}_{HLL}^{i-1/2,j,g+1}}{\frac{1}{2}\left(x^{i+1} - x^{i-1}\right)} + \frac{\bar{F}_{HLL}^{i,j+1/2,g+1} - \bar{F}_{HLL}^{i,j-1/2,g+1}}{\frac{1}{2}\left(y^{i+1} - y^{i-1}\right)} = \\ &\frac{\left(S_{tot}^{i,j,g+1}\bar{\bar{I}} + \bar{\bar{M}}^{i,j,g+1}\right) \cdot \bar{\Phi}^{i,j,g+1} - \left(S_{tot}^{i,j,g}\bar{\bar{I}} + \bar{\bar{M}}^{i,j,g+1}\right) \cdot \bar{\Phi}^{i,j,g}}{\epsilon^{g+1} - \epsilon^g} \\ &+ \bar{\bar{A}}^{i,j,g} \cdot \bar{\Phi}^{i,j,g} + \bar{\Gamma}^{i,j,g}. \end{aligned} \tag{6.10}$$

As in Eq. (6.9), the HLL flux is defined as

$$\bar{F}^{i+1/2,j,g}_{HLL} = \frac{\bar{F}^{i+1,j,g} + \bar{F}^{i,j,g}}{2} + \frac{\bar{\Phi}^{i+1,j,g} - \bar{\Phi}^{i,j,g}}{2}.$$

The discretized matrices are

$$\bar{\Phi}^{i,j,g} = \begin{pmatrix} \Psi_0^{i,j,g} \\ \Psi_{1x}^{i,j,g} \\ \Psi_{1y}^{i,j,g} \end{pmatrix},$$

$$\vec{\bar{F}}^{i,j,g} = \begin{pmatrix} \vec{\Psi}_1^{i,j,g} \\ \vec{\Psi}_{2x}^{i,j,g} \\ \vec{\Psi}_{2y}^{i,j,g} \end{pmatrix},$$

$$\bar{\bar{M}}^{i,j,g} = \begin{pmatrix} 0 & 0 & 0 \\ \sum_{p=x,y} \frac{e\left(\Psi_{2xp}^{i,j,g} - \frac{\Psi_{1x}^{i,j,g}\Psi_{1p}^{i,j,g}}{\Psi_0^{i,j,g}}\right)E_p^{i,j,g}}{\Psi_0^{i,j,g}} & 0 & 0 \\ \sum_{p=x,y} \frac{e\left(\Psi_{2yp}^{i,j,g} - \frac{\Psi_{1y}^{i,j,g}\Psi_{1p}^{i,j,g}}{\Psi_0^{i,j,g}}\right)E_p^{i,j,g}}{\Psi_0^{i,j,g}} & 0 & 0 \end{pmatrix},$$

$$\bar{\bar{A}}^{i,j,g} = \begin{pmatrix} -\frac{S_\epsilon^{i,j,g}}{2\epsilon^g} & \frac{e}{2\epsilon^g}E_x^{i,j,g} & \frac{e}{2\epsilon^{ig}}E_y^{i,j,g} \\ \frac{e}{2\epsilon^g}E_x^{i,j,g} & -\frac{S_\epsilon^{i,j,g}}{2\epsilon^g} - \nu_{tot}^{i,j,g} & -\frac{ev^g}{2\epsilon^g}B_z^{i,j,g} \\ \frac{e}{2\epsilon^g}E_y^{i,j,g} & \frac{ev^g}{2\epsilon^g}B_z^{i,j,g} & -\frac{S_\epsilon^{i,j,g}}{2\epsilon^g} - \nu_{tot}^{i,j,g} \end{pmatrix}$$

and

$$\bar{\Gamma}^{i,j,g} = \begin{pmatrix} -\frac{S_\epsilon^{i,j,g+1}\Psi_0^{m\ i,j,g+1} - S_\epsilon^{i,j,g}\Psi_0^{m\ i,j,g}}{\epsilon^{g+1}-\epsilon^g} + \frac{S_\epsilon^{i,j,g}}{2\epsilon^g}\Psi_0^{m\ i,j,g} \\ 0 \\ 0 \end{pmatrix}.$$

In the same way, the closure relation is discretized as $\bar{\bar{\Psi}}_2^{i,j,g} = \bar{\bar{\Upsilon}}^{i,j,g}\Psi_0^{i,j,g}$.

Finally the solution is

$$\begin{aligned} \bar{\Phi}^{i,j,g} = \left(\frac{S_{tot}^{i,j,g}\bar{\bar{I}} + \bar{\bar{M}}^{i,j,g}}{\epsilon^{g+1}-\epsilon^g} - \bar{\bar{A}}^{i,j,g}\right)^{-1} \cdot \Bigg(-\frac{\bar{F}_{HLL}^{i+1/2,j,g+1} - \bar{F}_{HLL}^{i-1/2,j,g+1}}{x^{i+1/2}-x^{i-1/2}} \\ - \frac{\bar{F}_{HLL}^{i,j+1/2,g+1} - \bar{F}_{HLL}^{i,j-1/2,g+1}}{y^{i+1/2}-y^{i-1/2}} + \frac{S_{tot}^{i,j,g+1}\bar{\bar{I}} + \bar{\bar{M}}^{i,j,g+1}}{\epsilon^{g+1}-\epsilon^g} \cdot \bar{\Phi}^{i,j,g+1} + \bar{\Gamma}^{i,j,g}\Bigg), \end{aligned} \tag{6.11}$$

where $\bar{\bar{I}}$ is the 3×3 identity matrix.

The CFL condition for the stability is

$$\Delta\epsilon \leq \frac{S_p}{\frac{1}{\Delta x} + \frac{1}{\Delta y}}, \tag{6.12}$$

assuming the EDF not too anisotropic.

In this section, we have treated the energy as an efficient time variable, solving from higher energies to lower ones. The causality principle imposes

$$S_{tot} = e\vec{E} \cdot \frac{\vec{\Psi}_1}{\Psi_0} + S_\epsilon.geq0,$$

which means that electrons only lose energy, as it happens in nonlocal transport. This condition is not always respected by plasmas irradiated by lasers, which induces hydrodynamic movement. This has practically limited our model to be applied for heat transport, but not for hydrodynamics. A split to energy gain and energy losses, computed by iteration, could be a way to overcome this limit and enlarge the domain of validity of the model.

6.2.3 Boundary conditions and the implemented algorithm

Here we explain the algorithm for coupling the kintic equation to a hydrodynamic code.

At each time step, a hydrodynamic code computes macroscopic plasma quantities as density, velocity and temperature. These data are transmitted to the M1 and P1 models for computing the heat transport. Equation (6.2) is solved by iterations, starting from the local electric field assumption (or the zero field assumption). Once the electric field converges, the EDF allows to compute all kinetic effects. In particular, the heat flux is derived as

$$\vec{q}_{P1,M1}^{i,j,g} = \sum_{g=\epsilon_{\min}(t)}^{\epsilon_{\max}(t)} \left(\epsilon^{g+1} - \epsilon^{g}\right) \vec{\Psi}_1^{i,j,g},$$

where $\epsilon_{\max}(t)$ and $\epsilon_{\min}(t)$ are the highest and lowest energy values accounted. Their choice is crucial for the performances of the scheme. We choose to use an energy mesh, varying in time and for which, $\epsilon_{\max}(t) = 18 \max[T_e(t,\vec{x})]$ and $\epsilon_{\min}(t) = \min[T_e(t,\vec{x})]/10$. Here, $\max/\min[T_e]$ are the maximum and minimum values of the electron temperature, in the computing box.

Equation (6.2) requires boundary conditions. If $\epsilon_{\max}$ is high enough, we can assume that

$$\begin{cases} \Psi_0(\vec{x}, \epsilon = \epsilon_{\max}) = 0 \\ \vec{\Psi}_1(\vec{x}, \epsilon = \epsilon_{\max}) = 0 \end{cases}.$$

The choice of spatial boundary conditions is more complicated. It is related to the choice of heat flux at the boundaries. If the system is isolated, since our transport model is stationary, we have to impose a zero flux at boundaries, otherwise all particles would escape. This condition implies also to impose a zero temperature derivative. There are only two boundary conditions which respect the required assumptions:

$$\begin{cases} \Psi_0(\vec{x} = \partial\vec{x}^+, \epsilon) = \Psi_0(\vec{x} = \partial\vec{x}^-, \epsilon) \\ \vec{\Psi}_1(\vec{x} = \partial\vec{x}^+, \epsilon) = 0 \end{cases}$$

and

$$\begin{cases} \Psi_0(\vec{x} = \partial\vec{x}^+, \epsilon) = \Psi_0(\vec{x} = \partial\vec{x}^-, \epsilon) \\ \vec{\Psi}_1(\vec{x} = \partial\vec{x}^+, \epsilon) = -\vec{\Psi}_1(\vec{x} = \partial\vec{x}^-, \epsilon) \end{cases},$$

where, in our formalism, $\partial\vec{x}$ denotes the spatial boundary and signs $+$ and $-$ mean outer and inner limits, respectively. Both assumptions give similar results. In case of symmetric systems, in which all hydrodynamic variables experience an even symmetry around the boundary axes, the boundary conditions read

$$\begin{cases} \Psi_0(\vec{x} = \partial\vec{x}^+, \epsilon) = \Psi_0(\vec{x} = \partial\vec{x}^-, \epsilon) \\ \vec{\Psi}_1(\vec{x} = \partial\vec{x}^+, \epsilon) = \vec{\Psi}_1(\vec{x} = \partial\vec{x}^-, \epsilon) \end{cases},$$

since $\vec{q}(\vec{x} = \partial\vec{x}^+) = \vec{q}(\vec{x} = \partial\vec{x}^-)$.

6.3 Diffusive and advective schemes at comparison

In this chapter we have presented numerical schemes for the solution of three models of a nonlocal transport. The first of them (AWBS-SNB) is of a diffusive form and so it is solved using classical numerical methods for diffusion equations. The other models (M1 and P1) are of an advective form, typical for the transport equations. The corresponding scheme is described above. In this section we compare the diffusive and the advective

equations for a simplified form of the system (6.2), their mathematical structure and the numerical schemes.

In order to develop an analytic approach, we simplify the system (6.2). The assumptions are the following:

- one spatial dimension;
- Lorentz gas approximation ($Z \gg 1$);
- nearly isotropic system ($\Upsilon = 1/3$);
- no electromagnetic fields.

Under these assumptions, the system reads

$$\begin{cases} \frac{\partial}{\partial x}\Psi_1 = \frac{\partial}{\partial \epsilon}\left(S_\epsilon \Delta\Psi_0\right) - \frac{S_\epsilon}{2\epsilon}\Delta\Psi_0 \\ \frac{1}{3}\frac{\partial}{\partial x}\Psi_0 = -\nu_{ei}\Psi_1 \end{cases}, \tag{6.13}$$

where $\Delta\Psi_0 = \Psi_0 - \Psi_0^m$. We want to compare the diffusive and the advective forms of this system and their numerical solutions.

6.3.1 Diffusive form

From the system (6.13), we can easily deduce the diffusive form, by injecting Ψ_1 from the second into the first equation:

$$-\frac{1}{3}\frac{\partial}{\partial x}\frac{1}{\nu_{ei}}\frac{\partial}{\partial x}\Psi_0 = \frac{\partial}{\partial \epsilon}\left(S_\epsilon \Delta\Psi_0\right) - \frac{S_\epsilon}{2\epsilon}\Delta\Psi_0. \tag{6.14}$$

Similarly to section 6.1, we discretize Eq. (6.14):

$$-\frac{1}{3}\frac{\frac{1}{\nu_{ei}^{i+1,g+1}}\frac{\Psi_0^{i+2,g+1}-\Psi_0^{i,g+1}}{x^{i+2}-x^i} - \frac{1}{\nu_{ei}^{i-1,g+1}}\frac{\Psi_0^{i,g+1}-\Psi_0^{i-2,g+1}}{x^i-x^{i-2}}}{x^{i+1}-x^{i-1}} = \frac{S_\epsilon^{i,g+1}\Psi_0^{i,g+1} - S_\epsilon^{i,g}\Psi_0^{i,g}}{\epsilon^{g+1}-\epsilon^g} - \frac{S_\epsilon^{i,g}}{2\epsilon^g}\Psi_0^{i,g}. \tag{6.15}$$

This discrete equation is simple and can be easily solved. However its generalization for accounting electromagnetic field is complicated.

6.3.2 Advective form

Following section 6.2.2, we write a compact form of Eq. (6.13) as:

$$\frac{\bar{F}_{HLL}^{i+1/2,g+1} - \bar{F}_{HLL}^{i-1/2,g+1}}{\frac{1}{2}\left(x^{i+1}-x^{i-1}\right)} = \frac{S_\epsilon^{i,g+1}\bar{\bar{K}}\bar{\Phi}^{i,g+1} - S_\epsilon^{i,g}\bar{\bar{K}}\bar{\Phi}^{i,g}}{\epsilon^{g+1}-\epsilon^g} + \bar{\bar{A}}^{i,g}\cdot\bar{\Phi}^{i,g} + \bar{\Gamma}^{i,g}, \tag{6.16}$$

were the matrices read

$$\bar{\bar{K}} = \begin{pmatrix} 0 & 0 \\ 0 & 1 \end{pmatrix},$$

$$\bar{\Phi}^{i,g} = \begin{pmatrix} \Psi_0^{i,g} \\ \Psi_1^{i,g} \end{pmatrix},$$

$$\vec{\bar{F}}^{i,g} = \begin{pmatrix} \Psi_1^{i,g} \\ \Psi_2^{i,g} \end{pmatrix},$$

$$\bar{\bar{A}}^{i,g} = \begin{pmatrix} -\frac{S_\epsilon^{i,g}}{2\epsilon^g} & 0 \\ 0 & -\nu_{ei}^{i,g} \end{pmatrix}$$

and

$$\bar{\Gamma}^{i,g} = \begin{pmatrix} -\frac{S_\epsilon^{i,g+1}\Psi_0^{m\ i,g+1} - S_\epsilon^{i,g}\Psi_0^{m\ i,g}}{\epsilon^{g+1}-\epsilon^g} + \frac{S_\epsilon^{i,g}}{2\epsilon^g}\Psi_0^{m\ i,g} \\ 0 \end{pmatrix}.$$

The HLL flux is defined as

$$\bar{F}_{HLL}^{i+1/2,g} = \frac{\bar{F}^{i+1,g} + \bar{F}^{i,g}}{2} + \frac{\bar{\Phi}^{i+1,g} - \bar{\Phi}^{i,g}}{2}.$$

Writing explicitly the two equations, from (6.16), we have

$$\begin{cases} \frac{\Psi_1^{i+1,g+1} - \Psi_1^{i-1,g+1}}{x^{i+1}-x^{i-1}} + \frac{\Psi_0^{i+1,g+1} - 2\Psi_0^{i,g+1} - \Psi_0^{i-1,g+1}}{x^{i+1}-x^{i-1}} = \frac{S_\epsilon^{i,g+1}\Delta\Psi_0^{i,g+1} - S_\epsilon^{i,g}\Delta\Psi_0^{i,g}}{\epsilon^{g+1}-\epsilon^g} - \frac{S_\epsilon^{i,g}}{2\epsilon^g}\Delta\Psi_0^{i,g} \\ \frac{1}{3}\frac{\Psi_0^{i+1,g+1} - \Psi_0^{i-1,g+1}}{x^{i+1}-x^{i-1}} + \frac{\Psi_1^{i+1,g+1} - 2\Psi_1^{i,g+1} - \Psi_1^{i-1,g+1}}{x^{i+1}-x^{i-1}} = -\nu_{ei}^{i,g}\Psi_1^{i,g} \end{cases}.$$

We now impose a diffusive form, as in Eq. (6.15): we inject

$$\Psi_1^{i,g} = -\frac{1}{\nu_{ei}}\left(\frac{1}{3}\frac{\Psi_0^{i+1,g+1} - \Psi_0^{i-1,g+1}}{x^{i+1}-x^{i-1}} + \frac{\Psi_1^{i+1,g+1} - 2\Psi_1^{i,g+1} - \Psi_1^{i-1,g+1}}{x^{i+1}-x^{i-1}}\right)$$

in the first equation of the system and we find

$$\begin{aligned} &-\frac{1}{3}\frac{\frac{1}{\nu_{ei}^{i+1,g+1}}\frac{\Psi_0^{i+2,g+1}-\Psi_0^{i,g+1}}{x^{i+2}-x^i} - \frac{1}{\nu_{ei}^{i-1,g+1}}\frac{\Psi_0^{i,g+1}-\Psi_0^{i-2,g+1}}{x^i-x^{i-2}}}{x^{i+1}-x^{i-1}} \\ &+\frac{\frac{1}{\nu_{ei}^{i+1,g+1}}\frac{\Psi_1^{i+2,g+1}-2\Psi_1^{i+1,g+1}+\Psi_1^{i,g+1}}{x^{i+2}-x^i} - \frac{1}{\nu_{ei}^{i-1,g+1}}\frac{\Psi_1^{i,g+1}-2\Psi_1^{i-1,g+1}+\Psi_1^{i-2,g+1}}{x^i-x^{i-2}}}{x^{i+1}-x^{i-1}} \\ &+\frac{\Psi_0^{i+1,g+1} - 2\Psi_0^{i,g+1} - \Psi_0^{i-1,g+1}}{x^{i+1}-x^{i-1}} = \frac{S_\epsilon^{i,g+1}\Psi_0^{i,g+1} - S_\epsilon^{i,g}\Psi_0^{i,g}}{\epsilon^{g+1}-\epsilon^g} - \frac{S_\epsilon^{i,g}}{2\epsilon^g}\Psi_0^{i,g}. \end{aligned} \tag{6.17}$$

Equation (6.17) differs from Eq. (6.15) by the second and the third term in the left hand side. Those additional terms may induce a numerical diffusion, which can become a source of error in the diffusive limit, which is typical for local and isotropic systems. In order to avoid this, in the case of a weak anisotropy, the system requires to be refined with a high number of spatial meshes, which may affect the performance of the code.

6.3.3 Code performance

In this chapter we have shown that numerically there are two different ways to deal with the description of nonlocal transport: a diffusive and an advective approach.

The diffusive approach is numerically simple and efficient to be solved. Issues related to this approach come only from the model nature: equations are too complex to account for electromagnetic fields and realistic collision operators.

The advective approach allows to deal with analytically more simple equations, which can account additional physical effects. However, as it is explained in this chapter, there are several numerical issues. The algorithm used is not efficient since it has to describe both nonlocal and local transport limits but, in the latter case, the description requires a mesh refinement, in order to avoid errors due to the numerical diffusion. Moreover, the model requires rather high values of the stopping power, in order to be stable. This condition is not respected in low-temperature plasmas.

In order to give some estimates of the code performance, we compare the computation time of the M1 model with the one of the SNB model, for the simulation performed in order to obtain Fig. 7.1. The results are shown in table below. The M1 computation time

is obtained with the meshing required for numerical convergence. The SNB computation time is evaluated once with the same meshing as of M1 and once with the meshing required for convergence. Using the same meshing, the SNB model is slower than M1. Nevertheless, it converges with fewer meshes (10 times less). The addition of magnetic fields does not modify the time of computation.

ϵ_{NL}	M1	SNB same meshing	SNB converged meshing
$\approx 2 \times 10^{-3}$	23 s	37.5 s	0.58 s
$\approx 2 \times 10^{-2}$	20 s	40 s	0.7 s
$\approx 2 \times 10^{-1}$	53 s	124 s	0.6 s

Work is in progress for the implementation of more efficient numerical schemes for the description of advective equations in the local regime. The most promising choice is the use of asymptotic-preserving schemes [56]. Nevertheless, issues related to numerical resolution of the advective equation do not minimize the importance of the physical models developed in this manuscript.

Part III

Applications

Chapter 7

Transport in unmagnetized plasmas

In the previous part we have presented a nonlocal kinetic model based on an angular development of the FP equation, closed by the angular entropy maximization principle [51]. This model, called M1 [52] for the first angular moment, has already been tested for a relativistic electron beam transport through matter [20], for applications of fast ignition [26] and radiotherapy.

In this chapter we apply the M1 model in the description of a nonlocal transport, comparing it with the P1, as well as the SNB model, in the stationary limit, and with a Landau-FP code, in the description of flux limitation. We show that the entropic closure allows an extension of the domain of application to stronger anisotropic cases, while the advective form of equations allows to account for more realistic electric fields. We present several examples in 1D and 2D geometry and we analyze the small scale kinetic effects in the transport affected zone.

In particular, in section 7.1, we compare the transport models in ICF conditions. In section 7.2, we discuss modifications of damping of electrostatic plasma waves and excitation of stream instabilities in the transport zone. Conclusions on the nonlocal transport in unmagnetized plasmas are drawn in section 7.3.

In this chapter, when not specified, we use the nonlocal definition (5.3), for the electric field, in order to compute the M1 and P1 transport.

7.1 Heat transport

In this section, the M1 model is applied for the description of a nonlocal heat transport. The M1 model is compared with the modified SNB nonlocal model (AWBS-SNB) and with the limited and unlimited SH model, in several representative cases. We also compare all the previous models with the solutions of the FP equation, in a particular test.

7.1.1 Transport along a temperature gradient

The transport along a temperature gradient has already been considered for testing nonlocal models [22]. This simple case captures the most important nonlocal features of the heat tansport.

Heat fluxes

The M1, P1 and AWBS-SNB models are able to recover local results, for a nonlocal parameter smaller than 2×10^{-3}. We show in what follows their predictions of nonlocal heat fluxes.

Let us consider a fully-ionized beryllium plasma ($Z = 4$) at a constant density of $4.5 \times 10^{22}\,\mathrm{cm}^{-3}$, having a steep temperature gradient given by

$$T_e(x) = \frac{|T_0 - T_1|}{2}\left[\frac{2}{\pi}\arctan\left(\frac{x}{\delta_{NL}}\right) + 1\right] + T_1, \tag{7.1}$$

with $T_0 = 5\,\mathrm{keV}$, $T_1 = 1\,\mathrm{keV}$ and $\delta_{NL} = 5\,\mu\mathrm{m}$.

Such a configuration is characterized by a maximum MFP $\lambda_0 = 3\sqrt{\frac{\pi}{2}}\frac{T_0^2}{4\pi n_e Z e^4 \Lambda_{ei}} \approx 3.15\,\mu\mathrm{m}$ (corresponding to the collision time $\tau_0 = \lambda_0\sqrt{m_e/T_0} \approx 0.12$ ps), located in the hot region. The minimum gradient length $L_T = T_e/||\vec{\nabla}T_e|| \approx 12\ \mu\mathrm{m}$ is located in the central region. Thus, the nonlocal parameter is $\lambda_0/L_T \approx 0.3 \gg 2 \times 10^{-2}$ and we have a representative test for nonlocal regimes.

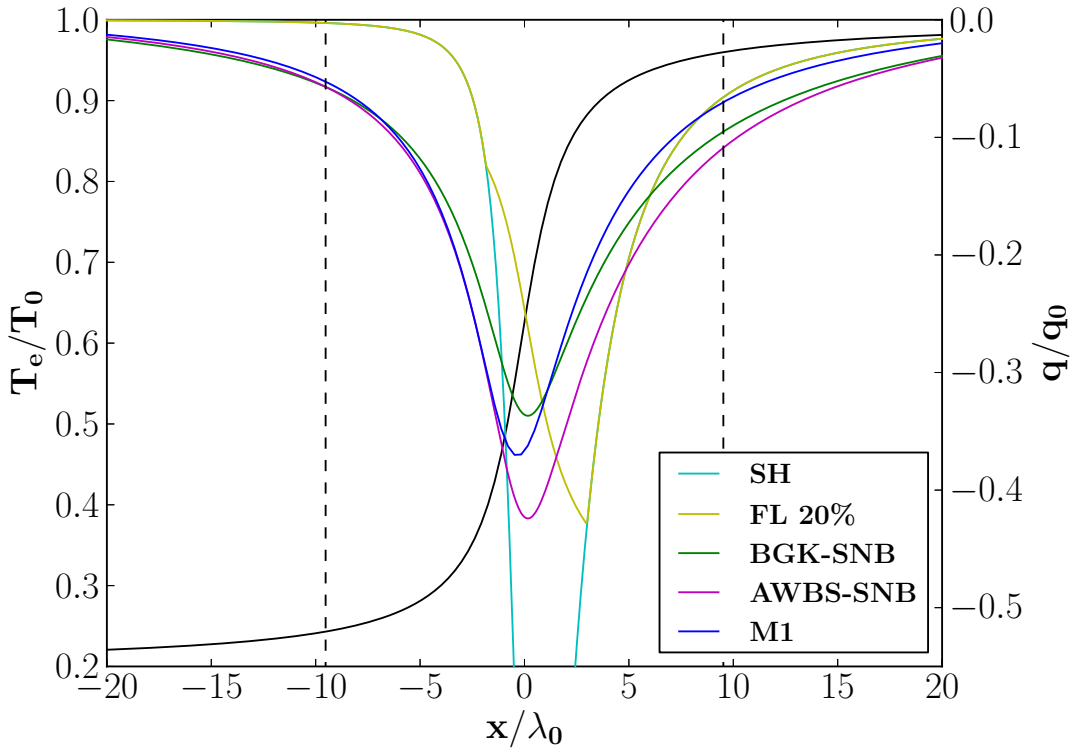

Figure 7.1: Comparison between the different heat flux models. In black the temperature, in celestial the SH flux, in yellow the 20% FL, in green and violet the SNB models using respectively the BGK and the AWBS collision operators and in blue the M1 model. The two vertical dashed lines indicate the regions where the kinetic analysis is performed.

Heat fluxes computed with the previously described models are compared in Fig. 7.1. The fluxes are normalized to the maximum value of the local flux (SH theory) $q_0 \approx 40\ \mathrm{PW/cm^2}$ and the space coordinate is measured with the standard thermal MFP $\lambda_0 \approx 3.15\,\mu\mathrm{m}$. The figure is zoomed in on nonlocal fluxes, in order to highlight the different descriptions.

Since $\lambda_0/L_T \gg 2 \times 10^{-2}$, suprathermal electrons penetrate deep inside the plasma, depositing their energy nonlocally. This implies a delocalization of the energy transported: it reduces the heat flux in proximity of the temperature gradient (flux limitation) and increases in the front of it (preheating). The M1, BGK-SNB and AWBS-SNB models qualitatively describe such a delocalization, but present some differences. The M1 and AWBS-SNB models predict a lower flux limitation, than the BGK-SNB model. They are based on the AWBS collisional operator, which is characterized by stronger physical assumptions than the BGK operator, used in the BGK-SNB model (see chapter 4). All

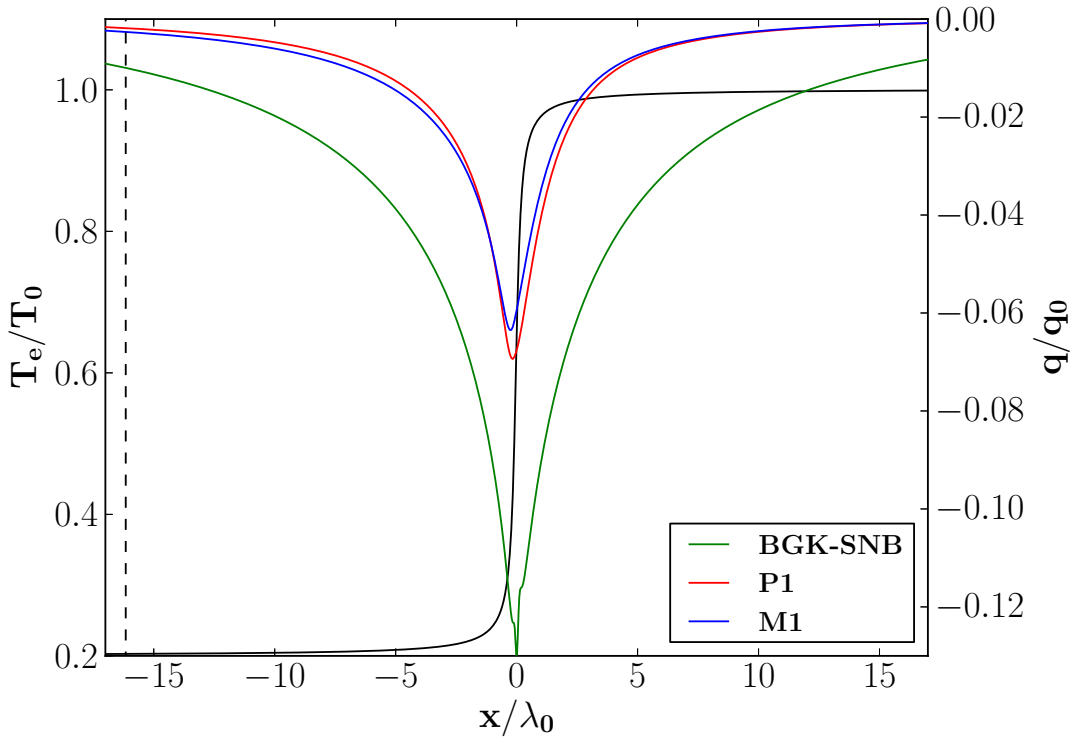

Figure 7.2: Heat fluxes for different models. The dashed line represents the place where the EDF is shown in panel 7.8.

the models mainly agree in the prediction of preheating in the front of the temperature gradient. In the hot region, nonlocal effects are not previewed. In fact, in this region, the M1 model predictions agree better with the local predictions, provided by the SH theory. Nevertheless, the BGK-SNB and the AWBS-SNB models predict an increase of the heat flux because they treat suprathermal electrons as a diffusion.

The flux limitation could be roughly described by the FL model. In order to recover results, we fixed the flux limiter to the 20% of the FS flux. However, this model does not describe the preheat and the heat flux maximum is shifted to the high temperature zone. Moreover, the appropriate choice of the value of flux limiter depends on the temperature profile.

All considered nonlocal models agree in the description of the kinetic heat flux. After the EDF integration over velocity, no differences can be seen between P1 and M1 models, so we show only the latter.

The differences between the M1 and the P1 models increase as the degree of anisotropy increases. In Fig. 7.2 we plot a case similar to the previous one but with a stronger temperature gradient. The temperature is described by Eq. (7.1), and differs from the above for one parameter only: $\delta_{NL} = 0.5\,\mu$m. This corresponds to a nonlocal parameter $\lambda_0/L_T \approx 3$. Nevertheless, even in this extreme case the models M1 and P1 are close. On the contrary, they differ a lot from the BGK-SNB model. We stress that the latter is based on the assumption of a small departure from locality, while this case is strongly nonlocal. Moreover, the BGK-SNB model predicts a small unphysical modulation of the flux near $x = 0$. It is due to the modeling of the electric field, which is discussed below.

Electric field

Local and nonlocal electric fields related to the plasma parameters discussed above (for $\delta_{NL} = 5\,\mu$m) are compared in Fig. 7.3.

All the models analyzed are based on the zero-current assumption. Thus, a flux of

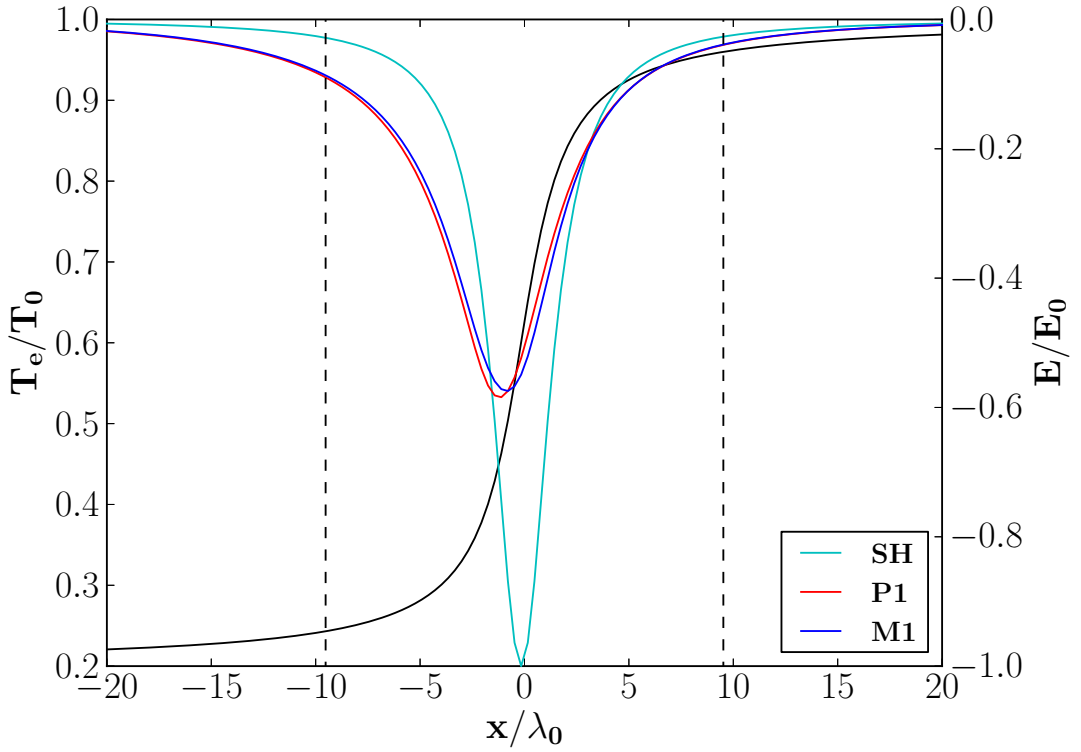

Figure 7.3: Local electric field spatial distribution compared with the nonlocal one. The first is computed using the SH theory and is used in the SH model and in the diffusive ones (BGK-SNB, AWBS-SNB). The latter is computed using the P1 and the M1 models.

electrons which carry the heat is coupled to an opposite flux of return current electrons. The latter is characterized by a larger number of electrons, with lower velocities. The electric field is related to these electrons.

As in the SH theory, the AWBS-SNB and the BGK-SNB models are based on the SH (local) electric field. This corresponds to the assumption that the electric field remains local, even if the heat flux is nonlocal. In weakly nonlocal regimes this is true because the return current electrons are less subjected to nonlocal effects, being slower than the electrons which transport the heat.

The curves M1 and P1 in Fig. 7.3 correspond to the nonlocal electric field (5.3), computed by iterating the system (5.1) till the field convergence. We stress that these models differ by the choice of the closure relation: Eq. (5.12), for M1, and Eq. (3.5), for P1. The results are obtained assuming the SH electric field, as a first guess.

Figure 7.3 shows that the difference between local and nonlocal electric fields is smaller than the difference between local and nonlocal heat fluxes. This difference weakly affects the heat flux.

The system is sufficiently close to the isotropic state that the differences between P1 and M1 models are negligible for electric fields, as for all macroscopic quantities.

In section 5.1.2 we have shown that there is another way of modeling the nonlocal electric field, more phenomenological but functional in case of strong density gradients or magnetic fields. Electron heat fluxes, computed with the local-kinetic electric field (5.4) are also obtained by iterating the M1 system (5.1), as explained above. They are compared in Fig. 7.4a with the M1 fluxes computed with the nonlocal electric field (5.3), previously used. The respective fields are shown in Fig. 7.4b.

The local-kinetic electric field is based on the assumption of being near-local. Thus, it presents a hybrid behavior, between the SH and nonlocal predictions: the field is stronger in modulus. The stronger is the electric field, the weaker is the heat flux, as shown in

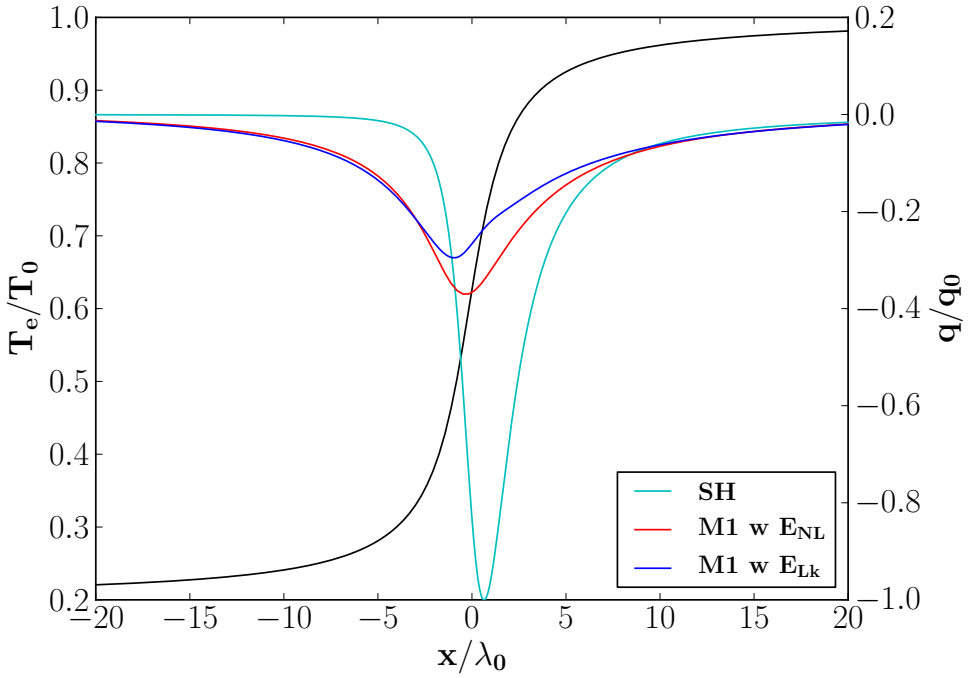

(a) Electric field modeling effect on the electron heat flux. The model M1 computes the electric field with Eqs. (5.3) (in red) and (5.4) (in blue). The SH model is shown in celestial, for comparison.

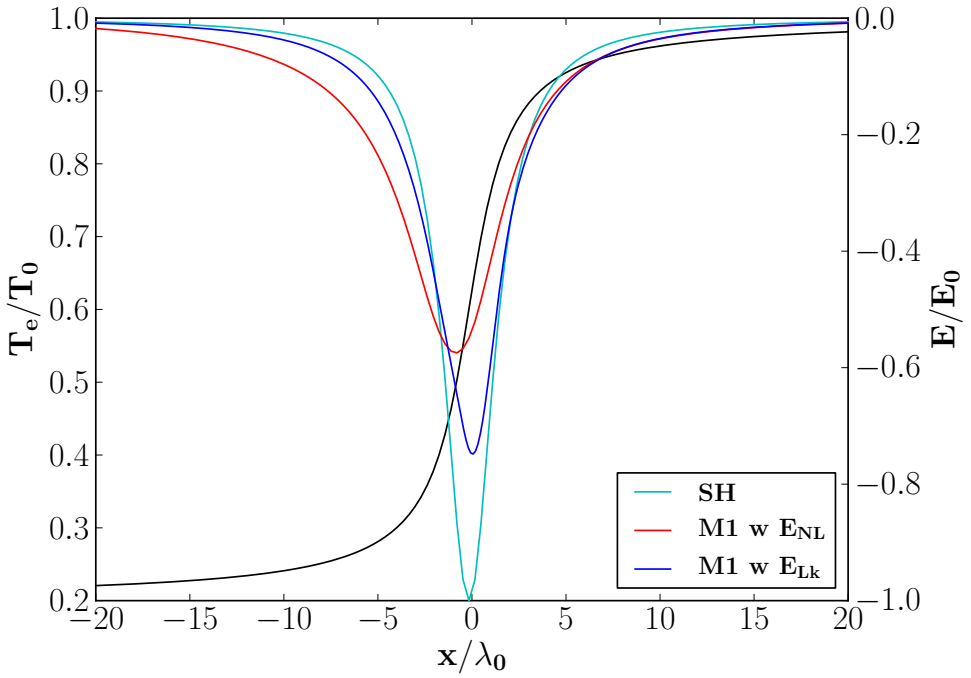

(b) Comparison of the electric fields (5.3) (in red) and (5.4) (in blue) with the SH (local) theory (in celestial)

Figure 7.4: Comparison of M1 predictions, using a different modeling for the electric field: the nonlocal formulation E_{NL}, given by Eq. (5.3), and the local-kinetic formulation the kinetic formulation E_{Lk}, given by Eq. (5.4).

Fig. 7.4a. Nevertheless, this figure shows also that the difference between these fluxes is of the same order of the differences between the other nonlocal models.

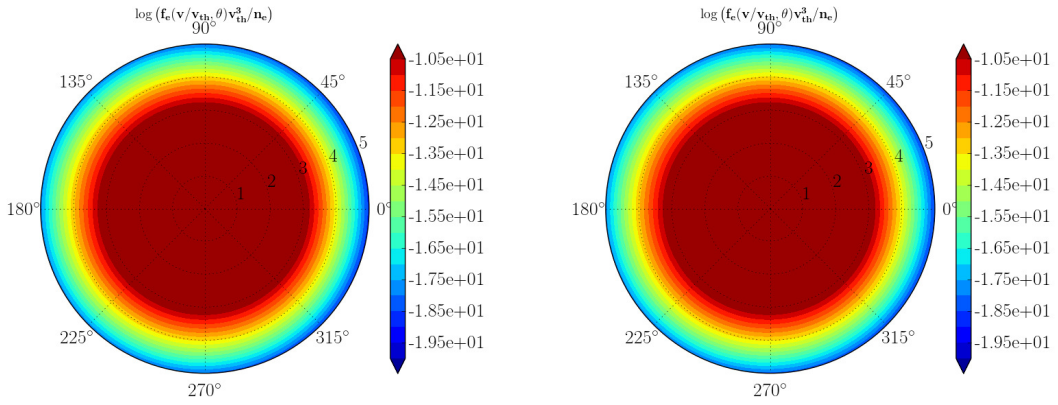

(a) P1 total EDF in the hot (right) region of plasma.

(b) M1 total EDF in the hot region of plasma.

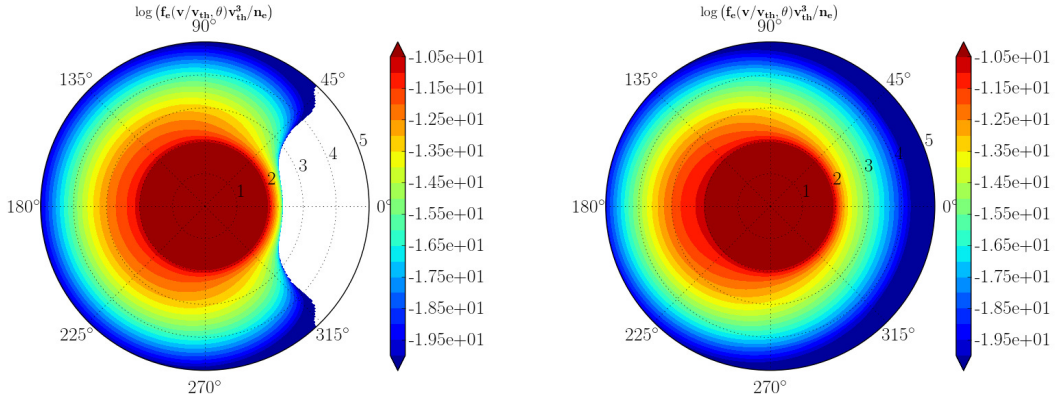

(c) P1 total EDF in the cold (left) region of plasma.

(d) M1 total EDF in the cold region of plasma.

Figure 7.5: Analysis of the EDF and its moments in the velocity space. Velocities are shown in the radial direction in polar plots. They are normalized on the thermal velocity in the hot region v_{th}. The out-of-bord values are uniformly painted with the bord colors.

Kinetic analysis

We proceed to a kinetic analysis of the system. We extract the EDF in the cold and hot regions of plasma, specified by black dashed vertical lines in Figs. 7.1 and 7.3.

Figure 7.5 shows the logarithm of the normalized total EDF for M1 and P1 in the cold and in the hot plasma regions. EDFs are shown as a polar color plot, in function of both the velocity modulus and direction. The first varies in the radial direction and is normalized on the hot region thermal velocity $v_{th} = \sqrt{T_0/m_e}$. The velocity direction varies in the polar direction (angles).

Suprathermal electrons ($\sim 3.7 v_{th}$), from the hot region, travel toward the cold region of the plasma, for a distance $\sim 187\lambda_0$. There, they deposit their energy.

In the hot region, the EDFs are expected to be almost isotropic because only a small fraction of electrons is moved away. The isotropy, in polar plots, is represented by concentric circles. This is what is predicted by both P1 and M1 models, respectively in Figs. 7.5a and 7.5b. Since these two models agrees in the isotropic description, no differences can be seen.

The suprathermal electrons coming from the hot region are more energetic than the thermal electrons in the cold region. They strongly affect the cold EDF, inducing its anisotropy. The latter is differently treated by P1 and M1 models, shown respectively in Figs. 7.5c and 7.5d. The P1 model assumes it as a linear correction. Nevertheless, for some velocities, it can be dominant, leading to negative EDFs (shown with a white zone

in the color plot). In particular we see that suprathermal electrons ($\gtrsim 2v_{th}$), moving from the right to the left ($\theta = 180°$), force the EDF to become negative for electrons moving in the opposite direction ($\theta = 0°$). On the contrary, the M1 model describes the anisotropy with an exponential dependence, which leads to a positively defined EDF, for all angles and velocities.

In order to better analyze the different EDF descriptions, in Fig. 7.6 we present the anisotropic part of EDF normalized to f_0: $(f_e - f_0)/f_0 = \Delta f_e/f_0$. In order to describe the heat flux, the P1 model adds a symmetric unphysical anisotropy in the opposite direction ($70° < \theta < 250°$). On the contrary, the M1 model is able to break this symmetry.

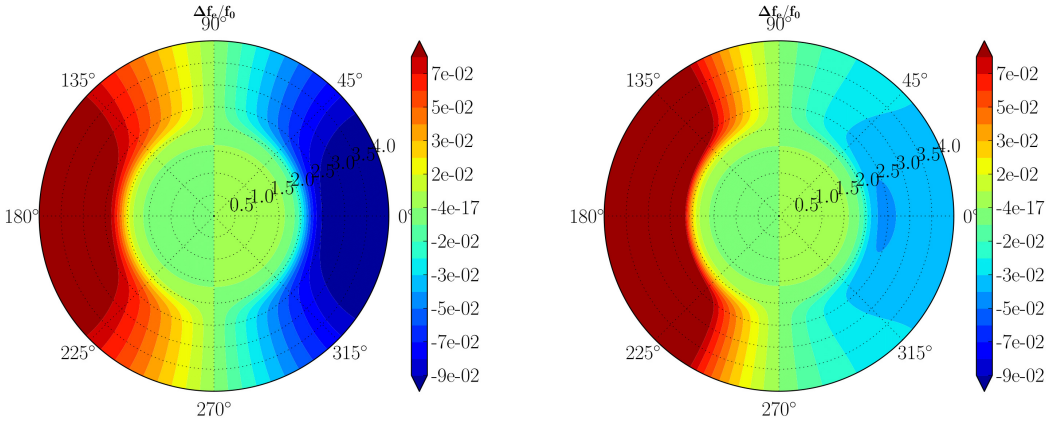

(a) P1 description. (b) M1 description.

Figure 7.6: Anisotropic part of the EDF (defined as $\Delta f_e/f_0 = f_e/f_0 - 1$) in the cold region of plasma (shown in Fig. 7.1), as a function of the velocity, normalized by the thermal velocity in the hot region.

Even if big differences appears at the kinetic scale, they become negligible after moment integration, as shown above, in the analysis of macroscopic quantities.

Another important information follows from the analysis of the heat flux integrand function $\sim f_1 v^5$. It is shown in Fig. 7.7a, for the hot region, and in Fig. 7.7b, for the cold region, previously analyzed. It is normalized to $v_{th}^2 n_e$.

The figures show the contribution to the heat flux carried by the suprathermal electrons with velocities $\sim 3v_{th}$. In contrast, the return current flux induced by the zero-current condition is carried by the electrons with smaller velocities. Figure 7.7a confirms that P1 and M1 models agree in the hot region, since the heat flux induced anisotropy is small. On the contrary, in the cold region, shown in Fig. 7.7b, some differences appear. Only the main heat flux is affected by these differences, while they are negligible for the return current. Note also that the heat flux maximum contribution in the cold region is displaced because of nonlocal effects: gradients are sharper, so a smaller MFPs (slower electrons) contribute to the energy transport in the cold region.

The same analysis is performed for the more anisotropic system, shown in Fig. 7.2. Figure 7.8 represents the heat flux integral function computed in the cold region denoted by a dashed vertical line in Fig. 7.2. Differences between M1 and P1 become stronger at high velocities, but, even for such an anisotropy, the return current is unaffected.

In summary, the M1 model succeeds in reproducing the nonlocal features: the natural flux limitation, the preheat in front of the temperature gradient and it shows a good agreement with the SNB model. Besides that, the M1 closure relation, compared to the P1 one, does not modify the flux calculation, but at a kinetic level it affects some parts of the EDF.

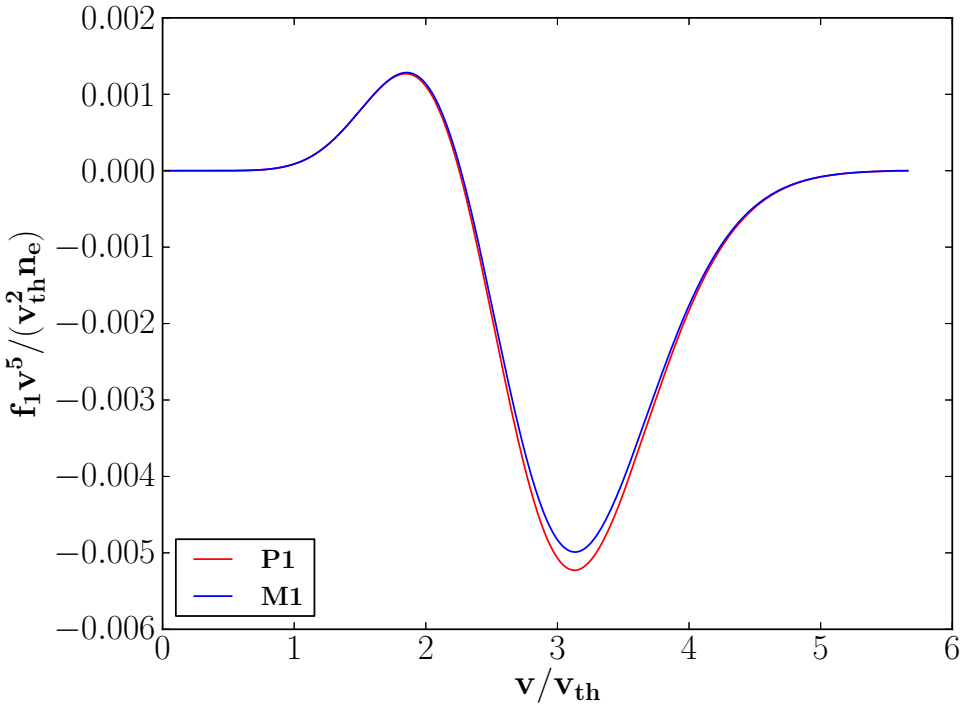

(a) Hot region of plasma.

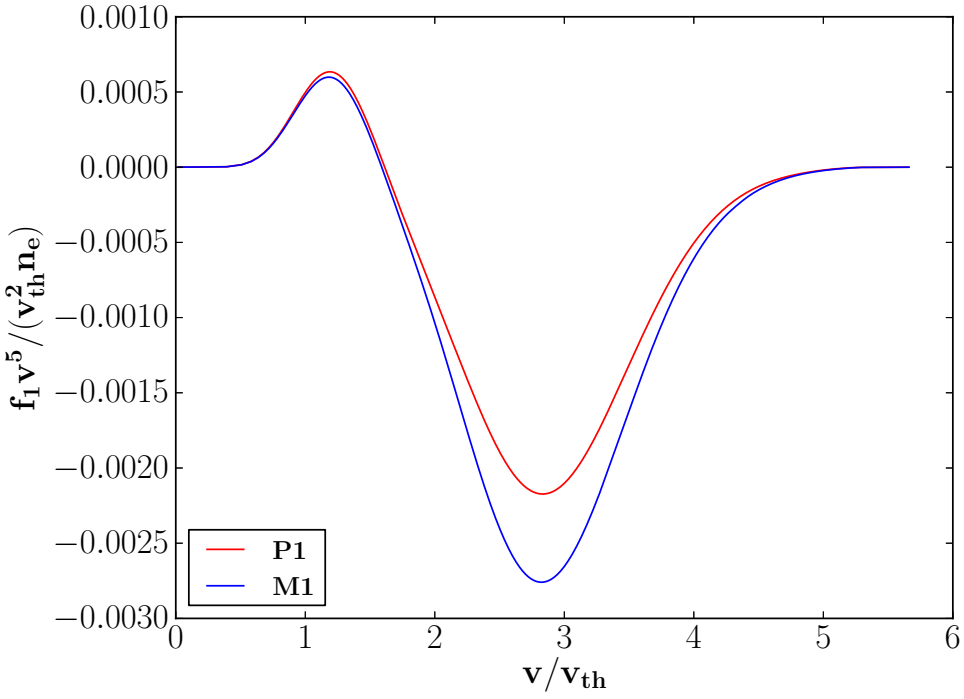

(b) Cold region of plasma.

Figure 7.7: Comparison of the M1 and P1 models for the heat flux integrand function in the hot and cold regions of plasma.

7.1.2 Temperature modulation

In this section we compare models in a wider range of nonlocal regimes, testing the heat flux limitation, in comparison with the results obtained with a FP code.

We consider the Epperlein-Short (ES) test [44]. It consists in the study of the flux limitation effect in the electron heat transport, for a plasma with a static temperature

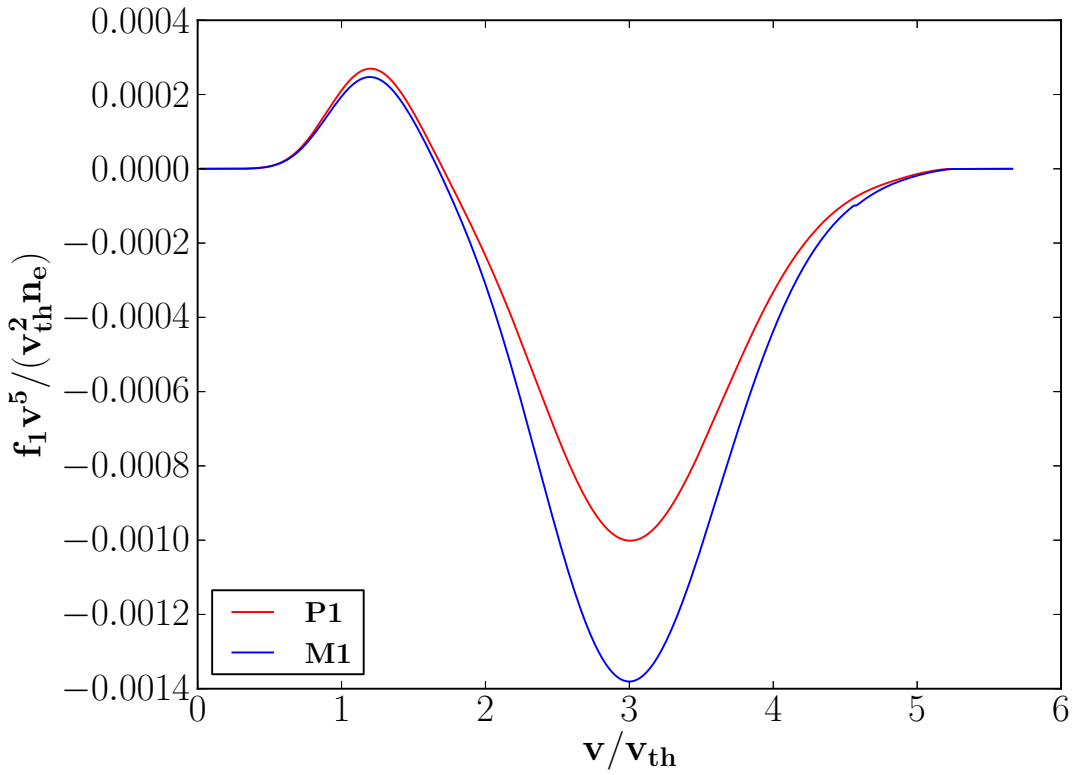

Figure 7.8: Integrand function of the heat flux, as a function of velocity for the two advective models.

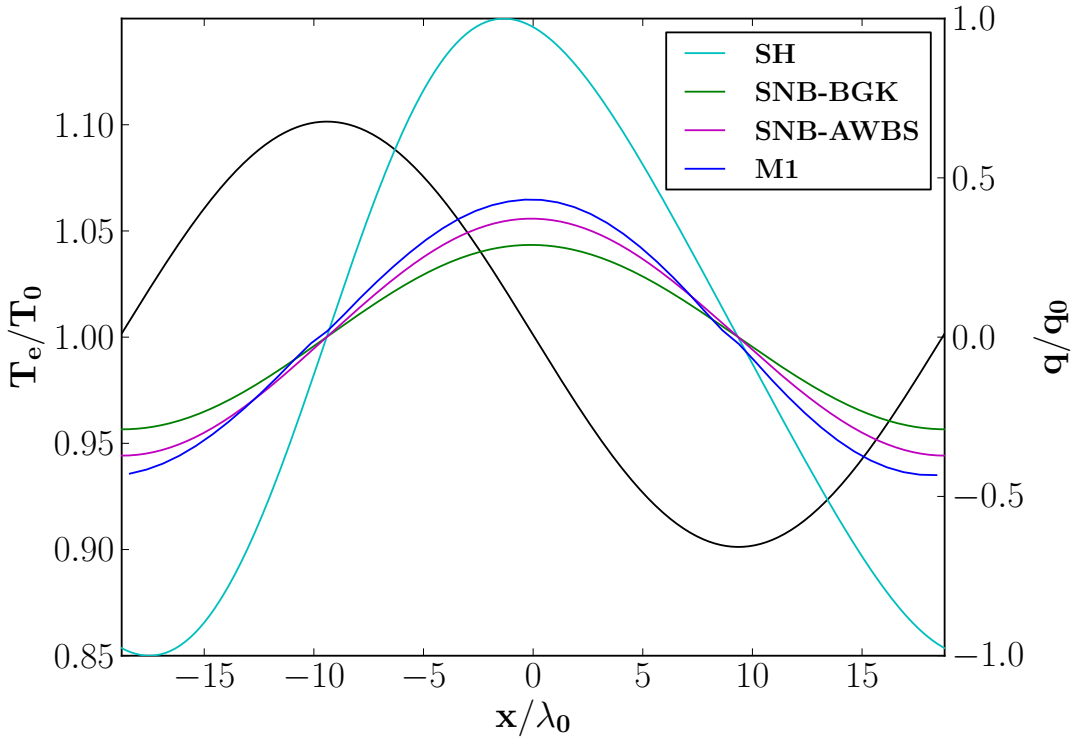

Figure 7.9: Study of the heat flux for a modulated temperature, with $k\lambda_0 = 0.17$, using the SH (local) model, the SNB models and the M1 one. P1 results are not shown because very similar to M1, black line shows the temperature modulation. Periodic boundary conditions are applied.

modulation

$$T_e(x) = T_0 + T_1 \sin(kx) \tag{7.2}$$

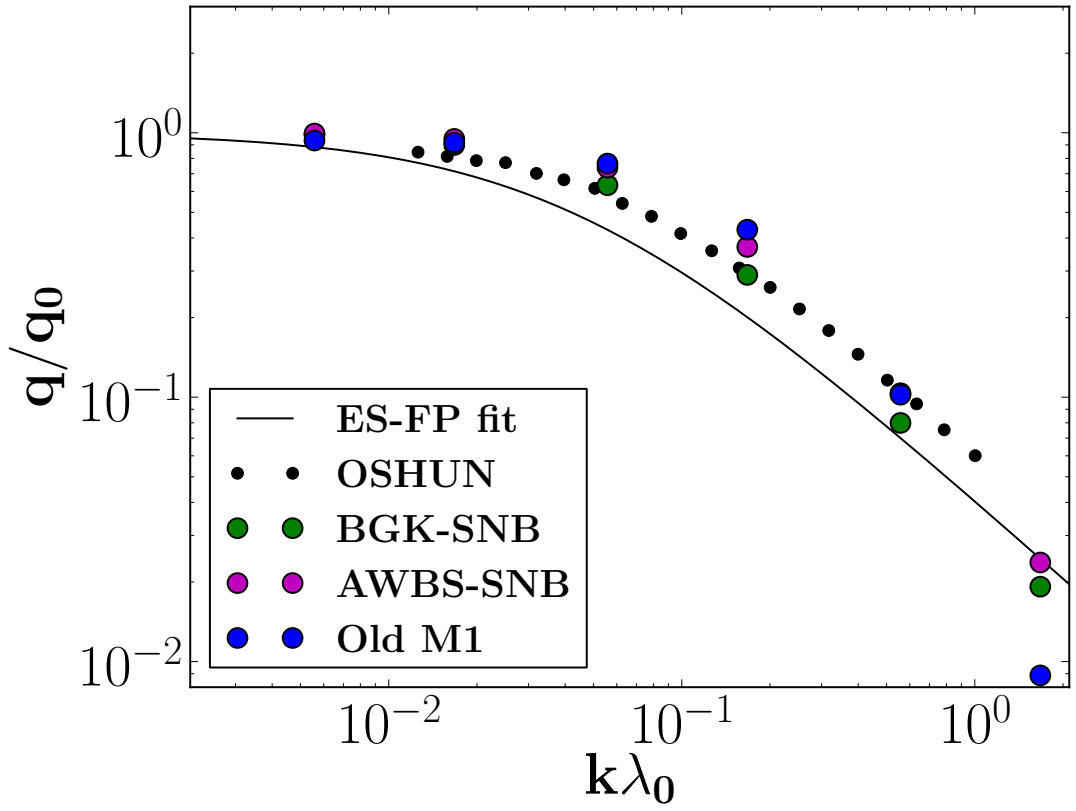

Figure 7.10: Heat flux limitation in the ES test. Solid line presents the Vlasov-FP fit, for a sinusoidal modulation of temperature. The results are given in function of the wavenumber normalized by the MFP.

where k is the wavenumber, $T_0 = 1\,\mathrm{keV}$ and $T_1 = 0.1\,\mathrm{keV}$. The plasma is a fully ionized beryllium of a constant density $4.5 \times 10^{22}\,\mathrm{cm}^{-3}$. As in the previous section, the heat flux is normalized on the SH maximum flux $q_0 = 1\ \mathrm{PW/cm^2}$ and the space on the MFP $\lambda_0 = 3\sqrt{\frac{\pi}{2}}\frac{T_0^2}{4\pi n_e Z e^4 \Lambda_{ei}} \approx 0.17\,\mu\mathrm{m}$. This is different from the original paper normalization $\lambda_{ES} = T_0^2/(4\pi n_e e^4 \sqrt{Z+1}\Lambda_{ei}) \approx 0.08\ \mu\mathrm{m}$ [44]. Figure 7.9 shows the heat flux in such a plasma in the case $k\lambda_0 \approx 0.17$. In this test P1 and M1 models give the same results, also for EDFs.

Figure 7.10 shows the complete results of the ES test. The analytical fit obtained from FP simulations is plotted as a function of the nonlocal parameter $k\lambda_0$, in different regimes: $q_{FP}/q_0 = 1/(1+50k\lambda_{ES})$. To this fit, we added recent discrete results performed by Marocchino et al. [25] using the FP code OSHUN [57]: the difference is non negligible.

It should be noted that the parameter $k\lambda_0$ is related to the nonlocal parameter λ_0/L_T by a factor $T_1/T_0 = 0.1$. Thus the case shown in Fig. 7.9 corresponds to the nonlinear parameter 0.017 quite similar to the case shown in Fig. 7.1. One can see that the flux limitation by a factor of ~ 2 is similar in Figs. 7.1 and 7.9, confirming the compatibility of both tests.

In general, the M1 model, as well as the AWBS-SNB and BGK-SNB models, agrees with the FP results. Nevertheless, models based on the AWBS collision operator slightly overestimate the nonlocal heat flux, compared to FP results, till $k\lambda_0 \approx 1.7$. For this value, the M1 model disagrees with the FP results. The reason is explained in what follows.

A monodimensional periodically modulated plasma temperature corresponds to two opposite directions of anisotropy and, thus, by heat fluxes which propagate in opposite directions. Let us assume that these fluxes are carried by the electrons with the characteristic velocity $v_{\max}$. Their MFP is $m_e^2 v_{\max}^4/(4\pi\sqrt{Z+1}n_e E^4 \Lambda_{ei}) = \lambda_{ES} v_{\max}^4/v_{th}^4$, while

the distance between two opposite gradients of the temperature is π/k. If the MFP of these electrons exceeds the distance between two peaks of the flux, they superpose. This condition reads

$$k\lambda_{ES} > \pi \frac{v_{th}^4}{v_{\max}^4}$$

or, using our normalization,

$$k\lambda_0 \gtrsim 6.5 \frac{v_{th}^4}{v_{\max}^4}. \tag{7.3}$$

As shown in Fig. 3.1, $v_{\max} \approx 3.7 v_{th}$ in the local limit. Nevertheless, in the nonlocal case, $v_{\max}$ decreases. In fact, the heat flux $\vec{q} = \int_{\mathbf{R}} d^3v f_e \epsilon \vec{v}$ is given by the balance between the density of electrons $d^3v f_e$ in the differential volume d^3v and their energy transported $\epsilon\vec{v}$. If the gradients becomes sharper, more electrons with a lower MFP (lower velocities) are present in the front of the gradient. Their contribution displaces $v_{\max}$.

In [58], a systematic study of $v_{\max}$ has been performed, as function of $k\lambda_{ES}$ ($k\lambda_0$): for $k\lambda_{ES} \approx 0.01$ ($k\lambda_0 \approx 0.02$), $v_{\max} \approx 3.5 v_{th}$, for $k\lambda_{ES} \approx 0.05$ ($k\lambda_0 \approx 0.11$), $v_{\max} \approx 3.2 v_{th}$, and for $k\lambda_{ES} \approx 0.2$ ($k\lambda_0 \approx 0.42$), $v_{\max} \approx 2.6 v_{th}$. According to Eq. (7.3), the fluxes start to superpose for $k\lambda_0 \approx 0.11$.

M1 and P1 models calculate fluxes assuming the dependence on the first two angular moments only. Let us consider the case of two equal fluxes which propagate in the opposite directions. The M1 EDF describing these fluxes is the sum of the two M1 EDFs

$$f_e(\vec{v}) \propto e^{\alpha_0 + \vec{\Omega}\cdot\vec{\alpha}_1} + e^{\alpha_0 - \vec{\Omega}\cdot\vec{\alpha}_1} \propto e^{\alpha_0} \sinh\left(\vec{\Omega}\cdot\vec{\alpha}_1\right),$$

which gives the first angular moment equal to zero for reasons of parity. So, in this case, the heat flux carried by such electrons is set to zero. This result is also valid for the P1 model, since it is a linear development of the exponential, around $\vec{\alpha}_1$. Hence M1 and P1 models are able to describe only one main direction of anisotropy. The case of two superposed opposite fluxes is out of the domain of validity of the first moment models, giving a zero flux. This phenomenon is observed for $k\lambda_0 > 0.7$. However, when this happens, the heat flux is already reduced by a factor greater than 50. Moreover, this limit, related to first moment models can be overcame by second moment models, such as M2 or P2.

The ES test is also shown in Fig. 7.11, which compares the different descriptions of electric fields in the M1 model, in a wide range of the domains of nonlocal transport. These fields are described in section 5.1.2. A particular case, for $k\lambda_0 = 0.17$, is shown in Fig. 7.11a, while the ES test is shown in Fig. 7.11. In general, the test shows no quantitative difference between the two electric field formulations, till $k\lambda_0 \approx 0.63$, where the field modeling effects become important. The flux limitation, using the local-kinetic electric field (5.4), is plotted in blue and shows to underestimate the flux, compared to the flux limitation using the nonlocal formulation (5.3), in red. This is expected, since the local-kinetic electric field overestimates nonlocal electric field predictions, being closer to local assumptions.

7.1.3 Flux rotation and counterstreaming

The M1 model provides also a good estimate for nonlocal fluxes in the two-dimensional geometry. Figure 7.12 shows with a color bar the temperature profile of a fully-ionized Beryllium plasma at a constant density of 4.5×10^{22} cm^{-3}. The analytic form of the temperature is

$$T_e(x,y) = T_e(x) e^{-(y/y_{max})^4} \left[\theta(x) \left(\frac{x_{\max}}{2x}\right)^{1/p(y)} + \theta(-x)\right], \tag{7.4}$$

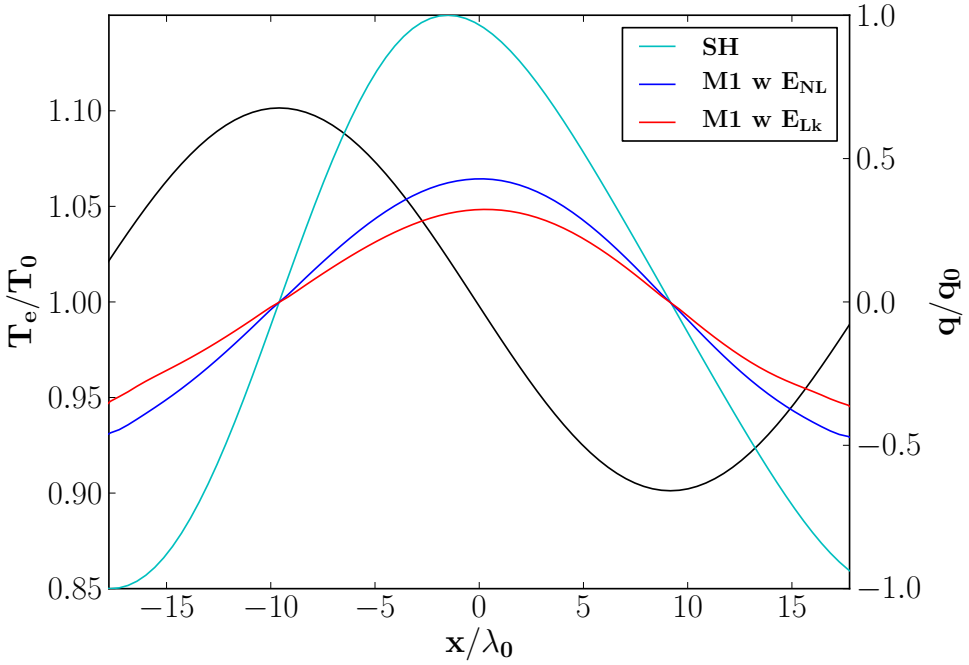

(a) Comparison of the two M1 and the SH heat fluxes, for $k\lambda_0 = 0.17$.

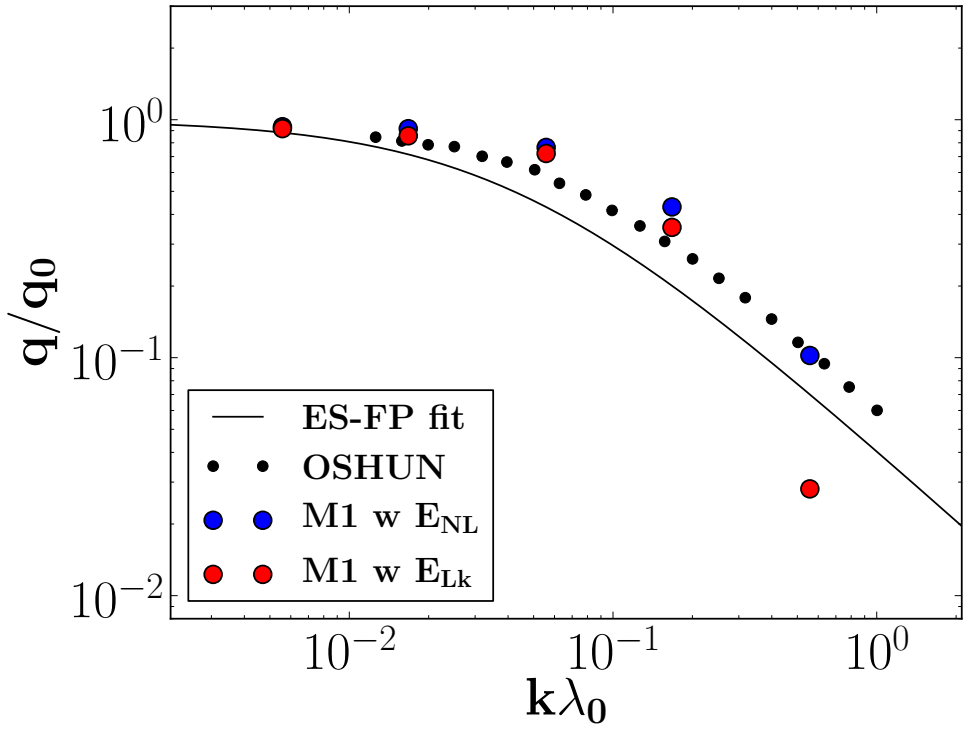

(b) ES test.

Figure 7.11: Comparison of M1 predictions for the ES test, using a different modeling for the electric field: the nonlocal formulation E_{NL} (blue), given by Eq. (5.3), and the local-kinetic formulation the kinetic formulation E_{Lk} (red), given by Eq. (5.4).

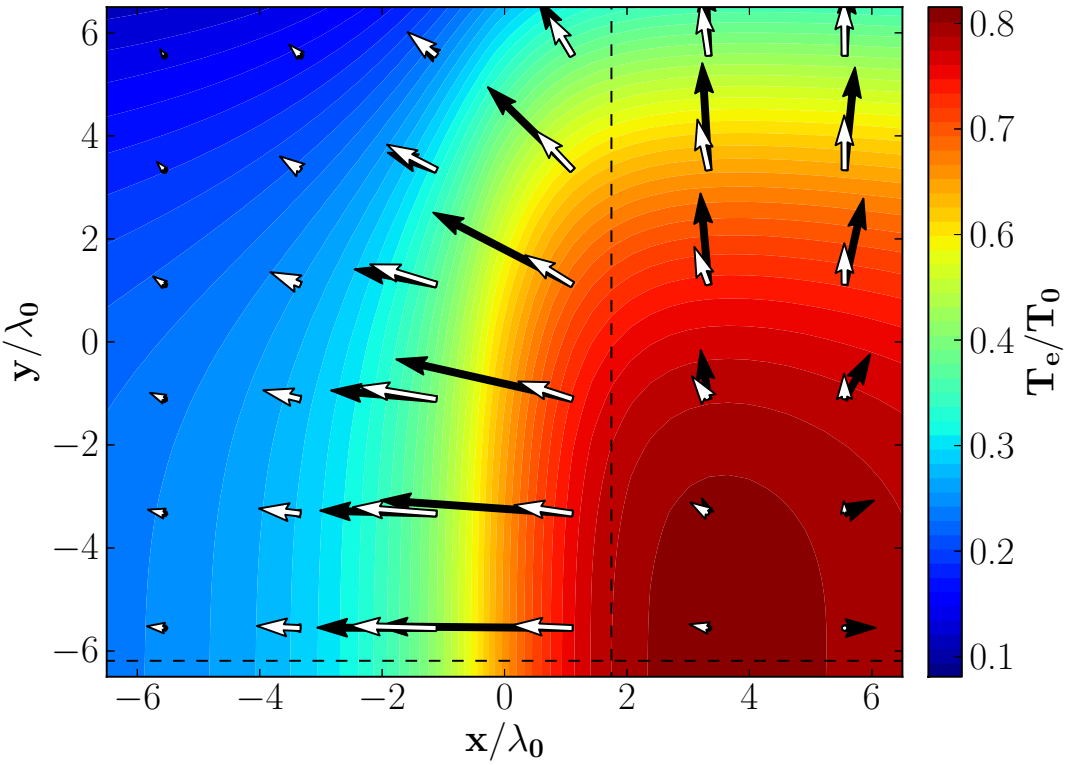

Figure 7.12: Two dimensional analysis of the heat transport. The color background traces the temperature. Arrows describe the magnitude and direction of heat fluxes. The SH model, in black, is compared with M1, in white. Dashed black lines denote the sections shown in Fig. 7.13.

where $T_e(x)$ is given by Eq. (7.1), $p(y) = 3\exp[y^2/(Lx_{\max})]$, $L = 200$ μm, $x_{max} = y_{max} = 50$ μm are the length of the target along the x and y axes and $\theta(x)$ is the Heaviside function.

We present here the results obtained with the M1 model. The P1 and SNB models provide very similar results.

In Fig. 7.12, white arrows indicate the SH (local) heat fluxes, while the black arrows indicate the M1 fluxes. In the local case, fluxes are always in the direction of the temperature gradient and their modulus increase as the gradient becomes sharper. In the nonlocal case, the fluxes are delocalized in the space. So we see the typical mono-dimensional nonlocal effects: the flux limitation close to the main temperature gradients and preheating in the front of them. Moreover, a two-dimensional nonlocal effect appears: the horizontal fluxes (due to sharper gradients) influences the vertical ones, inducing their rotation with respect to the temperature gradient.

Cuts along the horizontal and vertical axes, denoted by dashed lines in Fig. 7.4, are drawn in order to detail nonlocal effects. Fluxes are normalized on the SH maximum flux $q_0 \approx 40$ PW/cm^2.

In Fig. 7.13a, the horizontal cut shows that the temperature is characterized by two opposite gradients. In accordance with these gradients, the SH theory predicts a main flux in the direction of the main gradient and a secondary flux in the direction of the opposite and smoother gradient. On the contrary, M1 model predicts a counterstreaming flux: nonlocal effects at the main gradient influence the opposite one, leading to a unidirectional flux, in the direction opposite to the main gradient. Thus, in correspondence of the smooth gradient, the M1 model (as the other nonlocal models) predicts an anti-natural flux in the direction of the temperature gradient.

Figure 7.13b presents the vertical cut. Two M1 fluxes are plotted: one representing

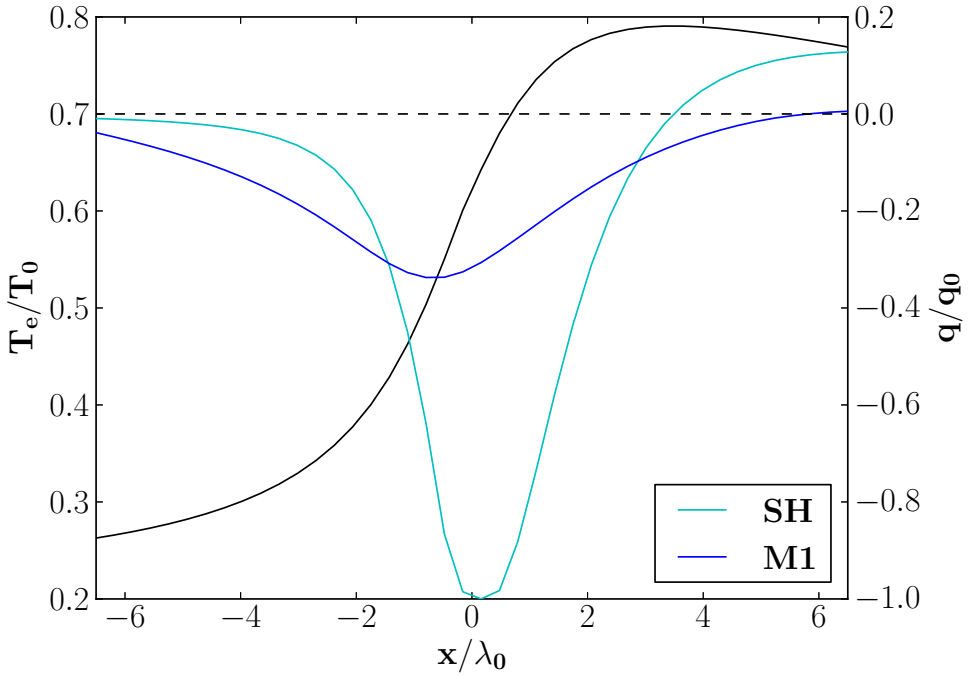

(a) Horizontal cut. The dashed horizontal line indicates the zero flux.

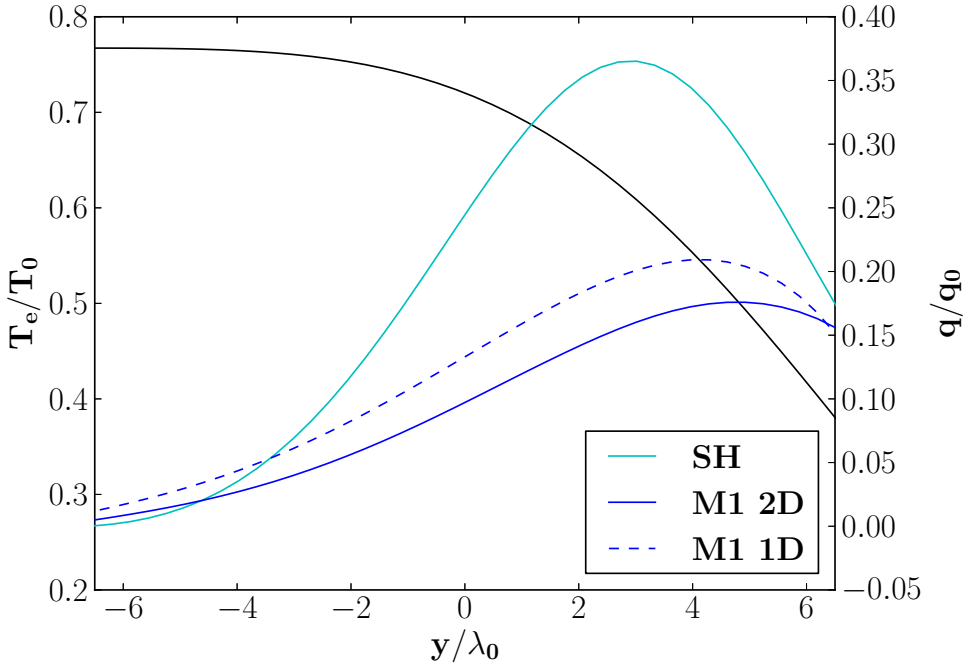

(b) Vertical cut. The dashed blue line describes a monodimensional simulation using the same vertical gradient.

Figure 7.13: Cuts of the fluxes of Fig. 7.12.

the vertical cut of Fig. 7.4 (M1 2D) and the second computed by mono-dimensional simulation, with the same gradient (M1 1D). The SH flux follows the temperature gradient line, while the nonlocal effect (M1 2D) corresponds to the flux limitation. Nevertheless, nonlocal fluxes are also subjected to a rotation, due to the opposite gradient. The latter leads to the differences between M1 2D and M1 1D.

In summary, the M1 model is also able to reproduce the main multidimensional non-local feature: the flux rotation due to a competition between the different temperature gradients.

7.2 Stream instabilities

In the previous chapter we have shown that the M1 model is able to describe complete EDFs, contrarily to the P1 model, which may lead to negative (unphysical) values. Besides heat transport, this property allows the kinetic description of a wide range of collective phenomena. Here, we focus on the study of the Landau damping [18] of longitudinal plasma waves: the Langmuir and the ion-acoustic waves [59, 60], in the nonlocal case of a steep temperature gradient considered in section 7.1.1.

7.2.1 Langmuir wave Landau damping

Langmuir waves have already been introduced in section 2.2.4. They are high-frequency electron oscillations corresponding to electric field and electron density perturbations on a microscopic scale. A modification of the EDF in the heat transport zone may strongly affect the stability of Langmuir waves, especially downstream the temperature jump. Since this phenomenon is not related to collisions, in a first step we neglect them, for the sake of simplicity.

A dispersion equation for the longitudinal waves corresponds to zeros of the longitudinal dielectric permittivity $\epsilon^l(\omega, k) = 0$. Because of their inertia, ions do not play a role in Langmuir waves and, as shown in Eq. (2.26), the dielectric permittivity reads [19, 18]

$$\epsilon^l(\omega, k) = 1 + \delta\epsilon_e^l = 1 + \frac{4\pi e^2}{k^2 m_e} \int_{\mathbb{R}^3} \frac{d^3v}{\omega - \vec{k}\cdot\vec{v}} \vec{k} \cdot \frac{\partial}{\partial \vec{v}} f_e(\vec{v}). \tag{7.5}$$

The temporal evolution of the wave amplitude depends on the imaginary part of the dielectric permittivity. Depending on its sign, it leads to a wave damping or growth. In the linear damping theory, the imaginary term is assumed to be small, compared to the real one. Defining the damping rate as $\gamma = -\Im(\omega)$, we have $\omega = \Re(\omega) - i\gamma$ where, according to Eq. (2.28), the damping rate reads

$$\gamma = \frac{\Im(\epsilon^l)}{\frac{\partial}{\partial\omega}\Re(\epsilon^l)}. \tag{7.6}$$

According to the general approach [19, 18], the dielectric permittivity is calculated by separating the denominator in Eq. (7.5) in the principal value and the pole:

$$\frac{1}{\omega - \vec{k}\cdot\vec{v}} = \frac{P}{\omega - \vec{k}\cdot\vec{v}} - i\pi\delta(\omega - \vec{k}\cdot\vec{v})$$

where P stands for principal value.

In the Cartesian coordinate system, the damping rate goes like

$$\gamma \propto -\left[v_\parallel \frac{\partial F_\parallel(v_\parallel)}{\partial v_\parallel}\right]_{v_\parallel = \omega/k}, \tag{7.7}$$

where $F_\parallel(v_\parallel) = \int d^2v_\perp f_e$ and the symbols $\parallel$ and $\perp$ corresponding to the parallel and the perpendicular directions with respect to the wavevector $\vec{k}$. Figure 7.14 shows the typical case where Langmuir wave instabilities develop. A positive gradient is induced by a population of hot electrons, which are transported to the cold region of plasma from the hot one. As our models are based on a spherical coordinate description of EDF, expressions for the damping rate are more complicated. The integrals in Eq. (7.5) are calculated in the spherical coordinate system with the vector $\vec{k}$ parallel to the temperature

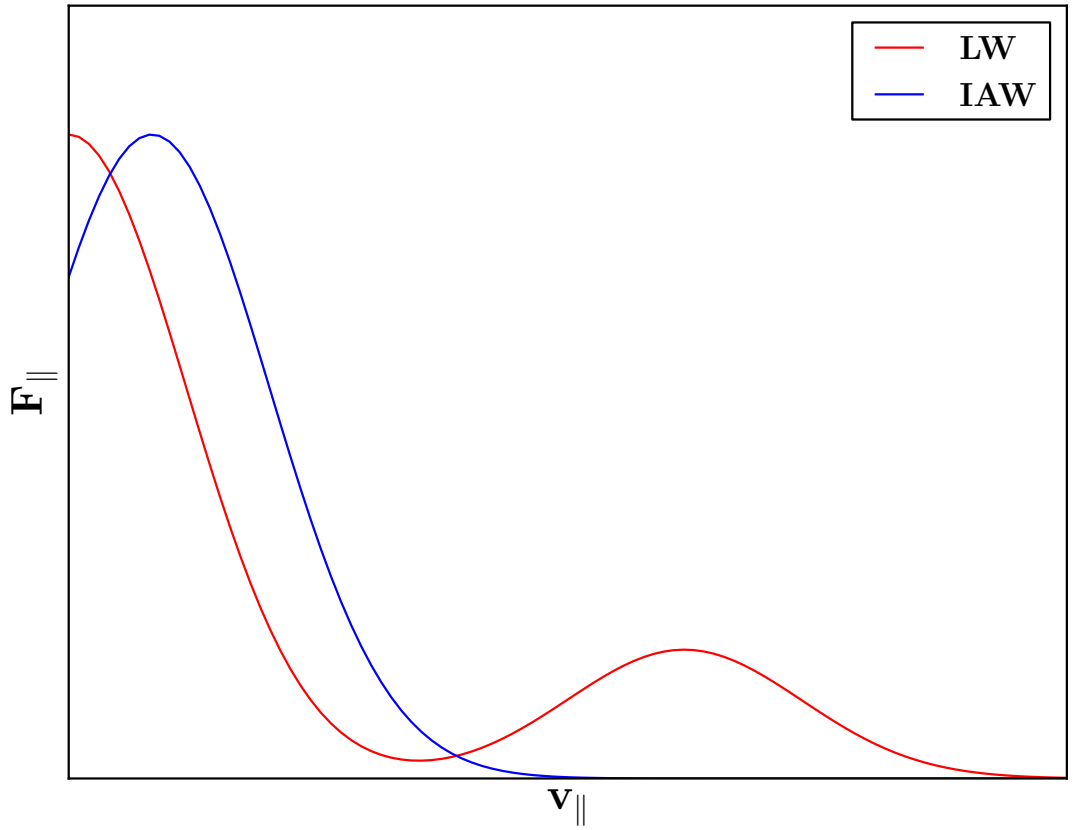

Figure 7.14: EDFs integrated over perpendicular velocity, as functions of the parallel velocity, in typical cases of instability development for Langmuir waves (LW) and for ion-acoustic waves (IAW).

gradient: $\vec{k}\cdot\vec{v} = kv\mu$. The M1 EDF is given by Eq. (5.11). Developing the denominator to the third order for the parameter $kv\mu/\omega \ll 1$, the real part of dielectric permittivity is

$$\Re(\delta\epsilon_e^l) = -\left(\frac{\omega_{pe}}{\omega}\right)^2 \frac{1}{n_e}\left\{\int_{\mathbb{R}^+} dv v^2 f_0 + 2\frac{k}{\omega}\int_{\mathbb{R}^+} dv v^3 f_0 I_1 + 3\left(\frac{k}{\omega}\right)^2 \int_{\mathbb{R}^+} dv v^4 f_0 I_2\right\}, \quad (7.8)$$

where $\omega_{pe} = \sqrt{4\pi e^2 n_e/m_e}$ is the electron plasma frequency and

$$\begin{cases} I_1 = \coth(\alpha_1) - \alpha_1^{-1} \\ I_2 = 1 - 2\alpha_1^{-1}\coth(\alpha_1) + 2\alpha_1^{-2} \end{cases}.$$

The imaginary part reads

$$\Im(\delta\epsilon_e^l) = \frac{\omega_{pe}^2\pi}{2n_e k^2}\left\{\frac{\omega}{k}\frac{f_0\left(\frac{\omega}{k}\right)\alpha_1\left(\frac{\omega}{k}\right)}{\sinh[\alpha_1\left(\frac{\omega}{k}\right)]}e^{\alpha_1\left(\frac{\omega}{k}\right)} - \int_{\frac{\omega}{k}}^{\infty} dv \frac{f_0\alpha_1^2}{\sinh(\alpha_1)}e^{\frac{\alpha_1\omega}{kv}}\right\},$$

so the damping rate is

$$\frac{\gamma}{\omega} = \left(\frac{\omega}{k}\right)^2 \frac{\pi}{4}\frac{\frac{\omega}{k}\frac{f_0\left(\frac{\omega}{k}\right)\alpha_1\left(\frac{\omega}{k}\right)}{\sinh[\alpha_1\left(\frac{\omega}{k}\right)]}e^{\alpha_1\left(\frac{\omega}{k}\right)} - \int_{\frac{\omega}{k}}^{\infty} dv \frac{f_0\alpha_1^2}{\sinh(\alpha_1)}e^{\frac{\alpha_1\omega}{kv}}}{\int_{\mathbb{R}^+} dv v^2 f_0 + 3\frac{k}{\omega}\int_{\mathbb{R}^+} dv v^3 f_0 I_1 + 6\left(\frac{k}{\omega}\right)^2 \int_{\mathbb{R}^+} dv v^4 f_0 I_2}. \quad (7.9)$$

The P1 damping rate is obtained from Eq. (7.9), in the linear limit for $\alpha_1 \approx 3f_1/f_0 \ll 1$:

$$\frac{\gamma}{\omega} = \left(\frac{\omega}{k}\right)^2 \frac{\pi}{4}\frac{\frac{\omega}{k}f_0\left(\frac{\omega}{k}\right) + 3\frac{\omega}{k}f_1\left(\frac{\omega}{k}\right) - 3\int_{\frac{\omega}{k}}^{\infty} dv f_1}{\int_{\mathbb{R}^+} dv v^2 f_0 + 3\frac{k}{\omega}\int_{\mathbb{R}^+} dv v^3 f_1 + 2\left(\frac{k}{\omega}\right)^2 \int_{\mathbb{R}^+} dv v^4 f_0}. \quad (7.10)$$

This relation can also be obtained by considering the EDF in Eq. (3.5).

The real part of the Langmuir wave frequency is not affected by the transport effects and it is given by the standard Bohm-Gross relation, $\Re(\omega) \approx \pm\omega_{pe}[1+(3/2)k^2\lambda_{De}^2]$. Here, $\lambda_{De} = v_{th}/\omega_{pe}$ is the local Debye length.

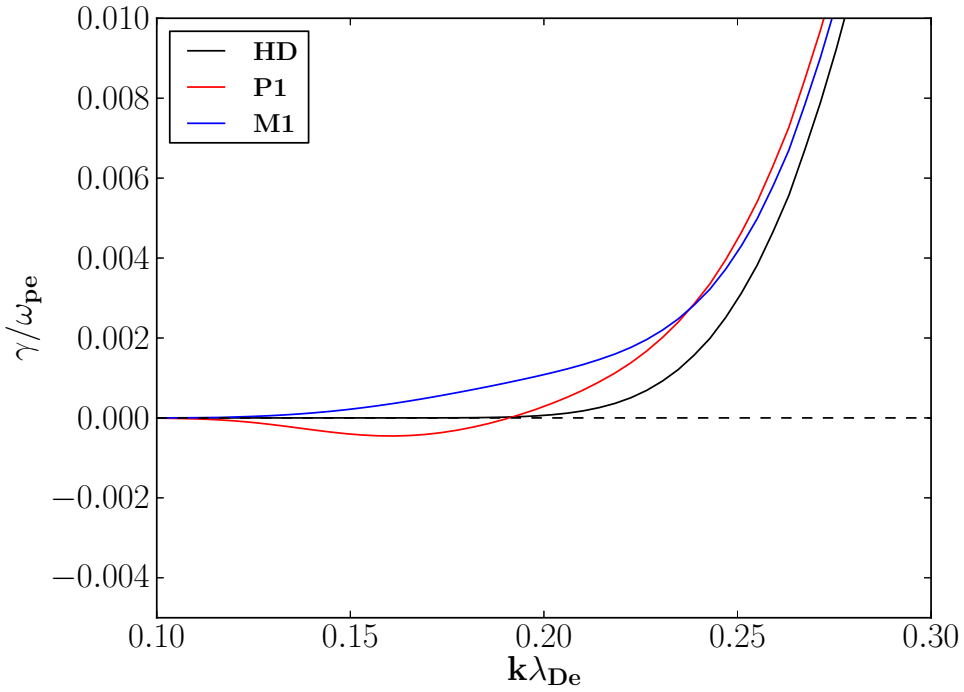

(a) Forward wave propagation.

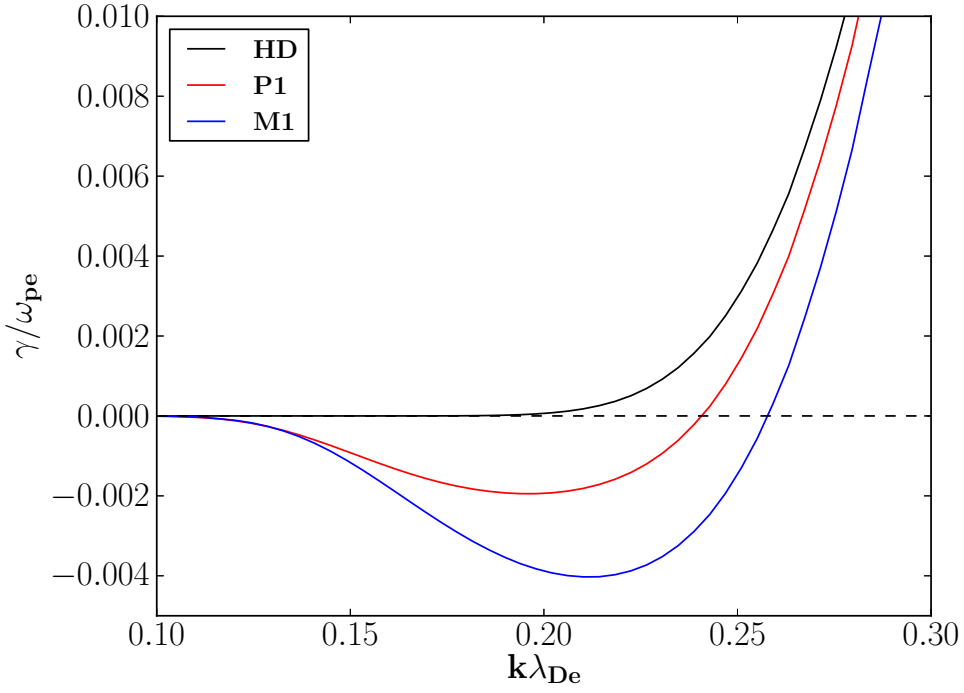

(b) Backward wave propagation.

Figure 7.15: Damping rate of Langmuir waves, normalized to the electron plasma frequency, as a function of the wavenumber normalized to the local Debye length, for the hydrodynamic theory (HD), and for M1 and P1.

We consider the heat transport along the temperature gradient for the cold EDFs shown in Fig. 7.5. The Langmuir wave damping rate is shown in Fig. 7.15 as a function of the wavenumber, for waves propagating forward and backward with respect to the

temperature gradient. The models shown are the hydrodynamic one (HD), P1 and M1. The damping rate for the HD model is given by Eq. (7.10), with $f_0 = f_0^m$ and $\vec{f_1} = 0$, which corresponds to the well-known Landau damping relation [18]

$$\frac{\gamma}{\omega_{pe}} = \sqrt{\frac{\pi}{8}} \frac{1}{k^3 \lambda_{De}^3} e^{-3/2 - 1/(k\lambda_{De})^2}.$$

Figure 7.15 shows that hot electrons disturb Langmuir waves, inducing instability in the direction of hot electron propagation (backward waves), for wavenumbers $k\lambda_{De} \approx 0.15 - 0.25$. The differences between the two nonlocal models are both quantitative and qualitative: damping rates are different but also may have different signs, depending on the wavenumber. Moreover, the P1 model produces a spurious instability in the forward direction because it transforms an unphysical behavior (negative total EDF) into an instability, as shown in Fig. 7.15a.

Collisions can be accounted for in the damping of Langmuir waves by adding an additional term in the imaginary part of the electron dielectric permittivity, $\Im(\delta\epsilon_e^l) = \omega_{pe}^2 \nu_{eff}/\omega^3$, where

$$\nu_{eff} = \frac{4\sqrt{2\pi}}{3} \frac{Z^2 e^4 n_i \Lambda_{ei}}{m_e^2 v_{th}^3}$$

is the effective collision frequency [19]. This term is the same for all models and corresponds to the collision term $-\nu_{eff}\delta f$ in the FP equation (2.19).

The results for the collisional Landau damping of Langmuir waves, for the downstream temperature zone in Fig. 7.5, are shown in Fig. 7.16. We see that the instability rate is reduced and the unphysical unstability for the forward propagating wave disappears. However, the difference between the models is evident: while the instability disappears for P1, it is still present for the M1 model. The expected growth rate $\gamma \sim 5 \times 10^{13}\,\mathrm{s}^{-1}$ corresponds to a time much shorter than the typical hydrodynamic time. Therefore one may expect that the Langmuir turbulence can be developed downstream the temperature gradient, possibly affecting the electron heat flux.

7.2.2 Ion-acoustic waves

Ion-acoustic waves have also been introduced in section 2.2.4. They are low-frequency waves ($\omega/k \ll v_{th}$) which involve electrons and ions. Similarly to the Langmuir waves, the spectrum of ion-acoustic waves is defined by zeros of the dispersion equation $\epsilon^l(\omega, k) = 0$, where $\epsilon^l = 1 + \delta\epsilon_e^l + \delta\epsilon_i^l$ includes the electron and the ion contribution. In calculation of the ion dielectric permittivity, we assume the ions to be cold, $\delta\epsilon_i^l \approx -\omega_{pi}^2/\omega^2$, where $\omega_{pi} = \sqrt{4\pi Z e^2 n_i/m_i}$ is the ion plasma frequency.

Calculating the electron dielectric permittivity, defined by (7.5), in the low frequency limit $\omega \ll k v_{th}$, we obtain the following expression in the spherical coordinates:

$$\Re(\delta\epsilon_e^l) = \frac{\omega_{pe}^2}{k^2} \frac{1}{n_e} \left\{ \int_{\mathbb{R}^+} dv f_0 - \int_{\mathbb{R}^+} dv f_0 \left[\frac{\alpha_1^2 \Xi(\alpha_1)}{\sinh(\alpha_1)} - \alpha_1 \coth(\alpha_1) + 1 \right] \right\},$$

where

$$\Xi(x) = \int_0^x dy \frac{\sinh(y)}{y}.$$

In the limit $\alpha_1 \ll 1$, the electron contribution reduces to $\Re(\delta\epsilon_e^l) = 1/(k^2\lambda_{De}^2)$. Correspondingly, the expression for the ion-acoustic wave frequency reads

$$\omega^2 = \frac{\omega_{pi}^2 k^2 \lambda_{De}^2}{1 + k^2 \lambda_{De}^2},$$

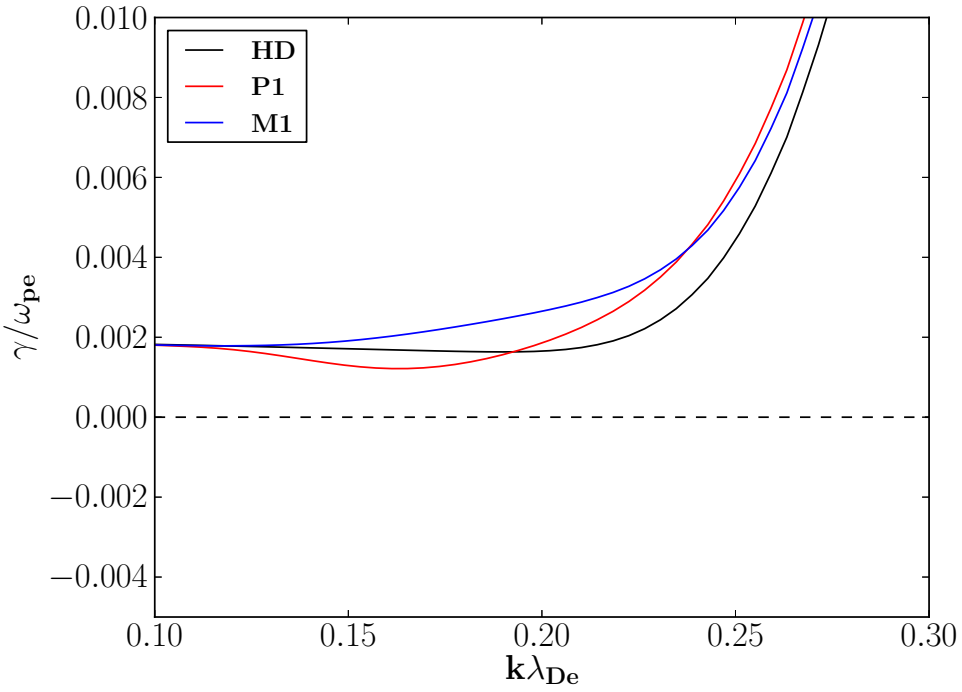

(a) Forward wave propagation.

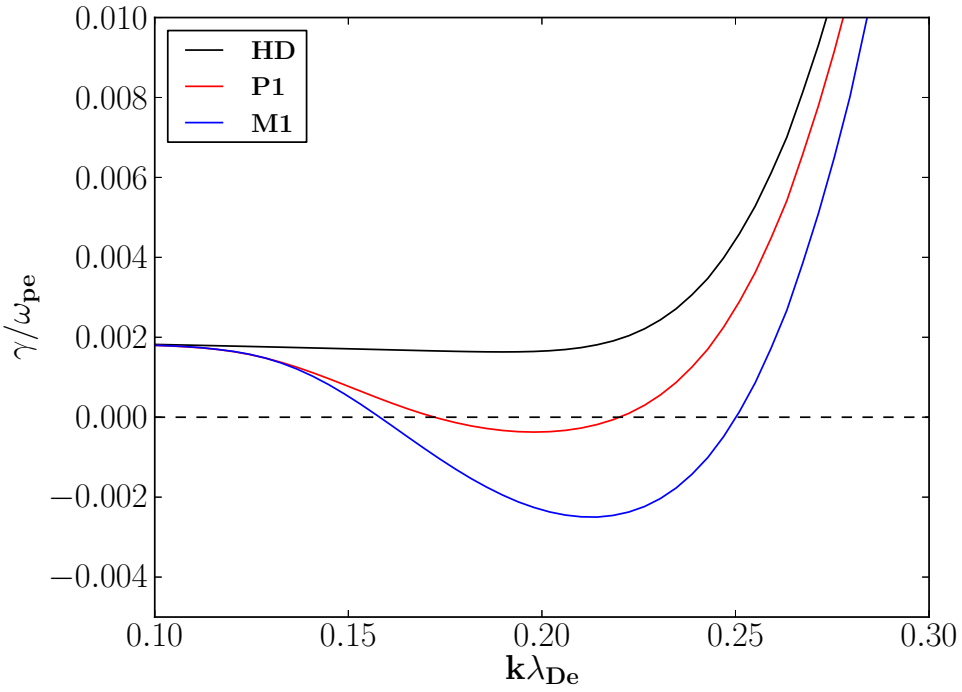

(b) Backward wave propagation.

Figure 7.16: Damping rate of Langmuir waves, accounting for the collision term.

where $\omega_{pi}\lambda_{De} = c_s$ is the local sound speed.

The general expression (7.6) also applies to the ion-acoustic wave damping. Following the procedure described for Langmuir waves (see also [59]), the damping rate of the ion-acoustic waves reads:

$$\frac{\gamma}{\omega} = \frac{\pi}{4} \frac{\frac{\omega}{k}\frac{f_0\left(\frac{\omega}{k}\right)\alpha_1\left(\frac{\omega}{k}\right)}{\sinh[\alpha_1\left(\frac{\omega}{k}\right)]} e^{\alpha_1\left(\frac{\omega}{k}\right)} - \int_{\frac{\omega}{k}}^{\infty} dv \frac{f_0\alpha_1^2}{\sinh(\alpha_1)} e^{\frac{\alpha_1\omega}{kv}}}{\int_{\mathbb{R}^+} dv f_0 - \int_{\mathbb{R}^+} dv f_0 \left[\frac{\alpha_1^2\Xi(\alpha_1)}{\sinh(\alpha_1)} - \alpha_1\coth(\alpha_1) + 1\right]}.$$

This expression simplifies in the linear limit in α_1, which corresponds to the P1 model

[59]:

$$\frac{\gamma}{\omega} = \frac{\pi}{4} \frac{\frac{\omega}{k} f_0\left(\frac{\omega}{k}\right) + 3\frac{\omega}{k} f_1\left(\frac{\omega}{k}\right) - 3\int_{\frac{\omega}{k}}^{\infty} dv f_1}{\int_{\mathbb{R}^+} dv f_0}.$$

For $f_0 = f_0^m$ and $\vec{f_1} = 0$, we recover the classical Landau damping formula, under the assumption of cold ions [18]:

$$\frac{\gamma}{\omega} = \sqrt{\frac{\pi}{8}} \frac{\omega}{k v_{th}}.$$

An example of the ion-acoustic wave damping is shown in Fig. 7.17 (forward and backward propagating waves), for the position $x = 0$ in Fig. 7.3. The damping is strongly modified near the maximum of the temperature gradient. The ion-acoustic waves propagating in the forward direction become unstable, while the waves propagating in the backward direction are stronger damped.

This ion-acoustic instability is induced by the return current, as it has been explained in [59]. In Fig. 7.14 it is schematically illustrated that the positive derivative of $F(v_\parallel)$ is induced by the shift of the maximum of the EDF due to the electric field, which induces the return current.

The instability is obtained for both models, however the location of the instability can be different because the difference of location of the electric field maximum, as shown in Fig. 7.3. The small differences between M1 and P1 models are explained by the fact that the ion-acoustic waves have very low phase velocities and the details of the EDF at high velocities do not have large importance.

For the plasma parameters presented in Fig. 7.1, the ion plasma frequency is of the order of $10^{14}\,\mathrm{s}^{-1}$ and the ion-acoustic instability can be excited in a few picosecond time scale. It could introduce an effective (turbulent) resistivity and suppress the heat transport [61].

7.3 On the unmagnetized transport

In this chapter we have applied the M1 model to unmagnetized HED plasmas, in the nonlocal regime.

The M1 model has been compared with two SNB models, using different collision operators and with the P1 model, in different conditions of heat transport. It reproduces all nonlocal features in one and two spatial dimensions and gives a better description of the EDF.

The model has been tested for two formulations of the nonlocal electric field. One derived from the kinetic theory but not generalizable to magnetized plasma, the second derived from phenomenological assumptions but generalizible to magnetized plasmas. Both have led to correct results.

The M1 approach provides access to small scale collective phenomena such as Landau damping of Langmuir and ion-acoustic waves. It is shown that in front of the temperature gradient and around the maximum of the temperature gradient, the Langmuir and the ion-acoustic instabilities may be developed, thus reducing the MFP of the electrons and consequently affecting the nonlocality of the flux.

The structure of the M1 model allows to naturally take into account electromagnetic fields, which is also a crucial issue for the HED physics applications.

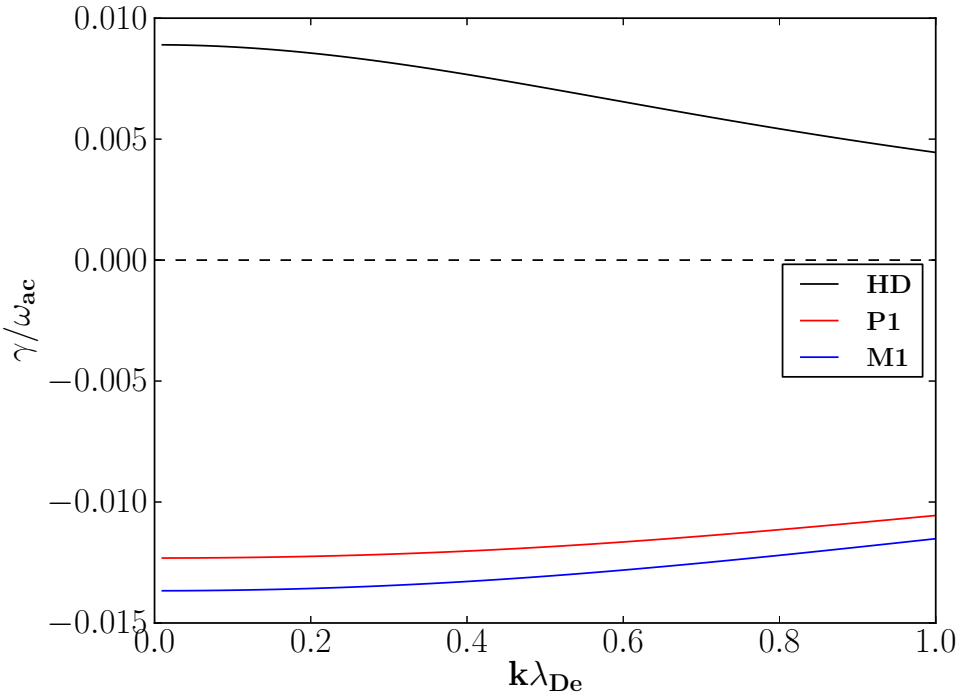

(a) Forward wave propagation.

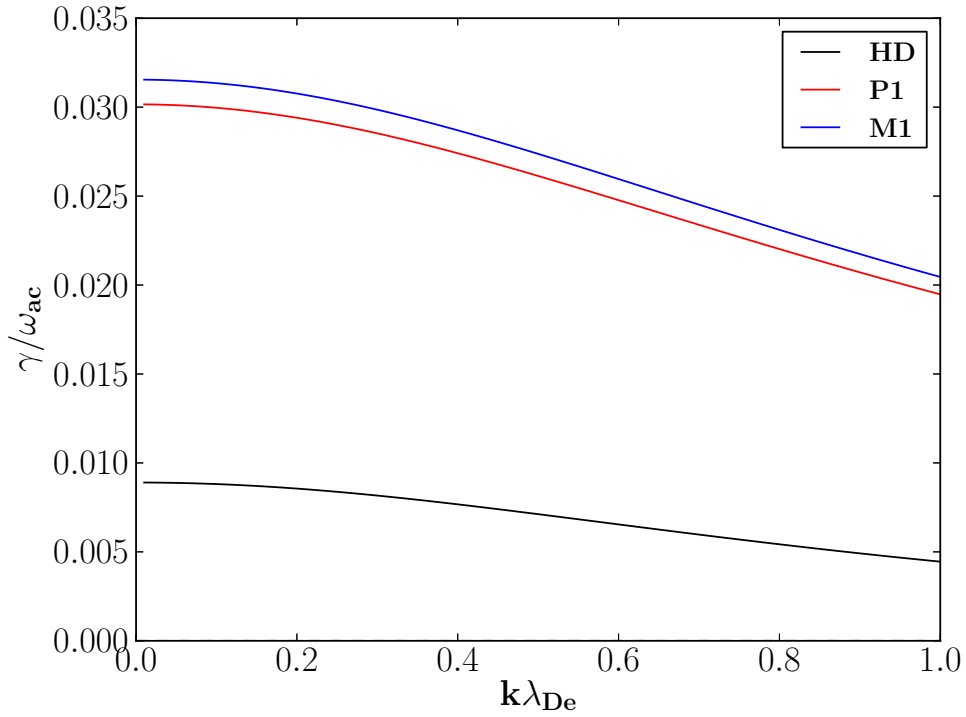

(b) Backward wave propagation.

Figure 7.17: Damping rate of ion-acoustic waves, normalized to the ion acoustic frequency $\omega_{ac} = kc_s$, as a function of the wavenumber normalized with the local Debye length.

Chapter 8

Transport in magnetized plasmas

Magnetic fields play an important role in many laboratory astrophysical processes as well as in ICF. In laser-produced plasmas related to astrophysics and ICF, an asymmetric irradiation may create magnetic fields. Indeed, noncollinear density and temperature gradients may induce self-generated magnetic fields strong enough to modify the energy distribution of the target [47].

In the direct drive scheme, assuming a spherical implosion, a target surface roughness or a laser speckle pattern may produce huge fields and change the target functioning. Moreover, recent ICF schemes consider external magnetic fields, in order to limit energy losses from the central hot spot [15]. These external fields could also modify the target symmetry during implosion, leading to the necessity of full simulations with magnetic fields.

In general, the laser-plasma simulations need a self-consistent description of magnetic fields. Models, which describe the effects of magnetization on the electron heat transport, are very complex [36, 38]; they involve tensor transport coefficients, which account for flux limitation effects as well as rotations. In particular, the model which is able to describe the magnetized nonlocal regime is characterized by an approximated description of electromagnetic effects on suprathermal electrons [24].

We propose here to use the M1 approach to analyze and calculate nonlocal effects as well as the magnetic field influence on the energy transfer. In this chapter, the M1 predictions for the magnetized heat transport are analyzed and tested. We consider variations of the magnetization, given by the Hall parameter $\omega_B \tau_e$, as well as variations of the nonlocal parameter.

In this chapter, electromagnetic fields are calculated according to the formalism presented in section 5.1.2. In section 8.1, the local regime is analyzed. In section 8.2, the magnetized nonlocal regime is studied. In section 8.3 the plasma relaxation to a thermal equilibrium is analyzed for both the magnetized and unmagnetized plasmas. Finally, in section 8.4, conclusions related to the magnetized nonlocal transport are drawn.

8.1 Braginskii limit

The first test that the magnetized M1 model has succeed to reproduce is the local limit, predicted by the Braginskii's theory [36].

Epperlein and Haines [38] (EH) proposed improved expressions for the Braginskii's coefficients. We use the EH coefficients, in order to validate the local limit of the M1 model.

We study a fully-ionized plasma, with a constant density, characterized by the steep temperature gradient (7.1), with $T_0 = 5\,\mathrm{keV}$, $T_1 = 0.5\,\mathrm{keV}$ and $\delta_{NL} = 500\,\mu\mathrm{m}$. The system is simulated in one dimension (x-direction) with a perpendicular magnetic field

(z-direction). The Hall parameter $\omega_B\tau_e$ is constant along the plasma, thus the magnetic field reads

$$B_z = \frac{m_e c}{e\tau_e}\omega_B\tau_e. \tag{8.1}$$

This geometry is schematically shown in Fig. 8.1.

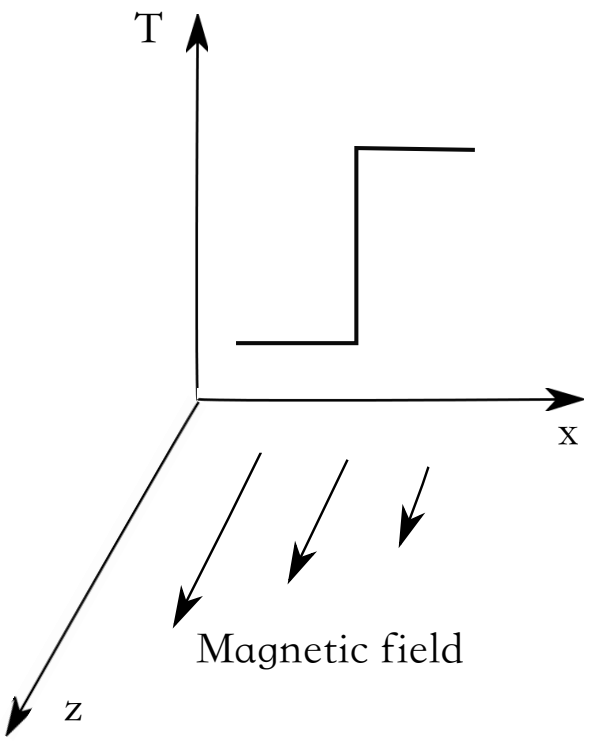

Figure 8.1: Geometry of the magnetized plasmas analyzed.

We test two perfect gas plasmas, one with $Z = 1$ and $n_e = 10^{23}$ cm^{-3} and the second with $Z \gg 1$ ($Z = 79$) and $n_e = 4 \times 10^{22}$ cm^{-3}.

For the plasmas described above, the initial temperature and magnetic field are plotted in Figs. 8.2a and 8.2b, respectively for $Z = 1$ and $Z = 79$. The magnetic field has been normalized on $B_0 = (m_e c v_{th})/(e\lambda_0)\omega_B\tau_e$, where $v_{th} \approx 30$ μm/ps and λ_0 (≈ 6 μm for $Z = 1$ and ≈ 0.21 μm for $Z \gg 1$) are computed for $T_e = T_0$. The field decreases as the temperature increases. Its spatial variation induces a current, given by the Ampere's law. This current is plotted in Figs. 8.3a, for $Z = 1$, and 8.3a, for $Z \gg 1$, normalized on $j_0 = c/(4\pi)L_T^{-1}B_0$, with $L_T = 890$ μm.

The nonlocal parameter is $\lambda_0/L_T \approx 6.7\times10^{-3}$ and $\approx 2.4\times10^{-4}$, respectively for $Z = 1$ and $Z \gg 1$. For these values, the system is in the local regime, and we can compare the local conductivities given by Braginskii, with M1 results.

8.1.1 Transport across the temperature gradient

In section 3.4.1 we have seen that magnetic fields add a new direction of anisotropy to the thermal transport, due to a coupling between the current and the electric field: the thermoelectric transport. In section 7.1.2, we have shown that the M1 model is limited to the description of one direction of anisotropy, hence it is valid if thermoelectric effects are negligible. Fortunately, this happens frequently in laser-matter interactions.

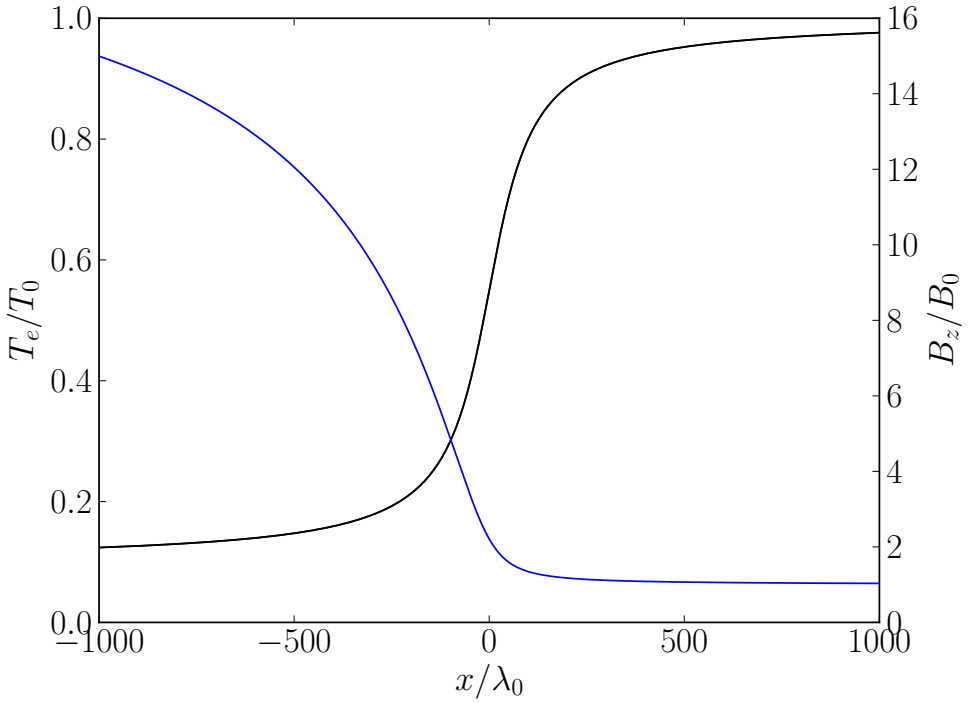

(a) $Z = 1$.

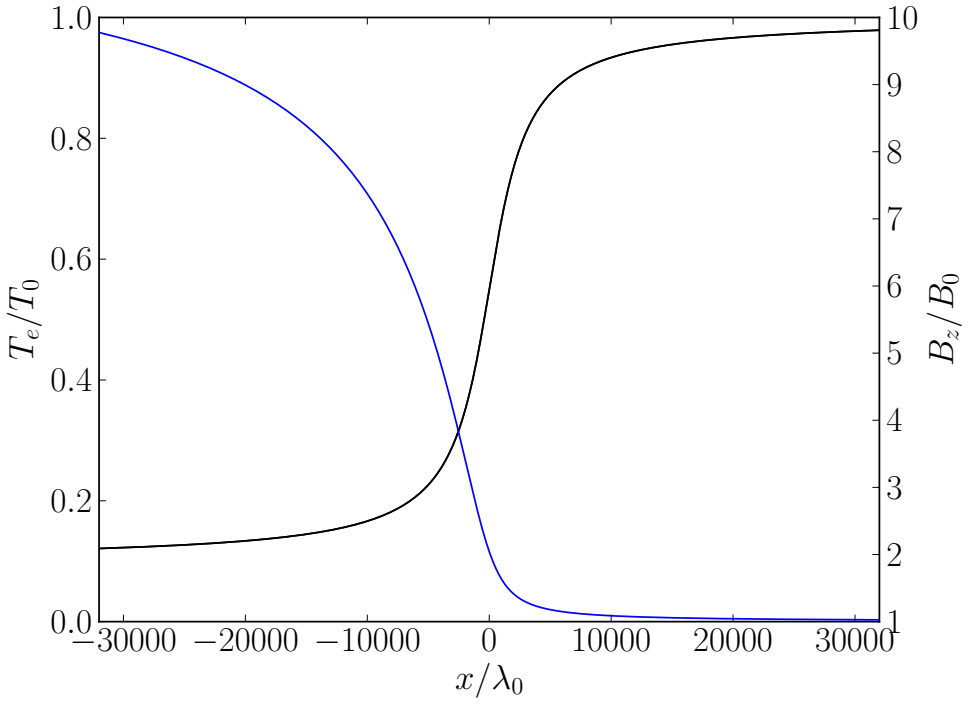

(b) $Z \gg 1$.

Figure 8.2: Initial electron temperature (in black) and magnetic field (in blue), plotted as functions of space.

The local heat flux is described by Eq. (3.25), which is composed by the thermal and the thermoelectric components. The thermoelectric heat flux is proportional to the current which has a nonzero value in the y-direction (crossed between the temperature gradient and the magnetic field). Since $\omega_B \tau_e$ is constant, $B_z \propto \tau_e^{-1} \propto T_e^{-3/2}$ and

$$\frac{\partial B_z}{\partial x} = -\frac{3}{2}\frac{B_z}{T_e}\frac{\partial T_e}{\partial x}.$$

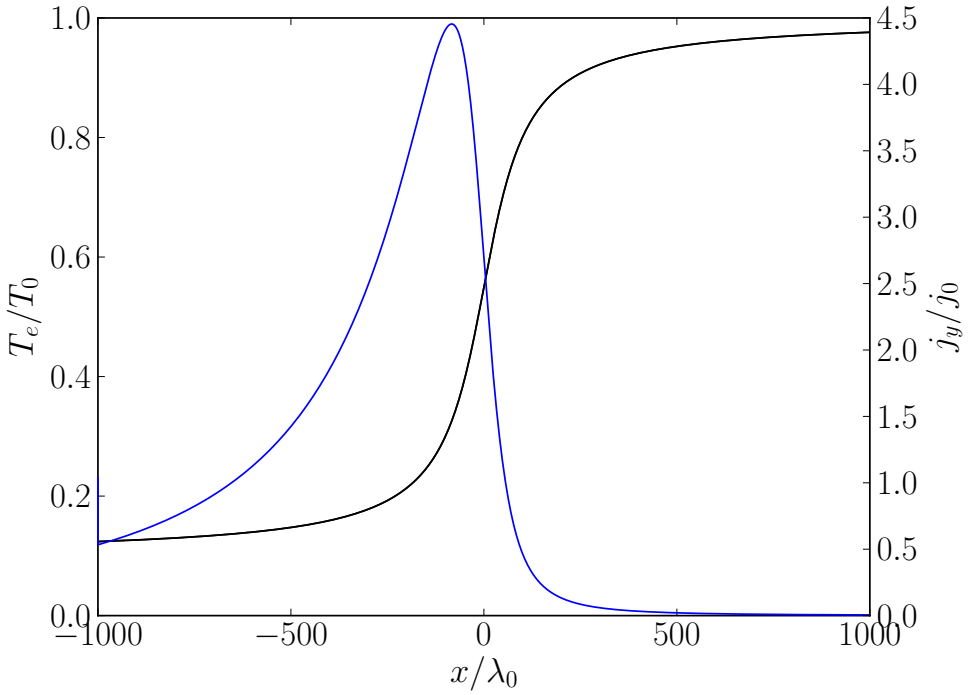

(a) $Z = 1$.

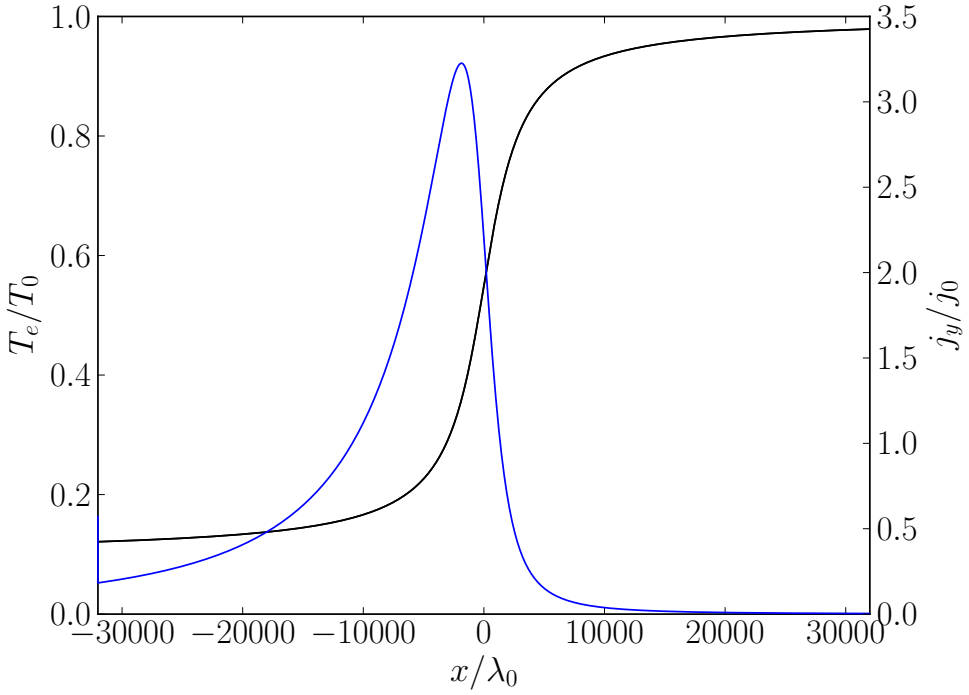

(b) $Z \gg 1$.

Figure 8.3: Initial electron temperature (in black) and electron current density (in blue), plotted as functions of space coordinate.

So, the current can be written as

$$j_y = \frac{3cB_z}{8\pi T_e}\frac{\partial}{\partial x}T_e$$

and, the y component of the heat flux, as

$$q_{By} = -k_\wedge \frac{\partial T_e}{\partial x}\left(1 + \frac{\beta_\perp}{k_\wedge}\frac{3cB_z}{8\pi e}\right).$$

It is much more useful to express the term in parenthesis as a function of the Hall parameter and of the dimensionless thermal conductivity $\bar{\bar{k}}^c = \bar{\bar{k}} m_e/(n_e T_e \tau_e)$. Normalizing by the SH flux $q_{SH}(x) = -k_\perp^c(\omega_B\tau_e = 0) n_e T_e \tau_e / m_e \partial T_e/\partial x$, we have

$$q_{By}/q_{SH} = -\frac{k_\wedge^c}{k_\perp^c(\omega_B\tau_e = 0)} \left(1 + \frac{\beta_\perp}{k_\wedge^c}\omega_B\tau_e \frac{3}{2}\frac{m_e c^2}{T_e}\frac{\nu_e^2}{\omega_{pe}^2}\right). \tag{8.2}$$

At the position $x = 0$, $T_e = 2.75$ keV, $\omega_{pe} = 1.8 \times 10^{16}$ s^{-1} and $\tau_e = 1.1 \times 10^{13}$ s^{-1}, for $Z = 1$, and $\omega_{pe} = 1.1 \times 10^{16}$ s^{-1} and $\tau_e = 2.9 \times 10^{14}$ s^{-1}, for $Z = 79$. Neglecting the thermoelectric contribution (second term in parenthesis), the error committed increases as $\omega_B\tau_e$ increases. In particular for the plasma with $Z = 1$ and for $\omega_B\tau_e = 30$, the error equals 0.06%. For the case $Z = 79$ and for $\omega_B\tau_e = 3$, the error is around 5.4% but for $\omega_B\tau_e > 3$, the analysis is stopped because the thermoelectric term needs to be accounted for. Thus, in the limit of our analysis ($\omega_B\tau_e \leq 30$ for $Z = 1$ and $\omega_B\tau_e \leq 3$ for $Z \gg 1$), thermoelectric effects can be neglected and we only consider the thermal conductivity. Then, the heat flux has the following form

$$\begin{cases} q_{Bx} \approx -k_\perp \frac{\partial}{\partial x} T_e \\ q_{By} \approx -k_\wedge \frac{\partial}{\partial x} T_e \end{cases} . \tag{8.3}$$

Epperlein and Haines calculated the electron transport coefficients [38] for a large range of the magnetization parameter and the ion charge. We want to reproduce this results, for thermal conductivities, by comparing the predictions by Braginskii [36] and EH [38] with the M1 calculations, in the central region of the plasmas described above, exploiting Eq. (8.3).

Figure 8.4a presents the dependence of $k_\perp^c$ versus the Hall parameter, for different models and different values of Z. As $\omega_B\tau_e$ increases, $k_\perp^c$ decreases. In accordance to Eq. (8.3), this corresponds to a decrease of the heat flux in the x-direction. In the crossed direction (y-axis), shown in Fig. 8.4b, the flux, as the conductivity, increases with the magnetization, till a maximum at $\omega_B\tau_e \approx 0.1 - 1$ (depending on the ion charge) and decreases for larger values of the Hall parameter. This departure can be roughly explained considering the magnetic acceleration experienced by an electron $= (e/m_e)(\vec{v}/c) \times \vec{B}$. It deviates electrons to the direction perpendicular to both $\vec{v}$ and $\vec{B}$ (y-direction). This induces a decrease of the heat transport in the x-direction and an increase in the y-direction (flux rotation). Moreover, if magnetization is sufficiently strong ($\omega_B\tau_e > 1$), electrons are forced to rotate collisionless around magnetic field lines, which reduces the MFP between two subsequent collisions to the Larmor radius.

A statistical and more precise description of the flux rotation and limitation, induced by magnetic fields, can be provided by Eq. (3.26). We interpret $\omega_B\lambda_{ei}^*/v$ as the kinetic version of the Hall parameter and assume $\omega_B\lambda_{ei}^*/v \sim \omega_B\tau_e$, as a leading term in the local limit. So, Eq. (3.26) asserts that the flux is reduced by a factor $1 + (\omega_B\tau_e)^2$, in the direction of the temperature gradient, while, by a factor $\omega_B\tau_e/[1 + (\omega_B\tau_e)^2]$, in the crossed direction, between the temperature gradient and the magnetic field. Thus, the flux is always reduced by the magnetization, in the direction of the temperature gradient, and it is increased for $\omega_B\tau_e \leq 1$ and reduced for $\omega_B\tau_e \geq 1$, in the crossed direction.

Figure 8.4a shows that the model M1 agrees with the theory [38], in the prediction of a flux limitation along the x-direction, due to a magnetic field. In the high-Z limit, the electron-electron collisions become negligible and the M1 model well agrees with the Braginskii's and EH theory.

In the low-Z limit, the M1 model weakly departs from the Braginskii's theory for $\omega_B\tau_e \gtrsim 10$. However, for such a strong Hall parameter, the magnetic field already strongly reduces the heat flux.

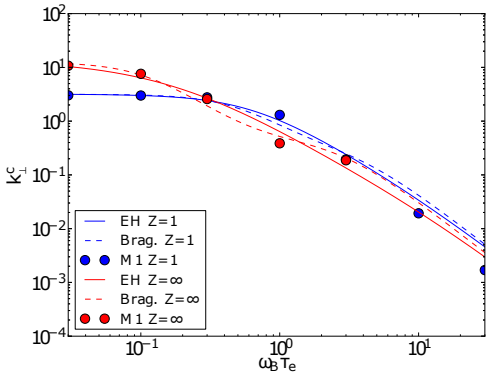

(a) Dimensionless thermal conductivity in the direction perpendicular to the magnetic field and parallel to the temperature gradient (axis x).

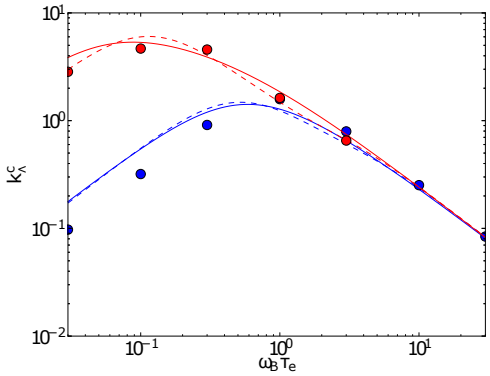

(b) Dimensionless thermal conductivity in the crossed direction between the magnetic field and the temperature gradient (axis y).

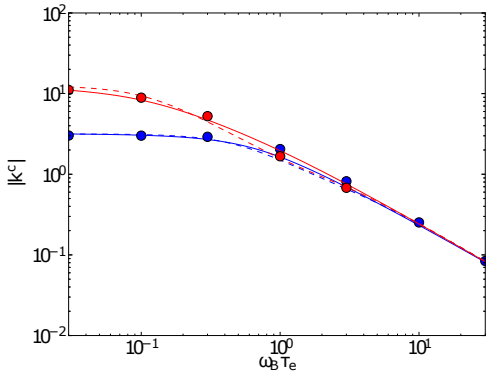

(c) Absolute value of the dimensionless thermal conductivity.

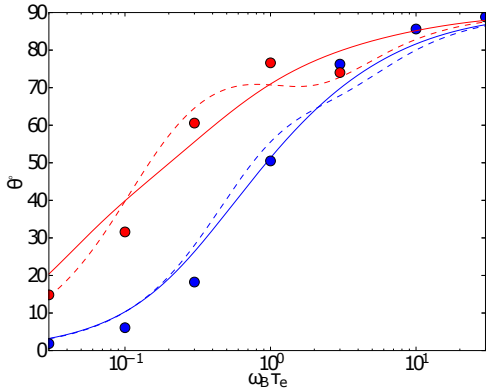

(d) Flux rotation.

Figure 8.4: Dependence of dimensionless local thermal conductivities, on the Hall parameter. The M1 model (points) is compared to the Braginskii's theory (continuous line) and the EH theory (dashed line). Comparison is presented for $Z = 1$ (blue) and $Z \gg 1$ (red). We stress that $\bar{\bar{k}}^c = \bar{\bar{k}} m_e/(n_e T_e \tau_e)$ is normalized on local variables, because we are performing a local analysis.

Also in the y-direction, shown in Fig. 8.4b, the M1 model agrees with the Braginskii's theory in the high-Z limit. In the low-Z limit it presents some differences when the effect of magnetic fields is weak. They are due to the inaccuracies of our collision operator, which are more visible for low-Z values. However, in this limit, the effect of the crossed heat transport is small.

8.1.2 Flux limitation and rotation

Figure 8.4 demonstrates that magnetic fields are responsible for two effects: flux limitation and flux rotation. By presenting the heat flux in the form of Eq. (8.3), we define a heat flux modulus as

$$|\vec{q_B}| = \sqrt{k_\perp^2 + k_\wedge^2} \left| \frac{\partial}{\partial x} T_e \right| = |k| \left| \frac{\partial}{\partial x} T_e \right| .$$

and its dimensionless form as $|k^c|$. The rotation angle is defined as

$$\theta = \arctan\left(\frac{q_{By}}{q_{Bx}}\right) = \arctan\left(\frac{k^c_\wedge}{k^c_\perp}\right) .$$

The magnetic field reduces the absolute value of the heat flux, as it is shown in Fig. 8.4c. Our model agrees in the description of the flux limitation, also in the low-Z limit. The main differences between the model and the theory [38] are in the flux rotation angle, shown in Fig. 8.4d. The figure shows that despite of some differences, the M1 model agrees with the theoretical predictions: the magnetic field tends to rotate the flux and the rotation angle increases with the Hall parameter. For Hall parameters higher than 1, the rotation angle approaches 90°.

In summary, we have tested our M1 model in the local regime, for a large range of Hall parameter values. The model shows some differences in the description of the flux rotation, especially for low Z-plasmas. They are due to the use of the simplified AWBS collision operator. However, differences remain small, demonstrating an acceptable accuracy of the M1 model in the local limit.

8.2 Magnetized nonlocal heat transport

The magnetized nonlocal transport regime is computed by iterating the M1 model, with Eq. (5.4), till the electric field convergence. This field modeling recovers the local limit (3.24), in the local regime.

8.2.1 Magnetized transport along and across the temperature gradient

In this section we analyze a particular case, where both phenomena are important: the heat flux magnetization and the nonlocal effects. We assume a perpendicular magnetic field, positive in the z-direction (given by Eq. 8.1), with a constant Hall parameter $\omega_B\tau_e = 0.5$. Periodic boundary conditions are assumed in the y-direction. This geometry is summarized in Fig. 8.1.

We consider a fully-ionized hydrogen plasma of a constant density $n_e = 10^{23}\,\mathrm{cm}^{-3}$. The temperature profile is given by Eq. (7.1) where $T_0 = 5$ keV, $T_1 = 0.5$ keV and $\delta_{NL} = 5\ \mu$m. The fluxes are normalized on the modulus of the maximum SH flux $q_0 = 86\ \mathrm{PW/cm}^2$ and the length to the maximum MFP $\lambda_0 = 3\sqrt{\frac{\pi}{2}}\frac{T_0^2}{4\pi n_e Z e^4 \Lambda_{ei}} \approx 5.98\,\mu$m. The degree of nonlocality of the system is $\lambda_0/L_T = 0.67$.

Since hydrodynamic variables are the same as the ones for the hydrogen plasma described in section 8.1.1 (except for δ_{NL}), according to Eq. (8.2), thermoelectric effects are negligible. As we will see, the nonlocal transport reduces even more thermoelectric effects, since they are related to the magnetization, and the magnetization effectively felt by nonlocal particles is smaller than the one felt by local electrons.

In order to demonstrate the magnetic field effect on the nonlocal transport, we compare the local and nonlocal models, with and without magnetic fields.

Figure 8.5a shows the heat flux along the temperature gradient. The difference between the local and nonlocal models is larger for unmagnetized models: the SH result is farther from the unmagnetized M1 result than the Braginskii's flux from the magnetized M1, which almost coincide. Thus, the effect of magnetic fields in the direction of temperature gradient is to reduce the nonlocal effect. On the contrary, the nonlocal effects are stronger in the perpendicular direction, as shown in Fig. 8.5b. In this case they suppress the heat flux and displace it toward a colder region. Thus, the nonlocal effect reduces the flux rotation due to the magnetic field.

We have seen that the effect of the magnetized nonlocal heat transport is to reduce both nonlocal and magnetic effects. This can be easily described by the simplified FP

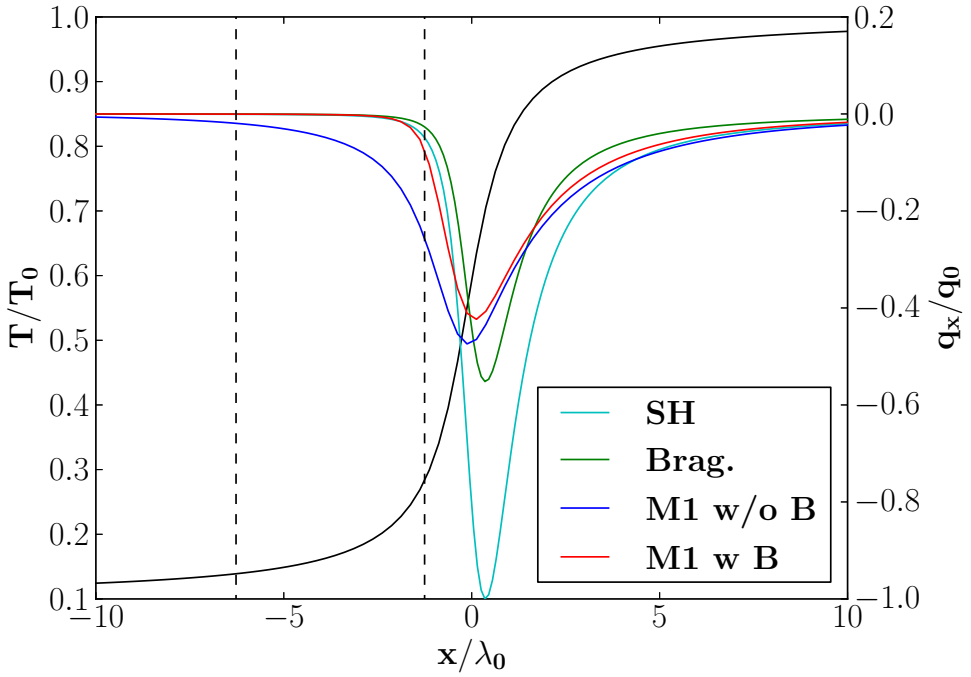

(a) Heat flux in the x-direction, as function of the x-axis.

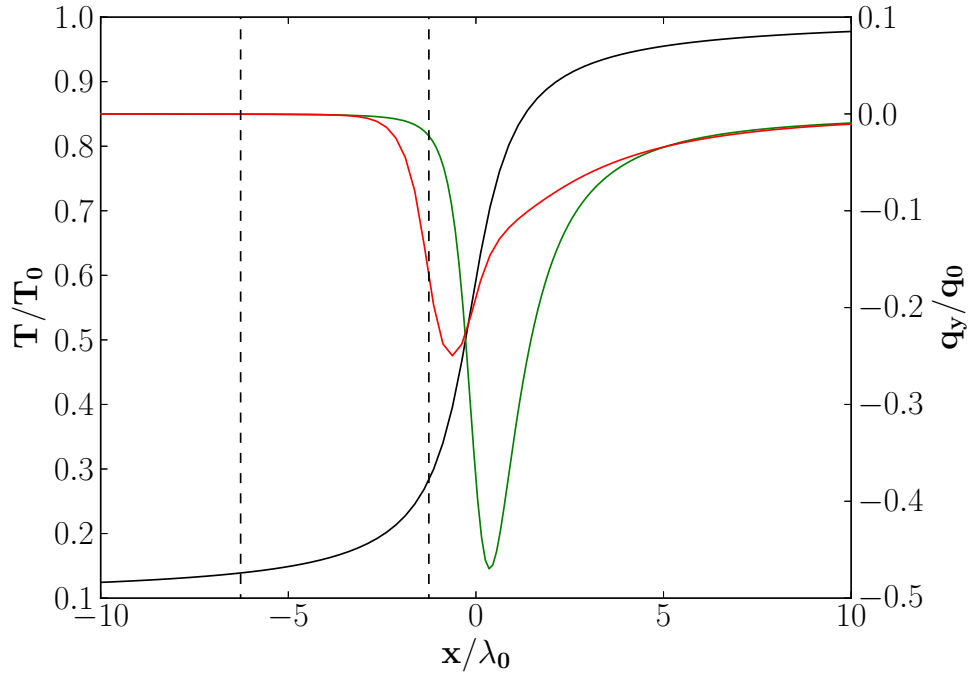

(b) Heat flux in the y-direction, as function of the x-axis.

Figure 8.5: Nonocal magnetized heat transport for a plasma with a temperature gradient in x-direction and periodic boundary conditions in the y-direction. In black it is shown the temperature profile, in celestial the local unmagnetized theory (SH model), in green the local magnetized one (Braginskii), in blue the nonlocal unmagnetized M1 model and in red the nonlocal magnetized M1 model. Vertical lines denote regions where the kinetic analysis is performed.

Eq. (3.26). The magnetization effectively experienced by an electron with a velocity v is

$$\frac{\omega_B \lambda^*_{ei}}{v} = \sqrt{\frac{2}{9\pi}} \omega_B \tau_e \left(\frac{v}{v_{th}}\right)^3 \frac{Z+0.24}{Z+4.2}, \tag{8.4}$$

and $\approx 0.063 \omega_B \tau_e (v/v_{th})^3$, for the hydrogen, while its effective MFP is $\lambda^*_{ei}/[1+(\omega_B \lambda^*_{ei}/v)^2]$.

It is reduced by magnetic fields for all velocities. A reduction of MFP implies a reduction of the nonlocal parameter λ_e/L_T to $\sim \lambda_e/\{L_T[1+(\omega_B\tau_e)^2]\}$, which necessarily leads to the reduction of nonlocal effects.

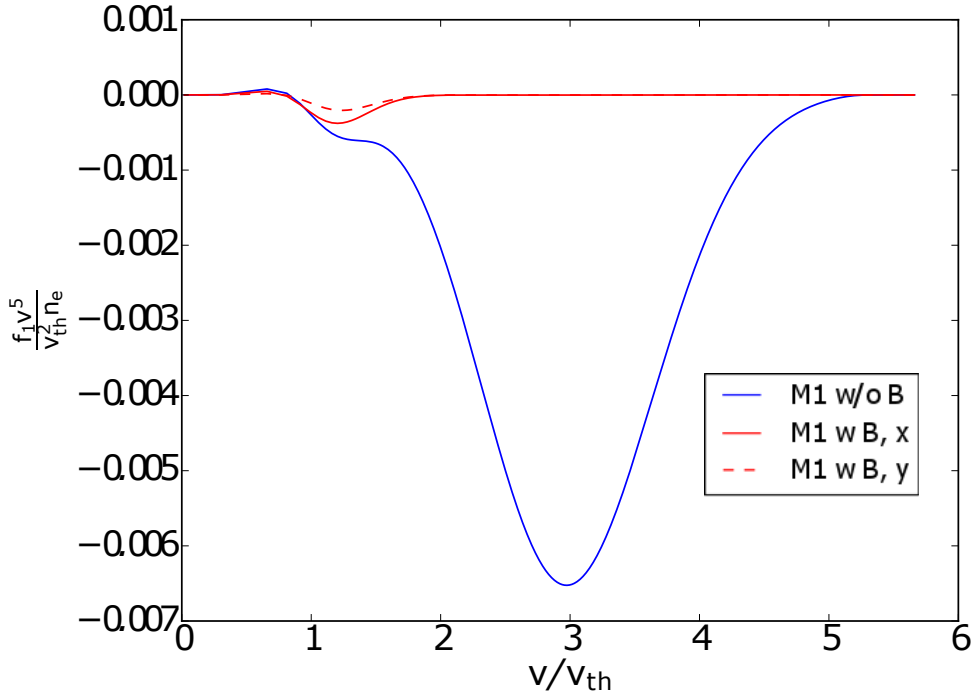

(a) Magnetized and unmagnetized heat flux integrand functions, in the cold region.

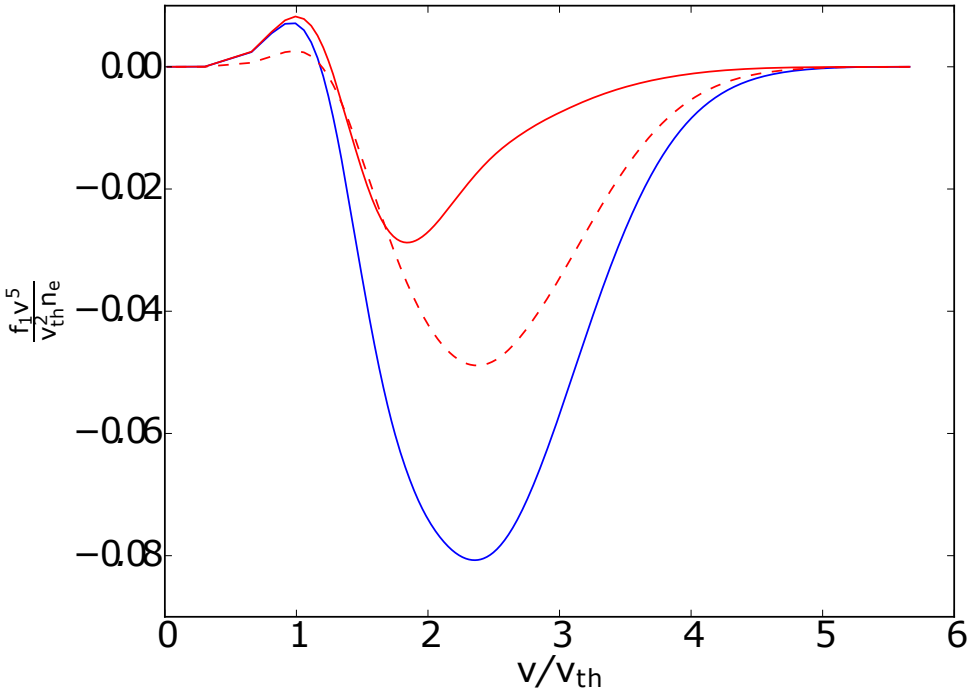

(b) Magnetized and unmagnetized heat flux integrand functions, in the central region.

Figure 8.6: Magnetized and unmagnetized integrand functions of the heat flux $\propto v^5\vec{f}_1$, in the cold and central region, denoted by dashed lines in Fig. 8.7d. They are plotted as functions of the velocity modulus. The magnetized flux is split in f_{1x}, in the x-direction (continuous line) and f_{1y}, in the y-direction (dotted line).

In Figs. 8.6a and 8.6b we plot the heat flux integrand functions $\propto v^5\vec{f}_1$, respectively

computed in the cold and central regions, denoted by dashed vertical lines in Fig. 8.5a. The local theory predicts the presence of two peaks along the direction of the temperature gradient f_{1x}. A positive peak at low velocities corresponds to the return current and a negative peak at higher velocities corresponds to the main heat flux. In the central region, variations of f_{1x} are small corrections. In the cold region of the unmagnetized plasma a hot nonlocal flux is deposited (higher peak of Fig. 8.6a), inducing a strong modification of the heat flux integrand function, compared to the magnetized case, more close to local predictions. This is due to the reduction of the effective MFP. Also the crossed direction (y-direction) f_{1y} is plotted in Figs. 8.6a and 8.6b, for the magnetized plasma, in order to show the flux rotation. We see that it becomes dominant for suprathermal velocities, especially close to the central region. Note that the maximum flux contribution is always displaced to the left, in comparison with the local value at $3.7v_{th}$.

In the local regime, electrons which transport the heat ($v \approx 3.7v_{th}$) experience a magnetization of $\approx 3.2\omega_B\tau_e$. In the nonlocal case, the characteristic velocity of these electrons decreases [58]: since gradients are sharper, slower electrons can also deposit the energy in the cold region. This implies a decrease of the effective Hall parameter experienced and so a decrease of the heat flux magnetization. In Figs. 8.6a and 8.6b we plot the heat flux integrand functions, respectively computed in the cold and central regions, denoted by dashed vertical lines in Fig. 8.7d. We assume that the flux is carried by electrons with a velocity given by the maximum contribution. According to Fig. 8.6b, in the central region, the heat flux characteristic velocity along the temperature gradient is $||(2v_{th}, 2.5v_{th})||\approx 3.2v_{th}$, which implies a reduction of the experienced magnetization to $\approx 2.1\omega_B\tau_e$.

We have performed also an analysis of the electron energy distribution. The EDFs in the unmagnetized and magnetized regimes are computed with the M1 model. In the cold region, shown in Figs. 8.5a and 8.5b by the left vertical line, the EDFs are shown in Fig. 8.7a (unmagnetized plasma) and in Fig. 8.7b (magnetized plasma). In the unmagnetized case the EDF presents a direction of anisotropy towards the colder region of the plasma (180°), due to electrons which transport the heat. Magnetic effects reduce and turn this anisotropy, affecting the macroscopic transport. Same effects are visible in the central region, but in this case the rotation is the dominant. The total EDFs are the ones shown in Figs. 8.7c (unmagnetized plasma) and 8.7d (magnetized plasma). Note that the Hall parameter experienced by a particle with a velocity $||(2.5v_{th}, 2.5v_{th})||\approx 3.5v_{th}$ is 1.4, for which corresponds to the rotation angle $= \arctan(f_{1y}(2.5v_{th})/f_{1x}(2.5v_{th})) \approx 70°$ (see Fig. 8.4d).

8.2.2 Temperature modulation in a magnetized plasma

The ES test has been presented in section 7.1.2, for the study of nonlocal transport. We extend this test to the case of a nonlocal transport in a magnetized plasma.

As in section 7.1.2, we consider a fully-ionized beryllium plasma, with a constant density $4.5 \times 10^{22}\,\mathrm{cm}^{-3}$ and the periodic temperature modulation (7.2), with $T_0 = 1\,\mathrm{keV}$ and $T_1 = 0.1\,\mathrm{keV}$. The magnetic field is applied in the perpendicular direction (z-direction), with a constant Hall parameter, as shown in Fig. 8.1. Periodic boundary conditions are applied to the x and y-directions. The length is normalized in space to the MFP $\lambda_0 \approx 0.17\ \mu\mathrm{m}$.

According to Eq. (8.2), thermoelectric effects can be neglected, because the error induced in the local regime, in $x = 0$, for $\omega_B\tau_e = 1$, is only 0.04% ($\nu_e = 2.2 \times 10^{13}\ \mathrm{s}^{-1}$) and even lower in the nonlocal transport regime, which experiences a lower magnetization.

Figure 8.8 shows a specific case of heat flux, normalized to $q_0 = 1\ \mathrm{PW/cm}^2$, for $k\lambda_0 = 0.17$. The Hall parameter is varied from the near-unmagnetized case ($\omega_B\tau_e = 0.1$),

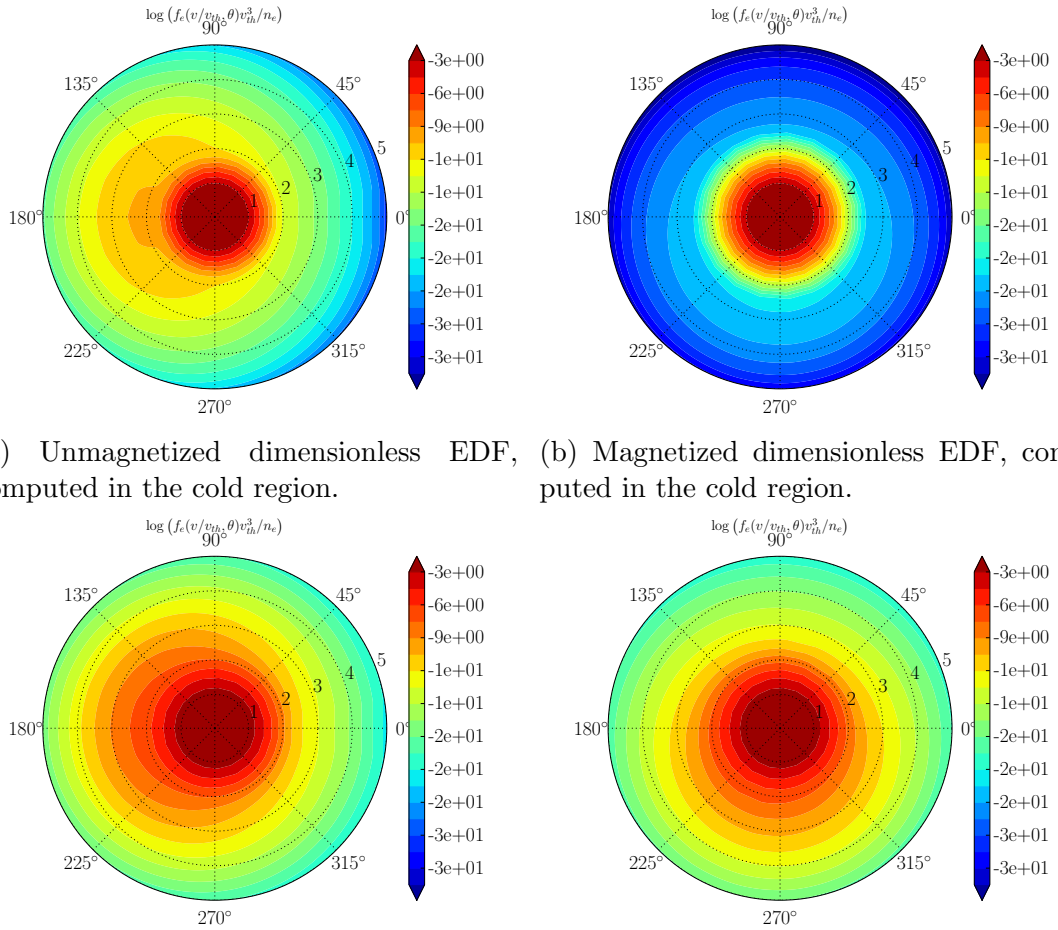

(a) Unmagnetized dimensionless EDF, computed in the cold region.

(b) Magnetized dimensionless EDF, computed in the cold region.

(c) Unmagnetized dimensionless EDF, computed in the central region.

(d) Magnetized dimensionless EDF, computed in the central region.

Figure 8.7: Magnetized and unmagnetized dimensionless logarithm of the EDF. The analysis is performed in function of the velocity magnitude (radial direction) and of the velocity angle with respect to the temperature gradient (x-axis), in the cold region and in the central region, as indicated by vertical lines, in Fig. 8.5a and 8.5b.

to $\omega_B\tau_e = 1$. For $\omega_B\tau_e = 0.1$, according to Fig. 8.4d, the magnetic effect on local transport is the flux reduction, in both directions. The nonlocal effect further reduces heat fluxes, in both directions. In particular, q_y is almost reduced to zero. This is because nonlocal effects are dominant, since the effective MFP is weakly reduced. On the contrary, for $\omega_B\tau_e = 1$, the effective MFP is strongly reduced and the differences between local and nonlocal fluxes are small. For this regime of magnetization, the flux in the y direction becomes dominant, while in the x-direction it is reduced by a factor $\gtrsim 10$.

The same study is performed in the ES test, for different values of $k\lambda_0$, focusing on the flux limitation, where the modulus of fluxes is maximum. The heat flux limitation is obtained normalizing the heat flux on the maximum value of the Braginskii's flux. This study is repeated for the flux module, in Fig. 8.9a and for their components, in Figs. 8.9b (x-direction) and 8.9c (y-direction).

The analysis of the flux module shows that the nonlocal flux limitation is reduced, increasing the Hall parameter. This confirms the reduction of nonlocal effects, induced by the reduction of the effective MFP, as described in the previous section. In particular, the flux magnitude is nearly-unmagnetized for $\omega_B\tau_e = 0.1$ and nearly-local for $\omega_B\tau_e = 1$. In the first case, nonlocal effects become important for $k\lambda_0 \gtrsim 10^{-2}$, in the second, for $k\lambda_0 \gtrsim 10^{-1}$. The heat flux components show that the flux is subjected to nonlocal effects in both directions, especially for $k\lambda_0 = 0.1$, till $k\lambda_0 = 0.17$. For $k\lambda_0 > 0.17$, the error

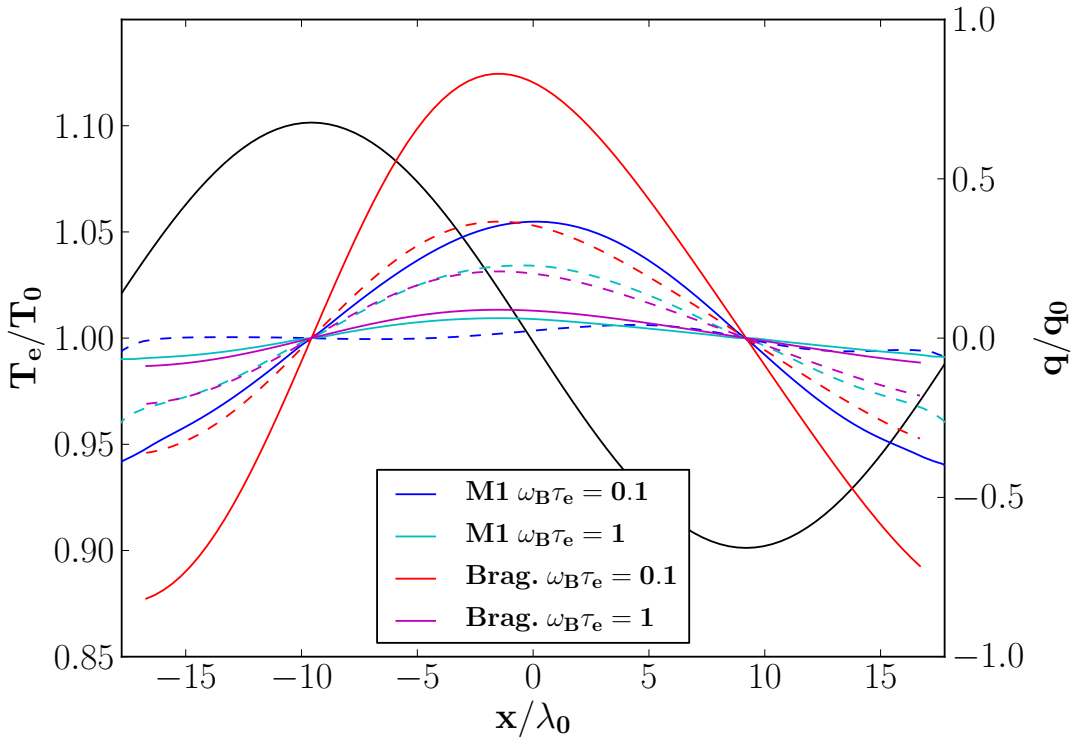

Figure 8.8: Comparison of the M1 and Braginskii's heat fluxes, subjected to different magnetizations, for $k\lambda_0 = 0.17$. The continuous lines indicate the flux q_x, in the direction of the temperature gradient, and the dashed lines the flux q_y in the crossed direction between the temperature gradient and the magnetic field (y-direction). Normalizations are on the maximum of the SH flux $q_0 = 1$ PW/cm^2.

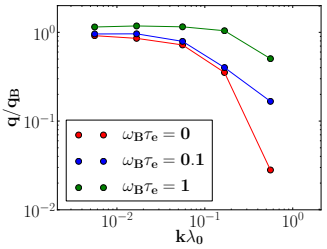

(a) Modulus of the heat flux limitation, normalized on the maximum of the modulus of Braginskii's local theory. The lines join the points, for clarity.

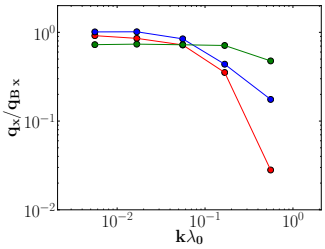

(b) Heat flux in the direction of the temperature gradient (x-direction), normalized on the maximum of x-flux by Braginskii's theory. The lines join the points, for clarity.

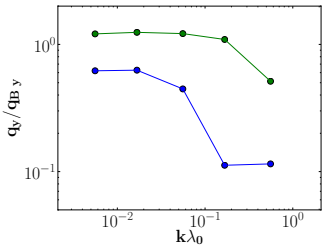

(c) Heat flux in the crossed direction between the temperature gradient and the magnetic field (y-direction), normalized on the maximum of y-flux by Braginskii's theory. The lines join the points, for clarity.

Figure 8.9: ES test, in a magnetized plasma. The magnitude of the fluxes is normalized on the modulus of Braginskii's predictions. Different colors represent different values of the Hall parameter, form 0.1 to 1.

committed computing the electric fields E_y with Eq. (5.4) becomes significant for the crossed flux q_y. However, for these cases, the absolute value of q_y is rather small.

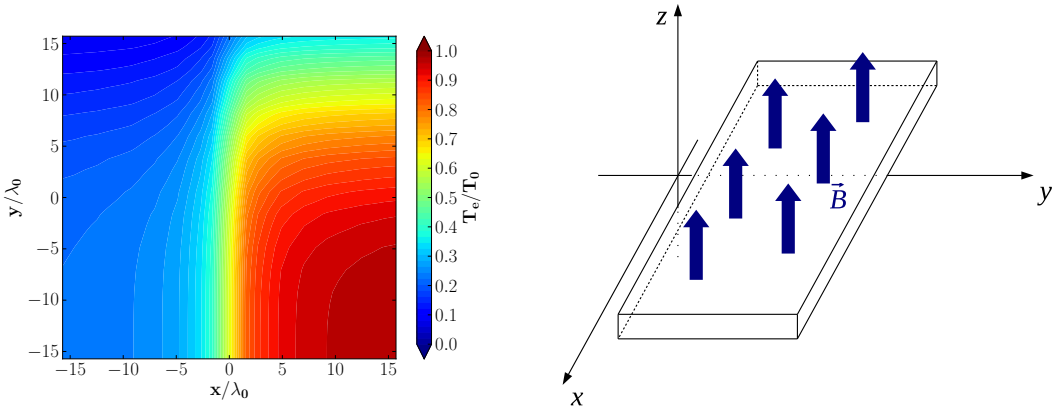

(a) Initial electron temperature.

(b) Geometry of the system described in section 8.3.

Figure 8.10: Parameters of the plasma analyzed in section 8.3.

8.3 Thermal wave propagation in magnetized plasmas

The purpose of this section is to describe the propagation of a thermal wave in a magnetized plasma, in the conditions of the nonlocal transport, using the M1 model coupled to the hydrodynamic code CHIC.

8.3.1 Plasma parameters

We consider a fully-ionized beryllium plasma of constant density 4.5×10^{22} cm^{-3}. Initially, this plasma is characterized by the electron temperature (7.4), with $T_0 = 5\,\mathrm{keV}$, $T_1 = 1\,\mathrm{keV}$, $\delta_{NL} = 5\,\mu\mathrm{m}$ and $x_{max} = y_{max} = 100\ \mu\mathrm{m}$ are the lengths of the target along x and y axes. The temperature profile is shown in Fig. 8.10a. The plasma is simulated with symmetric conditions at boundaries:

$$T_e(\vec{x} = \partial\vec{x}^+, t) = T_e(\vec{x} = \partial\vec{x}^-, t),$$

at each time t, where, in our formalism, $\partial\vec{x}$ denotes the spatial boundary and signs $+$ and $-$ mean outer and inner limits, respectively. So, for example, in the right border $T_e(x = 16\lambda_0 + dx, t) = T_e(x = 16\lambda_0, t)$, where dx is the cell length and $\lambda_0 =\approx 3.15\,\mu\mathrm{m}$ the maximum MFP.

This plasma is subjected to a constant magnetization $\omega_B\tau_e$, in space and time, induced by a perpendicular magnetic field, which varies according to

$$B_z(\vec{x}, t) = \frac{m_e c}{e\tau_e(\vec{x}, t)}\omega_B\tau_e.$$

The geometry of the system is resumed in Fig. 8.10b.

In such a plasma electrons transport heat, generating a thermal wave, which smooths the temperature gradient, till to reach a constant temperature at the thermal equilibrium. We assume that the temporal evolution of the temperature is given by the heat equation for electrons, which reads

$$\frac{3}{2}n_e\frac{\partial}{\partial t}T_e + \vec{\nabla}\cdot\vec{q}_e = 0, \tag{8.5}$$

in the perfect gas approximation. The assumption of a constant density can be justified as follows. In the point $(x = 0, y = -15\lambda_0)$ the gradient attains its maximum. The gradient length is $L_T \approx 11\ \mu\mathrm{m}$. So the characteristic hydrodynamic time is $\tau_{hydro} \sim L_T/c_s \approx 24$ ns,

where the acoustic velocity is $c_s = \sqrt{ZT_0/m_i} = 0.46$ μm/ps. The characteristic time of thermal diffusion is $\tau_{diff} \sim n_e L_T^2/\chi \approx 1.3$ ps, where $\chi \sim n_e v_{th}^2 \tau_e$ is an effective thermal conductivity, with $\tau_e = 3\sqrt{\frac{\pi}{2}} \frac{m_e^{1/2} T_0^{3/2}}{4\pi n_e Z e^4 \Lambda_{ei}} \approx 0.11$ ps and $v_{th} = \sqrt{T_e/m_e} \approx 30$ μm/ps. Since $\tau_{hydro} > \tau_{diff}$, the hydrodynamic motion can be neglected. The characteristic time of ion diffusion is $\sim 1.5 \times 10^3 \tau_{diff}$, thus it can be neglected too.

According to Eq. (8.2), thermoelectric effects can be neglected, making an error of $\sim 0.3\%$, for $\omega_B \tau_e = 10$.

In what follows we compare the time evolution of the system, using three models for the heat flux $\vec{q}_e$: the Braginskii's theory, the M1 and the SNB model, in different regimes of magnetization. The analysis is performed for dimensionless quantities. The temperature is normalized by the initial maximum of the temperature profile $T_0 = 5$ keV, the space by the maximum MFP $\lambda_0 \approx 3.15\,\mu$m and the heat fluxes over the maximum of the magnitude of the initial SH heat flux $q_0 = 40$ PW/cm^2. We expect to see a thermal wave which smooths temperature gradients in time, till to reach a constant temperature at the equilibrium. We are interested in studying how the magnetization and nonlocal transport influence this process.

8.3.2 Analysis of initial conditions

Figures 8.11 show electron heat fluxes induced by the initial electron temperature profile, shown in background, as a color plot. Fluxes are computed for increasing values of the Hall parameter (constant in space) and are represented as arrows. For each figure, three models are compared: the Braginskii's model (local theory), the M1 model and the magnetized generalization of the SNB model. They are respectively represented in black, white and green.

Figure 8.11a, corresponding to the case $\omega_B \tau_e = 0$, shows that the local heat flux is always perpendicular to the temperature gradient. The case of a weak magnetization ($\omega_B \tau_e = 0.1$), reported in Fig. 8.11b, shows a local flux rotation, respect to the unmagnetized case. Increasing the magnetization ($\omega_B \tau_e = 0.2$), in Fig. 8.11c we see another effect: the reduction of the local flux. These two effects become dominant in Fig. 8.11d, for $\omega_B \tau_e = 0.5$ and in Fig. 8.11e, for $\omega_B \tau_e = 1$. Finally, for a high degree of magnetization ($\omega_B \tau_e = 10$), in Fig. 8.11f we see the flux suppression.

Figure 8.12 shows the degree of nonlocality of the system studied, in the first instant. It represents the logarithm of the ratio between the electron MFP and the temperature gradient length (nonlocal parameter). A nonlocal regime corresponds to the values higher than -2. The chosen parameters correspond to highly nonlocal conditions.

Figure 8.11a shows the main effects of unmagnetized nonlocal transport, described in the previous chapter. A flux limitation can be seen near $x \approx 0$, the preheating near $x \approx -5$ and the rotation is negligible. The M1 and the SNB models quite well agree in the description of nonlocal fluxes.

When a small magnetization is imposed ($\omega_B \tau_e = 0.1, 0.2$), the direction of heat flux deviates from the direction of the temperature gradient, due to magnetic fields. The flux rotation, in nonlocal models, appears weaker compared to the local case. This qualitative effect can be seen in both M1 and SNB models; however, they slightly differ in the value of this rotation. The M1 model corresponds to smaller deviations, compared to the SNB model. For both models, the flux reduction, due to magnetic fields, becomes important for $\omega_B \tau_e = 0.5$ (a higher degree of magnetization than in the local model). Thus, we confirm that nonlocal fluxes are less affected by magnetic fields, compared to their local counterparts. This conclusion is in accordance with Brantov's studies, presented in Fig. 6 of [62].

As the magnetization becomes strong ($\omega_B \tau_e = 0.5, 1$), nonlocal models approach the

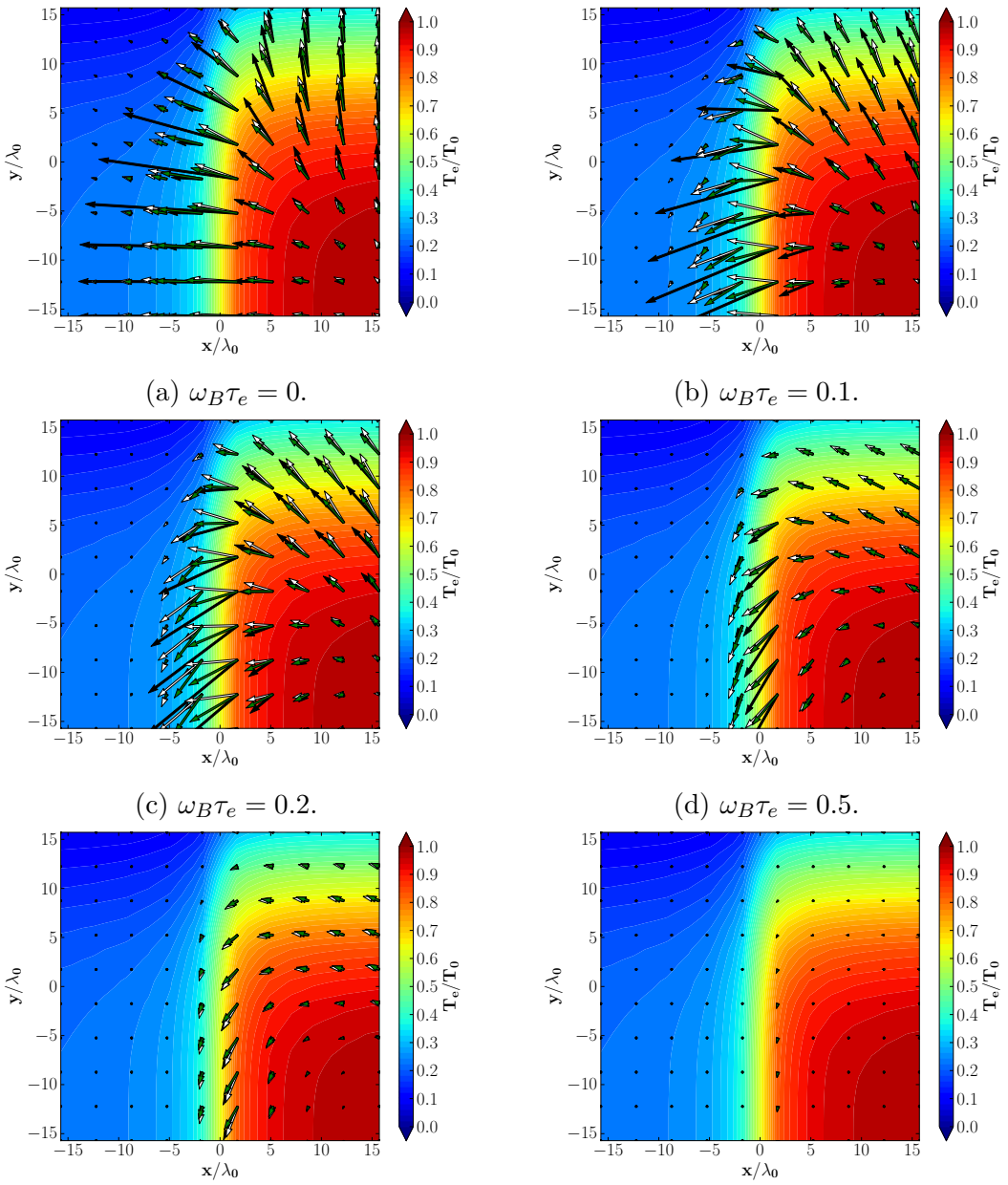

(a) $\omega_B\tau_e = 0.$ (b) $\omega_B\tau_e = 0.1.$

(c) $\omega_B\tau_e = 0.2.$ (d) $\omega_B\tau_e = 0.5.$

(e) $\omega_B\tau_e = 1.$ (f) $\omega_B\tau_e = 10.$

Figure 8.11: Initial distribution of the electron temperature and the heat flux of the plasma. The initial electron temperature profile is shown by the background colors and arrows indicate heat fluxes predicted by different models: the Braginskii's theory (in black), the M1 (in white) and the SNB model (in green). The panels correspond to different values of the Hall parameter.

local predictions. These models superpose in the case of flux suppression ($\omega_B\tau_e = 10$). This is due to a reduction of the MFP, induced by magnetic fields [24].

Thus the nonlocal heat fluxes q_{NL-B} in presence of magnetic fields provide intermediate values between the magnetized local values q_B and the unmagnetized nonlocal values q_{NL}. For the flux along the gradient direction we find the following relations $q_B \leq q_{NL-B} \leq q_{NL}$. The M1 and SNB models give the same values for the fluxes.

8.3.3 Temporal evolution

Equation (8.5) conserves the total energy in the simulation box, regardless of the model used.

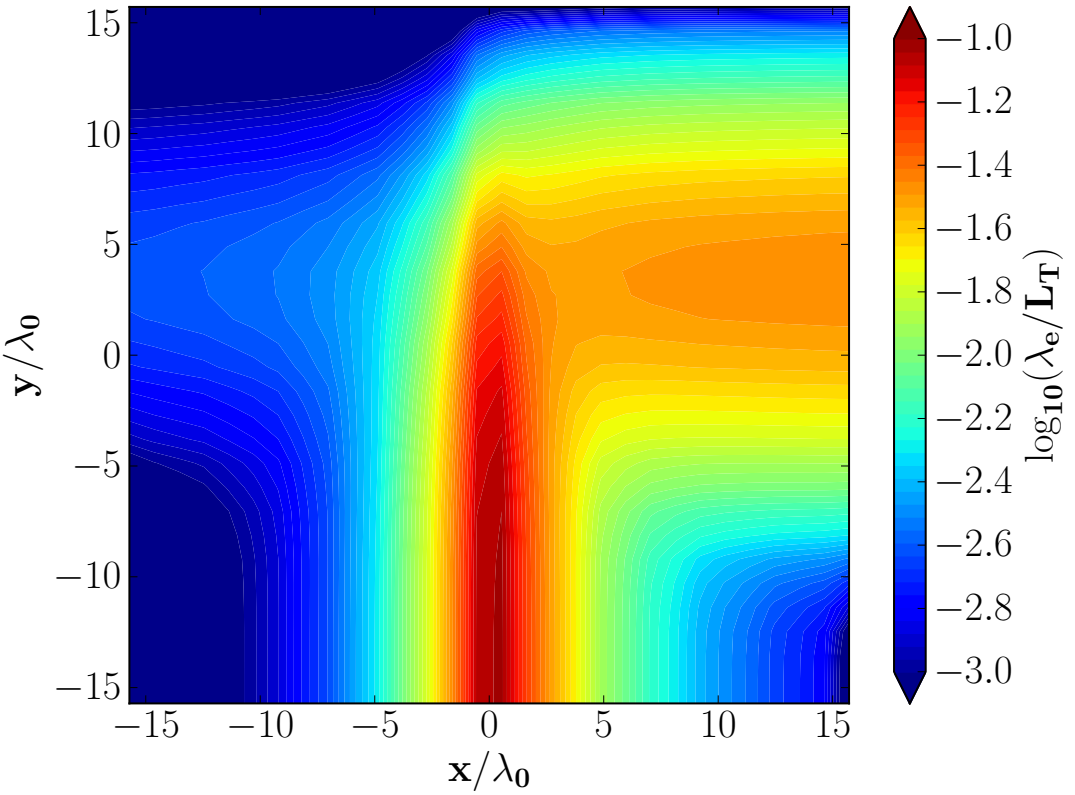

Figure 8.12: Logarithm of the nonlocal factor, as a function of the space, in the initial instant of the plasma analyzed in section 8.3.

Electrons, in the hot region, have a velocity $\sim v_{th} = \sqrt{T_0/m_e} \approx 3 \times 10^9$ cm/s. The maximum distance of the simulation box is $45\lambda_0$ (diagonal direction). In the unmagnetized regime, electrons take $45\tau_e \approx 5$ ps to travel along the simulation box. At this time, the differences between models are maximum. In subsequent times, they are smoothed, since electron gradients are enough smooth.

Figures 8.13a, 8.13b and 8.13c show respectively the Braginskii's, the SNB and the M1 predictions, after $45\tau_e$, in the unmagnetized regime. The local heating is more efficient, because of the flux limitation which characterizes nonlocal models. The local flux smooths the temperature gradients more than in nonlocal case.

Dashed lines in Fig. 8.13 indicate the regions where monodimensional cuts have been performed, in order to simplify the analysis. A cut along the x-direction is shown in Fig. 8.14a, while along the y-direction in Fig. 8.14b. Both cases show the gradient smoothing, while a weak preheating is visible in front of the temperature gradient, along the x-direction, induced by nonlocal transport. SNB and M1 predictions agree.

Adding a weak degree of magnetization ($\omega_B\tau_e = 0.1$) to the system, we add the effect of flux rotation ($\sim 5 - 10°$, in the local case), related to magnetic fields. Temperature predictions are shown in Figs. 8.13d (Braginskii's predictions), 8.13e (SNB predictions) and 8.13f (M1 predictions). Figures 8.15a and 8.15b show the horizontal and vertical cuts. The Braginskii's theory predicts that the gradients are less smoothed than in the magnetized case. On the contrary, nonlocal models (M1, SNB) are mainly not affected by such a weak magnetization. In summary, with a weak degree of magnetization, local and nonlocal predictions are closer but nonlocal electrons mainly behave as if they do not experience any magnetization. The SNB and M1 models give very similar results.

With $\omega_B\tau_e = 0.5$, the effective MFP is reduced by a factor $\sim 1/(1 + C\omega_B^2\tau_e^2)$, with $C \sim 1$, thus fluxes are reduced: the temperature gradients are less smoothed by the heat transport, as shown in Fig. 8.13g. Despite a high degree of nonlocality, no differences can

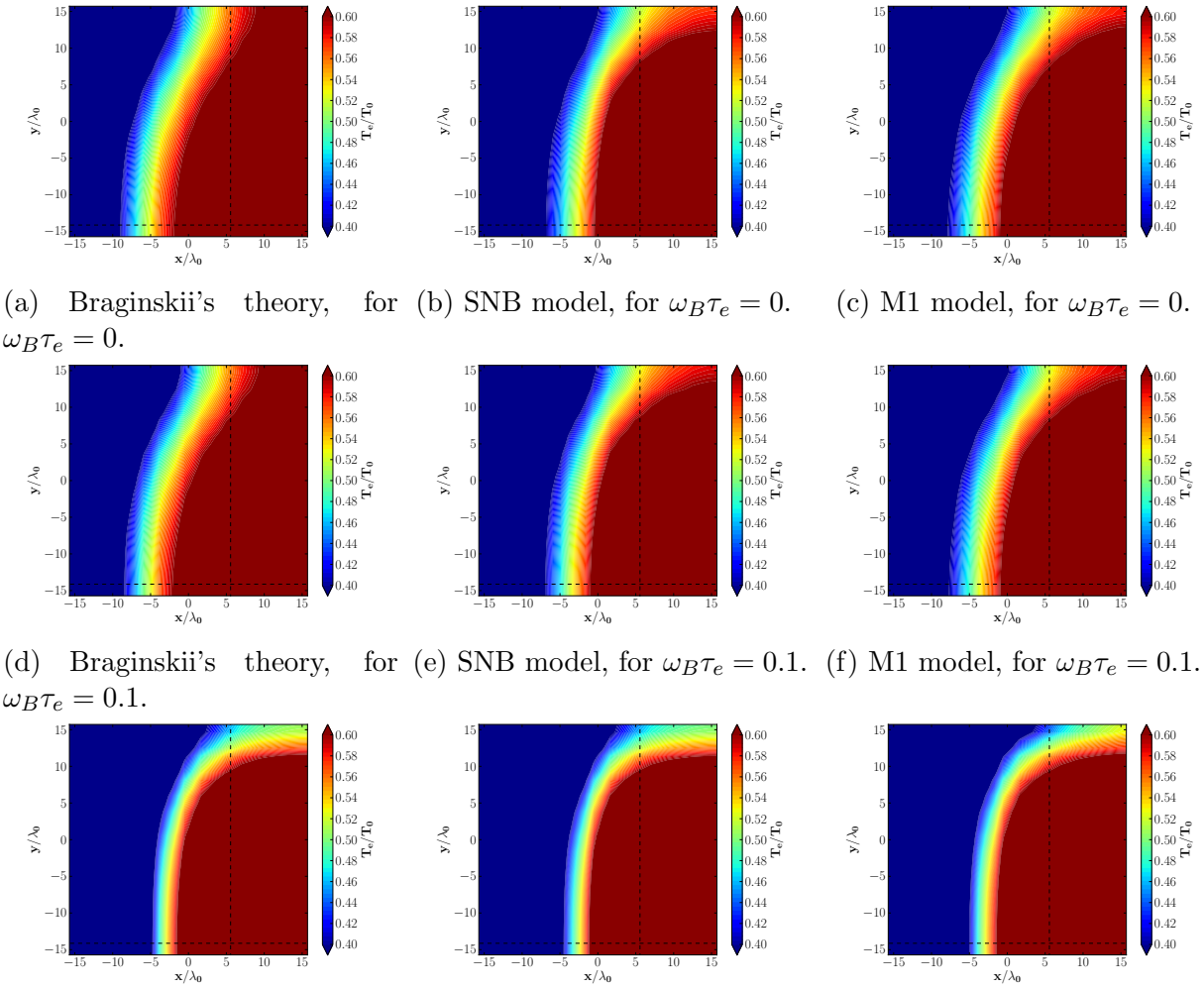

(a) Braginskii's theory, for $\omega_B\tau_e = 0$. (b) SNB model, for $\omega_B\tau_e = 0$. (c) M1 model, for $\omega_B\tau_e = 0$.

(d) Braginskii's theory, for $\omega_B\tau_e = 0.1$. (e) SNB model, for $\omega_B\tau_e = 0.1$. (f) M1 model, for $\omega_B\tau_e = 0.1$.

(g) Braginskii's theory, for $\omega_B\tau_e = 0.5$. (h) SNB model, for $\omega_B\tau_e = 0.5$. (i) M1 model, for $\omega_B\tau_e = 0.5$.

Figure 8.13: Plasma electron temperature distribution, after 5 ps of relaxation to the thermal equilibrium. Dashed lines indicate the regions where monodimensional cuts have been performed. Upper line corresponds to the case without magnetic field, middle line to $\omega_B\tau_e = 0.1$ and bottom line to $\omega_B\tau_e = 0.5$. Three columns correspond to the Braginskii model (left), SNB model (center) and M1 model (right). Note that the temperature scale is changed from above, in order to higlight the shapes of gradients.

be find between Braginskii's, SNB and M1 predictions, shown in Fig. 8.13h and Fig. 8.13i, respectively. Horizontal and vertical cuts in Figs. 8.16a and 8.16b confirm that. Because of the flux reduction, heating effects require a longer time to appear. We need to perform a temporal analysis.

Figures 8.17a, 8.17b and 8.17c show a temporal evolution of the temperature profile, in the x-direction ($y \approx 14\lambda_0$), from 0 to 50 ps ($450\tau_e$), in steps of 10 ps ($90\tau_e$). As expected, temperature gradients decrease with time leading to a homogeneous temperature at the equilibrium. Considering the temperature difference evolution with time, $\Delta T_e(t) = \max[T_e(t)] - \min[T_e(t)]$, for $\omega_B\tau_e = 0$, the local theory predicts a faster thermalization then in nonlocal model, since the heating is not delocalized. The SNB and M1 models agree in this prediction. When we add a weak magnetization $\omega_B\tau_e = 0.1$, the thermalization time predicted by the Braginskii's theory is weakly reduced, while the Hall parameter is not sufficiently high to affect the nonlocal transport. So nonlocal models behave as in the case $\omega_B\tau_e = 0$.

A different result is obtained with a magnetization of $\omega_B\tau_e = 0.5$. In this case,

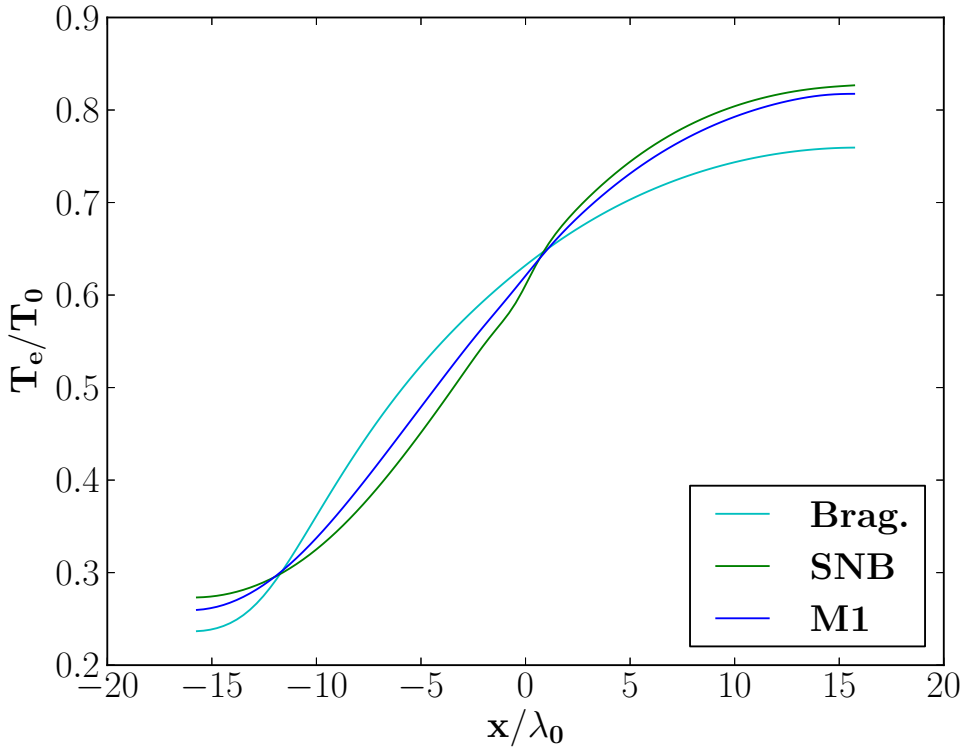

(a) Cut along the x-direction.

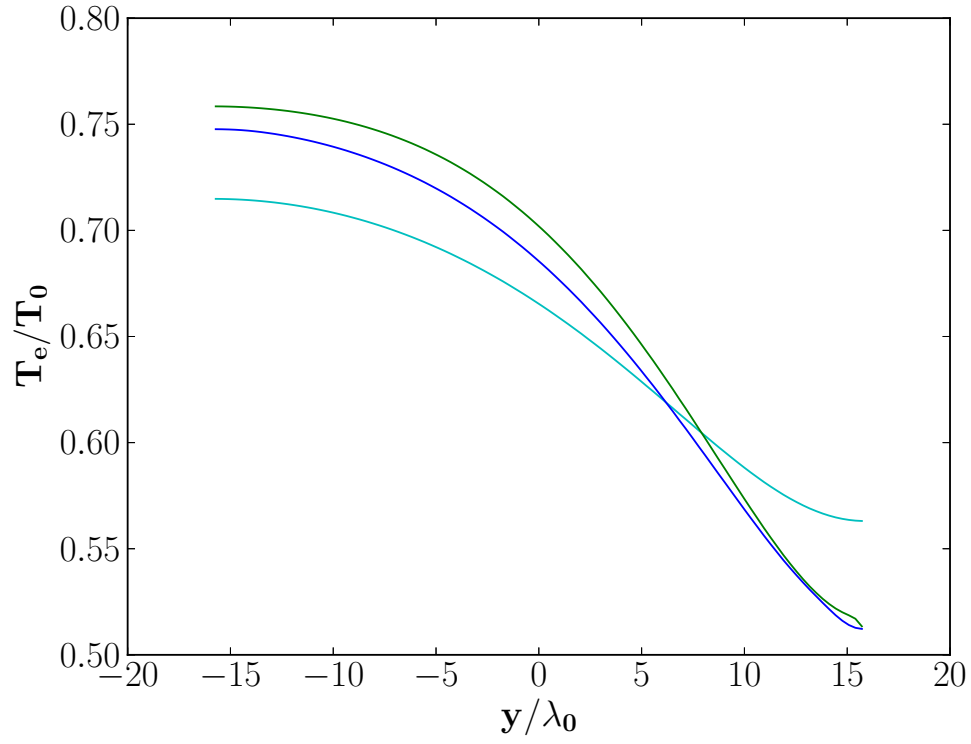

(b) Cut along the y-direction.

Figure 8.14: Cuts along the x and y-directions of the temperature profiles shown in Fig. 8.13, with $\omega_B \tau_e = 0$.

the magnetization is enough strong to affect both local and nonlocal models. In the local simulations the thermalization time is strongly increased because the heat flux is reduced. The SNB model gives a local heat flux. On the contrary, the M1 model predicts a thermalization time longer than the local model. This result is surprising, since it is opposite to usual expectations from the nonlocal effects. Its explication is related to the

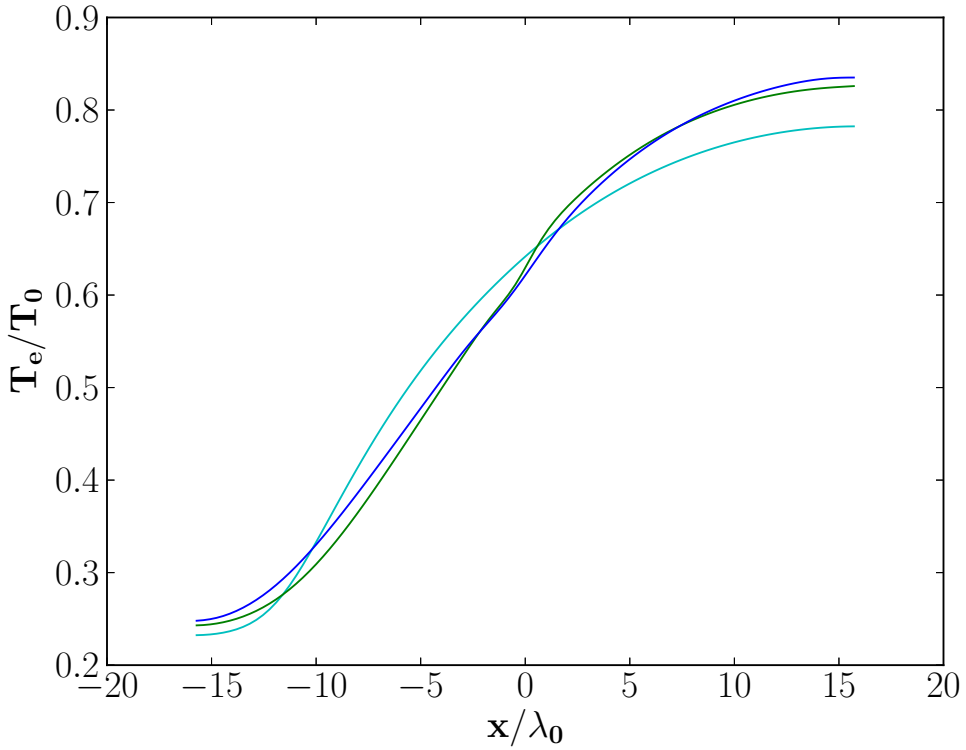

(a) Cut along the x-direction.

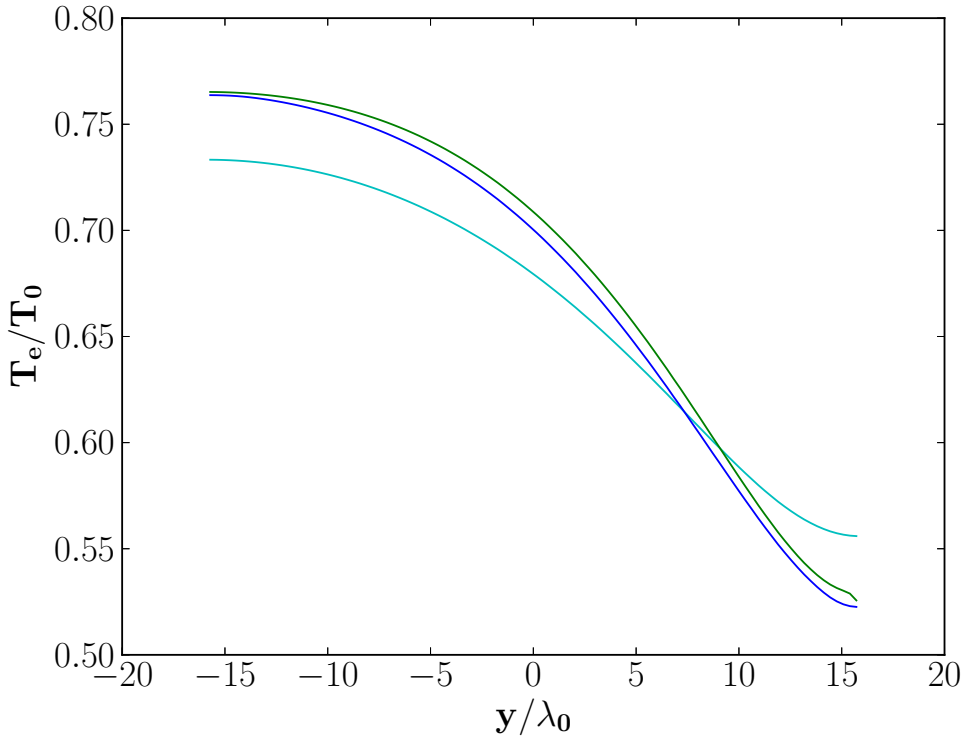

(b) Cut along the y-direction.

Figure 8.15: Cuts along the x and y-directions of the temperature profiles shown in Fig. 8.13, with $\omega_B \tau_e = 0.1$.

heat flux rotation, shown in Fig. 8.11d. This rotation is weaker in the M1 simulation because of nonlocal effects, leading to a configuration in which the horizontal component of the flux in $x \approx 0$ (main flux) is the same for the M1 model and for the Braginskii's theory. Nevertheless, in the nonlocal case, another flux is present: the preheating at $x \approx 3\lambda_0$, which is absent in the local case. The preheating flux is what increases the

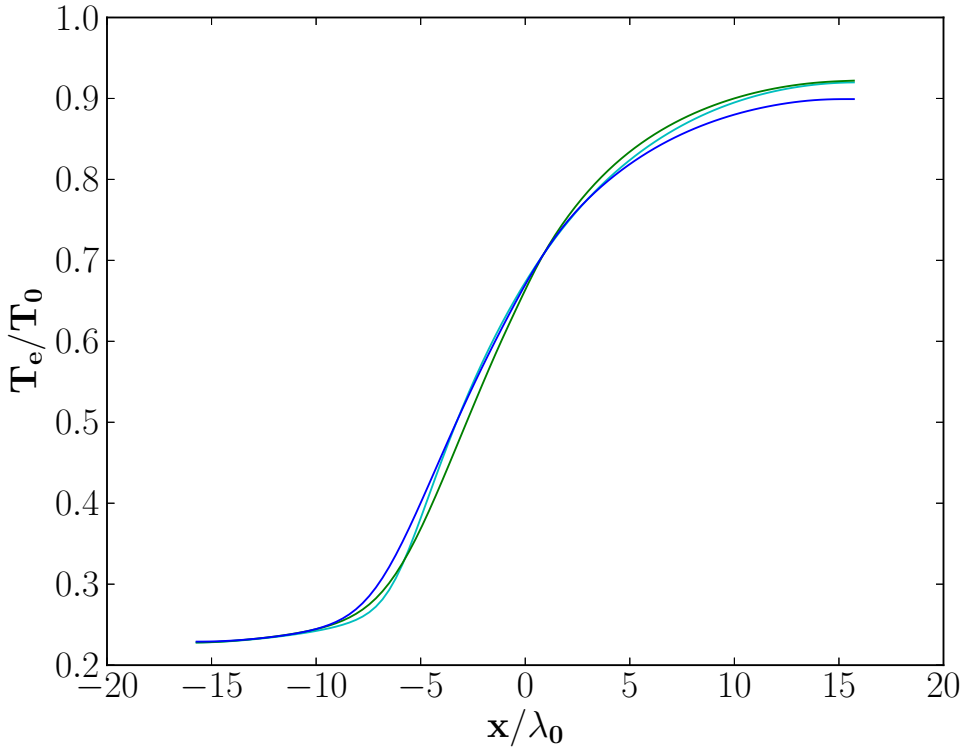

(a) Cut along the x-direction.

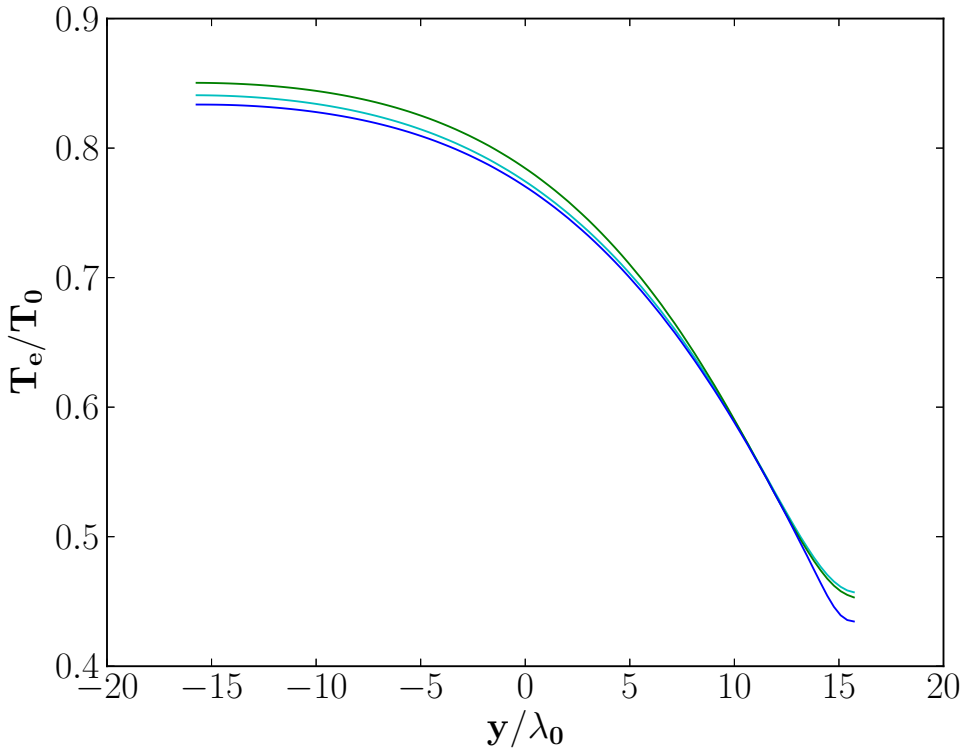

(b) Cut along the y-direction.

Figure 8.16: Cuts along the x and y-directions of the temperature profiles shown in Fig. 8.13, with $\omega_B \tau_e = 0.5$.

heating efficiency, in the horizontal direction.

Compared to the M1 model, the SNB model seems to overestimate the effects of magnetization. This difference is due to the different treating of magnetic fields, which, for the SNB model is phenomenological, while for the M1 model is more correct. For this

reason we suggest that the M1 prediction is more realistic, being based on more physical approximations. Nevertheless, a comparison with a Vlasov-FP simulation is required in order to validate this supposition.

8.4 On the magnetized transport

In this chapter we have applied the M1 model to study the magnetized plasmas.

We have demonstrated that the model is able to reproduce the Braginskii's theory, in the local regime. We have also studied the nonlocal limit. The magnetic field reduces nonlocal effects but also nonlocal transport reduces magnetic field effects.

We have also performed a temporal analysis of a thermal wave propagation through a magnetized plasma. The study has revealed that, for weakly magnetized plasmas, the thermalization takes more time with the nonlocal model than with the local one because of the flux-limitation. On the contrary, in strongly magnetized plasmas, nonlocal effects are reduced.

Magnetic fields can induce the heat flux rotation in the plane perpendicular to the direction of the magnetic field and the suppression of the nonlocal transport: the understanding of the magnetized nonlocal transport is important for the control of the ablation in the laser target interactions.

The temporal analysis has also revealed a weak disagreement between the M1 and the SNB model, since the latter seems to overestimate the effects of magnetization, compared to M1, which is based on more solid physical assumptions. Such a simulation, performed with the M1 model, has been run in the two-dimensional geometry for 50 ps, with 100×100 cells, a temporal step $\Delta t = 0.2$ ps and an energy step 0.05 times the CFL condition (6.12). The M1 model, in order to compute the nonlocal electric field, has been forced to iterate 5 times. In such a condition, the code takes 10 hours to compute 3 ps, indicating that the numerical scheme has to be improved to reach a reasonable computational time.

In conclusion the M1 model is able to deal with magnetized plasmas. Compared to the SNB model, due to its structure, it is based on more physical hypothesis, which increases the domain of validity of this description to more anisotropic regimes and to the kinetic scale.

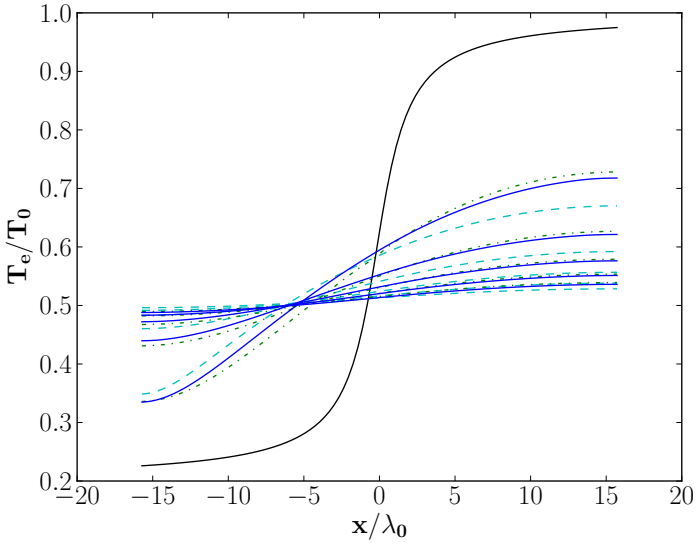

(a) $\omega_B \tau_e = 0.$

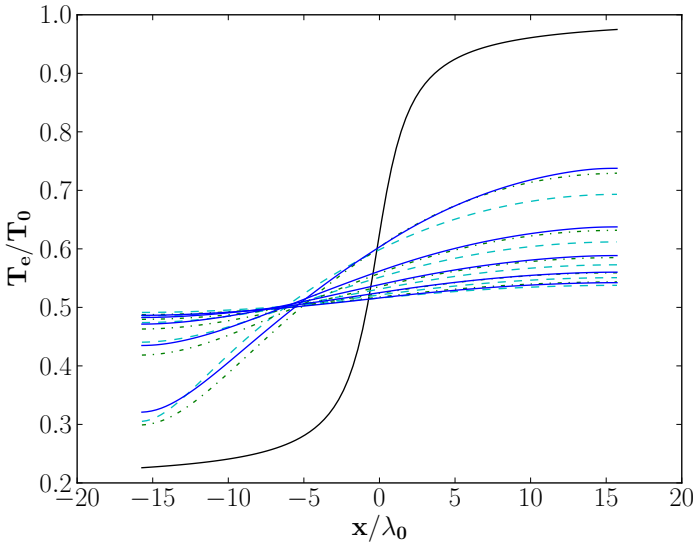

(b) $\omega_B \tau_e = 0.1.$

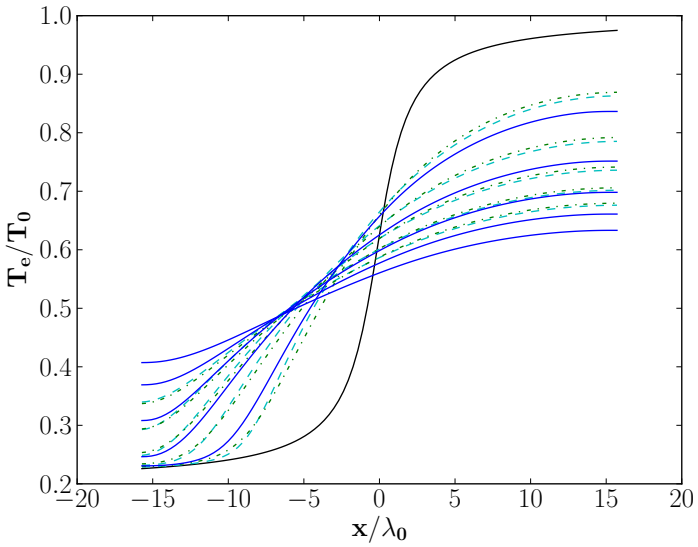

(c) $\omega_B \tau_e = 0.5.$

Figure 8.17: Temporal evolution of the temperature profiles along the x-direction. The black curve represents the initial condition, the subsequent curves represent, by steps of 10 ps, the temperature predicted by the local (dashed celestial lines), the SNB (dashed-dotted green lines) and the M1 (continuous blue lines) models, for different degrees of magnetization.

Chapter 9

Conclusions

This work is dedicated to the studies of the plasma electron transport, in the nonlocal regime. In this regime, kinetic effects become important and affect macroscopic quantities, such as heat fluxes and plasma waves.

Starting from first principles, we have developed a new approach to the description of the nonlocal electron transport, with the purpose of being simple and accounting for strong deviations from equilibrium, in angles and energies, considering the effect of electron transport on microscopic plasma stability and dealing with magnetized regimes. This model has to be fast enough to be implemented into a multidimensional hydrodynamic code.

9.1 Simplification of the kinetic equation

The model M1 is derived from the Landau-FP equation, which describes the time evolution of electrons in a plasma. However, this equation is too time consuming and, for our purpose, requires some simplifications.

Since the heat is transported by suprathermal electrons, the Landau collision operator has been reduced through the assumption of fast electrons colliding with a background of thermal electrons and inertial ions. This reduced collision operator conserves the number of particles, momentum and energy and respects the second law of thermodynamics. It has been simplified again, making explicit the thermalization and neglecting the energy diffusion term, compared to the friction term. This has led to the AWBS collision operator.

The AWBS collision operator conserves the number of particles but nor energy nor momentum, neither entropy. Nevertheless, it has shown good properties in the description of the energy losses of suprathermal electrons which thermalize. Moreover, it is also able to account for the different velocity-contributions. It has been compared with the simpler collision operator used in the nonlocal SNB model: the BGK operator. The latter does not conserve the number of particles. Comparisons between both models have shown a better treatment of heat-carrying electrons by the AWBS operator.

For both its simplicity and its precision, the AWBS collision operator has been chosen for the construction of our model. So the Landau-FP equation has been reduced to the AWBS-FP equation

$$\frac{\partial}{\partial t} f_e + \vec{v} \cdot \vec{\nabla} f_e + \vec{a} \cdot \vec{\nabla}_v f_e = \nu_{ee} v_e \frac{\partial}{\partial v} (f_e - f_e^m) + \frac{\nu_{ee} + \nu_{ei}}{2} \frac{\partial^2}{\partial \vec{\Omega}^2} f_e.$$

Continuing the simplification of the kinetic equation, we have analyzed the characteristic times. We have seen that the characteristic time evolution of kinetic systems, described by FP equations, is given by the effective collision time $\sim \sqrt{\tau_{ee}\tau_{ei}}$. Since this time is very short compared to the characteristic hydrodynamic time $\sim L_\nabla / c_s$ (with c_s

as the sound speed and L_∇ as the gradient length), electrons have the time to adjust themselves to the hydrodynamic conditions. It is reasonable to assume that the time derivative can be neglected, and to deal with a stationary equation.

Despite previous simplifications, the equation remains dependent from too many dimensions to be solved at any time step of a hydrodynamic code. To reduce once again the system, a moment integration of the AWBS-FP equation, over the velocity directions $\vec{\Omega} = \vec{v}/v$ has been performed.

The moment integration has led to the transformation of the AWBS-FP equation to a hierarchy of moment equations, each one dependent from the higher moment. The choice of the closure relation plays a key role in the physics we want to describe. The well-known classical P1 approach assumes linear anisotropies. This model has been developed and improved in this manuscript, for comparison with the M1 model.

The M1 model is based on an entropic argument: the underlying EDF maximizes the angular entropy

$$H_v[f_e] = -\int_{S_2} d^2\Omega \left(f_e \log f_e - f_e\right).$$

This entropic closure leads to a positively defined EDF and to a natural limitation of the flux. Moreover, we have seen that the M1 closure tends toward the P1 closure, in the limit of small anisotropies.

9.2 Calculation of electric and magnetic fields

In order to be closed, the M1 model requires a definition for electric and magnetic fields.

In the unmagnetized regime, the charge conservation implies a zero current condition. Associated with a simplified FP equation, this condition leads to an analytic form for the nonlocal electric field, which is function of the EDF moments. Numerically, it can be computed by iterating the M1 model, starting from a zero or a local electric field, till its convergence.

An analytic form for the electric field cannot be found in a magnetized plasma. We suggest to use the local equation as a starting iteration guess. This equation depends on the hydrodynamic quantities. In order to account for nonlocal effects, these quantities have been replaced by the moments of the EDF, calculated with the M1 model. The resulting electric field is obtained by iterations.

Magnetic field is assumed not to be modified by the kinetic effects and calculated with the magnetohydrodynamic code.

9.3 Numerical resolution

The AWBS collision operator, the quasi-stationary assumption, the assumptions on the electromagnetic fields and the moment hierarchy stopped at the first moment with an entropic closure constitute our M1 model. The kinetic equation is numerically solved in energy, proceeding from the highest to the lowest energy group. This preferred direction can be interpreted as an analogous of the causality principle: an electron can lose energy but not gain it. This algorithm works well for energy losses, which are accounted for with the AWBS collisional operator, but it is limited by the condition of a collisional stopping power higher than the electric field one.

Moreover, the algorithm is characterized by the appearance of a numerical diffusion, by solving an advective system in the diffusive limit. This can be overcame by increasing the spatial resolution but this procedure affects the computational time and the performance of the code.

For the reasons above, the algorithm presented is useful to validate the model but should be improved in order to become more practical in all regimes.

9.4 Validation of the model

The M1 model has been tested for unmagnetized plasmas [63], revealing agreement with Landau-FP code, and with the previous nonlocal models. The two main nonlocal effects (flux limitation and the preheating) are correctly computed.

It has been shown that EDF moments, computed with a P1 and a M1 closure, weakly disagree and that differences become negligible if integrated over velocities. The moments have been used in order to reconstruct the total EDFs, which has highlighted the main properties of the M1 model: the EDF is always well defined, unlike in the P1 model.

We have also tested the M1 model in a multidimensional configuration, reproducing the monodimensional nonlocal effects, plus the flux rotation, induced by the contribution of different gradients. We stress that before our model, only one model has shown to be able to work in two-dimensions: the SNB model.

The M1 model has also been tested for magnetized plasmas.

The first test of the M1 model in magnetized plasmas has been performed in the local regime, that is described with the Braginskii's theory. For all degrees of magnetization, the M1 model is able to reproduce the heat flux limitation and rotation, induced by magnetic fields.

We have studied the competition between nonlocal and magnetic effects and shown the predominance of each of them, in function of plasma conditions.

9.5 Application to the plasma wave stability

A kinetic analysis of the unmagnetized heat transport has been performed [63]: the study of the stream stability in a nonlocal plasma, induced by the transport along a temperature gradient.

An example is given by the Langmuir waves: high-frequency electron oscillations corresponding to the electric field perturbations on a microscopic scale. The nonlocal transport can perturb these waves, inducing the wave instability in the cold region of a plasma. Such a phenomenon has been studied with our M1 and P1 models. The M1 model has shown to be able to predict instabilities where expected. On the contrary, the P1 model has shown to predict also nonphysical instabilities where its total EDF becomes negative.

Also ion-acoustic waves can become unstable in the regimes of interest for the nonlocal transport. Their instability can be induced by an electron drift created by electric fields. In this case the M1 model has shown to work as well as the P1 model, since electrons involved are weakly anisotropic and in these conditions the M1 model tends to the P1 model.

9.6 Application to the thermal wave propagation

A propagation of a thermal wave through a magnetized plasma has been studied, in order to shed light on non-stationary effects of the magnetized nonlocal transport. This process has been analyzed considering different degrees of magnetization.

The stationary analysis has revealed that nonlocal fluxes require a higher degrees of magnetization, compared to their local counterpart, in order to be affected by magnetic fields.

The temporal analysis has also revealed a weak disagreement between the M1 and the SNB model, since the latter seems to overestimate the effects of magnetization, compared to the M1 model, which is based on better justified physical approximations.

The study has shown that in both nonlocal and magnetized regimes more time is required in order to smooth temperature gradients.

9.7 Perspectives

In summary, we have developed and successfully tested a new model for nonlocal transport [63]. This model, based on first principles, is able to

- account for strong deviations from equilibrium, in angles and energies;
- consider the effect of electron transport on microscopic plasma stability;
- account for external and self-generated magnetic fields.

Moreover, it works in multidimensional configurations.

Some issues are still open. Improvement on the numerical scheme should be considered, in order to account for the energy gain processes, which play a role in the heating of laser-cold matter interactions. A direct comparison with a Landau-FP simulation should be performed in order to definitively validate the M1 model at the kinetic scale and in the nonlocal magnetized regime. However, the already obtained results are promising.

The M1 model is based on the assumption of the angular entropy maximization principle, which assures the entropy maximization. This assumption has been already tested in highly anisotropic regimes, leading to correct results. This work constitutes a first test of the validity of the angular entropy maximization principle, in weakly anisotropic regimes, which adds reliability to this assumption.

The ability to account for strong deviations from equilibrium motivates the use of the M1 model for the description of the nonlocal transport. The modern theory of HED physics, especially the ICF, has shown the need of accounting for strongly anisotropic kinetic phenomena, such as relativistic electron beams or beams induced by parametric instabilities, in order to predict and control the energy transport. The M1 model, as it has been developed in this manuscript, can describe weakly as well as strongly anisotropic kinetic phenomena. Thus, the work provides a way to describe all kinetic phenomena in HED physics, with a single model.

Considering the effect of electron transport on the microscopic plasma stability, at hydrodynamic times, opens to future studies in order to account for them in transport predictions.

We have seen that magnetic fields can induce the flux rotation in a preferred direction and the suppression of the nonlocal transport. The comprehension of the magnetized nonlocal transport is related to the control of the ablation, which defines the compression performances of laser irradiated plasmas, with applications to astrophysical experiments and ICF.

Part IV

French Version: Une Approche Entropique au Transport Non local et aux Autres Phénomènes Cinétiques dans les Plasmas à Hautes Densités d'énergie

Chapter 10

Résumé court

Les simulations hydrodynamiques pour la physique de haute densité d'énergie ainsi que pour la fusion par confinement inertiel exigent une description détaillée de flux d'énergie. Le mécanisme principal est le transport électronique, qui peut être un phénomène non local qui doit être décrit avec des modèles de Fokker-Planck, stationnaires et simplifiés dans les codes hydrodynamiques à grande échelle.

Mon travail thèse est consacré au développement d'un nouveau modèle de transport non local basé sur l'utilisation d'une méthode de fermeture entropique pour la résolution des premiers moments de l'équation de Fokker-Planck agrémentée d'un opérateur de collision dédié.

Une telle fermeture permet une bonne résolution des fortes anisotropies de la fonction de distribution électronique dans les régimes où le développement d'instabilités électrostatiques à petite échelle le requiert. Ce modèle aux moments (M1) est comparé avec succès au modèle de Schurtz, Nicolaï et Busquet (SNB), référent dans le domaine du transport électronique non local. Ce modèle, basé sur l'hypothèse d'une faible anisotropie de la fonction de distribution sous-jascente induisant une relation de fermeture polynomiale (P1), utilise un opérateur de collision simplifié dont nous avons proposé une amélioration.

Après avoir considéré plusieurs configurations typiques de transport de chaleur, nous avons montré que le modèle M1 multidimensionnel peut prendre naturellement en compte des effets d'un plasmas magnétisés sur le transport électronique. De plus, ce modèle permet de calculer des fonctions de distribution utiles aux études cinétiques comme la stabilité du plasma dans la zone de transport.

Nous confirmons avec notre modèle que le transport d'énergie électronique peut fortement modifier l'amortissement des ondes de Langmuir et des ondes acoustiques ; contrairement aux modèles non locaux simplifiés, M1 décrit les modifications de la fonction de distribution et l'amortissement des ondes du plasma. La structure du modèle permet également de prendre en compte naturellement des champs magnétiques autogénérés, qui jouent un rôle crucial dans des simulations multidimensionnelles. Ces champs magnétiques pourraient également être étudiés pour concentrer l'énergie dans les schémas d'ignition. Enfin, nous montrons que le modèle M1 reproduit les résultats de la théorie locale élaborée par Braginskii pour tous les niveau de magnétisation et propose de nouveaux résultats pour le régime non local. Ce travail constitue une première validation de l'utilisation des fermetures entropiques, dans les régimes de faibles anisotropies, qui va s'ajouter aux tests dans les régimes fortement anisotropes.

MOTS-CLEFS: Fusion par confinement inertiel, Physique de haute densité d'énergie, Plasmas produits par lasers, Simulations hydrodynamiques, Transport de la chaleur non local, Stabilité microscopique du plasma.

Chapter 11

Introduction

La matière à l'équilibre thermodynamique peut être classée selon sa densité et sa température. La figure 11.1 montre, en fonction de ces paramètres, la plupart des états connus de la matière. Les axes suivent une échelle logarithmique, ce qui permet de représenter les différents régimes qui peuvent être trouvés dans l'univers.

En bas à gauche de la figure 11.1, on trouve la matière neutre. En augmentant la température (en ce déplaçant du bas vers le haut), la matière devient partiellement ionisée. En augmentant encore la température, on obtient un état où la pression totale (interne et de radiation) atteint la valeur de 1 Mbar, la matière devient entièrement ionisée et se trouve dominée par les effets radiatifs.

En partant du bas à gauche vers la droite (densité croissante), on rencontre deux

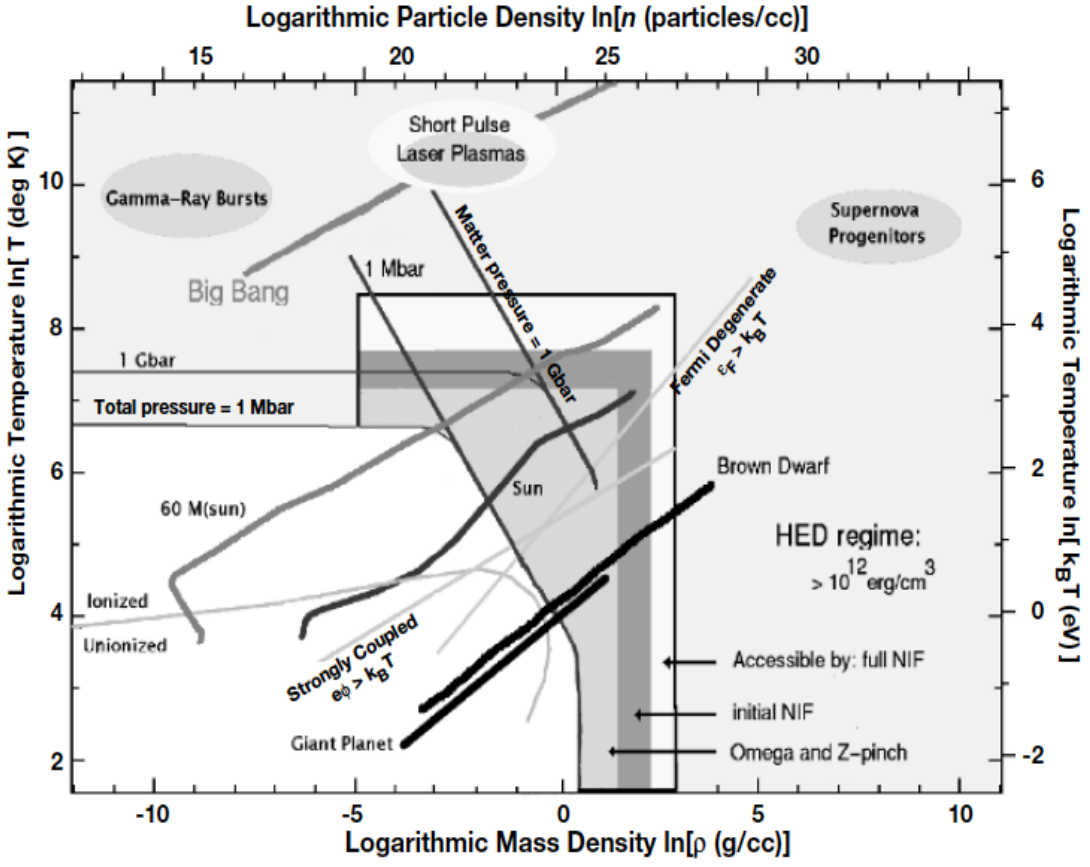

Figure 11.1: Les régimes de la physique à hautes densités d'énergie, classifiés par leur densité de masse (axe x) et leur température (axe y). La figure est issue du livre de R. P. Drake [1].

courbes : les frontières des plasmas fortement corrélés et dégénérés. Sous la courbe fortement couplée, les interactions multiples des particules définissent la structure de la matière. La courbe de dégénérescence sépare la matière classique (en haut) de la matière dans laquelle les effets quantiques électroniques sont dominants (en bas). On voit que les états fortement couplés et dégénerés s'étendent des états ionisés (plasma) aux états solides et liquides. Dans cette région de frontière on trouve la matière tiède et dense, un état particulier mélangeant les effets d'interactions multiples, quantiques et des plasmas. En augmentant la densité, on rencontre la courbe 1 Mbar, qui représente la région où la pression interne est comparable avec la densité d'énergie d'un atome d'hydrogène. La matière sous une telle pression se compose d'électrons et d'ions et non plus de particules neutres. Cette matière ionisée est considérée comme plasma, mais les théories des plasmas classiques ne peuvent être appliquées qu'aux gaz ionisés raréfiés. Les propriétés de la matière dense à une telle pression ne sont pas encore bien connues. Les systèmes soumis à une pression supérieure à 1 Mbar sont définis comme plasmas à hautes densités d'énergie [1] et sont représentés en gris, dans la figure 11.1.

De nombreux phénomènes astrophysiques appartiennent au domaine de la haute densité d'énergie.

Les étoiles et les planètes sont également représentées dans la figure, de leur cœur (au sommet de la courbe) à leur surface externe. Les naines brunes, autant que les planètes géantes, sont composées par différents états de la matière, s'étendant des hautes densités d'énergie aux états fortement corrélés et dégénérés. Notre Soleil, aussi bien que des étoiles plus massives, s'étend entre la haute densité d'énergie et la matière classique, ionisée et neutre.

Les explosions de rayons gamma sont les processus les plus énergetiques observés dans l'univers. Ils sont dans le régime dominé par les radiations, de la physique des hautes densités d'énergie (en haut à droite de la figure 11.1). Les dernières étapes de l'évolution du big bang font également partie de ce régime.

Dans cette figure on rencontre beaucoup de phénomènes naturels, situés dans le domaine des hautes densités d'énergie. Tous sont liés à l'astrophysique. Cependant, sur Terre, dans nos laboratoires, nous pouvons nous approcher de telles conditions, grâce, par exemple, au Z-pinch et aux lasers. Des lasers de générations futures pourront créer, pour des temps très courts, des plasmas correspondant aux conditions présentes dans les premiers stades du big bang. Au sein de la nouvelle génération de lasers très énergétiques, nous pouvons trouver le laser Omega, situé au Laboratory for Laser Energetics de l'Université de Rochester et le laser le plus puissant construit à ce jour : le National Ignition Facility (NIF), situé au Laurence Livermore National Laboratory. Les régimes de matière induits par ces lasers sont dans le domaine de la haute densité d'energie.

La recherche dans le régimes de la haute densité d'energie intéresse aussi bien l'astrophysique de laboratoire que la production contrôlée d'énergie nucléaire par confinement inertiel. On décrira plus en détail ces 2 points dans les sections 11.1 et 11.2. Dans la section 11.3 on présente la manière d'obtenir en laboratoire une matière à haute densité d'énergie, au moyen de lasers de puissance. Dans la section 11.4, on étudie un processus clé des interactions laser-matière, dans les régimes d'intérêt : le transport électronique. Finalement dans la section 11.5, nous présentons l'objectif de cette thèse et comment nous l'aborderons dans ce manuscrit.

11.1 Astrophysique de laboratoire

La physique des hautes densités d'énergie concerne les objets astrophysiques aussi bien que les plasmas créés par laser. Les lasers de haute énergie ouvrent de nouvelles perspectives pour étudier de nombreux phénomènes astrophysiques. Nous considérons deux exemples.

11.1.1 Dynamo dans les planètes géantes

En portant la matière à haute densité d'énergie en laboratoire on peut réaliser des études expérimentales sur les équations d'état dans des régimes extrêmes, qui ont un intérêt astrophysique. On peux aussi aborder l'étude des processus à l'œuvre à l'intérieur du cœur des planètes géantes, responsables de la génération de champs magnétiques planétaires [2, 3].

Particulièrement dans le cœur de Jupiter, la nature de la transition à l'état métallique contraint la manière dont les champs magnétiques peuvent être produits. Depuis longtemps la connexion entre les équations d'état et les champs magnétiques est connue, mais son étude expérimentale n'est devenue réalisable qu'à partir des années 1980, en raison de l'apparition de dispositifs d'énergie pulsée. Ils ont ouvert une possibilité d'accélérer des échantillons de matériaux à haute vitesse et de créer la matière à haute densité d'énergie par la collision de deux d'entre eux [1, 2].

11.1.2 Instabilités d'interface dans les supernovas avec un cœur collapsé

De nombreux processus astrophysiques sont regis par l'hydrodynamique. Les équations hydrodynamiques sont invariantes d'échelle : ce qui se passe dans un laboratoire, dans des petits intervalles de temps ($\sim$ ns), peut être généralisé à l'espace interstellaire et aux longues périodes de temps associées. De fait, les expériences de physique des hautes densités d'énergie peuvent reproduire des phénomènes astrophysiques, tels qu'ils se passent. Un exemple d'expérience bien rééchelonné est l'étude d'instabilités d'interface dans les supernovas avec un cœur collapsé [1, 4].

Les étoiles assez grandes, sont composées par des couches de matériaux différents. Les plus légers sont situés sur la surface tandis que le cœur est composé par le fer. La pression de gravitation comprime la matière et allume les réactions de fusion dans chaques couches de l'étoile, jusqu'au fer, qui est le noyau le plus stable. Une fois que l'étoile accumule une masse de Chandrasekhar (1.4 masse solaire) de fer, le cœur collapse, produisant une étoile à neutrons. En même temps, une onde d'explosion apparaît, provoquant une énorme augmentation de la luminosité observée. Cependant, seul un percentage de l'énergie hydrodynamique est émis comme lumière visible. Ceci est dû à un mouvement non symétrique, lié aux instabilités hydrodynamiques [5], montré dans la figure 11.2.

Les expériences, pour étudier le développement des instabilités hydrodynamiques dans une configuration convenablement adimensionnée ont été exécutées au début du vingt-et-unième siècle, dans le but de valider les codes par l'observation directe, grâce à une analyse tridimensionnelle [4]. En utilisant le laser de Nova, les auteurs de [4] ont examiné la perturbation initiale d'un unique mode sur une cible plate, reproduisant et validant la théorie.

On a vu deux exemples dans lesquels les prédictions de l'astrophysique de laboratoire peuvent être utiles à la physique des hautes densités d'énergie. Dans la section suivante on présente le second domaine principal de recherche dans la physique des hautes densités d'énergie : la fusion par confinement inertiel.

11.2 Fusion par confinement inertiel

Dans la section précédente nous avons dit que des expériences de physique des hautes densités d'énergie peuvent être réalisées pour reproduire des phénomènes astrophysiques. Cependant, certains processus comme le confinement gravitationel ne peuvent être reproduits en labo. Le but principal de la fusion par confinement inertiel est d'imploser la

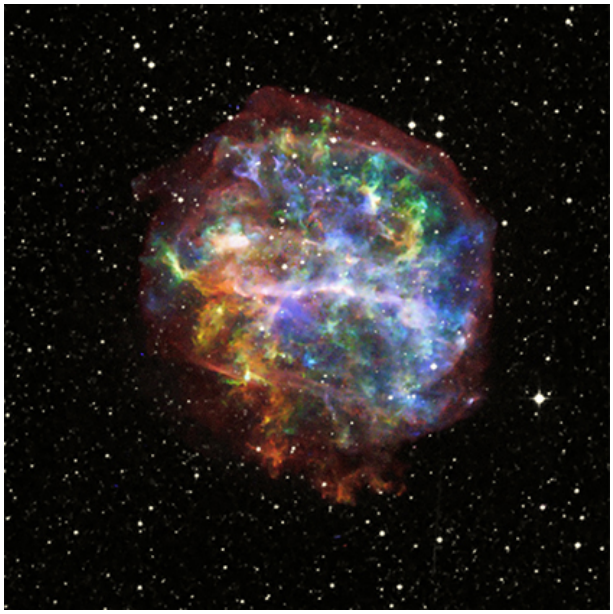

Figure 11.2: Instabilités hydrodyamiques dans une supernova avec un cœur collapsé.

matière en remplaçant la pression de gravitation avec une pression inertielle induite par les lasers très puissants. Les schémas de fusion par confinement inertiel essayent de comprimer une cible de deutérium-tritium, jusqu'à l'état permettant l'allumage des réactions de fusion nucléaires et de le confiner grâce à l'inertie de la cible. Ce comportement est décrit en détail dans ce qui suit.

11.2.1 Réactions nucléaires

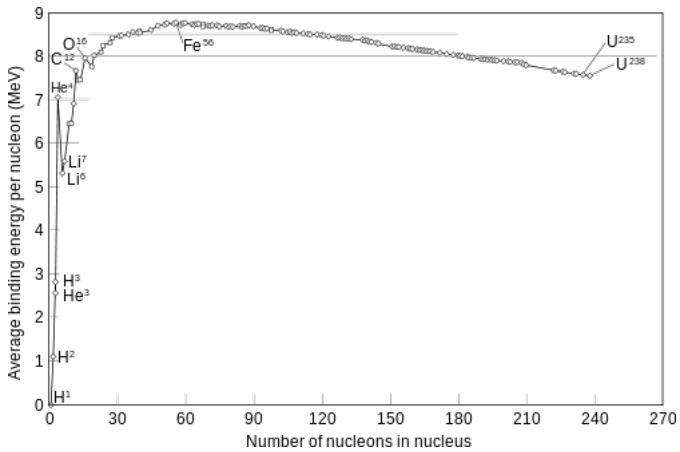

Figure 11.3: Énergie de liaison nucléaire par nucleon en fonction du nombre de nucleon.

La figure 11.3 montre l'énergie de liaison par nucleon en fonction du nombre de nucleons. On peut faire une distinction entre les noyaux plus légers et ceux plus lourds que le fer. Pour des noyaux plus lourds que le fer, l'énergie peut être gagnée en les divisant. Ce processus est appelé la fission et il est utilisé depuis les années 1940, pour créer de grandes quantités d'énergie.

Pour des noyaux plus légers que le fer, l'énergie peut être créée par la fusion de deux noyaux. Particulièrement, une des réactions les plus faibles à obtenir d'un point de vue énergique, est la fusion des isotopes d'hydrogène :

$$D + T \rightarrow {}^{4}\mathrm{He}(3.5\ \mathrm{MeV}) + \mathrm{n}(14.1\ \mathrm{MeV}), \tag{11.1}$$

où D et T sont les noyaux de deutérium et tritium, ^{4}He est le noyau d'hélium et n signifie neutron. La figure 11.4 récapitule la réaction schématiquement.

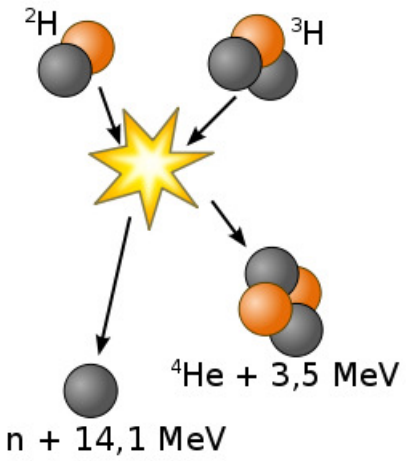

Figure 11.4: Schéma de la réaction D-T.

La figure 11.5 montre les conditions de témperatures nécessaires pour fusionner deux noyeaux. On voit qu'en dessous de quelques keV, la section efficace devient négligeable. De plus, les noyeaux doivent être en nombre suffisant et confinés suffisamment longetemps pour atteindre le critère d'allumage. Ce dernier est de la forme :

$$\tau_{fus} = \frac{1}{\langle \sigma v \rangle \, n_i},$$

Où n_i est la densité d'ions, σ est la section efficace de collision pour des interactions nucléaires et v la vitesse des ions. La condition d'allumage peut être exprimée comme

$$\tau_{fus} \langle \sigma v \rangle \, n_i > 1$$

et on la connaît comme le critère Lawson [6].

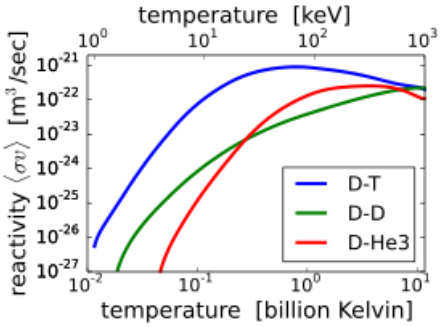

Figure 11.5: Réactivité, en fonction de la température, pour des noyeaux legers.

Dans des étoiles, les atomes sont confinés ensemble grâce à la gravitation.

Dans la fusion par confinement magnétique, le but est de réaliser le confinement du plasma en exploitant des champs magnétiques forts. En effet aucun materieaux ne peux supporter de telles températures. Ces champs confinent le plasma en forçant les particules à suivre des trajectoires hélicoïdales fermées. Le confinement le plus efficace est réalisé dans une machine appelée Tokamak, dont on peut voir la coupe dans la figure 11.6. Dans

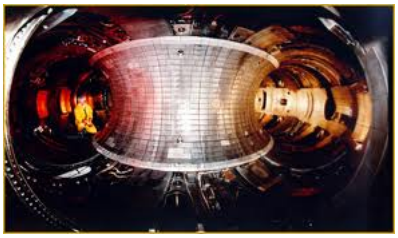

Figure 11.6: Interieur d'un réacteur Tokamak pour la fusion par confinement magnétique.

un Tokamak les densités de particules sont typiquement de l'ordre de 10^{14} cm^{-3}, pour une température de quelques keV [7]. Le temps nécessaire pour satisfaire le critère Lawson est ~ 1 s. Les Tokamak ont pour but d'opérer en régime stationnaire.

Il est également possible de confiner les noyeaux fusibles en exploitant l'inertie d'une cible induite par la compression des lasers. Cette approche est appelée fusion par confinement inertiel. Dans ce type de confinement la densité doit être augmentée à $\sim 10^{25}$ cm^{-3} et la température à ~ 10 keV [7]. En effet, dans ce régime, le temps de confinement, n'excede pas ~ 100 ps, du fait de la dislocation de la cible.

Dans la prochaine section on présente les différents schémas de fusion par confinement inertiel.

11.2.2 Schéma direct

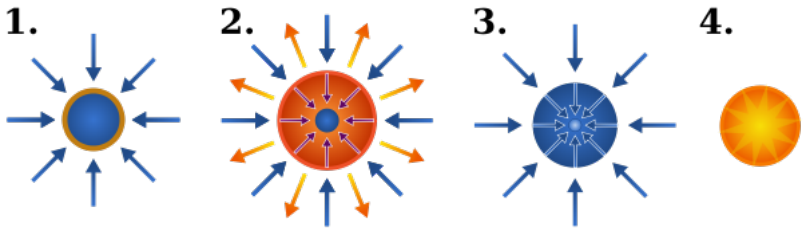

Figure 11.7: Schéma direct.

Historiquement, le premier schéma proposé pour obtenir la fusion par confinement inertiel, était un schéma direct [8]. Il est résumé sur la figure 11.7 : une cible sphérique, composée par un mélange équimolaire de deutérium et tritium est sphériquement illuminée par des lasers à très puissants (1). On utilise le dêpot de l'énergie du laser pour imploser la cible et transformer l'énergie cinétique en energie interne (2), jusqu'à atteindre une ignition centrale (3). Les conditions de densité et de température ne peuvent être maintenues que grâce à l'inertie de la masse (4) [7]. Cependant, jusqu'à présent, ceci n'est jamais arrivé, mettant en evidence un mauvaise compréhension des processus mis en jeu.

Ces processus sont liées à trois facteurs principaux [7]. Tout d'abord, l'uniformité de la compression semble insuffisante, en raison du développement d'instabilités hydrodynamiques, dûes aux imperfections de fabrication de la cible ou aux défauts d'éclairement laser. Deuxièmement, les prévisions théoriques négligent, ou approximent fortement, les effets cinétiques, qui peuvent jouer un rôle non négligeables dans les régimes d'intérêt. Ceux-ci sont liés, par exemple, au transport non local d'énergie par des électrons très énergiques. Enfin, les interactions laser-plasma non-linéaires et les instabilités paramétriques, comme la décomposition deux plasmons, ainsi que la retrodiffusion Brillouin et Raman, semblent mal décrites.

Bien que le premier point soit en dehors du champ d'investigation de cette thèse, nous presentons dans la section suivante differents schémas améliorant la stabilité de compression. Dans les parties I, II et III, nous présentons la partie principale de ce manuscrit, c'est à dire la modélisation du second point. En effet, un rôle dominant est joué par les effets cinétiques dans le transport d'énergie. On développe un modèle pour leur description, de telle façon qu'il puisse être généralisé à la description hydrodynamique d'autres effets cinétiques. L'analyse est réalisée en une et deux dimensions et une généralisation à trois dimensions peut être facilement effectuée.

11.2.3 Schémas stabilisants

Dans la section précédente nous avons vu qu'un des points importants pour le succès de l'ignition est le contrôle de la stabilité d'implosion. Dans la littérature, d'autres schémas ont été proposés, pour stabiliser la compression[9, 10, 11, 12].

Dans le schéma indirect [9] le but est de comprimer la cible, en utilisant un rayonnement de type corps noir, obtenue par l'éclairement de l'intereur d'une cavité d'or [13], comme montré dans la figure 11.8. De cette façon, la cible est soumise à un bain de ray-

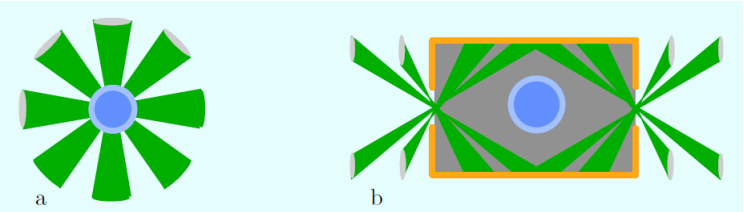

Figure 11.8: Deux schémas d'allumage : le direct (a) et l'indirect (b).

onnement bien plus homogène qu'en attaque directe. Ce schéma a été considéré comme l'approche la plus prometteuse pour réaliser la fusion nucléaire. Cependant, l'échec récent de la campagne d'ignition sur le NIF a mis en évidence un écart entre les prévisions théoriques, numériques et les résultats expérimentaux. Même une fois que l'ignition sera réalisée, ce schéma possède un rendement en énergie plus faible, comparé à celui de l'approche directe.

Ces dernières années, les développements des lasers d'impulsions pétawatt ont ouvert de nouvelles possibilités. L'idée principale du schéma d'allumage rapide [10, 7] est d'allumer le combustible précomprimé par un vecteur externe, séparé. Ce vecteur consiste en un faisceaux d'électrons relativistes, accélérés par une impulsion laser ultra-intense ($\sim 10^{19}$ W/cm^2). Ces électrons doivent se propager sur une grande distance entre la zone du dépôt laser et la partie compressée de la cible. Cette distance peut être réduite à une centaine de microns grâce à l'introduction d'un cône dans la cible, comme le montre la figure 11.9. La séparation de la phase de compression de la cible, de la phase de formation du point chaud simplifie le design des cibles. Il exige toujours une forte compression du combustible, pour garder l'énergie d'allumage, mais il permet de relâcher significativement les exigences de symétrie. Cependant, dans [14], il a été montré que la collimation du faisceau électronique ne peut pas être facilement réalisée. Des améliorations récentes proposent une utilisation de champs magnétiques externes pour augmenter le guidage et la collimation du faisceau [15].

Le schéma d'allumage par choc [11, 12] consiste en l'envoi d'un choc fort, à la fin de la phase de compression, montrée sur le panneau (3), de la figure 11.7. Ce choc est induit par une impulsion laser de forte puissance, environ $200 - 300$ TW. Une implosion typique est présentée sur la figure 11.10 [16]. S'il est synchronisé, le choc convergent rencontre le choc

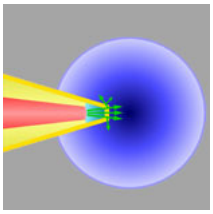

Figure 11.9: Schéma d'allumage rapide.

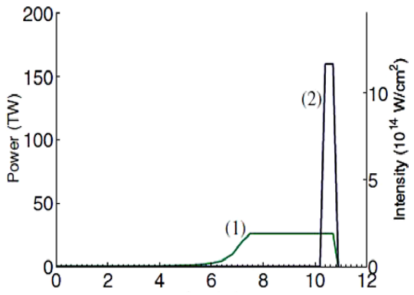

Figure 11.10: Impulsion lasers dans le schéma d'allumage par choc : (1) l'impulse de compression et (2) l'impulsion de choc.

principal au moment de sa divergence. Le choc transmis au centre, après la collision, surchauffe le cœur de la cible, induisant l'allumage. Cette approche réduit significativement l'énergie exigée, qui pourrait être obtenue avec les lasers existants. Cependant, à ces régimes, les interactions laser-plasma sont fortement non-linéaires et les effets de transport d'énergie non local deviennent importants. Cette méthode fait actuellement l'object de recherches actives et les premiers résultats sont encourageant [16].

11.3 Interactions laser-matière aux régimes de la physique des hautes densités d'énergie

Dans les sections précédentes nous avons vu que la physique expérimentale des hautes densités d'énergie ouvre un large domaine d'application. Le but de cette section est de montrer comment porter la matière à des hautes densités d'énergie en laboratoire.

Il y a deux façons principales de produire les conditions d'hautes densités d'énergie pour nos régimes d'intérêt : les Z-pinch et les lasers.

La compression dans un Z-pinch consiste dans l'exploitation d'un courant électrique axial, qui produit un champ magnétique azimutal compressant cylindriquement le plasma [17]. Dans ce manuscrit on s'intéresse principalement à la matière des hautes densités d'énergie, produite par laser. On ne détaillera donc pas ce processus et on se concentrera sur l'utilisation des lasers.

La compression laser directe est conduite par des lasers intenses, ayant des intensités s'étendant entre 10^{14} et 10^{15} W/cm^2. Une description détaillée de l'interaction laser-matière à ces régimes peut être trouvée dans [7]. Nous récapitulons les processus principaux dans ce qui suit.

Les faisceaux lasers ne peuvent se propager au sein du plasma, au delà d'une certaine densité, appelée densité critique, qui dépend seulement de la longueur d'onde laser. Dans les unités cgs, elle est

$$n_c = 1.1 \times 10^{21} \lambda_L^{-2} \text{ cm}^{-3}, \tag{11.2}$$

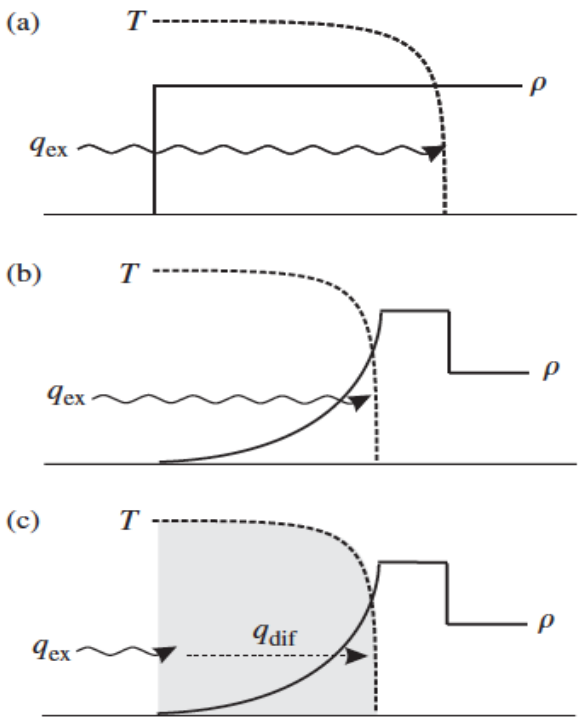

Figure 11.11: Les types de chauffage induits par interaction laser-matière : (a) le chauffage supersonique, (b) le chauffage ablatif et (c) le chauffage ablatif optiquement épais. La figure est prise de [7].

où λ_L doit être exprimé en μm. Cette densité est typiquement 1-2 ordres de grandeur plus petite que la densité du solide, cependant, une partie de l'énergie déposée pénètre plus profondément dans le plasma. L'absorption d'énergie laser diminue quand la température augmente.

On considére une cible solide illuminée par une source laser externe, de flux d'énergie q_{ex}. Aux premiers instants d'interaction, le laser chauffe directement la cible solide, comme indiqué dans le panneau (a) dans la figure 11.11. Puisque l'absorbtion diminue avec la température, comme le solide est chauffé, la radiation peut pénétrer plus en profondeur.

Après quelques dizaines de picosecondes, l'augmentation de température induit une augmentation de pression et un mouvement hydrodynamique, appelé flux d'ablation, qui peut produire une onde de choc dûe à la conservation du moment. Une onde de choc est une discontinuité dans le profil de densité, comme indiquée dans la figure 11.12. Les équations Rankine-Hugoniot réagissent à sa dynamique. Pour les gaz parfaits, la densité originale, derrière le choc, peut être augmentée de quatre fois.

Pendant que l'onde de choc se propage à l'intérieur de la cible, une onde de raréfaction se propage dans la direction opposée, incitant l'ablation. Le recul du moment comprime la matière encore plus. Si la cible est optiquement mince, comme dans le panneau (b) de la figure 11.11, l'ablation est directement induite par la source laser externe. Au contraire, si elle est optiquement épaisse, l'énergie laser est déposée à la densité critique. De là, elle est transportée au front d'ablation avec le flux de chaleur q_{dif}, voir le panneau (c) dans l'image 11.11. Pour des matériaux avec une numéro atomique petit ou intermédiaire, ce flux de chaleur est dû au transport électronique. Pour des matériaux avec une haute charge ionique, le transport radiatif est également important. Les panneaux (b) et (c) dans l'image 11.11 correspondent au régime quasi-stationnaire. Le cas (c) est partic-

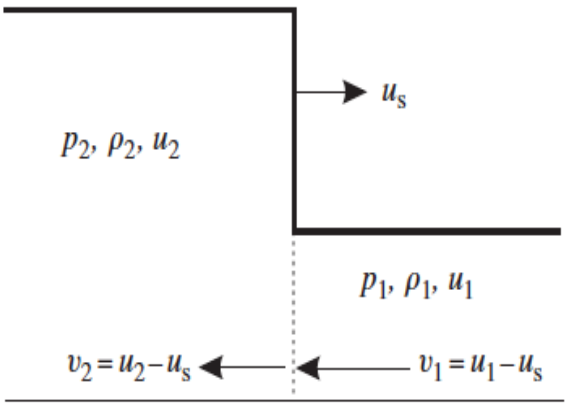

Figure 11.12: Schéma d'ondes de choc.

ulièrement intéressant pour la physique des hautes densités d'énergie. Dans ce manuscrit, on considére des matériaux numéro atomique faible et intermédiaire et on se concentre sur le transport électronique.

En résumé, dans le régime quasi-stationnaire des plasmas faits de matériaux avec un numéro atomique faible et intermédiaire, le laser pénètre dans la couronne (zone sous dense) de la cible et dépose son énergie jusqu'à la densité critique. De la zone critique, l'énergie est transportée par la conduction de chaleur électronique, jusqu'au front d'ablation. Cette région est appelée la zone de conduction et apparait en gris dans la figure 11.11 (c). L'énergie déposée dans la partie dense de la cible induit le processus d'ablation. Au dela, par réaction apparait la région choquée, qui est dans un état de matière tiède et dense. Enfin plus en amont, on rencontre le front de choc et, après, le solide non perturbé.

Le régime stationnaire se termine quand le choc atteint le côté arrière de la cible. Si le laser continue d'illuminer la cible, une phase d'accélération commence. Si la cible est sphériquement ou cylindriquement irradiée, comme indiqué sur la figue 11.13, la phase d'accélération mène à la compression de la cible. Les deux types de compression mènent aux régimes de hautes densités d'énergie.

Dans cette section, on a vu comment on peut créér la matière de hautes densités d'énergie. Particulièrement, pour les plasmas auxquels nous nous intéressons dans ce manuscrit, nous avons vu que le rôle-clé est joué par le transport électronique. Ce processus est présenté en détail dans la section suivante.

11.4 Entropie et transport électronique

Les particules dans un plasma (électrons et ions) suivent les lois de la mécanique classique [18]. Elles entrent en collision et dérivent sous l'action des champs électromagnétiques. Leurs quantités macroscopiques (moyennées) sont caractérisées par la température, la densité et la pression.

Une inhomogénéité spatiale de ces paramètres donne naissance au phénomène de transport.

Boltzmann et Maxwell ont développé une approche statistique [19], une théorie cinétique, décrivant les systèmes hors équilibre composés de nombreuses particules. La princi-

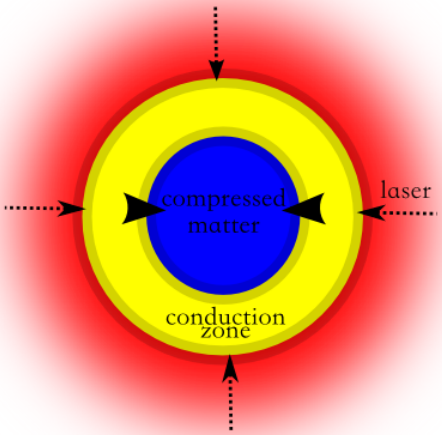

Figure 11.13: Compression sphérique d'une cible.

pale propriété de ce processus cinétique dans un système fermé est la perte d'information ou, en d'autres mots, l'augmentation du désordre, ce qui macroscopiquement correspond à une augmentation de l'entropie (H théorème). L'équilibre thermodynamique correspond à un état ou l'entropie est maximum.

La direction temporelle vers les états plus probables, décrite par le H théorème , brise la symétrie temporelle, menant au monde macroscopique du transport quantitatif comme nous le voyons.

Dans ce manuscrit nous étudierons principalement le transport électronique qui est lié aux mouvements des électrons induits par les inomogénéités spatiales de densité et de température. Dans la théorie hydrodynamique, dans laquelle l'échelle des inhomogénéités caractéristiques est bien plus grande que le libre parcours moyen des électrons, elle est décrit par une équation de diffusion. Cette équation correspond aux régimes proches de l'équilibre thermodynamique local, ce qui n'est pas toujours le cas dans les conditions de la physiques des hautes densités d'énergie. Ci dessous nous résumons les cas où cette hypothèse de diffusion locale n'est pas valable.

Dans le schéma d'allumage rapide l'énergie est transmise au plasma par un faisseau d'électrons relativistes qui est fortement anisotrope. Ce processus cinétique ne peut être décrit par les théories hydrodynamiques. Touati et al. [20] ont utilisé un modèle cinétique basé sur une direction principale du transport et sur une hypothèse de maximisation de l'antropie angulaire locale pour de tenir compte du fort degré d'anisotropie de la fonction de distribution électronique (EDF).

Les interactions laser-matière non linéaires deviennent importantes pour des intensités supérieures à $\sim 10^{15}$ W/cm^2. Elles peuvent générer des faisseaux électroniques très énergétiques et très anisotropes [7]. Le transport de ces électrons joue un rôle clé dans les processus d'implosion menée par laser, en particulier dans le schéma d'allumage par choc [16].

La physique des hautes densités d'énergie s'intéresse à des régimes où l'échelle des inhomogénéités de température se rapproche du libre parcours moyen des électrons. Ainsi les électrons chauds peuvent pénétrer et déposer leur énergie profondemment dans les régions froides, ne laissant pas de temps pour la thermalisation. Ce genre de transport est apellé non local car les électrons se déplacent à l'échelle hydrodynamique.

L'une des quantité les plus modifiées par les effets non locaux est le flux de chaleur, ce

dernier est régit par les électrons suprathermiques. Il peut être significativement modifié, comparé à la limite de diffusion classique, modifiant ainsi les simulations plasma et leur stabilité à une échelle microscopique.

Les modèles non locaux proposés dans [21, 22, 23] sont basés sur des hypothèses phénomènologiques et sont limités à la description des flux de chaleur dans des conditions de faible écart à l'approximation de diffusion. En particulier le modèle monodimensionnel de Liciani Mora et Virmont [21] décrit le flux de chaleur non local comme une combinaison de flux locaux, avec un coefficient phénomènologique dépendant du libre parcours moyen. Ce modèle n'a pas été généralisé aux configurations multidimensionnelles et aux forts gradients de température. Le modèle de Schutz Nicolaï et Busquet [22] (SNB) généralise l'expression du flux de chaleur à trois dimensions et tient compte de la dépendance du libre parcours moyen de l'électron avec son énergie. Cela a été réinterprété comme une approche cinétique pour les électrons suprathermiques avec un modèle collisionnel phénomènologique fortement simplifié. Le champ électrique est induit par le courant de retour des électrons froids. Son effet sur les électrons suprathermiques est considéré comme une réduction empirique du libre parcours moyen. Ce modèle est limité aux petites anisotropies. Sa généralisation afin de tenir compte des effets du champ magnétique [24] est mathématiquement compliqué.

Enfin par les modèles utilisé, celui développé par Colombant, Manheimer et Goncharov [23] la séparation des contributions thermiques et suprathermiques est directement effectuée par les propagateurs de flux de chaleur, dont les coefficients sont donnés par des arguments cinétiques phénomènologiques. Ce modèle n'a pas été généralisé ni à trois dimensions ni aux plasmas magnétisés, et est plus cher en temps de calcul que le modèle SNB [25].

Notre but est de généraliser l'approche entropique du modèle M1, utilisé pour des faisseaux d'électrons relativistes [20, 26], au transport non local d'électrons suprathermiques afin d'améliorer la description du transport électronique dans les cas de forts gradients de température et de champs magnétiques externes.

11.5 Objectifs et structure de la thèse

Les objectifs de ce travail de thèse sont les suivants.

- **Deriver un modèl du transport électronique, capable de décrire les fortes déviations à l'équilibre, en angles et en énergies** Cette propriété est caractéristique de la description cinétique qui est chère en temps de calcul. Notre but est de réduire cette description à deux étapes. Dans un premier temps nous simplifierons le modèle collisionnel, avec l'hypothèse que le transport électronique est principalement dû aux électrons suprathermiques qui entrent en collision avec les électrons thermiques et les ions. Dans un second temps nous diminuerons le nombre de dimensions au travers des moyennes angulaires de l'équation réduite, fermée grâce au principe de maximisation de l'entropie angulaire. Cette fermeture définira notre modèle M1 comme une fonction exponentielle de l'angle qui permettra de préserver cette description même par des fortes anisotropies angulaires.

- **Considérer l'effet du transport électronique sur la stabilité microscopique des plasmas.** La description cinétique effectuée par notre modèle tiendra compte de toutes les contributions énergétiques et proposera une meilleure description de la fonction de distribution des électrons comparée aux modèles basés sur une hypothèse d'anisotropie linéaire. Il permettra l'étude des effets cinétiques à petite échelle, comme le développement d'instabilités microscopiques induites par le transport électronique dans le cadre de la description hydrodynamique. Des exemples

d'instabilités de plasmas électroniques et d'ondes acoustiques-ioniques, modifiées par le flux de chaleur, seront présentées et comparées à la description linéaire en angle.

- **Adapter le modèle du transport électronique aux champs magnétiques externes et auto-génerés.** Les modèles locaux et non locaux qui décrivent le transport d'électrons thermiques magnétisés sont mathématiquement très compliqués car ils sont fonction de coefficients de transport tensoriels. Notre modèle s'attaquera à ce problème d'une façon différente. Comme l'équation cinétique réduite tient compte du champ magnétique, il sera mathématiquement simple et basé sur des hypothèses plus physiques. Cette adaptation aux régimes magnétisé est obtenue en définissant le champ électrique non local magnétisé grâce à des hypothèses phénoménologiques.

Le manuscrit est organisé en trois parties. Dans la partie I, l'état de l'art de la physique des plasmas et des théories non locales du transport sont résumés. La partie II traite du développement théorique de notre modèle non local, appelé M1. Dans la partie III, le modèle M1 est appliqué à la description du régime non local des plasmas de hautes densités d'énergie.

Plus en détail, dans le chapitre 2, les théories principales pour la description de la physique des plasmas (la théorie cinétique, l'électrodynamique classique et l'hydrodynamique) sont discutées. Dans le chapitre 3 l'état de l'art des théories non locales du transport est détaillé, présentant une perspective historique des modèles développés et mettant en évidence ceux qui jouent un rôle-clé dans le manuscrit. Dans le chapitre 4 une analyse d'opérateurs de collision réduit est realisée, pour choisir le plus approprié. Dans le chapitre 5, le modèle M1 est développé, tandis que sa mise en œuvre numérique est discutée dans le chapitre 6. Les applications stationnaires du modèle M1 aux plasmas non magnétisés sont étudiées dans le chapitre 7 et aux plasmas magnétisés, dans le chapitre 8. Finalement, les conclusions sont tirées dans le chapitre 12.

Chapter 12

Résumé long et conclusions

Ce travail est dédié à l'étude du transport électronique au sein du plasma dans le régime non local. Dans ce régime les effets cinétiques deviennent importants et modifient les quantités macroscopiques telles les flux de chaleur et les ondes plasma.

Nous avons développé une nouvelle approche pour la description du transport non local des électrons, basée sur des principes fondamentaux, avec pour objectif d'être simple et de tenir compte de fortes déviations hors équilibre en angle et en énergie tout en considérant l'effet du transport électronique sur la stabilité du plasma à l'échelle microscopique ainsi que par des régimes magnétisés. Le modèle ainsi développé doit être suffisamment rapide pour être inclu au sein d'un code hydrodynamique multidimensionnel.

12.1 État de l'art

Il existe plusieurs façons de décrire un plasma. La plus détaillée est la description cinétique. Cette description est basée sur des suppositions probabilistes. Néanmoins cette théorie est chère en temps et il est pas raisonnable de l'utiliser pour décrire les processus qui ont lieu sur plus de quelque temps de collision. Pour décrire ces processus, une théorie moyennée doit être utilisée. Ainsi, les équations hydrodynamiques sont basées sur des moyennes sur les moments en vitesse, ce qui réduit le nombre de variables à traiter. Mais cet ensemble d'équations doit être fermé avec, entre autres choses, une relation pour le flux de chaleur électronique.

D'autre part, les codes hydrodynamiques assument d'être près de l'équilibre thermodynamique local. Cette supposition impose des gradients de température suffisamment long, comparé au libre parcours moyen électronique, de telle façon que la chaleur est déposée localement. Physiquement, le transfert d'énergie sur de longues distances peut provoquer un déséquilibre de la fonction de distribution électronique, car la chaleur est transportée par des électrons suprathermiques ($\sim 3.7 v_{th}$). Quand des gradients de température deviennent raides, c'est-à-dire quand le libre parcours moyen électronique surpasse 2×10^{-3} la longueur de gradient de température, la théorie locale n'est plus valables et des modèles non locales sont nécessaires.

12.2 Simplification de l'équation cinétique

Le modèle non local M1 à été dérivé de l'équation Landau-FP, qui décrit l'évolution temporelle des électrons dans un plasma. Cependant, cette équation, complexe et chère en temps de calcul pour notre étude, requière quelques simplifications.

Comme la chaleur est transportée par les électrons suprathermiques, l'opérateur de collisions Landau a été réduit grâce à l'approximation selon laquelle les électrons rapides

n'entrent en collision qu'avec les électrons thermiques et les ions inertiels. Cet opérateur de collision réduit conserve le nombre de particules, le moment et l'énergie du système, il respecte également la seconde loi de la thermodynamique. Il a été à nouveau simplifié, pour rendre explicite la thermalisation en négligeant le terme de diffusion énergétique comparé au terme de frottements. Ceci a mené à l'opérateur de collisions dit AWBS [42].

L'opérateur de collision AWBS ne conserve que le nombre de particules. Néanmoins il a montré de bonnes propriétés dans la description des pertes d'énergie d'électrons suprathermiques qui se thermalisant. De plus il est capable de considérer les différentes contributions en vitesses. Il a été comparé à l'opérateur de collision, plus simple, utilisé dans le modèle non local SNB : l'opérateur BGK. Ce dernier ne conserve pas le nombre de particules. La comparaison des deux modèles a montré un meilleur traitement des électrons porteur de chaleur par l'opérateur AWBS.

À la fois pour sa simplicité et sa précision, l'opérateur de collision AWBS a été choisi pour la construction de notre modèle. Ainsi l'équation Landau-FP a été réduit à l'équation AWBS-FP suivante

$$\frac{\partial}{\partial t} f_e + \vec{v} \cdot \vec{\nabla} f_e + \vec{a} \cdot \vec{\nabla}_v f_e = \nu_{ee} v_e \frac{\partial}{\partial v} (f_e - f_e^m) + \frac{\nu_{ee} + \nu_{ei}}{2} \frac{\partial^2}{\partial \vec{\Omega}^2} f_e.$$

En poursuivant la simplification de l'équation cinétique, nous avons analysé les temps caractéristiques. Nous avons vu que le temps caractéristique d'évolution des systèmes cinétiques, décrit par les équations FP, est donné par le temps de collision effectif $\sim \sqrt{\tau_{ee}\tau_{ei}}$. Comme ce temps est très court comparé au temps caractéristique hydrodynamique $\sim L_\nabla / c_s$ (avec c_s la vitesse du son et L_∇ la longueur du gradient), les électrons ont le temps de s'ajuster aux conditions hydrodynamiques. Il est raisonnable d'assumer que le terme de dérivée temporelle peut être négligé, et ainsi d'utiliser une équation stationnaire.

En dépit des précédentes simplifications l'équation reste dépendante de trop de dimensions pour être résolue à chaque itération temporelle d'un code hydrodynamique. Pour réduire à nouveau le système nous avons effectué une série intégrations aux moments de l'équation AWBS-FP selon les directions des vitesses $\vec{\Omega} = \vec{v}/v$.

Cette intégration a mené à la transformation de l'équation AWBS-FP en une hiérarchie d'équations aux moments, chacune dépendante du moment supérieur. Le choix de la relation de fermeture joue un rôle clé dans la physique que nous voulons décrire. L'approche classique, bien connue, basé sur l'utilisation de polynôme de Legendre, le modèle P1, suppose des anisotropies linéaires. Ce modèle a été développé et amélioré dans ce manuscrit afin de le comparer au modèle M1.

Le modèle M1 est basé sur un argument entropique : la fonction de distribution électronique maximise l'entropie angulaire

$$H_v[f_e] = -\int_{S_2} d^2\Omega \, (f_e \log f_e - f_e) \, .$$

Cette fermeture entropique mène à une fonction de distribution électronique définie positive ainsi qu'à une limitation naturelle du flux. De plus nous avons vu que la fermeture du modèle M1 tend vers celle du modèle P1 dans la limite des faibles anisotropies.

12.3 Prise en compte des champs électrique et magnétique

Afin d'être fermé, le modèle M1 demande une définition pour les champs électriques et magnétiques.

Dans le régime non magnétisé, la conservation des charges implique une condition de courant nul. Associée à une équation FP simplifiée cette condition mène à une forme semi-analytique du champ électrique non local qui dépend des moments de la fonction de distribution électronique. Numériquement on le calcule par itération du modèle M1 en partant d'un champs électrique local ou nul jusqu'à convergence.

Il est impossible d'obtenir une forme simple du champ électrique pour un plasma magnétisé. Nous proposons d'utiliser l'équation locale comme point de départ des itérations. Cette équation dépend de quantités hydrodynamiques. Afin de tenir compte des effets non locaux ces quantités ont été remplacées par les moments de la fonction de distribution des électrons, calculée avec le modèle M1. Le champ électrique est obtenu de manière iterative.

Nous considérons que le champ magnétique n'est pas modifié par les effets cinétiques, et est calculé grâce à un code magnéto-hydrodynamique.

12.4 Résolution numérique

L'opérateur de collision AWBS, l'hypothèse de quasi stationnarité, les hypothèses sur le champ électromagnétique et la hiérarchie des moments limitée au premier moment avec la fermeture entropique constituent notre modèle M1. L'équation cinétique est résolue numériquement en énergie, du groupe en energie le plus haut vers le plus bas. Cette direction préférentielle peut être interprétée comme un analogue du principe de causalité : un électron peut perdre de l'énergie mais pas en gagner. Cet algorithme fonctionne bien pour les pertes d'énergie, calculée avec l'opérateur collisionnel AWBS, mais il est limité par le fait que le pouvoir d'arrêt collisionnel doit être supérieur à celui du champs électrique.

De plus cet algorithme est caractérisé par l'apparition d'une diffusion numérique, en résolvant un système advectif dans la limite diffusive. On peut s'affranchir de cet effet en augmentant la résolution spatiale mais cette procédure affecte le temps de calcul et les performances du code.

Pour les raisons ci-dessus cet algorithme est utile pour valider le modèle M1 mais doit être amélioré pour un cadre plus géneral.

12.5 Validation du model

Le modèle M1 a été mis à l'épreuve pour les plasmas non magnétisés [63], révélant un bon accord avec le code Landau-FP et avec les précédents modèles non locaux. Les deux principaux effets non locaux (la limitation du flux et le préchauffage) sont correctement calculés.

Les moments de la fonction de distribution électronique, calculées avec P1 et M1, montrent un faible désaccord, qui devient négligeable si l'on intégre sur les vitesses. Les moments ont été utilisés pour reconstruire les fonctions de distribution électroniques totales, ce qui a mis en évidence la principale propriété du modèle M1 : la fonction de distribution électronique est toujours bien définie, contrairement au modèle P1.

Nous avons également testé le modèle M1 dans une configuration multidimentionnelle, reproduisant les effets non locaux monodimensionnels et la rotation du flux induite par la contribution de différents gradients en espace. Précisons qu'avant notre modèle, seul le modèle SNB a montré la capacité à fonctionner en deux dimensions.

Le modèle M1 a également été testé avec des plasmas magnétisés.

Le premier essai du modèle M1 pour les plasmas magnétisé a été effectué dans le régime local, qui est décrit par la théorie de Braginskii. Pour tous les degrés de magnétisation le

modèle M1 est capable de reproduire la limitation du flux de chaleur et la rotation induite par les champs magnétiques.

Nous avons enfin étudié la compétition entre les effets non locaux et les effets magnétiques, et montré la domination de chacun d'entre eux en fonction des conditions plasma.

12.6 Application à la stabilité des ondes du plasma

Une analyse cinétique du transport de chaleur sur ondes plasma a été effectuée [63] : L'étude de la stabilité des faisseaux dans un plasma induite par le transport non local le long du gradient de température.

Un exemple est donné avec les ondes de Langmuir : des oscillations électroniques haute fréquence correspondant aux perturbations du champ électrique sur une échelle microscopique. Le transport non local peut perturber ces ondes, induisant une instabilité dans la région froide du plasma. Ce phénomène a été étudié avec nos modèles M1 et P1. Le modèle M1 a montré sa capacité à prédire les instabilités, au contraire du modèle P1 qui prédit des instabilités non physiques où la fonction de distribution électronique devient négative.

Les ondes acoustiques-ioniques peuvent aussi devenir instables dans les régimes d'interêt du transport non local. Leur instabilité peut être induite par une dérive des électrons créée par le champ électrique. Dans ce cas le modèle M1 comme le modèle P1 fonctionnent correctement car les électrons mis en jeu sont faiblement anisotropiques et dans ces conditions le modèle M1 tend vers le modèle P1.

12.7 Application à la propagation des ondes thermiques

Afin de comprendre les effets non stationnaires du transport non local magnétisé nous avons étudié la propagation d'ondes thermiques à travers un plasma magétisé. Ce processus a été analysé en ajoutant divers degrés de magnétisation.

Une étude stationnaire a montré qu'afin d'être modifiés par le champ magnétique, les flux non locaux demandent de plus hauts degrés de magnétisation que leur contrepartie locale.

L'analyse temporelle a également montré un désaccord léger entre M1 et le modèle SNB. Ce dernier semble surestimant les effets de la magnétisation du plasma.

Cette étude a montré que le chauffage est moins performant à la fois dans les régimes non locaux et les régimes magnétisés, du fait d'un temps requis pour aplanir les gradients de température plus grand.

12.8 Perspectives

Nous avons développé et testé avec succés un nouveau modèle pour le transport non local [63]. Ce modèle, basé sur des principes fondamentaux, est capable de :

- tenir compte de fortes variations hors équilibre, en angle et en énergie;
- tenir compte de l'effet du transport d'électrons sur la stabilité microscopique du plasma;
- tenir compte d'un champ magnétique externe, ainsi que de champs magnétiques auto-induits.

De plus il fonctionne dans des configurations multidimensionnelles.

Il reste quelques problèmes ouverts. On peut améliorer le schéma numérique afin de tenir compte des processus de gain d'énergie qui jouent un rôle dans le chauffage lors de l'interaction laser-matière froide. Une comparaison directe avec des simulations Landau-FP doit être effectuée afin de valider définitivement le modèle M1 à l'échelle cinétique et dans le régime magnétisé non local. Cependant les premiers résultats sont prometteurs.

Le modèle M1 est basé sur l'hypothèse que le principe de maximisation de l'entropie angulaire assure la maximisation de l'entropie. Cette hypothèse a déjà été testé dans des régimes fortement anisotropiques, menant à des résultats corrects. Ce travail constitue donc une première étape dans la validation du principe de maximisation de l'entropie angulaire dans les régimes faiblements anisotropes, ce qui ajoute une certaine fiabilité à cette hypothèse.

La capacité à tenir compte de fortes déviations hors équilibre motive l'utilisation du modèle M1 pour la description du transport non local. La théorie moderne de la physique des hautes densité d'énergie, particulièrement la fusion par confinement inertiel, a montré le besoin de tenir compte de phénomènes cinétiques fortement anisotropes, tels un faisseau d'électrons relativites, ou des faisseaux induits par des instabilités paramétriques, afin de prédire et contrôler le transport d'énergie. Le modèle M1, tel qu'il a été développé dans ce manuscrit, peut décrire tant les phénomènes cinétiques faiblements anisotropes que ceux fortements anisotropes. De plus ce travail fournit un moyen de décrire tous les phénomènes cinétiques de la physique des hautes densités d'énergie à l'aide d'un seul modèle.

Être capable de considérer l'effet du transport électronique sur la stabilité du plasma ouvre la voie au processus inverse : tenir compte des modifications du transport non local, dû aux instabilités d'ondes plasma.

Nous avons vu que le champ magnétique peut induire une rotation du flux dans une direction préférentielle ainsi que la suppression du transport non local. Une bonne description du transport non local magnétisé est d'une grande importance pour le contrôle de l'ablation par laser. Ce dernier permet d'ajuster les conditions de température et de densité du plasma en fonction des paramètres laser, avec des applications aussi bien en astrophysique qu'en fusion par confinement inertiel.

Part V

Annexes

List of acronims

AWBS	Albritton, Williams, Bernstein and Swartz [42]
CMG	Colombant, Manheimer and Goncharov [23]
EDF	electron distribution function
EH	Epperlein and Haines [38]
ES	Epperlein and Short [44]
FL	flux limitation
FP	Fokker-Planck
FS	free streaming
HED	high-energy-density
ICF	inertial confinement fusion
LMV	Luciani, Mora and Virmont [21]
M1	see section 5.3.3
MFP	mean free path
P1	see section 5.2.1
SH	Spitzer and Härm [33]
SNB	Shurtz, Nicolaï and Busquet [22]

List of publications and contributes

Publications

- Del Sorbo, D., et al. "Extension of the Reduced Entropic Model to Magnetized Nonlocal Regimes of High-Energy-Density Plasmas." to be submitted.

- Del Sorbo, D., et al. "Reduced entropic model for studies of multidimensional nonlocal transport in high-energy-density plasmas." Physics of Plasmas (1994-present) 22.8 (2015): 082706.

- Del Sorbo, D., et al. "Approach to the study of fast electron transport in cylindrically imploded targets." Laser and Particle Beams 33.03 (2015): 525-534.

Proceedings

- Del Sorbo, D., et al. "Study of Electron Transport in Cylindrically Compressed Matter", 11th Kudowa Summer School "Towards Fusion Energy" Programme & Contributions, OP-24 (2012) 157-160.

Oral contributions

- Del Sorbo, D., et al. "Entropic Moment Model for Description of Nonlocal Transport in High-Energy-Density Physics", Lisbon, invited for a seminar 2015.

- Del Sorbo, D., et al. "Nonlocal Heat Transport Model Based On Entropic Closure Of Moment Equations", Lisbon, ICPP 2014.

- Del Sorbo, D., et al. "Study of Electron Transport in Cylindrically Compressed Matter", Kudowa Summer School "Towards Fusion Energy" 2012.

Poster contributions

- Del Sorbo, D., et al. "Nonlocal Transport Studies with a First Moment Kinetic Model Based on an Entropic Closure", Lisbon, European Physical Society 2015.

- Del Sorbo, D., et al. "Kinetic Study of the Heat Transport with a Energy-Diffusion Nonlocal Model", Orcières, Forum ILP Lasers and Plasmas 2014.

- Del Sorbo, D., et al. "Effect of Nonlocal Heat Transport on the Structure of the Laser Induced ablation Front", in Ohio Summer School, "High Energy Density Physics" 2013.

- Del Sorbo, D., et al. "Study of Electron Transport in Cylindrically Compressed Matter", in Crete Summer School, "Applications of Electronics in Plasma Physics" 2012.

Bibliography

[1] R Paul Drake. *High-energy-density physics: fundamentals, inertial fusion, and experimental astrophysics*. Springer Science & Business Media, 2006.

[2] WJ Nellis, M Ross, and NC Holmes. Shock-compressed liquid hydrogen: Implications for the interior of jupiter. *Oceanogr*, 16:786, 1971.

[3] M Koenig, E Henry, G Huser, A Benuzzi-Mounaix, B Faral, E Martinolli, S Lepape, T Vinci, D Batani, M Tomasini, et al. High pressures generated by laser driven shocks: applications to planetary physics. *Nuclear fusion*, 44(12):S208, 2004.

[4] BA Remington, J Kane, RP Drake, SG Glendinning, K Estabrook, R London, J Castor, RJ Wallace, D Arnett, E Liang, et al. Supernova hydrodynamics experiments on the nova laser. *Physics of Plasmas (1994-present)*, 4(5):1994–2003, 1997.

[5] Lord Rayleigh. *Scientific Papers*, 301(192), 1950.

[6] John D Lawson. Some criteria for a power producing thermonuclear reactor. *Proceedings of the Physical Society. Section B*, 70(1):6, 1957.

[7] Stefano Atzeni and Jürgen Meyer-ter Vehn. *The Physics of Inertial Fusion: Beam-Plasma Interaction, Hydrodynamics, Hot Dense Matter: BeamPlasma Interaction, Hydrodynamics, Hot Dense Matter*, volume 125. Oxford University Press, 2004.

[8] John Nuckolls and Lowell Wood. Laser compression of matter to super-high densities: Thermonuclear (ctr). *Nature*, 239:139, 1972.

[9] John Lindl. Development of the indirect-drive approach to inertial confinement fusion and the target physics basis for ignition and gain. *Physics of Plasmas (1994-present)*, 2(11):3933–4024, 1995.

[10] Max Tabak, James Hammer, Michael E Glinsky, William L Kruer, Scott C Wilks, John Woodworth, E Michael Campbell, Michael D Perry, and Rodney J Mason. Ignition and high gain with ultrapowerful lasers*. *Physics of Plasmas (1994-present)*, 1(5):1626–1634, 1994.

[11] VA Shcherbakov. Ignition of a laser-fusion target by a focusing shock wave. *Sov. J. Plasma Phys.(Engl. Transl.);(United States)*, 9(2), 1983.

[12] R Betti, CD Zhou, KS Anderson, LJ Perkins, W Theobald, and AA Solodov. Shock ignition of thermonuclear fuel with high areal density. *Physical review letters*, 98(15):155001, 2007.

[13] John R Howell, Robert Siegel, and M Pinar Menguc. *Thermal radiation heat transfer*. CRC press, 2010.

[14] C Bellei, PA Amendt, SC Wilks, MG Haines, DT Casey, CK Li, R Petrasso, and DR Welch. Species separation in inertial confinement fusion fuels. *Physics of Plasmas (1994-present)*, 20(1):012701, 2013.

[15] DJ Strozzi, M Tabak, DJ Larson, L Divol, AJ Kemp, C Bellei, MM Marinak, and MH Key. Fast-ignition transport studies: Realistic electron source, integrated particle-in-cell and hydrodynamic modeling, imposed magnetic fields. *Physics of Plasmas (1994-present)*, 19(7):072711, 2012.

[16] D Batani, S Baton, A Casner, S Depierreux, M Hohenberger, O Klimo, M Koenig, C Labaune, X Ribeyre, C Rousseaux, et al. Physics issues for shock ignition. *Nuclear Fusion*, 54(5):054009, 2014.

[17] SV Lebedev, JP Chittenden, FN Beg, SN Bland, A Ciardi, D Ampleford, S Hughes, MG Haines, A Frank, EG Blackman, et al. Laboratory astrophysics and collimated stellar outflows: The production of radiatively cooled hypersonic plasma jets. *The Astrophysical Journal*, 564(1):113, 2002.

[18] R.J. Goldston and P.H. Rutherford. *Introduction to Plasma Physics*. Institute of Physics Publishing, 1995.

[19] L.D. Landau and E.M. Lifshitz. *Phyisical Kinetics*. Robert Maxwell, M.C., 1981.

[20] Michaël Touati, JL Feugeas, Ph Nicolaï, JJ Santos, L Gremillet, and VT Tikhonchuk. A reduced model for relativistic electron beam transport in solids and dense plasmas. *New Journal of Physics*, 16(7):073014, 2014.

[21] JF Luciani, P Mora, and J Virmont. Nonlocal heat transport due to steep temperature gradients. *Physical review letters*, 51(18):1664, 1983.

[22] GP Schurtz, Ph Nicoaï, and M Busquet. A nonlocal electron conduction model for multidimensional radiation hydrodynamics codes. *Physics of Plasmas (1994-present)*, 7(10):4238–4249, 2000.

[23] Wallace Manheimer, Denis Colombant, and Valeri Goncharov. The development of a krook model for nonlocal transport in laser produced plasmas. i. basic theory. *Physics of Plasmas (1994-present)*, 15(8):083103, 2008.

[24] Ph Nicolaï, J-L Feugeas, and GP Schurtz. A practical nonlocal model for heat transport in magnetized laser plasmas. *Physics of Plasmas (1994-present)*, 13(3):032701, 2006.

[25] A Marocchino, M Tzoufras, S Atzeni, A Schiavi, J Mallet, V Tikhonchuk, and J-L Feugeas. Comparison for non-local hydrodynamic thermal conduction models. *Physics of Plasmas (1994-present)*, 20(2):022702, 2013.

[26] D Del Sorbo, Y Arikawa, D Batani, F Beg, J Breil, H Chen, JL Feugeas, S Fujioka, S Hulin, M Koga, et al. Approach to the study of fast electron transport in cylindrically imploded targets. *Laser and Particle Beams*, pages 1–10, 2015.

[27] L.D. Landau and E.M. Lifshitz. *Mechanics*. Butterwroth-Heinenann, 1976.

[28] Prabhu Lal Bhatnagar, Eugene P Gross, and Max Krook. A model for collision processes in gases. i. small amplitude processes in charged and neutral one-component systems. *Physical review*, 94(3):511, 1954.

[29] John David Jackson and John D Jackson. *Classical electrodynamics*, volume 3. Wiley New York etc., 1962.

[30] Jérôme Breil and Pierre-Henri Maire. A cell-centered diffusion scheme on two-dimensional unstructured meshes. *Journal of Computational Physics*, 224(2):785–823, 2007.

[31] RM More, KH Warren, DA Young, and GB Zimmerman. A new quotidian equation of state (qeos) for hot dense matter. *Physics of Fluids (1958-1988)*, 31(10):3059–3078, 1988.

[32] Stanford P Lyon and James D Johnson. Sesame: the los alamos national laboratory equation of state database. *Los Alamos National Laboratory, Los Alamos, NM, LA-UR-92-3407*, 1992.

[33] Lyman Spitzer Jr and Richard Härm. Transport phenomena in a completely ionized gas. *Physical Review*, 89(5):977, 1953.

[34] J-L Feugeas, Ph Nicolai, X Ribeyre, G Schurtz, V Tikhonchuk, and M Grech. Modeling of two-dimensional effects in hot spot relaxation in laser-produced plasmas. *Physics of Plasmas (1994-present)*, 15(6):062701, 2008.

[35] A Marocchino, S Atzeni, and A Schiavi. Effects of non-local electron transport in one-dimensional and two-dimensional simulations of shock-ignited inertial confinement fusion targets. *Physics of Plasmas (1994-present)*, 21(1):012701, 2014.

[36] S. Braginskii. *Reviews of Plasmas Physics*. M. Leontovitch (Consultants Bureau, New York), 1965.

[37] JP Matte and J Virmont. Electron heat transport down steep temperature gradients. *Physical Review Letters*, 49(26):1936, 1982.

[38] EM Epperlein and MG Haines. Plasma transport coefficients in a magnetic field by direct numerical solution of the fokker–planck equation. *Physics of Fluids (1958-1988)*, 29(4):1029–1041, 1986.

[39] SH Glenzer, WE Alley, KG Estabrook, JS De Groot, MG Haines, JH Hammer, J-P Jadaud, BJ MacGowan, JD Moody, W Rozmus, et al. Thomson scattering from laser plasmas. *Physics of Plasmas (1994-present)*, 6(5):2117–2128, 1999.

[40] T Wyatt Johnston. Cartesian tensor scalar product and spherical harmonic expansions in boltzmann's equation. *Physical Review*, 120(4):1103, 1960.

[41] A Bendib, JF Luciani, and JP Matte. An improvement of the nonlocal heat flux formula. *Physics of Fluids (1958-1988)*, 31(4):711–713, 1988.

[42] JR Albritton, EA Williams, IB Bernstein, and KP Swartz. Nonlocal electron heat transport by not quite maxwell-boltzmann distributions. *Physical review letters*, 57(15):1887, 1986.

[43] JR Albritton. Laser absorption and heat transport by non-maxwell-boltzmann electron distributions. *Physical review letters*, 50(26):2078, 1983.

[44] EM Epperlein and RW Short. A practical nonlocal model for electron heat transport in laser plasmas. *Physics of Fluids B: Plasma Physics (1989-1993)*, 3(11):3092–3098, 1991.

[45] SI Krasheninnikov. On nonlocal electron heat conduction. *Physics of Fluids B: Plasma Physics (1989-1993)*, 5(1):74–76, 1993.

[46] Denis Colombant and Wallace Manheimer. Numerical fluid solutions for nonlocal electron transport in hot plasmas: Equivalent diffusion versus nonlocal source. *Journal of Computational Physics*, 229(11):4369–4381, 2010.

[47] RJ Kingham and AR Bell. Nonlocal magnetic-field generation in plasmas without density gradients. *Physical review letters*, 88(4):045004, 2002.

[48] I. P. Shkarofsky, T. W. Johnston, and M. P. Bachynski. *The Particle Kinetics of Plasmas*. McGraw-Hill, 1973.

[49] N.A. Krall and A.W. Trivelpiece. *Principles of Plasma Physics*. Addison-Wesley, 1966.

[50] M Sherlock, AR Bell, RJ Kingham, APL Robinson, and R Bingham. Non-spitzer return currents in intense laser-plasma interactions. *Physics of Plasmas (1994-present)*, 14(10):102708, 2007.

[51] Gerald N Minerbo. Maximum entropy eddington factors. *Journal of Quantitative Spectroscopy and Radiative Transfer*, 20(6):541–545, 1978.

[52] B Dubroca, J-L Feugeas, and M Frank. Angular moment model for the fokker-planck equation. *The European Physical Journal D-Atomic, Molecular, Optical and Plasma Physics*, 60(2):301–307, 2010.

[53] Brigitte Lucquin and Olivier Pironneau. Introduction au calcul scientifique. *Pour la Science*, (234):110, 1997.

[54] C Berthon, J Dubois, B Dubroca, TH Nguyen-Bui, and R Turpault. A free streaming contact preserving scheme for the m1 model. *Adv. Appl. Math. Mech*, 3:259–285, 2010.

[55] Pierre Degond, Lorenzo Pareschi, and Giovanni Russo. *Modeling and computational methods for kinetic equations*. Springer Science & Business Media, 2004.

[56] Sébastien Guisset, Stéphane Brull, Emmanuel D'Humières, and Bruno Dubroca. Asymptotic-preserving scheme for the fokker-planck-landau-maxwell system in the quasi-neutral regime.

[57] M Tzoufras, AR Bell, PA Norreys, and FS Tsung. A vlasov–fokker–planck code for high energy density physics. *Journal of Computational Physics*, 230(17):6475–6494, 2011.

[58] EM Epperlein and RW Short. Nonlocal heat transport effects on the filamentation of light in plasmas. *Physics of Fluids B: Plasma Physics (1989-1993)*, 4(7):2211–2216, 1992.

[59] VT Tikhonchuk, W Rozmus, V Yu Bychenkov, CE Capjack, and E Epperlein. Return current instability in laser heated plasmas. *Physics of Plasmas (1994-present)*, 2(11):4169–4173, 1995.

[60] AV Brantov, V Yu Bychenkov, and W Rozmus. Ion acoustic instability driven by a temperature gradient in laser-produced plasmas. *Physics of Plasmas (1994-present)*, 8(8):3558–3564, 2001.

[61] W Rozmus, VT Tikhonchuk, V Yu Bychenkov, and CE Capjack. Enhanced ion acoustic fluctuations in laser-produced plasmas. *Physical Review E*, 50(5):4005, 1994.

[62] AV Brantov, V Yu Bychenkov, W Rozmus, CE Capjack, and R Sydora. Linear theory of nonlocal transport in a magnetized plasma. *Physics of Plasmas (1994-present)*, 10(12):4633–4644, 2003.

[63] D Del Sorbo, J-L Feugeas, Ph Nicolaï, M Olazabal-Loumé, B Dubroca, S Guisset, M Touati, and V Tikhonchuk. Reduced entropic model for studies of multidimensional nonlocal transport in high-energy-density plasmas. *Physics of Plasmas (1994-present)*, 22(8):082706, 2015.